Hydrological extremes

Improving simulations of flood and drought in large river basins

Utrecht Studies in Earth Sciences

ISSN 2211-4335

Utrecht Studies in Earth Sciences 072

Hydrological extremes

Improving simulations of flood and drought in large river basins

Niko Wanders

Utrecht 2015

Department Physical Geography
Faculty of Geosciences - Utrecht University

Promotors:
Prof. Dr. S. M. de Jong
Prof. Dr. Ir. M. F. P. Bierkens
Prof. Dr. A. P. J. de Roo

Copromotor:
Dr. D. Karssenberg

Examination committee
Prof. Dr. E. F. Wood, Princeton University
Prof. Dr. L. M. Tallaksen, University of Oslo
Prof. Dr. W. Wagner, Vienna University of Technology
Prof. Dr. Ir. R. Uijlenhoet, Wageningen University
Dr. R. A. M. de Jeu, VU University Amsterdam

This research was funded by a grant from the User Support Program Space Research of NWO (contract number NWO GO-AO/30).

ISBN 978-90-6266-383-5

Cover illustration: A compilation of the study areas that were part of the different chapters in this thesis. Every chapter is represented in a part of the cover illustration.

Cover design: Niko Wanders

Printed in the Netherlands by WPS, Zutphen.

Hydrological extremes
Improving simulations of flood and drought in large river basins

Hydrologische extremen
Verbeteringen in overstromings- en droogtesimulaties van grote rivieren

(met een samenvatting in het Nederlands)

PROEFSCHRIFT

ter verkrijging van de graad van doctor aan de Universiteit Utrecht op gezag van de rector magnificus, prof. dr. G. J. van der Zwaan, ingevolge het besluit van het college voor promoties in het openbaar te verdedigen op vrijdag 24 april 2015 des middags te 2.30 uur

door

Niko Wanders

geboren op 29 november 1986 te Leiden

Promotoren:	Prof. dr. S. M. de Jong
	Prof. dr. ir. M. F. P. Bierkens
	Prof. dr. A. P. J. de Roo
Copromotor:	Dr. D. Karssenberg

Don’t worry be happy

Bobby McFerrin

Contents

List of Abbreviations

4DVAR	Four-Dimensional VARiational data assimilation
A-climate	Tropical climate
AEMET	Agencia Estatal de Meteorología
AMSR-2	Advanced Microwave Scanning Radiometer-2
AMSR-E	Advanced Microwave Scanning Radiometer-Earth Observing System
ASCAT	Advanced Scatterometer
B-climate	Desert/Arid climate
BestPrec	Best precipitation scenario
BMBF	Bundesministerium für Bildung und Forschung
C-climate	Temperate climate
CDF	Cumulative Density Function
CHMI-IWSS	Czech Hydrometeorological Institute - Integrated Warning Service System
CLUM	Continuous Local Uncertainty Model
CMIP3	Coupled Model Intercomparison Project Phase 3
CMIP5	Coupled Model Intercomparison Project Phase 5
CMORPH	Climate Prediction Center MORPHing
CONUS	Continental United States
CRU	Climatic Research Unit
CRU TS	Climatic Research Unit Time Series
CSUM	Continuous Spatial Uncertainty Model
D-climate	Snow climate
DGG	Discrete Global Grid product
DLUM	Discrete Local Uncertainty Model
DREAM	DiffeRential Evolution Adaptive Metropolis
DROUGHT-R&SPI	Fostering European Drought Research and Science-Policy Interfacing
E-climate	Polar climate
ECMWF	European Centre for Medium-Range Weather Forecasts
ECMWF-EPS	European Centre for Medium-Range Weather Forecasts - Ensemble Prediction System
EDI	Effective Drought Index
EDO	European Drought Observatory
EEA	European Environment Agency
EFAS	European Flood Awareness System
EnKF	Ensemble Kalman Filter
ERA-interim	ECMWF ERA-interim Reanalysis

ERA40	ECMWF ERA40 Reanalysis
ERS	European Remote Sensing
ESA	European Space Agency
ESA-ESTEC	European Space Agency European Space Research and Technology Centre
EU-JRC	European Commission Joint Research Centre
FAO	Food and Agriculture Organization
FEWS	Flood Early Warning System
FRIEND	Flow Regimes from International Experimental Network Data
GCM	General Circulation Model
GDIS	Global Drought Information System
GFMS	Global Flood Monitoring System
GHM	Global Hydrological Model
GloFAS	Global Flood Awareness System
GLUE	Generalized Likelihood Uncertainty Estimation
GPCC	Global Precipitation Climatology Centre
GRACE	Gravity Recovery And Climate Experiment
GRDC	Global Runoff Data Centre
GRI	Groundwater Resource Index
HBV model	Hydrologiska Byråns Vattenbalansavdelning model
IDW	Inverse Distance Weight
IPCC	Intergovernmental Panel on Climate Change
IPCC-SRES	Intergovernmental Panel on Climate Change Special Report: Emission Scenarios
IPCC-SREX	Intergovernmental Panel on Climate Change Special Report on Extremes
ISI-MIP	The Inter-Sectoral Impact Model Intercomparison Project
KS-test	Kolmogorov-Smirnov test
LISFLOOD	Hydrological model of EU-JRC used in EFAS
LPRM	Land Parameter Retrieval Model
LSMEM	Land Surface Microwave Emission Model
LST	Land Surface Temperature
MAP	Moving Average Precipitation threshold
MAQ	Moving Average Discharge threshold
MAS	Moving Average Soil moisture threshold
MedPrec	Medium precipitation scenario
MODIS	Moderate Resolution Imaging Spectroradiometer
NASA	National Aeronautics and Space Administration
NLDAS-2	Northern Land Data Assimilation System project phase 2

NOAA	National Oceanic and Atmospheric Administration
PCR-GLOBWB	PCRaster GLOBal Water Balance
PCRaster	Software for environmental modelling
PDF	Probability Density Function
PDSI	Palmer Drought Severity Index
PERSIANN	Precipitation Estimation from Remotely Sensed Information using Artificial Neural Networks
QQ-plot	Quantile – Quantile plot
RCM	Regional Climate Model
RCP	Representative Concentration Pathway
RFI	Radio Frequency Interference
SM	Soil Moisture
SMAP	Soil Moisture Active Passive mission
SMHI	Swedish Meteorological and Hydrological Institute
SMOS	Soil Moisture and Ocean Salinity
SPI	Standardized Precipitation Index
SRES	Special Report: Emission Scenarios IPCC
SSMI	Special Sensor Microwave Imager
SWAP	Soil Water Atmosphere Plant model
TMI	Tropical Rainfall Measuring Mission Microwave Imager
TMPA-RT	real-time TRMM Multi-satellite Precipitation Analysis product
TRMM	Tropical Rainfall Measuring Mission
TSDI	Total Storage Deficit Index
TU Wien	Technical University Wien
UNESCO-IHP	United Nations Educational, Scientific and Cultural Organization International Hydrological Programme
VIC	Variable Infiltration Capacity model
VUA	VU Amsterdam
WATCH	WATer and Global Change project
WFD	WATCH Forcing Data
WIMEK-SENSE	Wageningen Institute for Environment and Climate Research, School of Social and Natural Sciences of the Environment
WMO	World Meteorological Organisation

List of Symbols

$\alpha_{downhill}$	Downhill windcorrection factor
α_{path}	Average terrain slope correction factor
α_{uphill}	Uphill windcorrection factor
β	Relaxation factor
ϵ	Random error
$\gamma(lag)$	Variogram variance as function of the lag
μ	Mean
Ψ^f	Model forecast
Ψ^t	True model state
Ψ^a	Analysis state
Ψ	Ensemble model state
ψ	Individual model state
σ	Standard deviation
$\sigma_{retrieval}$	Satellite retrieval uncertainty
$\hat{\sigma}\epsilon_m$	Standard deviation of the random modelled soil moisture error
$\hat{\sigma}\epsilon_s$	Standard deviation of the random satellite soil moisture error
θ_5	$5th$ percentile soil moisture value
θ_{95}	$95th$ percentile soil moisture value
θ_{FC}	Soil moisture field capacity
θ_m	Model soil moisture value
θ_r	Residual soil moisture content
θ_s	Satellite soil moisture values
θ_s	Saturated soil moisture content
θ_{WP}	Soil moisture wilting point
θ	Volumetric soil moisture content
Θ_r	Real soil moisture
Θ_s	Satellite soil moisture random variable
Θ_m	Model soil moisture random variable
ε_m	Random error of the modelled soil moisture
ε_s	Random error of the satellite soil moisture
AID	Area In Drought
Asp	Aspect
b_{xin}	Xinanjiang shape parameter related to saturation degree
b	Bypass flow parameter
$bias$	Bias
$bias_s$	Systematic error of the satellite soil moisture
BS	Brier Score

$c_{downhill}$	Time dependent downhill wind correction
c_{path}	Time dependent average terrain slope correction
c_{pref}	Empirical shape parameter preferential macro-pore flow
c_{uphill}	Time dependent uphill wind correction
$CalMan$	Multiplier on channel Manning's roughness coefficient
$Chan_{N2}$	Multiplier for surface roughness surface runoff
COV	Coefficient of Variance
$CRPS$	Continuous Ranked Probability Score
$dDef_{clim}$	Climate induced changes in the drought deficit volume
$dDef_{combi}$	Combined climate and human induced changes in the drought deficit volume
$dDef_{human}$	Human induced changes in the drought deficit volume
$dVTMclim_t$	Climate induced changes in transient variable threshold
$dVTMhuman_t$	Human induced changes in transient variable threshold
D	Catchment size
DDF	Degree Day Factor
Def	Drought deficit volume
Def_{ctrl}	Deficit volume control period 1971-2000
Def_{future}	Deficit volume future period 2070-2099
$Dist$	Cloud travelling distance
DQX	SMOS retrieval uncertainty
Ds	Drought state
Dur	Drought duration
E	Evaporation
E_{act}	Actual evapotranspiration
E_i	Evaporation from leave interception
F	Meteorological forcing
FAR	False Alarm Rate
$Grad$	Terrain gradient
GW_{prec}	Maximum percolation rate upper to lower groundwater
h	Pressure head
H	Measurement operator
$HumanDef$	Deficit volume under human influence
$HumanVTM_t$	Transient variable threshold under human influence
Int	Drought intensity
$Ksat$	Saturated conductivity
lag	Variogram lag
lim	Limit
lnN	Lognormal random distribution
LAI_n	Perturbed MODIS LAI
LAI_o	MODIS observed LAI
LAI	Leaf Area Index
MAE	Mean Absolute Error

$MR1$	Matrix discretization of probability field realization of $Dur\text{-}StDef$
n	Manning's roughness coefficient
n_{Sc}	Relative occurrence of soil class
$nugget$	Variogram nugget
N	Total number
NS	Nash-Sutcliffe
p'	Perturbed parameterization
p_o	Original parameterization
P_{obs}	Observed precipitation
P_{ra}	Rainfall
P_{sat}	Satellite precipitation
P_{sn}	Snowfall
P_{th}	Precipitation throughfall
P^f	State error covariance matrix
P	Precipitation
p	Parameters
PDY	Percentage Drought per Year
POD	Probability Of Detection
Pr	Probability
$PrisDef$	Deficit volume under natural conditions
$PrisVTM_t$	Transient variable threshold under natural conditions
Q_b	Bypass flow
Q_{mod}	Modelled discharge
Q_{obs}	Observed discharge
Q_{out}	Runoff
Q_{ov}	Overland flow
Q_s	Recharge from unsature zone
Q_{sn}	Snow Melt
Q_x	x^{th} percentile discharge, for flood exceeded less than x% of the time, for drought exceeded for more than x% of the time
Q	Discharge
r^2	Correlation coefficient
r	Correlation
$range$	Variogram range
$rank$	Observation rank
R	Error-covariance matrix
$R1$	Probability field realization of $Dur\text{-}StDef$
$RAPB$	Relative Annual Precipitation Bias
Rch	Recharge to groundwater
$RMSE$	Root Mean Squared Error
$sill$	Variogram sill
S	External losses

Sc	Soil class
Sea	Distance to the sea
SI	Similarity Index
Sn	Snow storage
$SnCoef$	Snow melt rate
SS_{CR}	Soil Moisture Storage Critical Capacity
SS_{FC}	Soil Moisture Storage Field Capacity
SS	Soil Moisture Storage
$StDef$	Standardized Deficit Volume
t	Time
T_{lz}	Linear reservoir constant lower groundwater
T_{uz}	Linear reservoir constant upper groundwater
T	Total simulation length
u_{dir}	Dominant wind direction
VTM_t	Transient variable threshold
VTM	Variable threshold
$VTMctrl_t$	Transient variable threshold control period 1971-2000
$VTMfuture_t$	Transient variable threshold future period 2070-2099
W	White noise
x	Model state
X	Gaussian random variable
y	Observation
Y	Observations
z	Elevation
Z	Gaussian distributed variable

1 Introduction

1.1 Background

Hydrological extremes regularly occur in all regions of the world and as such are globally relevant phemomena with large impacts on society (Kundzewicz and Kaczmarek, 2000). Floods and drought are the most severe hydrological extremes, in terms of their societal impact and potential economic damage. Both extremes are the opposite of one another, where floods are caused by excessive water availability and drought is known as decreased water availability. A flood is caused by above normal streamflow, leading to inundation of areas which are normally not covered by water (European Union, 2007b; Davie, 2008). Drought is defined as below normal water availability (Wilhite, 2000; Tallaksen and Van Lanen, 2004; Mishra and Singh, 2010; Sheffield and Wood, 2011). While drought can occur in all parts of the hydrological cycle (precipitation, soil moisture, groundwater or streamflow), flood is mainly restricted to abnormal (high) levels in streamflow.

Floods and drought are amongst the most costly natural disasters, due to their often large spatial extent and high societal impact. Six of the ten most costly natural disasters of 2013 were either caused directly by these hydrological extremes or enduced by the extreme events, leading to an estimated damage of $77.2 billion for floods and $18 billion for drought events (Aon Benfield, 2014). The drought in the summer of 2003 over Europe caused around 70.000 fatalities, flooding in Vietnam in August 1971 caused 100.000 fatalities in one single event (Aon Benfield, 2014).

The high numbers of economical and human losses indicate the importance of accurate monitoring, forecasting and projection of high impact hydrological driven natural disasters. This is even more urgent for regions where resilience to natural disasters is low and where these events can have a multi-year impact on the economy of the region. In addition to prevention measures, there is a need for accurate alert systems that can help with decision making and early warning of hydrological extremes.

Decision support systems often suffer from high uncertainty from different sources, for instance in meteorological forcing or model parameterization. For accurate model simulations and forecasts of hydrological extremes it is important to reduce the uncertainty from all sources as much as possible. This will improve the predictions and will also result in an increased reliability of decision support systems. Increased reliability in combination with successfull forecasts while making the best possible use of various available data, will eventually lead to increased confidence in simulations of hydrological extremes.

The aim of this thesis is to assess the different sources of uncertainty in model simulations of hydrological extremes. Uncertainty in observations, model parameterization, model states and other components are dealt with at scales ranging from large-scale river basins to global scale hydrology. This introduction will describe the different time scales on which models are applied, the type of observational data available, the types of uncertainty in model simulations and will provide and a detailed description of the objectives of this thesis.

1.2 Simulation, reanalysis, monitoring, forecasting and projection of extremes

Hydrological extremes are often monitored and modelled with computer models that aim at accurately representing the current hydrological conditions. Additionally, these hydrological models are used to produce simulations, reanalysis products, provide forecasts, and make projections of future hydrological conditions (Beven and Young, 2013, example of timescales in Figure 1.1). Different levels of complexity are found for hydrological models, ranging from black box models, simple models consisting of a chain of conceptual buckets (linear reservoirs) to fully 3D models that describe water storage at multiple scales. The different hydrological timescales are described below and in Figure 1.1 their relative order can be found.

Hydrological simulations are defined as simulations of historic hydrological conditions. Typically historical hydrological simulations do not cover recent hydrological events of less than a month or week ago. Hydrological simulations are created with hydrological models that use observed meteorological forcing (e.g. precipitation, potential evaporation, temperature) and in more advanced simulations also components like water abstractions or other water losses in the catchment. Hydrological simulation of historic conditions is the most common application of hydrological models and used in numerous studies.

When historical hydrological simulations are combined with historical observations in a Bayesian framework to improve model simulations, this is called hydrological reanalysis. The aim of a reanalysis product is providing the most realistic simulation of the complete hydrological cycle, based on observations in this cycle. Reanalysis of past hydrological conditions is an important tool to understand the hydrological system (Van Dijk et al., 2014). For example, hydrological models can be benchmarked with a reanalysis dataset. Their capability to reproduce historic hydrological conditions provides valuable information on the quality of the hydrological simulations. An advantage of reanalysis products is that they provide an overview of the complete hydrological cycle and not only of one component of the hydrological cycle.

Monitoring and forecasting are defined as the most realistic simulation and short-term forecast of the current and near future state of the hydrological cycle based on near-

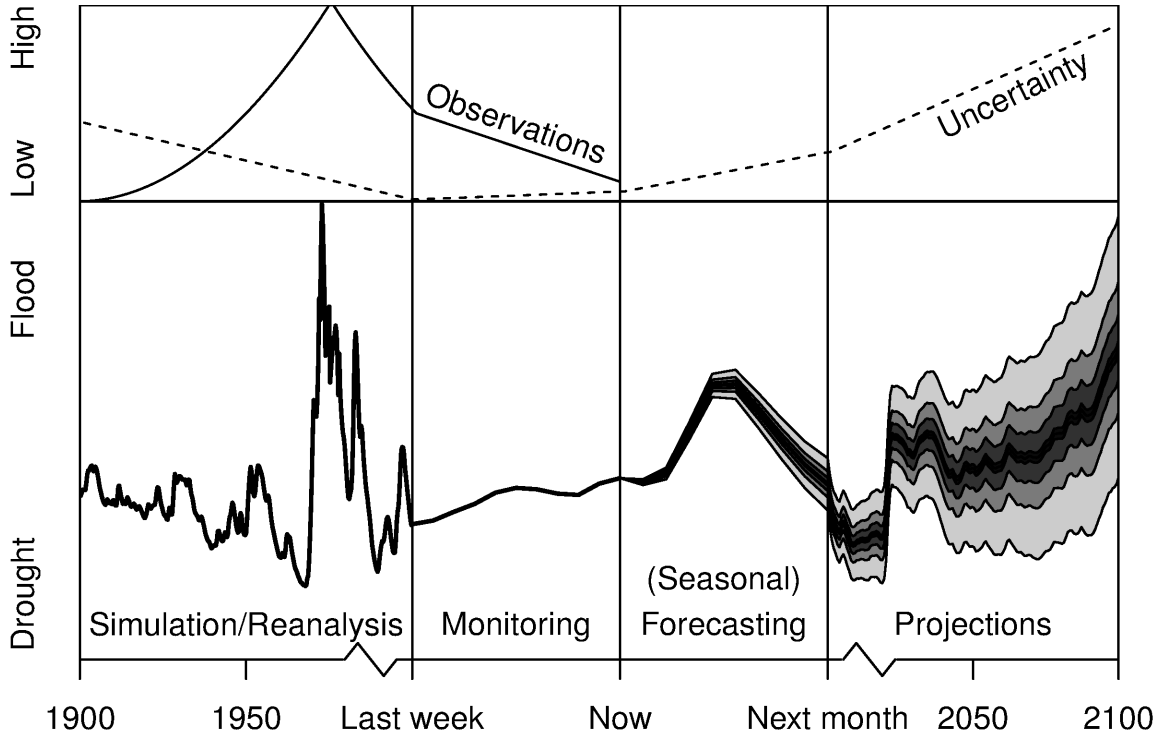

Figure 1.1 Different simulation periods used in hydrological modelling shown for a synthetic example. The hypothetical approximate number of observations available (black line) and the model simulation uncertainty (dashed line) are indicated in the top panel. The larger the spread in the synthetic model simulation, the higher the uncertainty in the hydrological simulations.

real time observations and model simulations. At the national and provincial level numerous hydrological models exist for monitoring real-time conditions and forecasting of small scale events. However, at the continental and global scale the number of operational hydrological systems is still limited. An example of a continental flood forecasting system is the European Flood Awareness System (EFAS, Thielen et al., 2009), developed by the European Commission Joint Research Centre (EU-JRC). At the continental scale the university of Maryland developed the Global Flood Monitoring System (GFMS) to monitor flood conditions from 50°S to 50°N (Wu et al., 2012). In a recent attempt to improve flood awareness, EU-JRC developed the Global Flood Awareness System (GloFAS) together with the European Centre for Medium-Range Weather Forecasts (ECMWF). The ultimate goal of GloFAS is to provide global flood forecasts with a 45 day lead time. Although GloFAS is still under development, it was able to predict recent floods in Pakistan (August 2013) and Sudan (September 2013) with a two week lead time. Recently more research has focussed on the development of drought monitoring and forecasting systems, both continentally and globally (Mishra and Singh, 2010). Examples are the effort of Princeton University to develop the African Drought Monitor, which allows for monitoring and

Table 1.1 Comparison between ground-based observations and observations from remote sensing.

	Temporal resolution	Spatial support	Spatial coverage	Record length	Product Uncertainty
Ground-based	High	Small	Small	Long	Low
Satellite	Medium	Large	Large	Short	High

forecasting of drought events in Africa with a 7 day lead time (Sheffield et al., 2014), and the European Drought Observatory (EDO) developed by EU-JRC, monitoring and forecasting droughts 14 days ahead. Although these are systems that allow for monitoring of drought conditions, the current forecast lead time of 7-14 days provides local authorities with a limited response time.

Simulations of the hydrological cycle for the next decade to century and estimates of potential changes in these periods are defined as hydrological projections. The impact of climate change on hydrological extremes has been of major interest in recent years (e.g. Bates et al., 2008; Feyen and Dankers, 2009; Dai, 2011; Sheffield and Wood, 2011; Seneviratne et al., 2012; Hirabayashi et al., 2013; Prudhomme et al., 2014). This is caused by the severe socio-economic impact related to changes in hydrological extremes. These projections are often based on simulations from Global Hydrological Models (GHMs) forced with results of General Circulation Models (GCMs, Seneviratne et al., 2012; Warszawski et al., 2014). Although these projections are highly uncertain, they do provide insight in possible changes in the hydrological regime and more important changes in hydrological extremes. The uncertainty reduces with new generation GCM simulations, however, uncertainties in GHMs still make projections highly uncertain (Prudhomme et al., 2014).

1.3 Observations

For accurate simulations of hydrological extremes at the global scale, it is important to have high quality observations (Wood et al., 2011). Input data varies from meteorological forcing to soil texture maps used to derive soil parameters. These inputs originate from multiple sources, varying from lab experiments, ground based measurements, airborne surveys to observations by satellites. However, it is important to stress that the spatial and temporal support of these observation types varies strongly (Table 1.1). In general, ground-based observations are deemed reliable, but their disadvantage is that they suffer from a very low spatial support, a small spatial coverage, and various types of measurement errors. Additionally, the density of ground-based observations is not equally distributed across the globe, see for example discharge

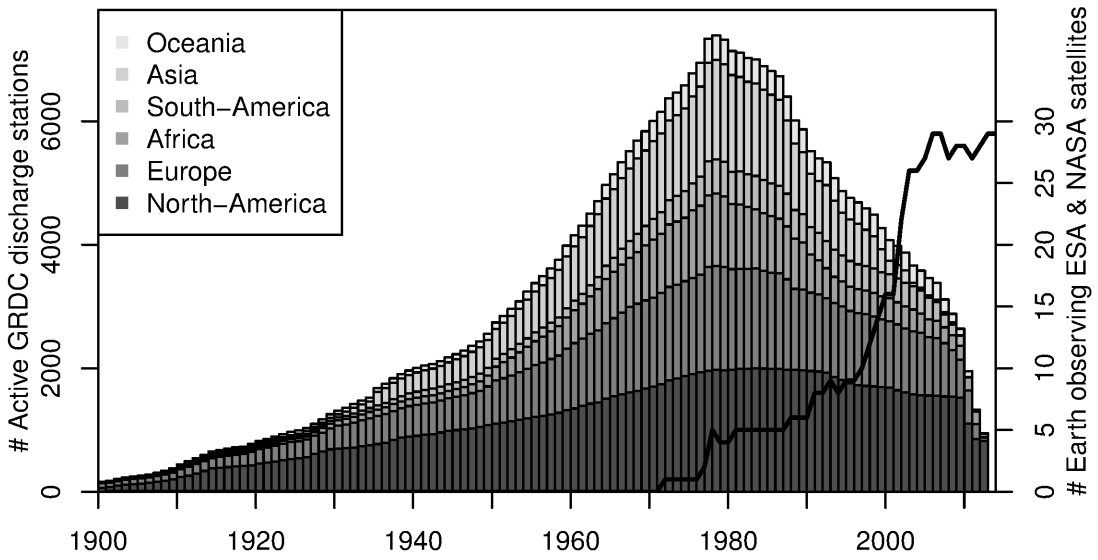

Figure 1.2 Time series of number of discharge (bars) and satellite observations (line). Number of discharge observations is obtained from the Global Runoff Data Centre (GRDC) and the number of earth observing satellites is obtained from the Earth observing programs of both National Aeronautics and Space Administration (NASA) and European Space Agency (ESA). The strong decline in data availability after 2000-2004 is mainly caused by a failure/delay of authorities to report (timely) to GRDC, the decline since 1980 is the real trend in discharge observations availability.

observations in Figure 1.2. In recent years the number of ground-based observations has steadily decreased, resulting in an even lower spatial coverage of ground-based observations (Figure 1.2). This is not only true for discharge observations, but it is a general trend found in ground-based observations (e.g. Lorenz and Kunstmann, 2012).

The decrease in ground-based observations is compensated by an increase in the amount of data available through satellite observations (Figure 1.2). These space-borne observations of different hydrological variables have large potential for hydrological monitoring. Examples are monitoring of precipitation (Kummerow et al., 2001; Huffman et al., 2010), top soil moisture (Wagner et al., 1999; Owe et al., 2008; Kerr et al., 2012) and land surface temperature (Holmes et al., 2009). A disadvantage of satellite observations is that they often provide raw, uncalibrated relative data or land surface parameters, which require ground-truth or other types of validation. Due to the large difference in spatial support of ground-based and satellite observations comparison between these products is often hampered. Nonetheless, satellite observations show a high potential to improve global coverage of important hydrological variables for monitoring the hydrological system. Additionally, they can improve hydrological simulations of the terrestrial water cycle.

1.4 Vagueness in terminology

A problem for simulation of hydrological extremes, is the definition of a hydrological extreme. It is difficult to forecast a hydrological extreme, when multiple definitions are used for different impacts in both nature and society. In flood monitoring and forecasting, thresholds (exceedance levels) are often used to describe which conditions are normal and which conditions are not. Different alert levels of the discharge are used to warn the general public of upcoming threats. Difficulties arise when the thresholds are not known due to limited local data. An often used solution is to make use of long-term simulations of a hydrological model, to assess what discharge values can be considered normal and what should be called exceptional.

For drought monitoring and forecasting it is even more difficult to find *below normal water availability* (Tallaksen and Van Lanen, 2004; Mishra and Singh, 2010; Sheffield and Wood, 2011). Due to the fact that drought occurs in all parts of the hydrological cycle, multiple definitions of drought exist. Additionally, drought should not be confused with water scarcity, which is insufficient water availability to meet local water demands (Tallaksen and Van Lanen, 2004; European Union, 2007a). Numerous indicators exist to define drought conditions, which all focus on different parts of the hydrological cycle (e.g. Keyantash and Dracup, 2002; Wanders et al., 2010). The extensive inventory reported by Wanders et al. (2010) indicates that some of the vagueness is also created by scientists and policy makers, by creating additional drought indicators for every impact. The World Meteorological Organisation (WMO) suggests the Standardized Precipitation Index (SPI) as the indicator to classify global drought (World Meteorological Organization, 2009). However, this neglects the diversity of drought events in the hydrological cycle. This example shows the clear need to make the definition of drought dependent on the impact under study.

1.5 Uncertainty in simulations of hydrological extremes

Uncertainty in hydrological modelling can play an important role in simulations, reanalysis, monitoring, forecasting or projection of hydrological extremes. Uncertainty in hydrological simulations is caused by uncertainty in meteorological forcing, initial conditions, parameterization, boundary conditions and model structure (e.g. Liu and Gupta, 2007, Figure 1.3). Reducing the model uncertainty will lead to improved hydrological simulations, which is highly desirable for monitoring of extremes or hydrological simulations in general. Here the different components that can add to the uncertainty in hydrological simulations are discussed, starting with meteorological forcing, followed by initial conditions, model parameterization and boundary conditions and concluding with the uncertainty as a result of assumptions about the model structure.

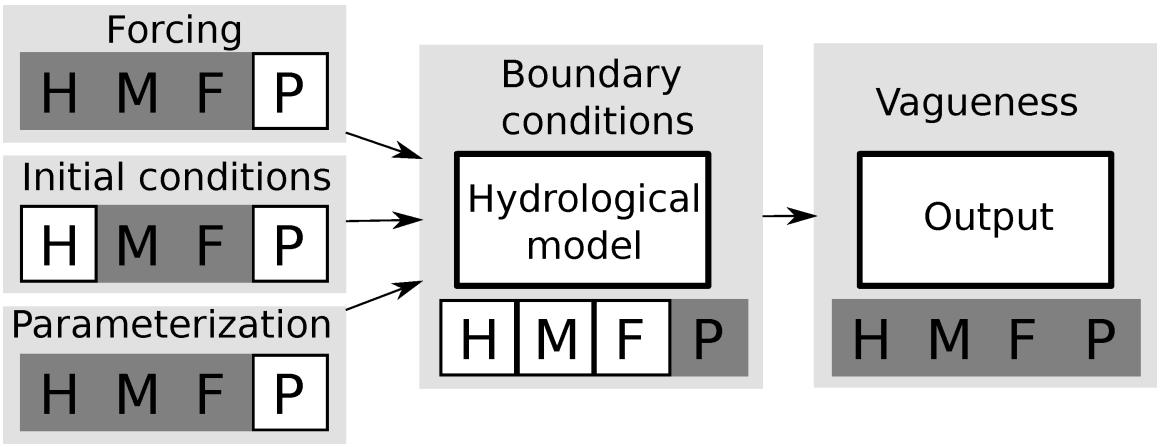

Figure 1.3 Types of uncertainty and vagueness addressed in this thesis. The capital letters refer to uncertainty for particular time periods, i.e. Historic (Simulation/Reanalysis, H), Monitoring (M), Forecasting (F) and Projection (P). Time periods for which uncertainty is discussed and reduced in this thesis are indicated by a dark grey box and white boxes indicate unadressed types of uncertainty.

1.5.1 Meteorological forcing

Meteorological forcing is important for most hydrological simulations, since the hydrological cycle is driven by precipitation and loss of water via evaporation. Uncertainty in meteorological forcing data can have significant impact on hydrological simulations (Fekete et al., 2004).

Precipitation is historically measured with rain gauges, however, the quality of these gauges varies strongly with time and with location. Uncertainty of over 10% as a result of undercatch due to wind effects is not unlikely (Groisman et al., 1991; Groisman and Legates, 1994). In recent years rain radar and other techniques have contributed to the increased availability of precipitation data at the global scale. However, the uncertainty in the precipitation estimates is still considerable.

Evaporation observations are sparse, since it is difficult to obtain observations of this flux from field data or remote sensing. Field observations suffer from low spatial support, which makes it difficult to obtain accurate area averaged values of this important variable. Daily satellite observations of evaporation suffer from a low spatial resolution, which makes it difficult to estimate sub-daily variations in evaporation rates at field scales. Monthly satellite-based evaporation products do not suffer from this low spatial resolution, but do lack the high temporal resolution and hence have reduced applicability in hydrological applications. Additionally, in most hydrological models the potential evaporation rate is transformed to the actual evaporation rate as a function of the available water and vegetation cover. This transformation from potential to actual evaporation introduces more uncertainties.

An approach to reduce this forcing uncertainty is to include additional observations of variables that are influenced by these processes. For example, soil moisture is directly impacted by precipitation, resulting in an increase in soil moisture content, and evaporation, in turn resulting in a decrease in soil moisture content. Observations of changes in soil moisture can thus be used to infer precipitation and actual evaporation rates. Additionally, a water balance approach (assuming no storage changes) can be used to estimate the ratio between inputs (precipitation) and outputs (evaporation and discharge). However, this method suffers from the fact that a longer time period is required for the calculation in order to neglect changes in the catchment storage.

1.5.2 Initial conditions

Simulation uncertainty caused by incorrect initial conditions is mainly important for forecasting of hydrological extremes. The impact of uncertainties in initial conditions can be up to several days for flood events, while for slower reacting drought events this impact can be several months (Wood and Lettenmaier, 2008). Incorrect estimates of the initial conditions will lead to incorrect estimates of the storage in the different components of the hydrological cycle (e.g. interception, soil moisture and groundwater), which will in turn result in incorrect simulation of the fluxes between storages. The traditional way to deal with incorrect initial conditions is to use a spin-up period to compute a dynamic equilibrium state of the hydrological cycle, leading to more balanced model simulations with lower uncertainty. Another approach is to use a data assimilation framework that combines observations and model simulations to estimate a initial state of the hydrological cycle. Data-assimilation has the advantage that shorter spin-up periods are required to correctly estimate storages in the hydrological cycle, due to the fact that observations are used to constrain the intial states.

1.5.3 Boundary conditions

Most models simulate a closed catchment assuming no water flow across the water divide, or without human influences. However, for most catchments one or both of these assumptions are not valid, which results in a mismatch between the simulated water availability and the observed water availability. Boundary flows are especially important in smaller catchments where the exact location of the boundary is often ill defined and the relative impact of the boundary fluxes is large compared to the other fluxes (e.g. precipitation and discharge). Small mismatches between actual hydrological boundaries and the simulation boundary could result in significant simulation errors. Another important uncertainty is introduced by human impacts on the hydrology. This can either be via dams, water abstractions or as a result of transport of water across catchment boundaries. While most hydrological models neglect both

these effects, it can introduce large uncertainties, depending on the scale and the degree of human activity in the catchment.

1.5.4 Parameterization

Model parameterization directly affects the process description in the model and thereby has a large impact on the hydrological simulations. Parameters can be derived from observations (e.g. soil type) or derived from tables that transfer observed characteristics to parameter values (e.g. saturated hydrological conductivity as a function of soil type). To reduce the uncertainty in model parameterization, models are calibrated against a set of observations or state variables. A large variety of calibration algorithms exist, e.g. the Generalized Likelihood Uncertainty Estimation (GLUE, Beven and Binley, 1992), DiffeRential Evolution Adaptive Metropolis (DREAM, Vrugt et al., 2008).

However, calibration of hydrological models is a complicated process and will never lead to a perfect result, due to the fact that models will remain a simplication of the real process (model structural error; see hereafter). Depending on the complexity of the model and the number of parameters, equifinality could occur, where several completely different parameter sets will result in a similar performance (Beven, 2006).

1.5.5 Model structure

Although often ignored and underestimated, the impact of model structure (i.e. the way in which a model simulates water flow through a catchment and the assumption made in the model) on hydrological simulations is significant (Kavetski and Fenicia, 2011). The uncertainty in hydrological projections is even more influenced by differences amongst models than differences amongst forcing datasets (Prudhomme et al., 2014). It is difficult to reduce this form of uncertainty since it requires a variety of models to be run simultaneously. Models are often selected because the user has experience with a particular model or prefers a particular model for other reasons. The model selection is also influenced by the trade-off between model calculation time and model complexity. Some Bayesian techniques exist to optimize the model structure; however, they have a high computational demand and are therefore not often applied.

1.6 Objectives and approach

Reducing uncertainty in hydrological simulations of hydrological extremes is of major importance to reduce socio-economic impacts of these extremes. This is particularly the case in large river basins, where the impact of these events can be devastating for large areas, resulting in high numbers of fatalities and economic damage at national

or even international level. As described above, numerous techniques exist to reduce the uncertainty in model simulations of hydrological processes in general and more specific of hydrological extremes. For example, Bayesian data assimilation methods provide a framework to reduce uncertainty in large scale hydrological models by combining model simulations and observations. Moreover, with an increasing number of observations from satellites, new opportunities arise to improve simulations of the terrestrial water cycle at large sales. Additionally, the impact of correct definitions for hydrological extremes has not been properly studied yet. It is important to agree upon a common terminology which can be used for hydrological simulations and analyses of hydrological extremes.

From the realization that uncertainty and vagueness play a decisive role in using model simulations of hydrologic extremes for disaster management, three research gaps in the current large scale simulations of hydrological extremes are identified that form the basis for the work presented in this thesis: (1) Satellite based observational data is underutilized and uncertainty in hydrological simulation could be reduced to improve parameterization of large-scale hydrological models; (2) A common terminology for hydrological extremes that allows for changes in the climate dynamics is lacking; (3) Quantification of the impact of climate change and human influence on future hydrological extremes.

The overall objective of this thesis is:

To reduce uncertainty in simulations, reanalysis, monitoring, forecasting and projections of hydrological extremes for large river basins.

To pursue this objective, the research presented in this thesis will attempt to answer the following specific research questions:

1. **Is it possible to reduce uncertainty in model simulations and forecasts with ground-based and remote sensing observations?**
   With the increasing availability of remote sensing data, these observations could be a valuable source for hydrological modelling. Currently only a limited number of earth-observing systems is used in hydrological modelling. To increase the potential benefit from remote sensing observations it is important to have an understanding of the uncertainty in the remote sensing observations and the spatial and temporal error structure of these observations. In **Chapter 2** the uncertainty of these remotely sensed soil moisture observations is evaluated over Spain and the temporal and spatial error structure of the observations is studied.

   An important input of hydrological models is precipitation, because it is the driving force behind the hydrology for most of these models. However, in large regions of the world the quality and availability of these data are limited due

to a limited number of ground-based observations. Especially in regions like Africa these limitations apply. Precipitation observed by satellites provides a solution to improve real-time hydrological monitoring in sparsely-gauged regions. Since many applications require a short latency between the observation and the availability of the data to the hydrological community, many satellite-based near real-time precipitation products have been developed. Typically, the uncertainty in these real-time products is larger than found in the reprocessed products that include ground-based observations of precipitation. However, these reprocessed products have a latency of over a week, which makes them unsuitable for real-time applications. To reduce the uncertainty in real-time satellite estimates of precipitation, other real-time observations of land surface variables (that are impacted by precipitation) could be used to reduce real-time retrieval uncertainty. In **Chapter 3** both soil moisture and land surface temperature satellite retrievals are used to reduce the uncertainty of satellite precipitation.

For applications that focus on hydrological reanalysis simulations on the global scale, this latency is not an issue. Typically, ground-based or reanalysis precipitation datasets are used as an input for this application, because they have global coverage and typically cover a longer time period than found for satellite precipitation retrievals (first mission in 1997). Still large uncertainties exist in both datasets due to the limited number of rain gauges in some regions and the uncertainty in rain gauge observations (e.g. undercatch). To reduce the uncertainty in these long-term precipitation records, additional ground-based observations could be used to correct for errors. Discharge observations could be used to quantify the uncertainty, since they provide an integral observation of the water balance over a catchment and hence can be used to infer precipitation. In **Chapter 4** a global discharge dataset is used to quantify uncertainties in precipitation and to create a reanalysis simulation of global hydrology. Additionally, parameterization of the hydrological model is improved with the use of a Bayesian framework.

The impact of model errors in hydrological simulations should be minimal, compared to the uncertainties obtained from the forcing data. A way to reduce simulation uncertainty is the calibration of hydrological models with observations. In many situations discharge data can be used. However, in areas where this type of data is not available, satellite observations of for instance soil moisture could provide valuable information regarding hydrological processes. In **Chapter 5** satellite soil moisture observations as obtained from space-borne microwave sensors are used to calibrate a hydrological model in a Bayesian framework and simulations are compared to simulations calibrated based on ground-based discharge observations.

The information on the temporal and spatial error structures of satellite soil moisture observations and improved parameterization of hydrological models could improve operational flood forecasting. Since the initial conditions are

better estimated with the extra information from additional observations, this could potentially lead to better forecasts. Improved parameterization will lead to more realistic simulations of the hydrological response to precipitation events. In **Chapter 6** the potential of microwave satellite observations of soil moisture and discharge observations is evaluated for operational flood forecasting in the Upper-Danube catchment.

2. **Is it possible to reduce the vagueness in hydrological drought terminology?**
   For monitoring, forecasting and projections of hydrological extremes it is of great importance to have a clear definition of the natural hazard under study. While for flooding this definition is often agreed upon, the definition of hydrological drought is still under debate by the hydrological community. Often meteorological extremes are used as a proxy to study hydrological extremes, while others use observations of discharge to study the same phenomena. In **Chapter 7** the correlation and similarity between different drought indicators is studied and evaluated on the global scale.

   With a changing climate the hydrological climatology will change, which in turn will result in a changed perception of hydrological extremes for both humans and nature. Studies that do not take account of these changes will only study the impact of changes in the hydrology with respect to the current climate. While these changes may be significant, the perception of hydrological extremes will also change in the 21^{st} century. An alternative approach would be to adjust the definition of hydrological drought, and hydrological extremes in general, with respect to a changing climate. In **Chapter 8** the impact of this changing definition of hydrological drought is studied for the 21^{st} century at a global scale.

3. **What is the uncertainty associated with the human and climate impact on projections of hydrological drought?**
   Most studies focus on changes in drought for the 21^{st} century at a global scale, without disentangling the different components that impact these changes. To get a better understanding on the factors (e.g. climate change, catchment characteristics, increased human water abstractions) that influence changes in future hydrological drought it is important to have a more controlled experimental design. In this way the individual impact of climatic changes could be studied, while the feedback with the catchment is identical for all simulations. In **Chapter 9** a synthetic catchment design is used to study the impact of changes in the climatology on hydrological drought for different climatic regions with a set of simulations from GCMs.

   Most GHMs do not incorporate simulations of human water abstractions and reservoir operations. However, these boundary conditions can be of significant importance for the changes in future hydrological extremes. Models that include these human impacts allow one to study the relative impact of human influence

on changes in hydrological extremes. In **Chapter 10** the combined impact of human and climate change on hydrological drought is studied and compared with hydrological drought only impacted by changes in the climatology.

1.7 Innovation and relevance

This work provides a first overview of the use of satellite soil moisture observations to address uncertainties in both meteorological input, model parameterization and flood forecasting initial conditions in hydrological models. The spatial error structure of three well-known satellite soil-moisture products is carefully evaluated and used to improve the potential benefit from these satellite data. This in turn improves flood forecasting skills of a large-scale hydrological model.

This is the first time discharge observations are used to simultaneously estimate model parameters and create a reanalysis product in a Bayesian framework. This results in a closed water balance reanalysis product at the global scale, which has not been achieved before.

Retrieval uncertainty in satellite precipitation is reduced with soil moisture and land surface temperature satellite observations, resulting in an improved real-time satellite product. The impact of land surface temperature observations is significant, which has not been shown before.

The concept of drought is re-evaluated, and by using a novel approach to characterize drought under climate change it is shown that the impact of drought largely depends on the drought perception. Additionally, it is shown that the magnitude of the drought impacts is strongly determined by the methodology that is applied to characterize the drought. This highlights the need for better, less vague, definitions of drought in hydrology.

Finally, it is shown that changes in climatology and human influences have a significant impact on future hydrological drought. These impacts are higher than previously assumed and have a significant impact on the uncertainties in hydrological drought projections.

Part I

Ground-based and satellite observations to reduce uncertainty in hydrological simulations

2 Observation uncertainty of satellite soil moisture products

This chapter is based on:
Wanders, N., Karssenberg, D., Bierkens, M. F. P., Parinussa, R. M., de Jeu, R. A. M., van Dam, J. C., de Jong, S. M., (2012), Observation uncertainty of satellite soil moisture products determined with physically-based modeling, Remote Sensing of Environment, 127, 341-356, doi:10.1016/j.rse.2012.09.004.

Abstract

Accurate estimates of soil moisture as initial conditions to hydrological models are expected to greatly increase the accuracy of flood and drought predictions. As in-situ soil moisture observations are scarce, satellite-based estimates are a suitable alternative. The validation of remotely sensed soil moisture products is generally hampered by the difference in spatial support of in-situ observations and satellite footprints. Unsaturated zone modelling may serve as a valuable validation tool because it could bridge the gap of different spatial supports. A stochastic, distributed unsaturated zone model (SWAP) was used in which the spatial support was matched to these of the satellite soil moisture retrievals. A comparison between point observations and the SWAP model was performed to enhance understanding of the model and to assure that the SWAP model could be used with confidence for other locations in Spain. A time series analysis was performed to compare surface soil moisture from the SWAP model to surface soil moisture retrievals from three different microwave sensors, including AMSR-E, SMOS and ASCAT. Results suggest that temporal dynamics are best captured by AMSR-E and ASCAT resulting in an averaged correlation coefficient of 0.68 and 0.71, respectively. SMOS shows the capability of capturing the long-term trends, however on short time scales the soil moisture signal was not captured as well as by the other sensors, resulting in an averaged correlation coefficient of 0.42. Root mean square errors for the three sensors were found to be very similar ($\pm 0.05\ m^3 m^{-3}$). The satellite uncertainty is spatially correlated and distinct spatial patterns are found over Spain.

2.1 Introduction

Soil moisture is an important variable in many applications and environmental studies, such as numerical weather prediction (Drusch, 2007), global change modelling (Henderson-Sellers, 1996), predicting surface runoff (Brocca et al., 2010), drought

monitoring (Sheffield and Wood, 2007) and modelling evaporation (Miralles et al., 2011). In small catchments ($\leq$ 700 km^2) soil moisture assimilation has been shown to improve discharge simulation (Brocca et al., 2010); the impact in larger scale river basins remains unknown. At this large scale, ground based soil moisture measurements are relatively scarce and therefore lack sufficient spatial density to be accurately up-scaled to improve flood forecasting for large river basins. Soil moisture is highly variable in space and time and thus a high spatial and temporal resolution of observations is required to retrieve good estimates of the actual soil moisture content (Western et al., 2002).

A possible solution to obtain spatially averaged soil moisture for large river basins is the use of soil moisture retrievals from spaceborne sensors measuring in the microwave frequencies. For several years passive and active microwave observations have been used for the retrieval of soil moisture from the Earth's surface. The current Soil Moisture and Ocean Salinity (SMOS) mission observes the Earth's surface in the L-band (1.41 GHz) frequency (Wigneron et al., 1995), because such low frequency observations are most sensitive to soil moisture. SMOS is the first dedicated satellite observing soil moisture from space and was launched in November 2009. In the past, several passive microwave sensors, such as the Advanced Microwave Scanning Radiometer-EOS (AMSR-E), have been used to retrieve soil moisture using multi-channel observations obtained at higher microwave frequencies (e.g. Njoku et al., 2003; Owe et al., 2008). AMSR-E, onboard NASA's Aqua satellite was launched in 2002 and was recently (October 2011) switched off due to rotation problems with its antenna. Also, several active microwave sensors, such as the Advanced Scatterometer (ASCAT) onboard ESA's MetOp satellite, were used for the same purpose. Backscatter measurements at three different azimuth angles are converted to surface soil moisture (Naeimi et al., 2009). Microwave observations are largely unaffected by solar illumination and cloud cover, but can be influenced by topography and active precipitation. Additionally, several studies (De Jeu et al., 2008; Dorigo et al., 2010; Parinussa et al., 2011) showed a decreasing quality of soil moisture retrievals with increasing vegetation density.

Microwave remote sensing provides areal ($625 - 2500$ km^2) averaged soil moisture content with a high temporal resolution (revisit time 1-3 days), which could be used for large scale hydrological applications (Walker and Houser, 2004). However, in operational hydrological modelling (e.g. data assimilation schemes) it is important to provide a good estimate of the uncertainty of the remotely sensed soil moisture product (Crow and Ryu, 2009). Some studies successfully used remotely sensed soil moisture in assimilation schemes showing the potential use of them to improve discharge simulations (e.g. Brocca et al., 2010; Draper et al., 2011). These studies used a single satellite product and made often arbitrary assumptions on the uncertainties in retrieved soil moisture. Also, spatio-temporal variation in uncertainty is mostly neglected. However, to make optimal use of (multiple) remotely sensed soil mois-

ture products in assimilation schemes, it is essential to determine the magnitude and spatial structure of the uncertainties of each product (Van Leeuwen, 2009).

One approach to determine the uncertainty of satellite soil moisture products is to use ground based observations. Unfortunately, this approach is generally hampered by a lack of ground based observation networks with sufficient spatial density (low coverage) to allow for accurate upscaling to the resolution of satellite based soil moisture retrievals (Scipal et al., 2008). Recently, in-situ observations became more readily available (Dorigo et al., 2011) resulting in several studies (e.g. Miralles et al., 2010) providing meaningful information about the differences in spatial resolution between in situ and remotely sensed soil moisture products. Evaluation results from these more traditional in situ validation were performed by e.g. Walker and Houser (2004); Wagner et al. (2007); Albergel et al. (2012). However, these studies did not take into account the difference in spatial resolution of in-situ observations and remotely sensed soil moisture. In these studies, it is assumed that the in-situ observation provides a valid value for the footprint scale modelled soil moisture while this assumption might not always be valid (Crow et al., 2012). Additionally, there is only a small number of in-situ soil moisture networks available with enough coverage to accurately up-scale in-situ observations to the spatial resolution of microwave products. For this reason several evaluation techniques (Crow and Zhan, 2007; Scipal et al., 2008; Dorigo et al., 2010; Crow et al., 2010) have been proposed which circumvent the need for extensive ground-based soil moisture observations.

An additional approach to validate remotely sensed soil moisture is process-based unsaturated zone modelling. An advantage of a physically-based unsaturated zone models is their capability to represent spatio-temporal variation in meteorological forcing, soil parameters and unsaturated zone processes (Finke et al., 1996; De Lannoy et al., 2006). This enables a validation at the spatial resolution of the microwave soil moisture products ($625 - 2500\ km^2$). Matching the spatial scales of remotely sensed soil moisture products and unsaturated zone models is essential to enable the calculations of the uncertainty of the remote sensing product itself (Bierkens et al., 2000). In this study, the physically based Soil Water Atmosphere Plant model (SWAP, Van Dam, 2000; Kroes et al., 2008) was applied, which was successfully used in various studies (e.g. Singh et al., 2006; Baroni et al., 2010). The SWAP model integrates local information (e.g. meteorological stations, soil data) with high spatial resolution (km-scale) remotely sensed imagery (e.g. , Leaf Area Index). Combining information from these different sources allows for up-scaling (also referred to as aggregating) of the high spatial resolution unsaturated zone model to match the spatial resolution of the remotely sensed soil moisture product. The SWAP model uses a high-resolution multi-layer approach in the vertical to deal with the different observation characteristics of the different satellite products, resulting in simulated soil moisture content at several depths, including the top-layer.

The assessment of uncertainty in modelled soil moisture is mostly unknown because uncertainties are not known at the satellite scale and errors made by the hydrological

model are ascribed as satellite error. In reality the model uncertainty could be very large and satellite uncertainty is highly overestimated, because model calibration is often done at locations with a single measurement per model grid point of $64 - 2500\ km^2$. In previous studies the assessment of uncertainty in modelled soil moisture was most of the time unknown because the magnitude and spatial structure of the error was not known. To deal with this problem, model uncertainties and uncertainties of the input parameters are considered in this study when up-scaling the SWAP model to satellite footprint scale.

The aim of this study is to accurately up-scale the high-resolution unsaturated zone model in order to provide a detailed assessment of the uncertainty of the satellite derived soil moisture product at the correct spatial and temporal support. To achieve this aim, the performance of the SWAP model was evaluated at different spatial scales and finally up-scaled to match the coarse resolution satellite soil moisture products. To deal with the unique observation depths of the different microwave systems a high-resolution multi-layer model simulation of SWAP was used. The SWAP model was validated for the REMEDHUS soil moisture network in Spain to investigate if the model could be applied in other regions of Spain for satellite validation, assuming the model could be used without further modifications. Thereafter, soil moisture was modelled for 79 locations in Spain and compared to timeseries of remotely sensed soil moisture product (AMSR-E, SMOS and ASCAT) and the magnitude and spatial structure of the uncertainties was determined.

2.2 Material and Methods

2.2.1 Satellite data

Three satellites that measure soil moisture are used for this inter-comparison study, namely SMOS, ASCAT and AMSR-E (Table 2.1). The SMOS satellite was launched on 2 November 2009 and the data for the level 2A soil moisture product have been available since January 2010 (Kerr et al., 2010). SMOS is the first dedicated soil moisture satellite and uses fully polarized passive microwave signals at 1.41 GHz (L-band) observed at multiple angles. SMOS is developed to measure soil moisture content with a target accuracy (standard error) of 0.04 m^3m^{-3} (Kerr et al., 2001). The overpass time at the equator is 6:00 AM/PM, with a maximum revisit time of 3 days at equatorial latitudes. In this study only morning overpasses have been used, because between midnight and early morning, the soil moisture has an equilibrium state and is not influenced by bare-soil evapotranspiration. The spatial resolution of SMOS is 35-50 km depending on the incidence angle and the deviation from the satellite ground track. The innovative observation technique and algorithms of SMOS are still relatively new and the retrieval algorithm is under constant development. Radio frequency interference (RFI) at L-band has been reported over large parts of Europe

Table 2.1 General sensor properties relevant for this study.

	SMOS	ASCAT	AMSR-E
Frequency (GHz)	1.41	5.3	6.9
Microwave type	Passive	Active	Passive
Spatial resolution (km)	35-50	25	36-54
Max revisit time (days)	3	3	3
Observation depth (cm)	0-5	0-2	0-2
Descending overpass (h)	6:00 PM	9:30 AM	1:30 AM

and Asia, which may impact its soil moisture retrieval (Anterrieu, 2011). RFI will affects SMOS soil moisture retrievals and especially for Europe the observations in the first half of 2010 are partly contaminated by RFI. In this study RFI influenced observations have been removed by filtering the data. SMOS retrievals with an RFI flag raised have been removed from the analysis as were retrievals with a large retrieval uncertainty ($DQX \geq 0.04\ m^3m^{-3}$). SMOS data are obtained from ESA and reprocessed data (Level 2 processor v501) from 2012 have been used for the entire evaluation period. For more detailed information about the SMOS algorithm and the level 2 product the reader is referred to Kerr et al. (2012).

AMSR-E is a multi-frequency (6 bands from 6.9 to 89.0 GHz) passive microwave radiometer and was the first widely used sensor for soil moisture retrievals. AMSR-E is in a sun synchronous orbit with local equator overpass times at 01:30 AM/PM. Several algorithms estimating surface soil moisture from AMSR-E observations exist (e.g. Njoku et al., 2003; Owe et al., 2008). All these algorithms use a combination of observations in several frequencies and/or polarizations, and some use auxiliary data. One of the algorithms using exclusively satellite observations is the Land Parameter Retrieval Model (LPRM) developed by scientists at NASA and the VU Amsterdam (VUA). This model uses a simple radiative transfer equation to retrieve soil moisture and vegetation optical depth from horizontal and vertical polarized brightness temperatures by partitioning the observed signal into its respective soil and vegetation emission components (e.g. De Jeu and Owe, 2003; Meesters et al., 2005). LPRM soil moisture products have been extensively validated against in situ observations (e.g. Wagner et al., 2007; De Jeu et al., 2008; Draper et al., 2009), models (e.g. Loew et al., 2009; Crow et al., 2010; Bisselink et al., 2011) and other satellite products (Wagner et al., 2007; Dorigo et al., 2010). These studies show that LPRM soil moisture captures a large part of the temporal variability (as shown by the correlation coefficient), which was confirmed by Crow et al. (2010) using a completely different approach and using soil moisture anomalies rather than absolute values. This skill was the main driver to select LPRM soil moisture retrievals for this study. AMSR-E makes both day- and night-time observations. In existing studies only night-time

observations were used as it was shown that soil moisture retrievals based on these are more reliable than those based on day-time observations (De Jeu et al., 2008).

Unlike SMOS and AMSR-E, ASCAT uses active microwave technology at a frequency of 5.3 GHz (C-band) to determine the soil moisture content (Wagner et al., 1999; Naeimi et al., 2009). ASCAT uses a change detection method in which the changes in the amount of backscatter are linearly related to changes in soil moisture content and vegetation cover (Naeimi et al., 2009). Data is provided as relative soil moisture content, with respect to the wettest and driest soil moisture conditions measured during the lifetime of ASCAT (Wagner et al., 1999). The spatial resolution of ASCAT is around 25 km and the temporal resolution equals a revisit time of 3 days at 9:30 AM/PM around equatorial latitudes. Only descending passes of ASCAT (9:30 AM) have been used. Reprocessed ASCAT data were obtained from the TU Wien archive.

All satellite soil moisture level 2 products are evaluated on an equal area Discrete Global Grid product (DGG). For the SMOS and ASCAT soil moisture product a DGG is available (Bartalis et al., 2006a), while for the AMSR-E product this DGG is not available. Therefore, the AMSR-E data was projected on the DGG of SMOS using the nearest neighbour approach because both satellites have roughly the same spatial resolution. The DGG of ASCAT uses equally spaced areas of 12.5 km while the other DGG uses a slightly lower resolution of 15 km between points.

ASCAT data, which are by default expressed as values between 0 and 100 (-), indicating very dry and very wet conditions, respectively, was converted to the dynamic range of the model. Although the passive microwave satellite missions, SMOS and AMSR-E, give absolute soil moisture values in m^3m^{-3}, all satellite data was converted using the same approach, to enable a comparison of the absolute errors of satellites. The new satellite values $\theta_{s,new}$ in m^3m^{-3} used here are calculated by:

$$\theta_{s,new} = \frac{\theta_s - \theta_{s,5}}{\theta_{s,95} - \theta_{s,5}}(\theta_{m,95} - \theta_{m,5}) + \theta_{m,5} \tag{2.1}$$

where θ_s are the observed satellite soil moisture values (m^3m^{-3} or -), θ_{95} and θ_5 are the $95th$ and $5th$ percentiles of satellite soil moisture values per DGG location respectively (m^3m^{-3} or -), $\theta_{m,95}$ and $\theta_{m,5}$ are the $95th$ and $5th$ percentiles of modelled soil moisture values for the same DGG location (m^3m^{-3}). Unlike cumulative density function (CDF) matching (e.g. Liu et al., 2011b; Brocca et al., 2011) this approach has the advantage that the shape of the probability density function of each product remains the same and temporal dynamics as well as temporal statistics like correlation are not influenced.

For the retrieval of near surface soil moisture frozen soils and RFI hamper soil moisture observations. Frozen soils hamper the soil moisture retrieval due to changes in the dielectric constant when water freezes. Therefore, retrievals done with an air temperature below $4°C$ were excluded from the analysis. For AMSR-E these observations are excluded by the LRPM algorithm because AMSR-E is capable of measuring the

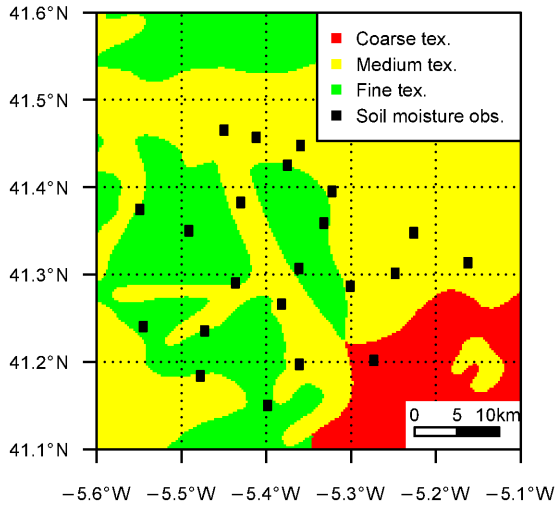

Figure 2.1 Locations of 22 soil moisture observation points and soil texture information derived from the JRC European soil texture map (Van Liedekerke et al., 2006) for the REMEDHUS site in Spain.

soil surface temperature. RFI distorts the incoming signal and the microwave signals measured by the satellites. Although the retrievals of all satellites suffer from RFI presence, SMOS appears to have the most RFI-related problems (Kerr et al., 2012). From the second part of 2010, the influence of RFI has, however, significantly been reduced for most countries in Europe, including Spain.

2.2.2 In-situ soil moisture measurement and meteorological data

The validation of the three remotely sensed near surface soil moisture products was carried out for the mainland of Spain. Spain was selected because of the presence of the REMEDHUS soil moisture network providing data for the period 2006-2011 at a high temporal resolution for a relatively large number of sampling locations (Martínez-Fernández and Ceballos, 2003; Sánchez et al., 2010). From the International Soil Moisture Network (Dorigo et al., 2011), in-situ soil moisture content is available at a depth of 5 cm for 22 locations (Figure 2.1). An additional advantage of Spain is the availability of a high number of meteorological stations distributed throughout Spain.

Data from 79 meteorological sites in Spain (Figure 2.2) obtained from the Spanish meteorological service (AEMET), were used for the evaluation of the three remotely sensed soil moisture products. These meteorological sites have meteorological data for the period January 2009-July 2011 including precipitation and the variables required to estimate Penman-Monteith reference evapotranspiration. It is also assumed that

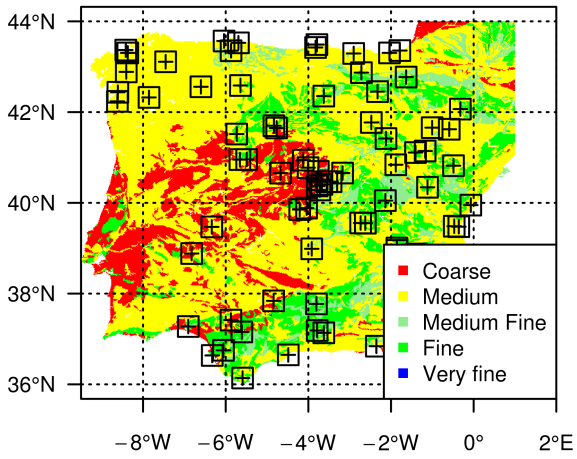

Figure 2.2 Soil map of Spain overlaid with meteorological sites (crosses) and model areas used for comparison with satellite soil moisture (squares); open water is excluded from the simulation.

up to a maximum distance of 35 km ground observations provide a good estimate of the precipitation and evapotranspiration for soil moisture modelling. The interception was calculated with the 8-day composite of the Leaf Area Index (LAI) from the Moderate Resolution Imaging Spectroradiometer (MODIS) sensor, provided at 1×1 km spatial resolution (Myneni et al., 2003). To determine Van Genuchten soil parameters for each simulation the European Commision - Joint Research Centre European soil texture map with a resolution of 1×1 km was used (Van Liedekerke et al., 2006). Joint probability distributions of the Van Genuchten soil physical parameters (Van Genuchten, 1980) per soil texture class were obtained from Meyer et al. (1997). With these joint distributions, spatial variability within each soil texture class is introduced such that the correlation between Van Genuchten parameters is preserved.

2.2.3 SWAP model set-up

SWAP is a physically-based model simulating flow processes in the unsaturated zone (Van Dam, 2000; Kroes et al., 2008). A short overview of the most important concepts and assumptions is given below. Soil water flow in the SWAP model is calculated with the Richards equation (Richards, 1931):

$$\frac{\partial \theta}{\partial t} = \frac{\partial}{\partial z}\left[K(\theta)\left(\frac{\partial h}{\partial z}\right) + 1\right] - S \tag{2.2}$$

where θ is volumetric soil moisture content ($m^3 m^{-3}$), h pressure head (m), z the elevation (m, positive upwards), t time (d), S a sink of the system ($m\ d^{-1}$) which

accounts for external losses like transpiration and evaporation and $K(\theta)$ the conductivity ($m\ d^{-1}$) as a function of water content (θ). The SWAP model uses an implicit, backward, finite difference scheme to solve the Richards equation. The Mualem-Van Genuchten relations are used to determine the hydraulic properties of the soil. The soil water content, θ, ($m^3 m^{-3}$) is modelled by:

$$\theta(h) = \theta_r + \frac{(\theta_s - \theta_r)}{[1 + |\alpha h|^n]^{1-1/n}} \tag{2.3}$$

where, h is the pressure head (m), θ_r, θ_s are the residual and saturated soil moisture content ($m^3 m^{-3}$), respectively, and α (-) and n (-) are the shape parameters (Van Genuchten, 1980). The parameters of Equation 2.3 are derived from the soil texture map. The model runs with an hourly timestep and is composed of 28 vertical layers representing the soil up to a depth of 150 cm below the soil surface (Figure 2.3). The first 10 cm was simulated using 10 layers of 1 cm, followed by 8 layers of 5 cm, followed by 10 layers of 10 cm. This high vertical resolution of soil layers was used in order to have a detailed estimate of the soil moisture content at different penetration depths of the radar signal. A free drainage bottom boundary condition is applied to the model. Soil water uptake by roots is assumed to be evenly distributed up to a depth of 70 cm, to simulate an average vegetation. Daily potential evapotranspiration was calculated with the Penman-Monteith equation following Allen et al. (2006) which requires air pressure, wind speed, air humidity and daily temperature (maximum, mean, minimum) from meteorological stations. The potential fluxes of transpiration and evaporation are modelled as a function of the LAI. The actual transpiration flux is calculated as described by Feddes et al. (1988). The actual evaporation flux is the minimum of the potential evaporation, the maximum soil water flux and the maximum evaporation flux according to Black et al. (1969). Interception of precipitation was calculated following Von Hoyningen-Hüne (1983) with an maximum interception capacity of 0.25 $mm\ LAI^{-1}$.

In this study a model was used which is normally applied to field scale unsaturated zone modelling instead of large scale applications. Lateral flow might be very important on the field scale (Harter and Hopmans, 2004), but is negligible at the support of satellites and is thus assumed zero. The effect of irrigation in Spain is assumed to be small since throughout Spain less than 10% of the land is irrigated (Siebert et al., 2007).

2.2.4 Evaluation of model performance and sensitivity analysis

The uncertainty of modelled soil moisture is assessed, using a Monte Carlo approach by perturbing the following input data and parameters of SWAP: precipitation (P), evapotranspiration (E), LAI and soil properties. Since P, E, LAI and soil physical parameters are found to have the largest influence on the simulation of near surface soil moisture (Finke et al., 1996; De Lannoy et al., 2006) other parameters were kept

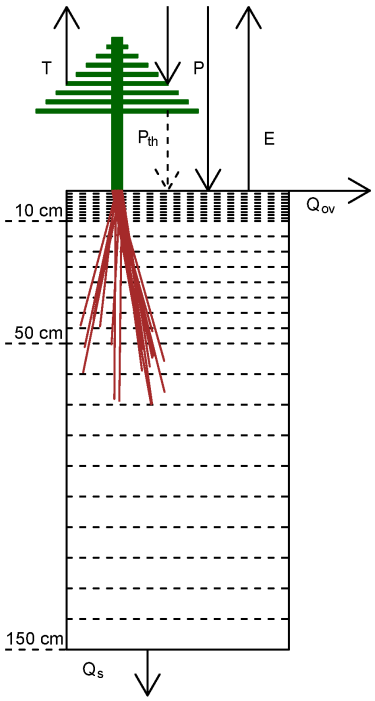

Figure 2.3 SWAP model set-up, precipitation (P), evaporation (E), throughfall from vegetation (P_{th}), transpiration from leaves (E_i), overland flow (Q_{ov}) and bottom out flux (Q_s). Model layers are indicated by the dotted horizontal lines.

constant and are assumed to have a negligible effect on the uncertainty of modelled soil moisture. The structural error was not taken into account either since it was assumed to be subordinate to errors in the model forcing and parameters.

Three error models were used to add uncertainty to the input data and parameters of the SWAP model (Table 2.2). In the Continuous Spatial Uncertainty Model (CSUM), variogram models and observations were used to create realizations of meteorological variables conditioned to observed values at the meteorological stations, $P_{obs}(x,t)$. For precipitation ($P(x,t)$, mm) it is assumed that:

$$P(x,t) = Z(x,t)^2 \tag{2.4}$$

where $Z(x,t)$ is a Gaussian distribution variable with spatial index x (Schuurmans et al., 2007). The spatial correlation of $Z(x,t)$ ($mm^{0.5}$) is given by a linear variogram:

$$\gamma(lag) = (sill - nugget)\frac{lag}{range} + nugget \tag{2.5}$$

where $\gamma(lag)$ is the variance as a function of the lag lag (m), the sill $sill$ (mm), the nugget $nugget$ (mm), and the range $range$ (m), of the variogram. The variogram was computed with observations from all 79 stations over a period of 2.5 years without

Table 2.2 Description of variables and used uncertainty model for each perturbed parameter of the SWAP model. Error models given are the Discrete Local Uncertainty Model (DLUM), Continuous Spatial Uncertainty Model (CSUM) and Continuous Local Uncertainty Model (CLUM).

Var	Description	Source	Error model
θ_s	Saturated soil moisture	Meyer et al. (1997)	DLUM
θ_r	Residual soil moisture	Meyer et al. (1997)	DLUM
$K(\theta)$	Unsaturated conductivity	Meyer et al. (1997)	DLUM
n	Van Genuchten n-parameter	Meyer et al. (1997)	DLUM
α	Van Genuchten α-parameter	Meyer et al. (1997)	DLUM
P	Precipitation	Meteo station	CSUM
E	Evapotranspiration	Meteo station	CSUM
LAI	Leaf Area Index	MODIS satellite	CLUM

making any distinction between the different seasons or different spatial scale of the precipitation events. Since the required data to create variogram models for individual precipitation events is not available it was decided to use a single variogram model. With this variogram a Gaussian random simulation conditioned to the observations $P_{obs}(t)$ (mm), was performed, obtaining realizations of maps of precipitation, $P(t)$ (mm), for each day of the simulation. Following the same approach a variogram model was fitted to the Penman-Monteith reference evapotranspiration calculated at the station locations. Evapotranspiration was not transformed and was assumed to have a Gaussian distribution with a linear variogram (Equation 2.5). This model was used to simulate possible fields of evapotranspiration for the reference locations, in order to assess the effects of evapotranspiration uncertainty.

The Continuous Local Uncertainty Model (CLUM) is used to introduce uncertainty in LAI values and is given by:

$$LAI_n(t) = LAI_o(t) \cdot X(\mu, \sigma) \tag{2.6}$$

where LAI_n is a random variable (m^2m^{-2}), LAI_o is the observed MODIS LAI value (m^2m^{-2}), $X(\mu, \sigma)$ is a Gaussian random variable with mean, μ, and standard deviation, σ. In this study μ (-) is set to 1 and σ (-) was based on a study from Yang et al. (2006) and is set to 0.1 introducing random error in the LAI used for the calculations of the SWAP model.

The Discrete Local Uncertainty Model (DLUM) is applied for the soil physical parameters and uses local properties to add uncertainty to parameters. With the DLUM the soil texture of a location is conditionally changed for 20% of the locations. Since errors in soil texture maps are not uncommon (Hengl and Toomanian, 2006) this 20%

error was introduced to account for the effect of misclassification. Realizations of soil texture were created by randomly changing the soil texture of cells. In creating a realization, for each cell, the probability of a newly selected soil class (c) is calculated as:

$$Pr(c) = \frac{n_{Sc,i}}{N - n_{Sc,j}} \tag{2.7}$$

where $n_{Sc,i}$ and $n_{Sc,j}$ are the relative occurrences of the perturbed and observed soil texture over Spain, respectively, and N is the total number of pixels on the 1×1 km soil texture map. If a misclassification occurs, the soil texture is changed and will not be ascribed to j again, resulting in newly assigned texture classes.

The predictive QQ-plot as described by Laio and Tamea (2007) was used to determine if the model uncertainties and combined uncertainty of the input data could explain the variation between different points of the REMEDHUS network. The predictive QQ-plot is a measure to check whether the obtained Monte Carlo simulation results in a probability density function (PDF) that corresponds to the PDF of the model prediction errors. In the predictive QQ-plot the probability integral transforms to:

$$z_i = \int_{-\infty}^{x_i} f(x)dx \tag{2.8}$$

where $f(x_i)$ is the PDF of model outputs obtained from the uncertainty analysis (Monte Carlo simulation), x_i is the value at observation location i and z_i the associated cumulative probability. Thus, z_i gives the probability of the observed values with respect to the distribution of predicted values from the Monte Carlo simulation. The z_i values are plotted against their cumulative density function, $Rank_i(x_i)$, which is produced from the observation rank $rank(x_i)$:

$$Rank_i(x_i) = \frac{rank(x_i)}{n+1} \tag{2.9}$$

where n is the total number of x_i values. When the z_i plotted against the $Rank_i$ are on the 1:1 line, the PDF from the uncertainty analysis correctly represents the prediction errors and the predictions are unbiased. The non-parametric Kolmogorov-Smirnov test (KS-test) is used to evaluate whether the results are within the 95% confidence interval of the 1:1 line. More details of the predictive QQ-plot are given in Laio and Tamea (2007).

The performance of the SWAP model at the REMEDHUS site was evaluated using the Pearson correlation:

$$r = \frac{\sum_{t=1}^{N}(\theta_o(t) - \mu_o)(\theta_m(t) - \mu_m)}{(N-1)\sigma_o \cdot \sigma_m} \tag{2.10}$$

where θ_o is the observed soil moisture (m^3m^{-3}), θ_m is the modelled soil moisture (m^3m^{-3}), μ_o is the average observed soil moisture over the entire simulation period (m^3m^{-3}), μ_m is the average modelled soil moisture over the entire simulation period

(m^3m^{-3}), σ_o and σ_m are respectively the standard deviation of the observed and modelled soil moisture (m^3m^{-3}) and N is the total number of time steps in the analysis. σ_o is calculated from the average observed soil moisture over the simulation period. The Root Mean Square Error ($RMSE$) is given by:

$$RMSE = \sqrt{\frac{\sum_{t=1}^{N}(\theta_m(t) - \theta_o(t))^2}{N}} \tag{2.11}$$

with N, the total number of observations. r for the evaluation of the remotely sensed soil moisture over Spain is calculated by:

$$r = \frac{\sum_{t=1}^{N}(\theta_m(t) - \mu_m)(\theta_s(t) - \mu_s)}{(N-1)\sigma_m \cdot \sigma_s} \tag{2.12}$$

where $\theta_s(t)$ is the satellite soil moisture (m^3m^{-3}), $\theta_m(t)$ is the modelled soil moisture (m^3m^{-3}), μ_s is the average satellite soil moisture over the entire simulation period (m^3m^{-3}), σ_m and σ_s are respectively the standard deviation of the modelled and satellite soil moisture (m^3m^{-3}) and N is the total number of time steps in the analysis. The model bias, $bias_m$ (m^3m^{-3}) is given by:

$$bias_m = \mu_o - \mu_m \tag{2.13}$$

where μ_o and μ_m, respectively, are the average observed and modelled soil moisture over the entire simulation period (m^3m^{-3}), where a negative value indicates an underestimation of the soil moisture. The REMEDHUS site was not used for calibration of the model, only to evaluate the model and to determine the errors in the modelled soil moisture and input data. Soil moisture was simulated for the entire period from 2006-2010. In total 2000 simulations were done with perturbed parameters and input data for the REMEDHUS site in order to accurately capture the full probability density functions of all parameters and input data. This high number of simulations also allowed to accurately calculate the model uncertainty and study the model sensitivity to the full range of possible parameters sets.

For all selected 79 meteorological stations, a Monte Carlo approach (150 realizations) was used to determine the overall modelled uncertainty at satellite footprint scale. Soil moisture around the meteorological site was simulated for a $0.5° \times 0.5°$ area centered around the location of the meteorological station. Larger simulation areas would require the use of interpolation techniques to derive values between stations which could result in large uncertainties leading to high model uncertainties. The comparison between SWAP and different satellite products was made on the scale of the specific satellite DGG by upscaling SWAP to the DGG resolution ($\approx 150 - 225\ km^2$) by taking the arithmetic mean of the model simulations over the satellite footprint area and penetration depth. The comparison between the model and different satellites is done at the overpass time of the satellite with a maximum temporal mismatch of 30 minutes due to the one hour simulation time steps. The correlation, random

error and biases between satellite and the mean of the Monte-Carlo simulations were used as performance indicator of the satellite soil moisture for each location. The correlation R for the evaluation of the remotely sensed soil moisture is calculated using Equation 2.12.
The satellite soil moisture is considered as a random variable composed of three terms:

$$\Theta_s(t) = \Theta_r(t) + \varepsilon_s - bias_s \tag{2.14}$$

where $\Theta_s(t)$ is a random variable (m^3m^{-3}) representing the satellite soil moisture, $\Theta_r(t)$ is the real soil moisture (m^3m^{-3}), ε_s is the random error of satellite soil moisture (m^3m^{-3}) and $bias_s$ is the systematic error of the satellite soil moisture (m^3m^{-3}). The satellite soil moisture bias ($bias_s$) compared to the model is calculated by:

$$bias_s = \mu_s - \mu_m \tag{2.15}$$

where μ_s is the average satellite soil moisture over the entire simulation period (m^3m^{-3}). In this study it is assumed that the $bias_s$ remains constant over time. The modelled soil moisture is considered as a random variable given by:

$$\Theta_r(t) = \Theta_m(t) + \varepsilon_m \tag{2.16}$$

where $\Theta_m(t)$ is a random variable (m^3m^{-3}) representing the modelled soil moisture and ε_m is the random error of modelled soil moisture (m^3m^{-3}). The satellite error over time is computed with:

$$\epsilon_s(t) = \theta_s(t) - \theta_m(t) - \epsilon_m(t) + bias_s \tag{2.17}$$

where $\epsilon_s(t)$ is the satellite error as a function of time (m^3m^{-3}) and $\epsilon_m(t)$ is the model error over time (m^3m^{-3}), where it is assumed that $\epsilon_m(t) = \theta_r(t) - \theta_m(t)$. In addition the satellite standard error is calculated as:

$$\hat{\sigma}\epsilon_s = \sqrt{\frac{\sum_{t=1}^{N}(\theta_s(t) - \theta_m(t) - bias_s)^2}{N}} - \hat{\sigma}\epsilon_m \tag{2.18}$$

where $\hat{\sigma}\epsilon_s$ is the standard deviation of the random satellite error (ε_s) over the time period $1...N$ and $\hat{\sigma}\epsilon_m$ is the standard deviation of ε_m (obtained from the Monte Carlo analysis). It is assumed that there is no correlation between the errors of the model and satellite and therefore the covariance is omitted in Equation 2.18.

The calculated $\hat{\sigma}\epsilon_s$ (Equation 2.18) values for each location are related to geographical and climatological properties of all 79 meteorological stations, in order to create a better understanding of the satellite performance as function of these environmental variables and possible error sources. Previous studies stated that several external factors may have a negative influence on soil moisture mapping performance, namely topography (Engman and Chauhan, 1995), dense vegetation (Njoku and Li, 1999; De Jeu et al., 2008; Parinussa et al., 2011), soil moisture wetness conditions (Troch

et al., 1996) and land-sea contamination (Njoku and Kong, 1977; Owe et al., 2008). The effect of these external factors on the mapping performance of microwave satellites was tested using the SWAP model simulations over Spain. External factors evaluated include the gradient ($Grad$), calculated as the average slope (%) over the support of the satellite and distance to the sea (Sea), calculated as the shortest distance between the location and the coast (km). To calculate these values the Digital Elevation Model of Spain, acquired by the Shuttle Radar Topography Mission, was used on a 30 meter resolution. The average soil moisture content (μ_m, m^3m^{-3}) and standard deviation of soil moisture content (σ_m, m^3m^{-3}) over time were calculated per location. Additionally the impact of the Leaf Area Index ($LAI(t)$, m^2m^{-2}) and the time dependent soil moisture content ($\theta(t)$, m^3m^{-3}) on the satellite error was evaluated. Their influence is evaluated on the time dependent satellite error $\epsilon_s(t)$, where (t) indicates the variation of error over time.

The spatial pattern of correlation (r) and standard error ($\hat{\sigma}\epsilon_s$) over Spain were studied for the three satellite products. Additionally, the spatial correlation between errors ($\epsilon_s(t)$) was investigated in order to determine if errors are randomly distributed or correlated in both space and also time. A variogram was calculated to determine to what distance errors are correlated (Cressie, 1993); changes in these patterns through seasons are not taken into account.

2.3 Results

2.3.1 SWAP model validation with in-situ observations

The obtained semi-variogram models of the square root of precipitation and Penman-Monteith reference evaporation from the meteorological observations are shown in Figure 2.4. The precipitation semi-variogram models obtained in this study show a great resemblance with those calculated for medium and large extent precipitation events (Schuurmans et al., 2007). It is assumed that these variogram models are valid to produce a realistic simulation of precipitation and reference evaporation uncertainty over Spain.

Modelled soil moisture at 5 cm depth was validated against in-situ measurements to examine if the SWAP model is capable of producing correct near-surface soil moisture simulations. Results show that mean modelled soil moisture by SWAP is in good agreement with the mean observed soil moisture values of the REMEDHUS network 2010 (Figure 2.5). A high correlation ($r = 0.878$) is found between the SWAP model mean and mean of observations, while the root mean square error ($RMSE$) is low (0.025 m^3m^{-3}). A small positive $bias_m$ of 0.01 m^3m^{-3} (Equation 2.13) exists between model mean and the observations which is mainly caused by overestimated soil moisture values in May and June. This behaviour is probably caused by an underestimation of evapotranspiration and only seen at the REMEDHUS site in 2010. It

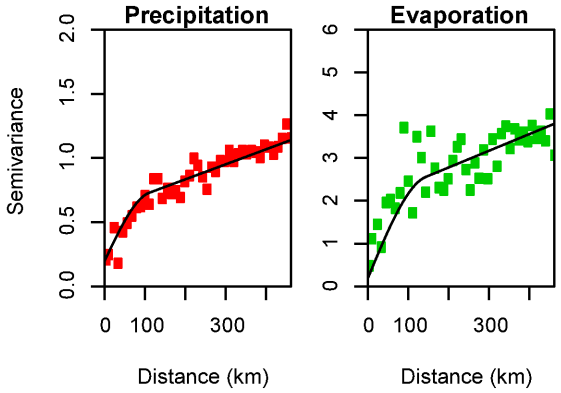

Figure 2.4 Semi-variograms of the square root of observed precipitation ($mm^{0.5}$) and Penman-Monteith reference evaporation (mm) for the period January 2009 - June 2011 over Spain based on observations of 79 meteorological stations.

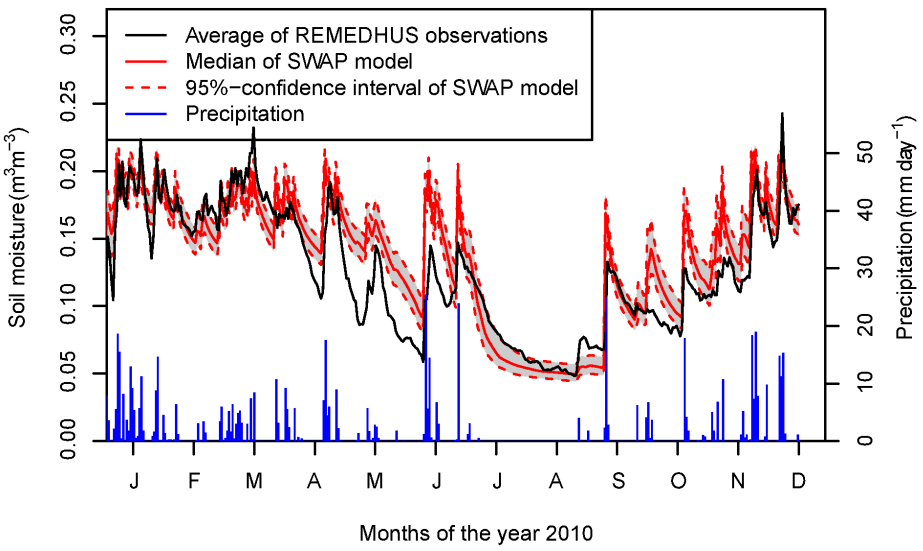

Figure 2.5 Comparison between the average SWAP modelled soil moisture at the REMEDHUS network and the average of the in-situ observations of the REMEDHUS network for the year 2010.

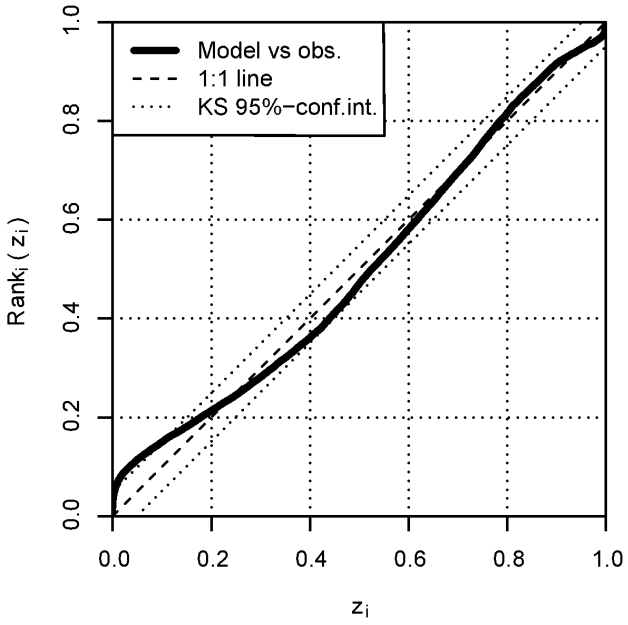

Figure 2.6 Predictive QQ-plot for validation of the observations of the REMEDHUS network (Equation 2.8) against the SWAP model (Equation 2.9) for the period 2006-2010. The 95% confidence interval of the Kolmogorov-Smirnov (KS) test is indicated as well as the 1:1 line.

was not found in other years. From the results of the REMEDHUS site it was found that the Van Genuchten pore-size distribution parameter $(n, -)$ should not exceed 2.55, which indicates very coarse sand. Higher values (e.g. coarse gravel) could lead to unrealistic soil moisture simulations at REMEDHUS and in some situations could lead to model instability. The model was also evaluated by comparing the full PDF of the model and the 22 observations at the REMEDHUS network with the predictive QQ-plot (Equation 2.8 and 2.9). The predictive QQ-plot (Figure 2.6) shows that the modelled soil moisture is within the 95%-confidence interval of the KS-test. The $bias_m$ of 0.01 m^3m^{-3} calculated with Equation 2.13 was also found in the predictive QQ-plot. The SWAP model slightly overestimates the amount of low soil moisture values compared to the observations as seen from a small deviation below 0.2 m^3m^{-3} soil moisture content. This deviation is however not significant as shown by the KS-test.

From Figure 2.5 and 2.6, as well as from the high r, low $RMSE$ and low bias, it is concluded that the overall performance of the SWAP model as well as the estimated uncertainty of the input data and parameters is of good quality for a proper simulation of observed soil moisture at 5 cm depth. The predictive QQ-plot shows that variation within and between soil units is well captured by the model at the REMEDHUS network. Without taking into account the structural error of the SWAP model, the simulations of soil moisture show a good agreement with the observations at a the

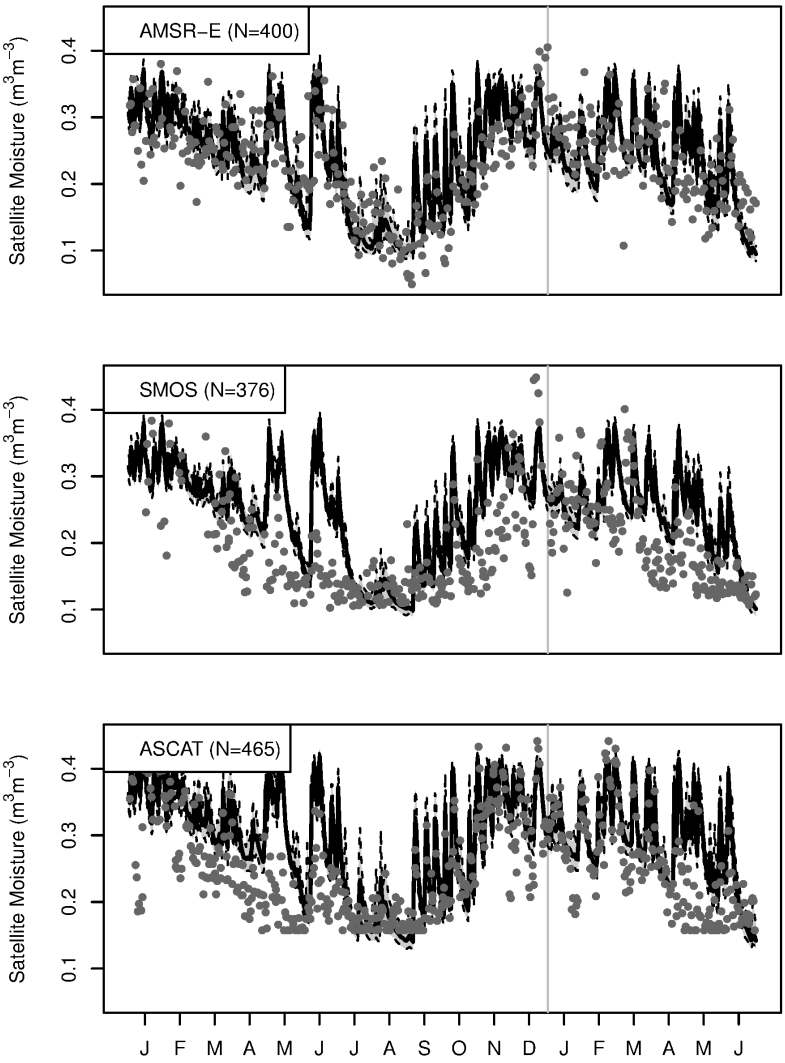

Figure 2.7 Three example time series for AMSR-E, SMOS and ASCAT (grey dots) compared with the satellite support averaged SWAP soil moisture (black line), including 95% confidence interval (grey), N is the number of satellite soil moisture retrievals for one location in North West Spain (42.9° N, 2.7° W).

scale of the satellite footprint (Figure 2.5) as well as with local observation points of the REMEDHUS network (Figure 2.6). Given the obtained results the SWAP model is used with confidence in other areas in Spain.

2.3.2 Remotely sensed soil moisture inter-comparison over Spain

The locations of the 79 reference stations, including the area modelled around each station (up to 35 km) were used as reference locations in this study (Figure 2.2). At

Table 2.3 Summary statistics of evaluation of three microwave satellites over Spain. The correlation (r, Equation 2.12), satellite standard error ($\hat{\sigma}\epsilon_s$, Equation 2.18) and bias ($bias_s$, Equation 2.15) are calculated between the satellite soil moisture product and SWAP modelled soil moisture.

	AMSR-E	SMOS	ASCAT
Number evaluated DGGs (-)	438	440	680
Correlation (-)	0.682	0.420	0.713
Satellite standard error (m^3m^{-3})	0.049	0.057	0.051
Bias (m^3m^{-3})	0.018	-0.014	-0.019

each reference location, a different number of satellite retrievals is available depending on the resolution of the Digital Global Grid (DGG) and the positioning of the reference location on the DGG of each satellite (Table 2.3). In general, the number of ASCAT DGG points per reference location is higher due to the higher density of the DGG ($\approx$ 12.5 to 15 km). As an example, Figure 2.7 presents time series of soil moisture retrievals from the different satellites in Northwest Spain (42.9°N, 2.7°W). Note that the values of $\theta_m(t)$ differ between satellites due to the different spatial resolutions of the data in both vertical and horizontal scales (see Table 2.1). More example time series for all satellites are given in Appendix A.

For AMSR-E the trend of high soil moisture values in winter and low soil moisture values in summer is captured very well resulting in low satellite errors. Individual rainfall events are all captured and some noisy values are observed at the end of summer. In general, AMSR-E is very well capable of capturing the soil moisture dynamics.

The SMOS soil moisture retrievals capture the long-term dynamics while short-term dynamics are quite poorly captured. Observations are somewhat noisy and scarce, especially in the beginning of the evaluation period. Although a rigorous filtering is performed there might still be some RFI disturbances which are not correctly flagged or detected. Successful retrievals show an underestimation of the soil moisture content and some unexpected peaks are present. These peaks are probably caused by an inaccurate assumption about the constant penetration depth during or shortly after precipitation events. In the second half of the evaluation period the performance of SMOS increases and precipitation events are captured more accurately. Also the number of retrievals is increased with exception of the period February 2011 when SMOS encountered technical problems with one of the arms of the satellite.

ASCAT shows a good correspondence with the modelled data, except for some small deviations in dry periods. The soil moisture response to precipitation events is captured well, resulting in high correlations (Table 2.3). A general characteristic of

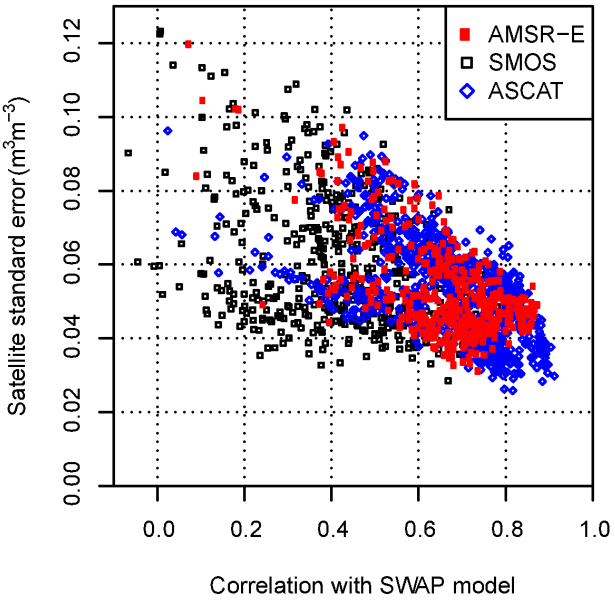

Figure 2.8 Year-round correlation and satellite standard errors for all Digital Global Grid (DGG) satellite locations compared with SWAP model simulations for the period January 2010 - June 2011 (each point is one DGG location).

ASCAT soil moisture at this location is the tendency to show some deviations in summer from soil moisture calculated by the SWAP model, when soil moisture conditions are drier. This could be the result of volume scattering at low soil moisture values (Dorigo et al., 2010).

The correlation (r, Equation 2.12) and satellite product standard error ($\hat{\sigma}\epsilon_s$, Equation 2.18) were used for the evaluation of all 79 reference locations and results are given in Figure 2.8 and Table 2.3. ASCAT and AMSR-E both have a high r with the SWAP model simulation at all the DGG locations, while the r of SMOS is considerably lower. The high r values found for ASCAT and AMSR-E can be explained by the capability of both satellites to represent the short term soil moisture dynamics (Figure 2.7). r values of 0.8 are exceeded for 12% and 17% of the DGG locations for respectively AMSR-E and ASCAT, while SMOS does not have r values above 0.8. The average $\hat{\sigma}\epsilon_s$ of both AMSR-E and ASCAT is slightly lower in comparison with SMOS. However, none of the satellites satisfies the 0.04 m^3m^{-3} accuracy set as a target for newly launched soil moisture missions like SMOS (Kerr et al., 2001; Walker and Houser, 2004). ASCAT shows for 167 DGG locations a $\hat{\sigma}\epsilon_s$ below 0.04 m^3m^{-3}, while for SMOS and AMSR-E satellite error values are only occasionally below this criterion (Figure 2.8). An inverse relation exists between the r and the $\hat{\sigma}\epsilon_s$, in which a high r corresponds to a low $\hat{\sigma}\epsilon_s$. After the transformation was applied (Equation 2.1) a small negative $bias_s$ (Equation 2.15) remains for SMOS and ASCAT (Table 2.3).

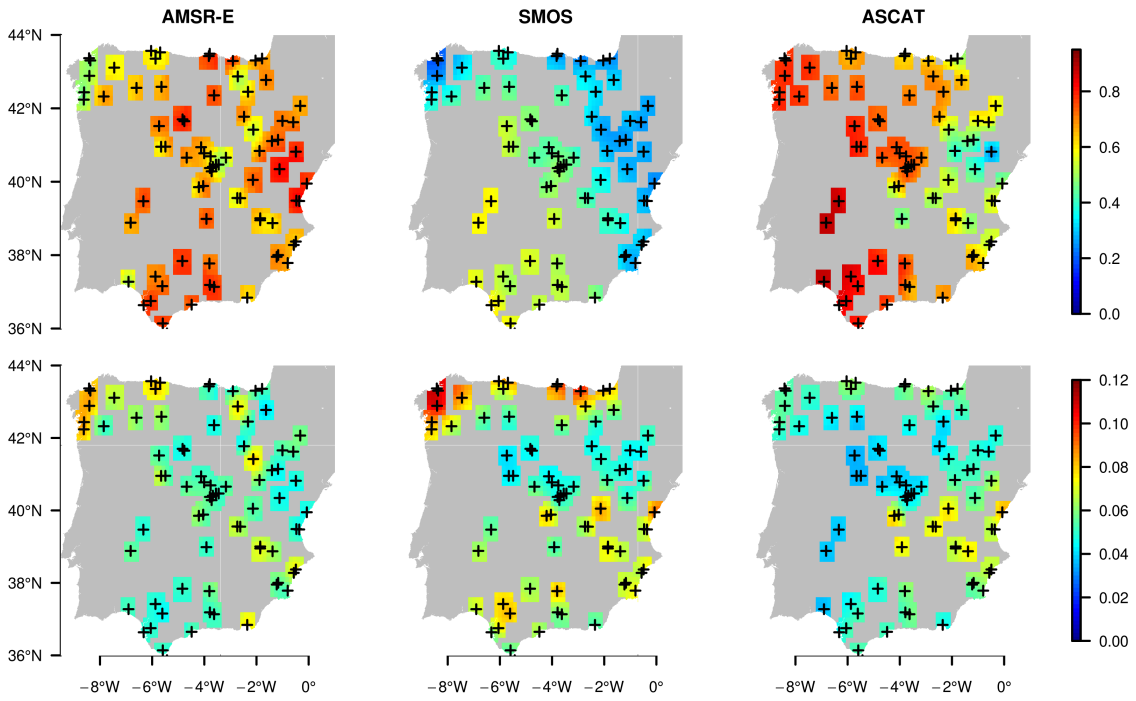

Figure 2.9 Correlation, r, (top) and satellite standard error, $\hat{\sigma}\epsilon_s$, (bottom) for the three satellite soil moisture products for the period January 2010 - June 2011 over Spain. Meteorological stations are indicated by crosses.

Furthermore, although satellite soil moisture time series are given for specific DGG points, the spatial support may slightly change over time.

A spatial evaluation of the r and $\hat{\sigma}\epsilon_s$ values for all satellite products is shown in Figure 2.9. The correlation values are highest in the Southwestern part of Spain for all three satellite products and lowest in the North-Eastern locations for SMOS and ASCAT. AMSR-E shows low r values in the Northwest and high r values in the South and interior of Spain. Values for $\hat{\sigma}\epsilon_s$ are lowest in Northern and central Spain with some high to very high values for AMSR-E and SMOS in the North-Western locations due to the proximity of the sea in combination with increased vegetation and topography. The spatial patterns of $\hat{\sigma}\epsilon_s$ for both AMSR-E and ASCAT show a great resemblance to the patterns found with triple collocation by Dorigo et al. (2010). The low r of ASCAT in the dry Eastern parts of Spain are most likely caused by the volume scattering effect in dry soils (Bartalis et al., 2006b). Satellite products were compared and correlations between the different products as well as the anomalies were determined. The highest satellite correlations were found between AMSR-E and ASCAT ($r = 0.536$), while correlations of SMOS with AMSR-E ($r = 0.376$) and with ASCAT ($r = 0.364$) are significantly lower. The correlation between AMSR-E and ASCAT is highest in the North-Western and Southern parts of Spain. These regions

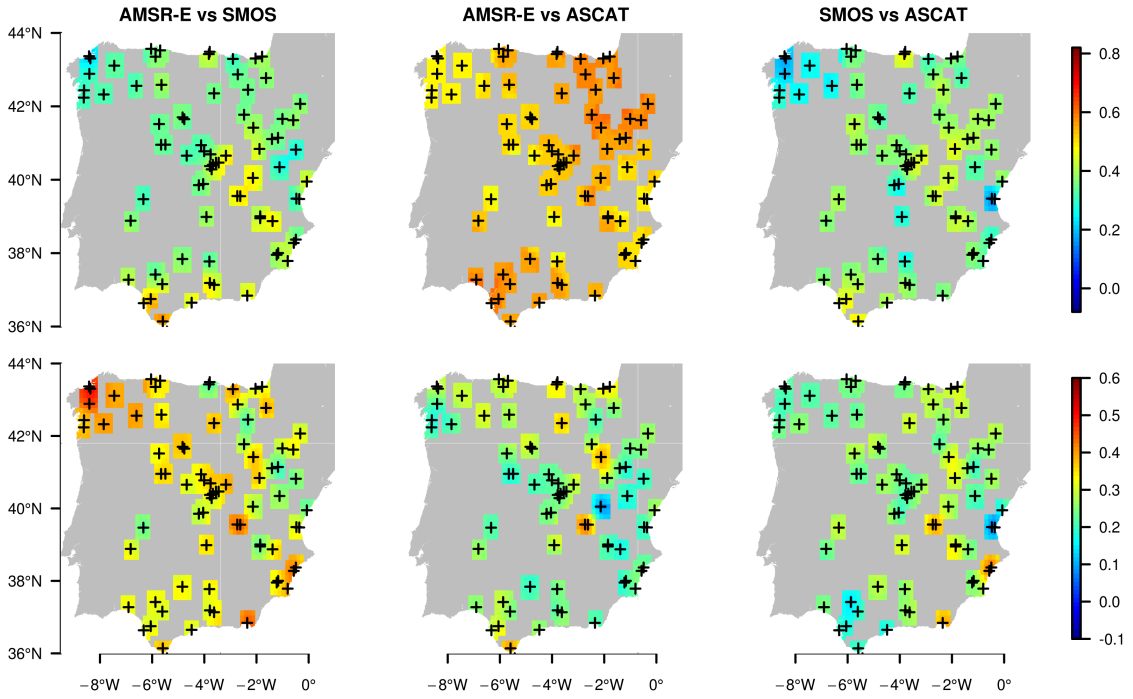

Figure 2.10 Correlation between satellite soil moisture products (top, r) and correlation between the satellite product errors (bottom, $\epsilon_s(t)$) of different satellite products for the period January 2010 - June 2011 over Spain. Meteorological stations are indicated by crosses.

are also the areas where individual correlations with the SWAP model are highest for both satellites. The spatial patterns of the correlation between satellite products and correlations in ϵ_s are shown in Figure 2.10.

r values computed for ASCAT are higher than those found by Parrens et al. (2012) for France, while correlations found for SMOS are slightly lower. Correlations computed for AMSR-E are higher than in a recent inter-comparison study with observed in-situ data from Brocca et al. (2011) over Europe; the r values found for ASCAT are in the same range. An older study from Rüdiger et al. (2009) over France found similar r values as in this study for ASCAT. For AMSR-E, r values found in this study are higher, which is caused by the use of an improved version of the LPRM model. Comparison between in-situ data and both ASCAT and SMOS by Albergel et al. (2012) found lower r values for ASCAT and higher values for SMOS than obtained in this study.

In general, AMSR-E and ASCAT show the highest correlation for most DGG locations and capture the temporal soil moisture dynamics very well. The trend in the $\hat{\sigma}\epsilon_s$ found in this study is similar to other studies (e.g. Brocca et al., 2011; Parrens et al., 2012; Albergel et al., 2012). However, a direct comparison is hampered by the fact that

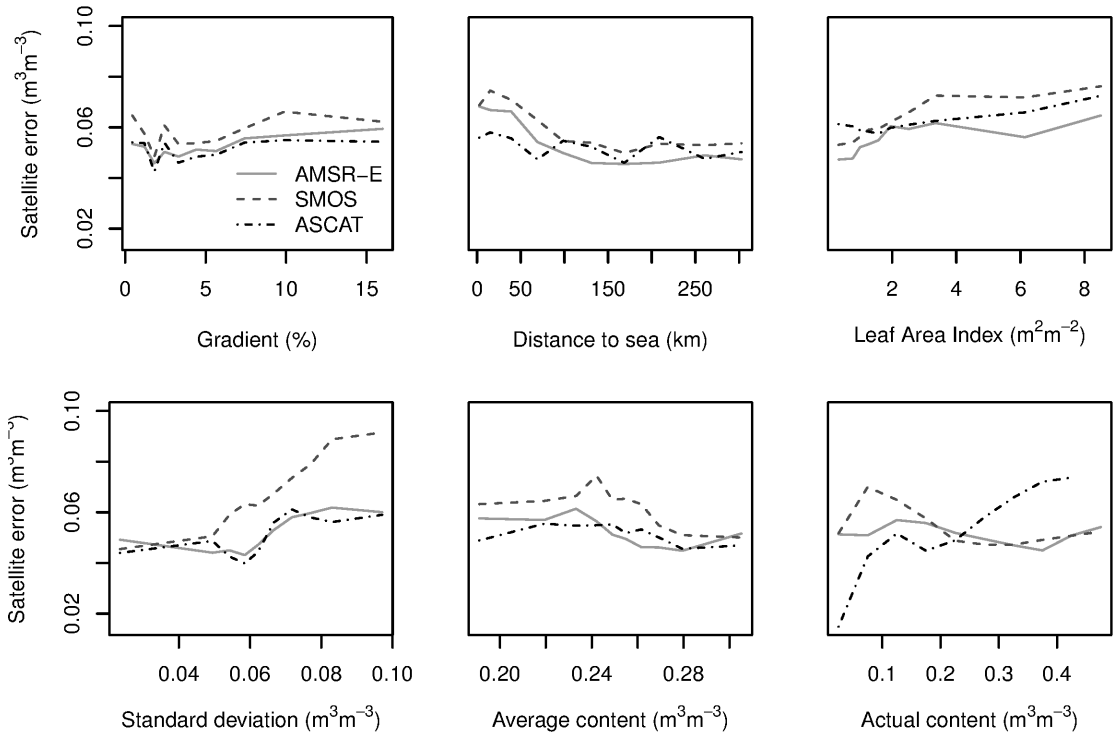

Figure 2.11 Satellite standard error of satellite soil moisture for different factors in comparison with SWAP model for the period January 2010 - June 2011 over Spain. The satellite error $\hat{\sigma}\epsilon_s$ (Equation 2.18) is given for: the gradient ($Grad$), distance to the sea (Sea), standard deviation (σ_m) and μ_m. For the Leaf Area Index ($LAI(t)$) and actual content ($\theta(t)$) the bin-average time dependent satellite error $\epsilon_s(t)$ (Equation 2.17) is shown.

these studies did not incorporate model errors. Our approach accounts for model uncertainty and therefore gives a more correct estimation of the $\hat{\sigma}\epsilon_s$ of satellite soil moisture products and the performance of space-borne sensors.

2.3.3 Satellite error characterization

The effect of several external factors on the satellite standard error ($\hat{\sigma}\epsilon_s$) is evaluated over Spain for all reference locations. The average slope of the location ($Grad$) is found to have negligible influence on the $\hat{\sigma}\epsilon_s$ (Figure 2.11), leading to the conclusion that gradients at the reference locations in Spain are too small to have a negative impact on $\hat{\sigma}\epsilon_s$. However, with an increase in the distance to the sea (Sea), $\hat{\sigma}\epsilon_s$ for AMSR-E and SMOS decrease. Above a distance of 100 to 150 km the influence of the sea is absent. An increase in the Leaf Area Index ($LAI(t)$) over time does influence the time dependent satellite error (ϵ_s, Equation 2.17) in a negative way, ϵ_s increases with an increase in vegetation. The performance of SMOS is most affected by the

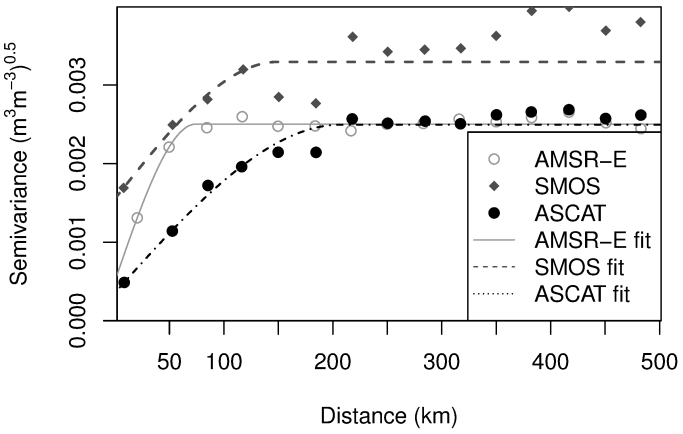

Figure 2.12 Semi-variograms of the bin-average time dependent satellite product error ($\epsilon_s(t)$) calculated for three satellite soil moisture products and the SWAP model, from all DGG locations for the period January 2010 - June 2011 over Spain.

average standard deviation of soil moisture (σ_m), where SMOS might have difficulties with highly dynamic soil moisture due to the high signal to noise ratio compared to AMSR-E and ASCAT. Over the entire modelling period (Jan 2010 - Jun 2011), the average soil moisture content (μ_m) does not significantly influence the satellite performance, while the actual soil moisture content ($\theta(t)$) does have a large influence on the temporal performance of ASCAT. Both passive microwave satellites show a small increase in the ϵ_s for $\theta(t)$ between 0.1 - 0.2 m^3m^{-3} and decrease thereafter. ASCAT shows an unambiguous increase in the ϵ_s with increasing $\theta(t)$. This could be the result of the strong response of ASCAT to precipitation events, while this response is less profound for AMSR-E and SMOS (Figure 2.7). Correlations were most affected by changes in the average footprint soil moisture content (μ_m) and the distance to the sea (Sea) of all external factors under study (not shown). In this study no strong relationship is found between the $\hat{\sigma}\epsilon_s$ and the $Grad$. Based on previous studies (e.g. Engman and Chauhan, 1995) it was expected that the satellite performance was related to these properties. A relationship was found for Sea, $LAI(t)$, σ_m, μ_m and $\theta(t)$ with $\hat{\sigma}\epsilon_s$. This finding is confirmed by other studies (e.g. Njoku and Kong, 1977; Troch et al., 1996; Njoku and Li, 1999; De Jeu et al., 2008; Owe et al., 2008; Parinussa et al., 2011).

Finally, the error for all the remotely sensed soil moisture products is spatially correlated. Ranges of the variogram of correlation are between 100 - 220 km, for the three satellites products (Figure 2.12). The correlation ranges, sill and nugget of the variogram are almost equal for all satellite products indicating that soil moisture errors have an almost identical spatial error pattern for AMSR-E, SMOS and ASCAT.

2.4 Conclusions

The soil moisture mapping accuracy of three satellite sensors was evaluated in this study. Satellites used in this study are passive microwave satellites AMSR-E and SMOS and the active microwave satellite ASCAT. Satellite soil moisture products were compared with the physically-based high resolution SWAP model. Soil moisture was modelled at a high vertical and horizontal resolution and averaged over the support of each satellite. A validation of the high-resolution SWAP model was performed on the REMEDHUS network situated in Spain. The mean modelled soil moisture from SWAP has a high correlation ($r = 0.878$) and low $RMSE$ ($0.025 m^3 m^{-3}$) with the median of observations at the REMEDHUS site. From the predictive QQ-plot it was concluded that the SWAP model was able to capture the full probability density function in both space and time for this site. The uncertainty added to meteorological input data as well as soil physical model parameters was enough to account for local variations in soil moisture values between observation points. From this validation at the REMEDHUS site it was concluded that the SWAP model can be used to simulate soil moisture with confidence over other areas of Spain.

The SWAP model was used to model the soil moisture content in Spain around 79 meteorological stations up to a distance of 35 km for the period January 2010 to June 2011. Satellite data was linearly transformed to match the dynamic range of the model to enable a valid comparison between satellite derived and modelled soil moisture. The AMSR-E data have a good correlation ($r = 0.685$) with modelled SWAP soil moisture at the satellite support and the general yearly soil moisture trend is captured well. The short-term temporal dynamics and individual precipitation events are captured very well by AMSR-E, which results in a high correlation. SMOS shows a fair correlation with the SWAP model ($r = 0.420$). The majority of precipitation events is captured, but in general soil moisture is underestimated compared to the model. However, it should be noted that the observation technique and algorithms of SMOS are still relatively new and improvements on the retrieval algorithm and flagging of RFI are constantly made leading to improved soil moisture retrievals. Of all products ASCAT showed the highest correlation with the SWAP model over Spain ($r = 0.713$), which is mainly caused by the fact that precipitation events are captured very accurately. However, in summer the soil moisture values of ASCAT showed some noise. Correlations found in this study are in agreement with previous studies based on the comparison between satellite soil moisture and observational or modelled soil moisture data.

The error was expressed by using the satellite standard error ($\hat{\sigma}\epsilon_s$), which also accounts for the model uncertainty. Therefore, $\hat{\sigma}\epsilon_s$ is not overestimated as a result of a large model uncertainty. Average $\hat{\sigma}\epsilon_s$ found were 0.049, 0.057, 0.051 $m^3 m^{-3}$ for AMSR-E, SMOS and ASCAT respectively, which is above the $\hat{\sigma}\epsilon_s$ 0.04 $m^3 m^{-3}$. Previous studies often lack a detailed assessment of the model uncertainty, resulting in an overestimation of $\hat{\sigma}\epsilon_s$. In this study the model uncertainty was assessed in great

detail, resulting in lower $\hat{\sigma}\epsilon_s$ values and thus a lower satellite product error compared to other studies. From this comparison it is concluded that for an accurate estimation of $\hat{\sigma}\epsilon_s$, a detailed assessment has to be made of the observation or model uncertainty in order not to overestimate the satellite product error. All three satellites have a bias ranging between -0.018 m^3m^{-3} and 0.019 m^3m^{-3} of which AMSR-E has the highest positive bias and ASCAT the lowest negative bias.

Additionally, a spatial comparison showed that all products show the highest correlation in the areas in the South West of Spain, which have a low average soil moisture content. The effects of land-sea contamination were found for AMSR-E and SMOS. Vegetation, soil moisture dynamics, average soil moisture content and the actual soil moisture content do have an impact on the satellite performance, where an increase of these factors negatively influences $\hat{\sigma}\epsilon_s$. SMOS shows an increase in $\hat{\sigma}\epsilon_s$ leading to the conclusion that SMOS has difficulties in accurately measuring soil moisture in highly dynamic soil moisture regimes. The performance of ASCAT was more correlated to actual soil moisture content, while there was no clear increase in $\hat{\sigma}\epsilon_s$ for AMSR-E and SMOS. Semi-variogram models of the errors of all satellite soil moisture products for the entire simulation period show a spatial correlation in the error up to a distance of 150 km.

In general AMSR-E and ASCAT currently produce the best soil moisture time series. However, all three satellite products contain valuable information about the near-surface soil moisture over Spain.

Acknowledgments

The authors would like to acknowledge Wouter Dorigo of the TU Wien, Jennifer Grant and Matthias Drusch at ESA-ESTEC, for their intellectual support on the topic of microwave remote sensing and especially on the topic of ASCAT and SMOS data. Both the Spanish meteorological service (AEMET) and the International Soil Moisture Network are acknowledged for making the meteorological and soil moisture data used in this study publicly available.

3 Correction of real-time satellite precipitation

This chapter is based on:
Wanders, N., Pan, M., Wood, E. F. (2015), Correction of real-time satellite precipitation with multi-sensor satellite observations of land surface variables, Remote Sensing of Environment, 160, 206-221, doi:10.1016/j.rse.2015.01.016.

Abstract

Precipitation is an important hydro-meteorological variable, and is a primary driver of the water cycle. In large parts of the world, real-time ground-based observations of precipitation are sparse and satellite-derived precipitation products are the only information source. Changes in satellite-derived SM and LST are used to reduce uncertainties in TMPA-RT. The VIC model was used to model the response of LST and SM on precipitation, and a particle filter was used to update TMPA-RT. Observations from AMSR-E (LPRM and LSMEM), ASCAT, SMOS and LST from AMSR-E were assimilated to correct TMPA-RT over the continental United States. Assimilation of satellite-based SM observations alone reduced the false detection of precipitation (by 85.4%) and the uncertainty in the retrieved rainfall volumes (5%). However, a higher number of observed rainfall events were not detected after assimilation (34%), compared to the original TMPA-RT (46%). Noise in the retrieved SM changes resulted in a relatively low potential to reduce uncertainties. Assimilation of LST observations alone increased the rainfall detection rate (by 51%), and annual precipitation totals were closer to ground-based precipitation observations. Combined assimilation of both satellite SM and LST, did not significantly reduce the uncertainties compared to the original TMPA-RT, because of the influence of satellite SM compared to the LST estimates. However, in central United States improvements were found after combined assimilation of SM and LST observations. This study shows the potential for reducing the uncertainties in TMPA-RT estimates over sparsely gauged areas.

3.1 Introduction

Precipitation is an important hydro-meteorological variable, which has a large impact on the global energy and water cycle and thus on weather, climatology, hydrology and ecosystems. Obtaining accurate ground-based measurements of precipitation is difficult, due to the high spatial and temporal variability of precipitation (McCollum

and Krajewski, 1998; Tustison et al., 2001). Real-time ground-based observations of precipitation with sufficient accuracy and availability are even sparser. However, real-time observations of precipitation are important for real-time monitoring and forecasting of floods and drought (Hong et al., 2007; Hossain and Huffman, 2008; Su et al., 2008; Gebremichael and Hossain, 2010; Pan et al., 2010). Satellite-based precipitation products like the real-time Tropical Rainfall Measuring Mission Multi-satellite Precipitation Analysis products (TMPA-RT, Huffman et al., 2007, 2010), Climate Prediction Center MORPHing product (CMORPH, Joyce et al., 2004), and Precipitation Estimation from Remotely Sensed Information using Artificial Neural Networks (PERSIANN, Hsu et al., 1999; Sorooshian et al., 2000), provide a solution to obtain real-time precipitation data for many sparsely gauged regions in the world. TMPA-RT gives the 3-hourly precipitation between 50°N and 50°S through combing rainfall estimates from microwave sensors (Kummerow et al., 1996; Olson et al., 1999; Kummerow et al., 2001) and infrared imageries (Joyce et al., 2001). Precipitation products like TMPA-RT usually suffer from the fact that they depend on satellite retrievals for their observations and thus require a satellite overpass. TMPA-RT products are derived from satellite overpasses in a 3-hour window (Huffman et al., 2007) and not all precipitation events are captured, since some precipitation events may have a smaller temporal scale than 3 hours. This is especially true for highly dynamic events (e.g. convective rainfall events), which occur in tens of minutes and could vanish in a similar time period. Some of these events can be missed by the TMPA-RT, while they can have a significant impact on the land-surface and the related processes. Although convective precipitation events might have a small spatial scale, they can have a large contribution to the annual precipitation totals (e.g. Laurent et al., 1998; Blamey and Reason, 2012). Especially in summer conditions with unstable atmospheric boundary layers, these events occur regularly and will impact the land-surface. Also, various other types of errors also occur in satellite precipitation products (Villarini and Krajewski, 2007; Sapiano and Arkin, 2009).

To correct for the problem of missed precipitation events and uncertainties in rainfall totals, TMPA is post-processed and corrected with ground-based observations (Huffman et al., 2010). This correction is not possible for the real-time version of TMPA which is used by real-time applications, which require observations of no less than a couple of hours after sensing.

The observations of several other land surface variables are available in near real time and they can potentially be used to help reduce the uncertainty in satellite precipitation. For example, soil moisture (SM) observations could provide valuable information on the spatial pattern of precipitation. An additional advantage is the fact that the wetting of the surface soil moisture could be detected for longer time periods (up to several days) and could be used to estimate the precipitation volume. The change in soil wetness at larger scales can be detected by space-born microwave sensors. Change detection in soil moisture is occasionally hampered when pre-storm soil moisture content is close to saturation or fully saturated. In these conditions

additional precipitation will not result in increased soil wetness, hence no change in soil moisture can be detected. Several studies showed the potential to reduce precipitation uncertainties using soil moisture retrievals from a single sensor (Crow and Bolten, 2007; Pellarin et al., 2008; Crow et al., 2009, 2011; Brocca et al., 2013; Pellarin et al., 2013; Brocca et al., 2014).

To partly overcome the limitation of soil moisture retrievals we propose the use of observations of land-surface temperatures (LST) are used to detect areas with precipitation amounts exceeding the storage capacity of the unsaturated zone. With increased water storage the soil temperatures will decrease, since more energy is required to warm the earth surface. This change could be detected in satellite-derived land-surface temperature based on microwave retrievals from the higher frequencies (Holmes et al., 2009).

The objectives of this paper are to study the potential of remotely sensed observations of land surface variables to correct for uncertainties in satellite-derived precipitation. More specific, do multi-sensor remotely sensed soil moisture retrievals and land surface temperature observations have the potential to correct real-time satellite based precipitation estimates? Additionally, the effect of the correction of precipitation is studied for both soil moisture and land surface temperature changes and the potential gain obtained by either of these sources.

To fulfill these objectives, TMPA-RT was perturbed and used to force a land-surface model. Changes in modeled soil moisture content and land surface temperature are compared with observations from satellites. The optimal realization was selected using a particle filter based approach to update TMPA-RT to a newly corrected real-time precipitation estimate. Although the potential gain of this approach may be large in poorly gauged regions like the continent of Africa, ground based observations with a high spatial and temporal resolution for validation are lacking. Therefore, the analysis was performed over the Continental United States (CONUS) to enable a comparison between the TMPA-RT, corrected estimates and a high quality ground-based observational precipitation dataset. The precipitation data from Northern Land Data Assimilation System project phase 2 (NLDAS-2; Xia et al., 2012) was used as best estimate of the precipitation over the Continental United States.

Changes in modeled soil moisture and land surface temperature were compared to observed precipitation to test the sensitivity of these observations to precipitation. Observations of satellite-derived soil moisture and land surface temperature have been assimilated to corrected precipitation and results were compared to ground-based observations of NLDAS-2 for the period 2010-2011. Uncertainties were evaluated and compared to the uncertainties of the original uncorrected TMPA-RT.

3.2 Material and Methods

3.2.1 Study area

CONUS was used as study area, covering the mainland of the United States and excluding Hawaii and Alaska. High quality ground-based observations are available for CONUS making it a suitable area for evaluation of the potential improvements of assimilation of satellite-derived SM and LST. However, observations of land surface parameters are in some areas hampered by the topography and dense vegetation (Rocky Mountains, Appalachian Mountains and dense forest in the East). It is assumed that potential gains will only be larger for areas with less complex terrain properties and low rain gauge densities, e.g. the Sahel in Africa, than gains obtained over CONUS.

Meteorological forcing data from NLDAS-2 (Xia et al., 2012) are used to force the land surface model, which are available on an hourly time step with a spatial resolution of 0.125° (aggregated to 3-hourly and 0.25° to match TMPA-RT resolution) for the entire CONUS. The precipitation fields in NLDAS-2 combine the estimates from radars and ground gauges (NOAA Stage IV product) and as well as regional reanalysis (for gap filling). The NLDAS-2 precipitation is treated as the best ground truth and use it for validation purposes.

3.2.2 Land-surface model

The VIC model (version 4.0.5) is used to simulate the hydrological responses of the land surface to precipitation for the period 2010-2011. VIC is a spatially distributed grid-based Land Surface Model that simulates the response of soil moisture, land surface temperature and other land surface variables at the land surface-atmosphere interface (Liang et al., 1994, 1996). Subgrid-scale variability in soil properties is represented by a spatially varying infiltration capacity such that the spatial variability in soil properties at scales smaller than the grid is represented statistically. Movement of moisture between the soil layers is modeled as gravity drainage, and the unsaturated hydraulic conductivity is a function of the degree of saturation of the soil. The VIC model solves the full energy balance to obtain land surface temperature.

VIC is used with a three hourly time step to allow a better comparison between VIC and the different satellite products. The model was forced with meteorological forcing from NLDAS-2 (aggregated to 3-hourly time step and 0.25° resolution) over CONUS. The meteorological forcing fields being used from NLDAS-2 consist of air temperature, vapor pressure, atmospheric pressure, wind and downward shortwave and longwave radiation.

3.2.3 Remotely sensed precipitation

The real-time Tropical Rainfall Measuring Mission Multi-satellite Precipitation Analysis products (TMPA-RT, Huffman et al., 2007) were used a baseline precipitation product. TMPA-RT (3B42RT) relies on multi-channel microwave and infrared observations to estimate precipitation rates. TMPA-RT is available from 50°S to 50°N with a 3-hourly time step and a spatial resolution of 0.25°.

3.2.4 Remotely sensed soil moisture and land surface temperature

Remotely sensed soil moisture and land surface temperature data from three satellite sensors are used to reduce uncertainties in satellite precipitation, namely AMSR-E, SMOS and ASCAT. Changes between consecutive overpasses have been used to infer the occurrence and amount of precipitation events (Table 3.1). For all observations the descending and ascending overpasses have been separated.

AMSR-E is a multi-frequency passive microwave radiometer and is a widely used sensor for soil moisture retrievals. In this study, two AMSR-E retrieval algorithms have been used to estimating surface soil moisture. The first algorithm is the Land Parameter Retrieval Model (LPRM), which is a widely used algorithm for soil moisture retrievals from AMSR-E (Owe et al., 2008; De Jeu et al., 2008). The second AMSR-E algorithm is a revised version of the Land Surface Microwave Emission Model (LSMEM, Drusch et al., 2001, 2004; Gao et al., 2004) developed by Pan et al. (2014). The LSMEM algorithm differs from the LRPM algorithm in the way the soil moisture and vegetation optical depths are retrieved simultaneously and iteratively instead of using a static relationship between the optical depth and the mean polarization difference index (MPDI). LSMEM has been validated against observations over continental United States and showed promising results (Pan et al., 2014).

SMOS is a dedicated soil moisture satellite using passive microwave signals at 1.4 GHz (L-band) observed at multiple angles (Kerr et al., 2012). SMOS retrievals which are potentially contaminated with Radio Frequency Interference (RFI) have been removed.

Observations in de active microwave frequency at 5.3 GHz (C-band) from ASCAT have been used to determine the soil moisture content (Wagner et al., 1999; Naeimi et al., 2009). ASCAT uses a change detection method (Naeimi et al., 2009) and data is provided relative to the soil moisture content of the wettest (field capacity) and driest (wilting point) soil moisture conditions measured (Wagner et al., 1999).

Land surface temperatures have been derived from ASMR-E 37 GHz (Ka-band) passive microwave observations (Holmes et al., 2009). The advantage of microwave retrievals of surface temperatures compared to infrared observations is their all-weather capability. When precipitation events occur, the sky is often cloud covered before and

Table 3.1 Satellite sensor retrieval algorithm properties and their average coverage of consecutive overpasses over the period 2010-2011.

	AMSR-E LPRM	AMSR-E LSMEM	ASCAT	SMOS	AMSR-E LST
Frequency (GHz)	6.9	10.7	5.3	1.41	37
Microwave type	Passive	Passive	Active	Passive	Passive
Observation depth (cm)	0-2	0-2	0-2	0-5	0-1
Descending overpass (h)	1:30 AM	1:30 AM	9:30 AM	6:00 PM	1:30 AM
Coverage consecutive overpasses	64%	62%	78%	45%	75%

after the rain event, limiting the potential for land surface temperature observations. Moreover, obtaining two consecutive overpasses is hard when satellite retrievals do not possess all-weather capability. Therefore, microwave land surface temperature observations have been used to reduce precipitation uncertainties in this study.

All satellite products have been projected on a 0.25° grid. A gridded soil moisture product at this spatial scale is available for SMOS and ASCAT. All satellite data were matched to the modeled climatology from the land surface model. Using cumulative density function matching (CDF-matching), the probability density functions (PDF) of all retrieved soil moisture time series and land surface temperature time series have been corrected to match the PDF of the modeled soil moisture and temperature (Reichle and Koster, 2004). This removed potential biases which could negatively impact the results of the assimilation. The CDF matching was performed for each 0.25° grid location and overpass type (descending, ascending) separately.

Frozen soils, snow accumulation and RFI hamper the soil moisture retrieval due to changes in the dielectric constant when water freezes. Therefore, retrievals done with 1) an air temperature below 4° C, 2) simulated snow accumulation and 3) the presence of RFI, were not used to update the precipitation estimates. For all satellites both ascending and descending retrievals have been used. However, they are seen as separate observations since the physical properties of ascending and descending retrievals could be significantly different and combining them would result in erroneous time series. Additionally, the overpass times are exactly matched to the modeled soil moisture and land surface temperatures to avoid temporal mismatches which could negatively impact the assimilation and correction of satellite-derived precipitation.

3.2.5 Particle Filter based filtering

In this study, a particle filter based approach is used to estimate the optimal input for the land surface model to obtain observed changes in soil moisture and land surface temperature. The particle filter is a Monte Carlo based approach used to adjust model inputs, model structures and model states (Doucet et al., 2000; Arulampalam et al., 2002; Moradkhani et al., 2005; Van Leeuwen, 2009). It is suitable for non-linear models and makes no assumptions on the prior and posterior distribution of the model states. This property of the particle filter makes it more suitable for this study compared to ensemble based data assimilation approaches whose optimality and performance depend on the linearity between input and output variables and having Gaussian distributed errors, for example, the Ensemble Kalman Filter (EnKF, Evensen, 2003; Reichle, 2008). Particle filter works by preferentially weighting the Monte Carlo samples according to their closeness toward observations while an ensemble filter adds additive adjustments to them. Precipitation is a highly non-Gaussian and non-negative variable, so preferential weighting will work much better than adding adjustments without the worry of negative values.

The land-surface model VIC is used to transform precipitation and other meteorological variables into changes of soil moisture content and land-surface temperatures. The forward model of VIC is given by:

$$x_i(t+1) = f(x(t), F_i(t)), \tag{3.1}$$

where $x(t)$ is the initial model state, $x_i(t+1)$ is the model state after each realization i and $F_i(t)$ is the meteorological forcing for each realization. For all simulations the initial conditions are identical for each particle (total number of particles = N) and obtained from the base run of the land surface model forced by observed precipitation and other meteorological variables. However, the meteorological forcing ($F_i(t)$) in the forward model differs per realization leading to different realizations of the model states $x_i(t+1)$. Precipitation is perturbed from the original TMPA-RT product to generate the different particles. To generate possible precipitation particles for 3 hourly observations at a particular location, observations were randomly selected from a sampling area of 1.75° x 1.75° around the selected location. Additionally, precipitation observations are sampled from the sampling area for the actual time ±3 hour (Figure 3.1). The values within the sampling area are not weighted and are randomly sampled. Since no detailed information is available on the likelihood of each sample and interpolation is used to obtain some of the observations, a uniform priori distribution of the weights was used for the particles. A multiplicative error is added to the randomly resampled precipitation which is given by $lnN(\mu = 0,\ \sigma = 0.5)$. Other meteorological forcing was not perturbed and identical for each particle. This resampling approach will result in N realizations of the precipitation resulting in x_n realizations of the model states (soil moisture and land surface temperature). Changes in these realizations were compared to the observed changes by remotely sensed observations to determine the most likely rainfall, given the observations and

the initial conditions $x(t)$. The posterior probability of the state of each particle (i) is calculated by:

$$P(x_i|y) = P(F_i|y) = e^{\frac{(y-x_i)^2}{-2\sigma^2}}, \tag{3.2}$$

where y is the change in remotely sensed observation, x_i the modeled change in the corresponding model state and σ the uncertainty in the observed changes. The individual posterior probability of each particle for the different observations is used to reduce uncertainties in the TMPA-RT when single sensor assimilation is performed. When a multi-sensor assimilation is performed available weights for each observation are combined by:

$$P(x_i|Y) = \sum_{j=1}^{N_r} P(x_i|y_j), \tag{3.3}$$

where N_Y is the total number of observations from ascending and descending overpasses of AMSR-E, SMOS and ASCAT and y are the individual observations from each sensor. The posterior probability of each observation is not multiplied, because some individual values of $P(x|y)$ are zero (even with high retrieval uncertainty values) due to erroneous satellite retrievals. These erroneous retrievals will lead to a $P(x|Y)$ value of zero for all particles, thereby reducing the information of all other observations. This could for example happen in a case where erroneous satellite observations with relatively low uncertainty are used and none of the particles is likely to represent this erroneous observation. In this situation multiplication of the weights would lead to a zero probability due to the erroneous observations, while other observations might be perfectly represented. To prevent this, values of $P(x|y)$ were aggregated to $P(x|Y)$ improving the assimilation potential of multi sensor retrievals.

The particle filter based assimilation approach is run for every sample location separately since the land surface model is not sensitive to changes in adjacent cells. This will significantly reduce the number of required particles. Since precipitation fields are different for each realization, this is the only variable that is updated. The realization with the highest posterior probability (i.e. maximum a posteriori) and the median of the accumulated posterior probability were selected and the matching precipitation for these realizations was used as best estimate for the corrected precipitation (Figure 3.1). Uncertainties in the obtained retrievals are estimated from the uncertainties given by each algorithm. Uncertainties in the changes in satellite-derived soil moisture and land surface temperature are derived by:

$$\sigma = \sqrt{2\sigma^2_{retrieval}}, \tag{3.4}$$

where $\sigma_{retrieval}$ is the retrieval uncertainty. In single sensor assimilation the impact of $\sigma_{retrieval}$ is non-existing for the highest probability, since the particle closest to the observation will always be selected ($BestPrec$). This is a result of the assumption that all particles have the same a priori likelihood. This is not the case for the median sample, where the impact of $\sigma_{retrieval}$ results in a different cumulative posterior distribution ($MedPrec$).

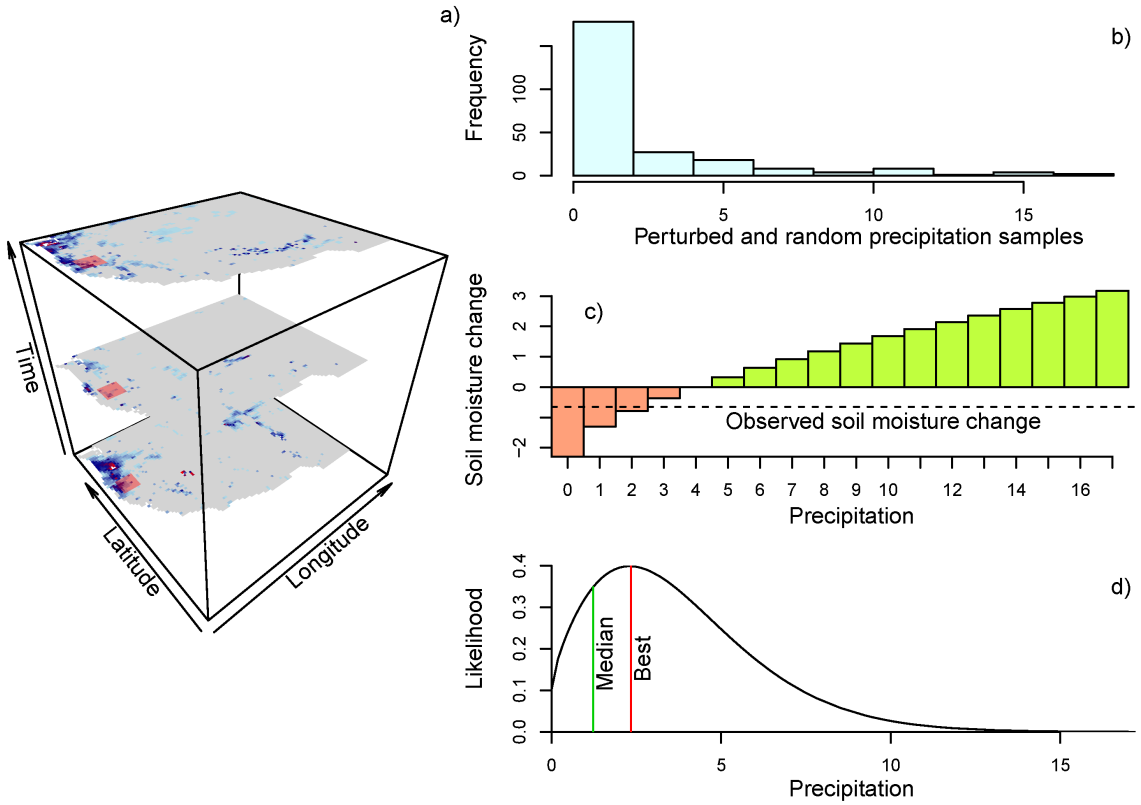

Figure 3.1 Theoretical example of precipitation update with 250 realizations. a) Observations of satellite retrieved soil moisture for Western United States. The red square indicates the sampling area of 1.75°x 1.75° with a retrieval for every three hours (vertical axis). The location for the precipitation correction is in the center of the red square, precipitation observations are sampled from the sampling area for the actual time ± 3 hour. b) The resampled precipitation values including a random multiplicative error for each sample, i.e. the prior particles. c) Soil moisture changes derived from the land surface model using the precipitation samples. Values are averaged over each bin. The real observed soil moisture change is indicated by the dashed horizontal line. d) The posterior probability of each precipitation sample producing the observed changes in soil moisture and the selection of the sample with the highest probability ($BestPrec$) and the median of the cumulative posterior probability ($MedPrec$).

A synthetic experiment was performed to test if the proposed framework could be used to reduce uncertainties in precipitation forcing with synthetic true soil moisture and land surface temperature changes.

3.2.6 Sensitivity analysis

To better understand how precipitation will result in changes in surface SM and LST in the VIC model and assess how much information SM/LST can provide about precipitation, a sensitivity analysis was performed. Here VIC is forced by precipitation from NLDAS-2. Changes in the state variables have been correlated with the amount of precipitation that is observed. When the changes in soil moisture content are correlated to the amount of precipitation, this indicates that the model is sensitive to precipitation and that observations of changes in soil moisture can be used to invert precipitation amounts. However, the correlation is limited by the saturation of the surface soil moisture during some events. This saturation effect together with the added noise from evapotranspiration will result in a relationship between precipitation and soil moisture which is non-trivial but where precipitation normally would result in increased soil moisture. Theoretically this will result in a positive correlation between precipitation and soil moisture.

For land surface temperature a similar relation should exist within the land surface model, to enable any benefit from updating with land surface temperatures. However, the correlation between land surface temperature and precipitation is negative since the rain water is usually cooler than the soil and a wet soil would require more energy to warm than a dry soil. This will result in lower land surface temperatures after a precipitation event. Additionally, higher precipitation totals will result in higher energy demand to warm the land surface. Therefore, the high precipitation amounts with fully saturated surface soil moisture could still be detected using land surface temperature. However, the relationship between land surface temperature and precipitation is further complicated by changes in air temperatures between days. Since air temperature largely impacts the land surface temperature, this could add noise to the relation between precipitation and land surface temperature.

The changes in satellite observations have been tested for sensitivity by calculating their correlation with observed precipitation. However, the observations from satellites are independent of the observed precipitation data, because none of the ground-based precipitation observations are used for the satellite retrievals. Hence, this will result in lower and less significant correlations. An additional problem occurs from the fact that satellite overpasses should be on consecutive days to enable the computation of the changes in the variable. When the period between overpasses is longer than 24 hours, the relation is less significant and will therefore not be used. Satellite observations have also been correlated with TMPA-RT precipitation to see where the relations are strongest and where the potential to update the TMPA-RT product is the highest compared to the NLDAS-2 precipitation. When high correlations exist between NLDAS-2 and the remotely sensed observations, there is a high potential to correct TMPA-RT. This would be more difficult for weak correlations due to the less significant relationship between changes in the observed variable and precipitation.

Table 3.2 Scenarios under study for correction of original TMPA-RT, including the description of the data and the satellite observations used to reduce uncertainties in TMPA-RT.

Scenario	Description	Satellite observations
SM + LST	All data	LPRM, LSMEM, ASCAT, SMOS, AMSR-E LST
SM	Soil moisture data	LPRM, LSMEM, ASCAT, SMOS
LST	Land surface temperature	AMSR-E LST
SM-LPRM	LPRM soil moisture	LPRM
SM-LSMEM	LSMEM soil moisture	LSMEM
SM-ASCAT	ASCAT soil moisture	ASCAT
SM-SMOS	SMOS soil moisture	SMOS

Changes in daily observations have been compared to the accumulated precipitation over that time period. For the satellite retrievals the difference between two overpasses is calculated and correlated to the accumulated precipitation over the same period. This ensures that no temporal mismatch will occur between the precipitation and the changes in either soil moisture or land surface temperature. Additionally, the correlations have been tested for significance using a Mann-Kendall test (p-value $<$ 0.05).

3.2.7 Scenarios

A synthetic experiment has been performed to test the capability of the framework to correct for errors in precipitation. NLDAS-2 precipitation was used to generate changes in SM and LST (synthetic observations). Thereafter, these observed changes were used to correct perturbed NLDAS-2 precipitation over a 3-month period (June August 2010). The sample size was varied up to 500 particles to estimate the optimal number of samples required. Additionally, the synthetic experiment was used to evaluate the performance of the assimilation framework for three scenarios (first three scenarios Table 3.2). Instead of satellite observations the synthetic observations were used to correct the precipitation.

Seven scenarios have been tested in this study to estimate the impact of changes in SM and LST retrievals to reduce the uncertainty in TMPA-RT precipitation (Table 3.2). For every scenario, the initial conditions are obtained from a simulation of the land surface model forced with NLDAS-2 precipitation. Thereafter, the model uses the perturbed precipitation fields to simulate changes in soil moisture and land surface temperature. These changes are compared with a set of satellite observations depending on the scenario under study. The model framework is described in more detail in the flowchart given in Figure 3.2.

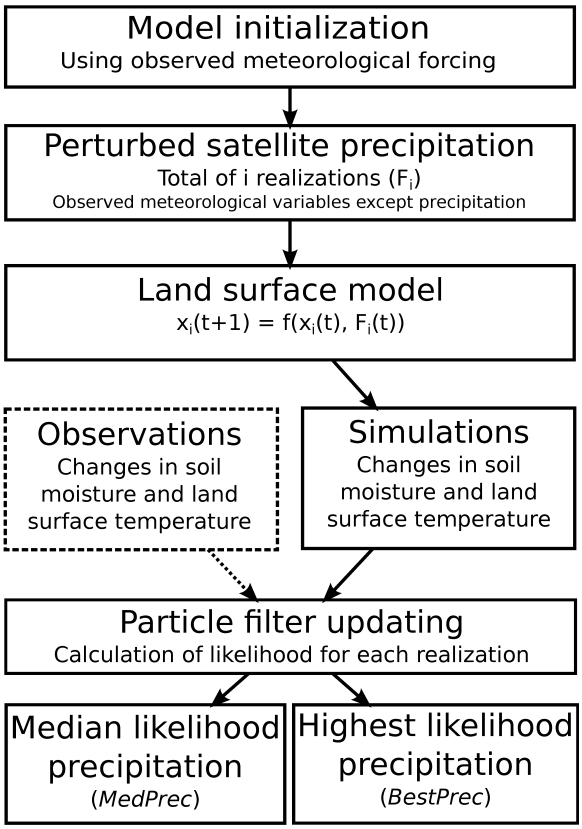

Figure 3.2 Flowchart of the updating procedure and the assimilation for observations to reduce uncertainties in satellite.

3.2.8 Evaluation

All scenarios have been evaluated based on the Probability Of Detection (POD), False Alarm Rate (FAR), Relative Annual Precipitation Bias ($RAPB$) and the Brier Score (BS, Brier, 1950). The POD is calculated by:

$$POD = P(P_{sat} > lim | P_{obs} > lim), \tag{3.5}$$

where the likelihood of having a rain event above threshold lim in both the observations ($P_{obs} > lim$) and in the satellite retrieval ($P_{sat} > lim$) is calculated, which means that the higher the likelihood, the better the retrieval. The thresholds for rain events were set on 0 mm and 2 mm, to study the sensitivity of the FAR and POD to the rain threshold. The 2 mm threshold has been applied by Crow et al. (2011) to account for overestimation of rain gauge precipitation in low intensity precipitation events. The percentage of missed rain events is calculated by $1 - POD$, which gives an indication of the potential improvements in the retrieval. The FAR indicates the likelihood of having a rain event in the satellite observation while the ground-based

observation was dry. The FAR is given by:

$$FAR = P(P_{sat} > lim | P_{obs} \leq lim), \tag{3.6}$$

where the likelihood of having a rain event in the satellite product and dry conditions in the observations ($P_{obs} \leq lim$) is calculated. A low FAR indicates a high retrieval quality, especially when low FAR is combined with a high POD.

The RAPB is the error in retrieved annual precipitation relative to observed annual precipitation and given by:

$$RAPB = \frac{\sum_{t=1}^{T}(P_{sat} - P_{obs})}{\sum_{t=1}^{T} P_{obs}}, \tag{3.7}$$

where P_{sat} indicates the retrieved precipitation and P_{obs} is the observed precipitation. A $RAPB$ close to zero indicates no bias in the satellite precipitation, while positive values indicate too high annual precipitation totals in the satellite observations and negative values are too low annual precipitation totals.

To test the accuracy of the product in terms of rainfall detection the Brier score was calculated by:

$$BS = \frac{1}{T}\sum_{t=1}^{T}(sgn(P_{sat}) - sgn(P_{obs})), \tag{3.8}$$

where $sgn(P_{sat})$ and $sgn(P_{obs})$ are binary values indicating rain event (1) or no rain event (0) for retrieval and observation, respectively. For the BS the same precipitation event thresholds (0 mm and 2 mm) are applied as were used for the POD and FAR. All the evaluation criteria were used to analyze the uncertainties in the obtained precipitation products and the original TMPA-RT.

3.3 Results

3.3.1 Sensitivity to precipitation

Simulations from the land surface model VIC have been correlated to changes in precipitation and it was shown that changes in VIC SM and LST are sensitive to precipitation (Figure 3.3). Changes in SM show a high sensitivity to precipitation, while changes in LST were less sensitive to precipitation. This could partly be explained by changes in air temperature that impact LST, while positive changes in SM can only be ascribed to precipitation. Overall it was concluded that with accurate observations of the changes in SM and LST should be possible to improve the precipitation pattern and magnitude.

The correlation between SM and LST changes and the observed precipitation has been studied (Figure 3.4). Changes in satellite observations from consecutive satellite

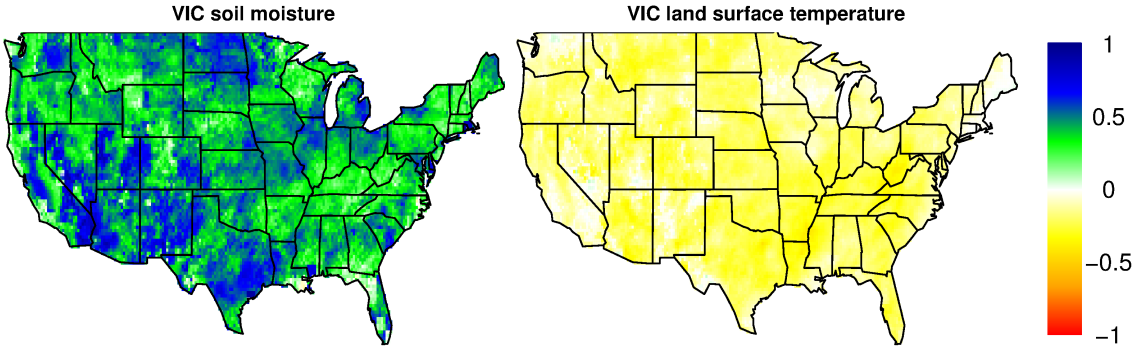

Figure 3.3 Correlation between NLDAS-2 precipitation and changes in modeled surface soil moisture and land surface temperature. Correlations are only calculated for days with rain.

overpasses, from different sensors were correlated to the precipitation amount between these overpasses. It is shown that changes in soil moisture from AMSR-E are highly correlated to precipitation especially over central CONUS. In general the LSMEM retrieval algorithm shows a higher correlation with precipitation, although AMSR-E retrieval algorithms show higher correlations than the other soil moisture products. Changes in ASCAT soil moisture in general suffer from a low number of consecutive overpasses at lower latitudes, reducing the potential for these retrievals to improve precipitation patterns. Descending SMOS overpasses suffer from non-significant correlations between changes in soil moisture and precipitation, due to a low number of consecutive retrievals. However, the ascending overpass shows high correlation for central CONUS. A similar pattern as for AMSR-E retrievals is obtained, although the spatial consistency of the pattern is lower for SMOS. The changes in land surface temperature show high correlations with precipitation for Eastern CONUS, while correlations in the Western part of CONUS are mostly non-significant.

Finally sensitivity between TMPA-RT and changes in satellite SM and LST was studied. In general correlation between TMPA-RT and the different satellite observations are lower than correlations between NLDAS-2 and these observations (Figure 3.5). This would support the hypothesis that uncertainty in TMPA-RT could be corrected with observations from other remote sensing products. The highest correlations are again found for the AMSR-E for central CONUS, while ASCAT and SMOS retrievals suffer from lower correlations and non-significant correlations. The correlations with changes in land surface temperature are still found for South-Eastern CONUS, however, these correlations are lower than when compared to NLDAS-2.

From this sensitivity analysis it is concluded that the changes in VIC SM and LST are sensitive to precipitation. Changes in satellite based retrievals of SM and LST are sensitive to ground-based observations of precipitation from NLDAS-2. Therefore,

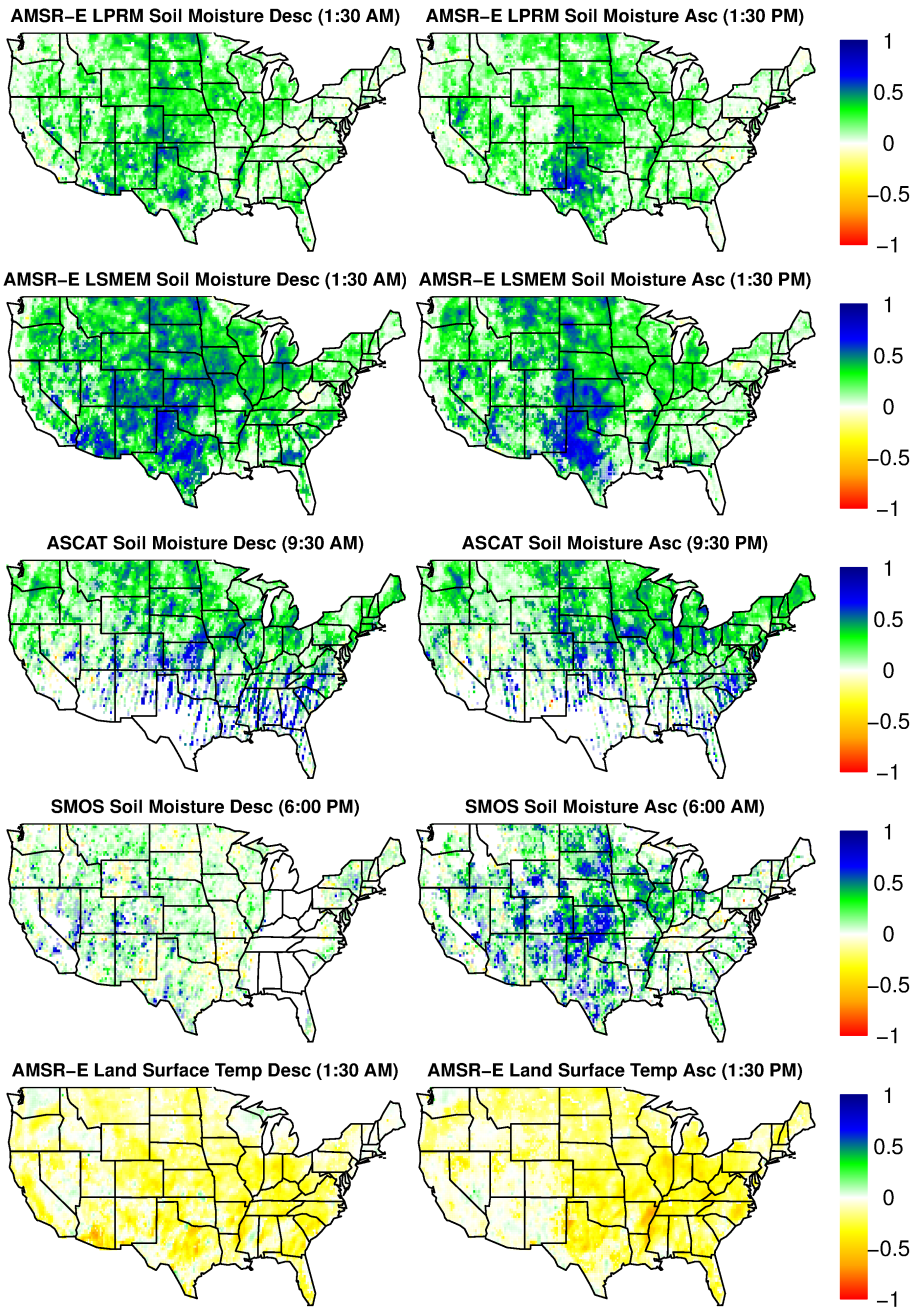

Figure 3.4 Correlation between NLDAS-2 precipitation and changes in satellite-based observations of surface soil moisture (top 4 rows) and land surface temperature (lower row). Correlations are only calculated for days with rain and consecutive satellite overpasses. Non-significant correlations are given in light colours, while dark colours indicate significant correlations.

Table 3.3 Performance of the particle filter based assimilation procedure to retrieve precipitation occurrence based on synthetic observations of soil moisture (SM) and land surface temperature (LST). The skill scores given are derived from the synthetic experiment for the period June 2010 – August 2010. Performance has been given for the median of the posterior probability ($MedPrec$) and the maximum probability ($BestPrec$) sampling method (Figure 3.2).

Scenario	POD	FAR	BS
SM + LST ($MedPrec$)	0.932	0.178	0.114
SM ($MedPrec$)	0.926	0.178	0.115
LST ($MedPrec$)	0.932	0.179	0.114
SM + LST ($BestPrec$)	0.880	0.007	0.072
SM ($BestPrec$)	0.879	0.020	0.078
LST ($BestPrec$)	0.894	0.034	0.075

satellite retrieved SM and LST could be used to improve satellite based estimates of precipitation.

3.3.2 Synthetic experiment

A synthetic experiment was done to test the capability of the assimilation approach to adjust for errors in precipitation. It was found that the assimilation framework is capable to correct for errors in precipitation (Table 3.3). In general the $MedPrec$ sampling has a higher POD and a very high FAR, which will in turn result in a high BS. The $BestPrec$ sampling is more balance, although some skill is lost for the POD. The LST scenario shows the highest POD, while the combined assimilation of SM and LST results in the lowest FAR and BS. The limited POD of mainly SM assimilation is caused by the saturation problem, where pre-storm soil moisture is already saturated so no changes are detected. The detection of very low rainfall rates ($< 0.1\ mm$) is also difficult due to their low impact on the changes in LST and SM.

A total number 250 particles is deemed ideal for the assimilation procedure. The POD, FAR and BS do not change significantly for more than 250 particles, while the computation demand doubles. The $BestPrec$ sampling method has been selected to be used for optimal performance. The $MedPrec$ sampling has an overall low skill and the high FAR makes the $MedPrec$ sampling less reliable. Although the POD of the $BestPrec$ is slightly lower, the $BestPrec$ sampling is deemed superior due to the high skill of the FAR and BS and is therefore used in this study.

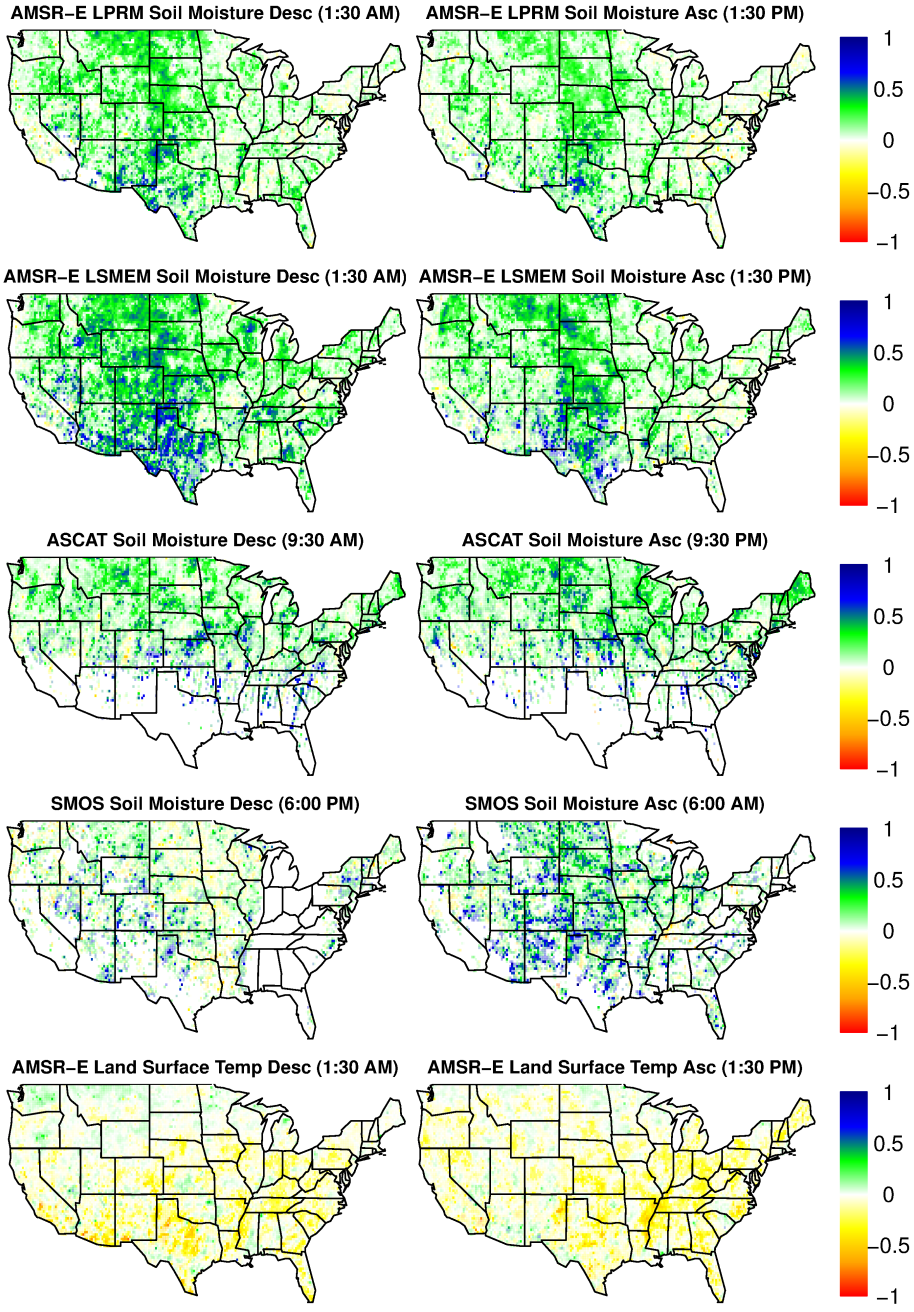

Figure 3.5 Correlation between TMPA-RT precipitation and changes in satellite-based observations of surface soil moisture (top 4 rows) and land surface temperature (lower row). Correlations are only calculated for days with rain and consecutive satellite overpasses. Non-significant correlations are given in light colours, while dark colours indicate significant correlations.

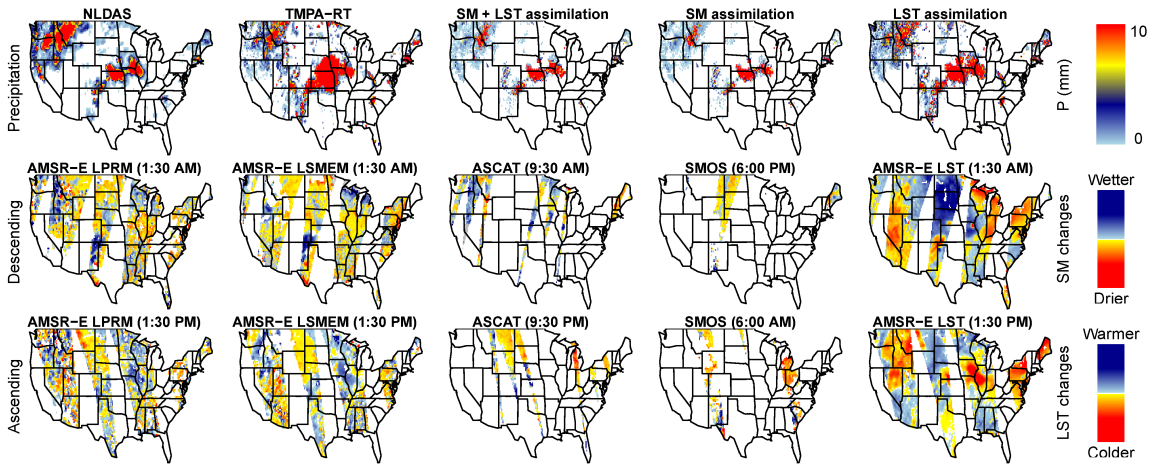

Figure 3.6 Assimilation example of satellite based observations to reduce uncertainties in TMPA-RT for 2 June 2011. Top left indicates the ground-based observations of precipitation from NLDAS-2 (truth), TMPA-RT indicates the original TMPA-RT product and corrected precipitation of three different assimilation scenarios is given. SM+LST includes all available data, SM includes only all soil moisture observations and LST includes only observations of land surface temperature. The middle and lower rows indicate the changes in observed soil moisture (SM) and land surface temperature (LST) from different sensors for different trajectories. The colour scale differs, depending on the variable under study.

3.3.3 Real experiments

The particle filter has been used to update the TMPA-RT product for 2010-2011 based on changes in observations of SM and LST derived from remote sensing. It is shown that both variables have the potential to correct for errors in precipitation retrievals and these variables are sensitive in the land surface model. Assimilation of observations is only possible at locations with consecutive satellite overpasses of AMSR-E, ASCAT or SMOS, since the difference between observations from two consecutive days is used in the assimilation procedure. This will result in a reduced number of observations, especially for the lower latitudes, where consecutive overpasses are less frequent due to their polar orbiting trajectory. Figure 3.6 gives an example of all available satellite observations for one day (2 June 2011). The ground-based precipitation observations from NLDAS-2, TMPA-RT and the corrected TMPA-RT after assimilation are also included. From Figure 3.6 it is clear that uncertainties exist between TMPA-RT and NLDAS-2, for this specific day especially over central CONUS. After assimilation of SM the precipitation is significantly reduced, however, a dry bias occurs. The SM assimilation causes a significantly drier precipitation simulation than the NLDAS-2. The large area of rain present in TMPA-RT that is not present in NLDAS-2 is reduced by SM assimilation, so the false detection of rain in TMPA-RT is reduced. This is most likely due to the saturation effect that limits the benefits of

soil moisture assimilation and the limited information over wet soil where the rainfall amounts are underestimated.

The LST assimilation leads to significantly reduced uncertainties over central CONUS and after assimilation the product is almost identical to NLDAS-2. Precipitation along the coast is still underestimated, which is partly caused by the method used to generate the particle. The initialization of the particles is largely dependent on the original TMPA-RT and does not allow for rain to be created at long distances from retrieved TMPA-RT. Where no LST observations are present (e.g. Eastern part of New Mexico) the original TMPA-RT is not improved and uncertainties are not reduced. When both SM and LST changes are assimilated the data availability increases, however, the dry SM bias partly returns.

From Figure 3.6 it is shown that some changes in SM show unexpected problems compared to the observed precipitation (e.g. AMSR-E in Arizona). Noise in the retrievals resulted in a noise pattern of changes in SM which cannot be explained by the observed precipitation. The pattern of LST changes is more stable, which might potentially influence the assimilation.

The obtained results give confidence to apply the methodology to the entire time period. Additionally, single sensor assimilation scenarios are added to the analysis.

3.3.4 Performance of different assimilation scenarios

Precipitation from TMPA-RT was corrected by the assimilation of remotely sensed SM and LST observations for the period 2010-2011. The obtained uncertainties of TMPA-RT and the correction after assimilation are given in Table 3.4. The POD only improved when LST is used for the detection of rain, while the assimilation of SM deteriorates the POD. This implies that retrieved changes in satellite LST contain more information on the precipitation occurrence, than found for satellite-derived SM changes. The combination of LST and SM shows an intermediate performance, where POD is still reduced due to the high number of SM observations compared to LST observation. Single sensor satellite retrieved SM changes will result in lower PODs compared to TMPA-RT, however, PODs are higher than the combined SM scenario. This is partly due to the lower number of observations for assimilation compared to the SM scenario.

The FAR of TMPA-RT is reduced with the assimilation of both SM and LST, where even the assimilation of single sensor satellite SM resulted in an improvement in the FAR. It is concluded that TMPA-RT in general has too many rain days compared to the observations and this characteristic is corrected by the assimilation of land surface variables.

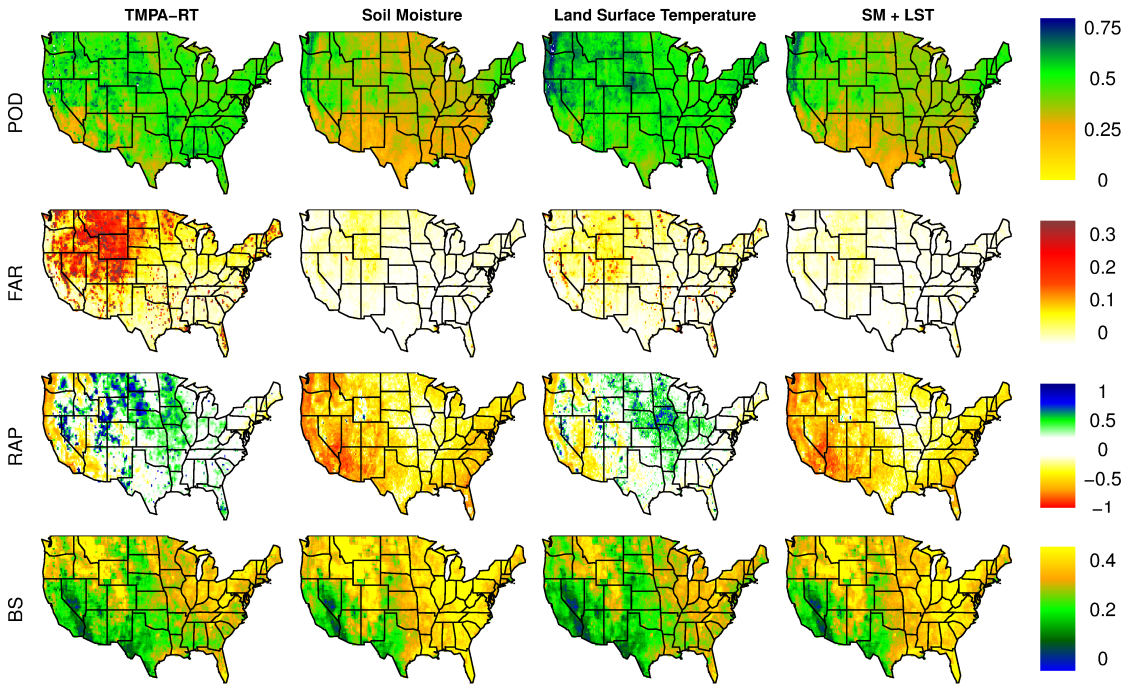

Figure 3.7 Skill scores of TMPA-RT and TMPA-RT after assimilation of soil moisture, land surface temperature or both. Skill scores are calculated based on comparison with ground-based precipitation from NLDAS-2 with a 0 mm rain threshold to distinguish between a rain event and dry conditions.

The BS is a lumped measure of the number of correctly observed rain and dry days. The TMPA-RT BS for a 0 mm event threshold is only reduced when either a combined assimilation of satellite LST and SM changes is done or only LST changes are used. With a higher threshold of 2 mm the BS is in all scenarios reduced to lower values, indicating higher skill. This indicates that assimilation of SM changes has a positive impact for medium and high intensity rain events that exceed the 2 mm threshold.

The Spearman correlation is found to improve for all scenarios indicating that assimilation of additional satellite observations has a positive impact on the ranked probability. The best results are obtained after the assimilation of LST changes, which shows the highest Spearman correlation after assimilation.

The negative impact of the assimilation of SM changes in POD and the BS (0 mm threshold) is a result of a dry bias found in the SM assimilation. Figure 3.7 also shows an on average dry correction of TMPA-RT, which is also found over the two year assimilation period. This results in low POD and FAR values, since the product is in general dry biased, which will reduce the skill to detect rain and will enhance the skill to predict dry days.

Table 3.4 Skill scores of TMPA-RT and TMPA-RT after different assimilation scenarios. Skill scores are calculated based on comparison with ground-based precipitation from NLDAS-2 with a 0 mm rain threshold.

	POD		FAR		BS		Spearman	Percentage
	0 mm	2 mm	0 mm	2 mm	0 mm	2 mm	Correlation	available (%)
TMPA-RT	0.456	0.573	0.092	0.072	0.316	0.186	0.555	100
SM + LST	0.378	0.353	0.010	0.017	0.314	0.123	0.615	95.7
SM	0.336	0.307	0.013	0.017	0.337	0.126	0.576	94.7
LST	0.505	0.590	0.033	0.049	0.262	0.152	0.676	75.5
SM-LPRM	0.382	0.409	0.042	0.036	0.328	0.145	0.559	64.3
SM-LSMEM	0.388	0.439	0.042	0.038	0.325	0.144	0.566	61.6
SM-ASCAT	0.384	0.423	0.041	0.034	0.326	0.143	0.565	77.9
SM-SMOS	0.398	0.466	0.060	0.048	0.329	0.158	0.545	44.6

3.3.5 Seasonal impact of assimilation

The quality of the TMPA-RT product varies throughout the year as is the impact of different assimilation scenarios (Tables 3.5 and 3.6). The skill of TMPA-RT is lowest for the winter, while the other seasons show in general much higher skill. For the winter season all skill scores show an improvement after the assimilation of remotely sensed SM or LST changes. The LST has a year-round positive impact on the skill of the precipitation detection. PODs are increased, especially for the winter and spring. BS is always reduced with a very high skill for the spring and autumn.

For the assimilation of SM and SM+LST the skill decreased for the summer and autumn with an exception for the FAR, which is always lower compared to TMPA-RT. These results show that even when the overall year-round skill is reduced by the assimilation of satellite SM changes a positive impact was found for winter and spring. The assimilation of summer SM changes negatively impacts precipitation retrievals in terms of skill and POD.

3.3.6 Spatial impact of assimilation

The quality of the the assimilation was evaluated spatially to assess where the potential gain of the assimilation of satellite-derived changes in SM and LST was the largest (Figure 3.7). TMPA-RT shows high POD throughout CONUS, however, the FAR is very high for the area in and around the Rocky Mountains. The $RAPB$ shows a dry bias along the West coast and a wet bias in and on the Eastern border of the Rocky Mountains. BS was highest for the South West, where the FAR is low and POD is high.

Table 3.5 Skill scores of TMPA-RT and TMPA-RT after different assimilation scenarios for different seasons. Skill scores are calculated based on comparison with ground-based precipitation from NLDAS-2 with a 0 mm rain threshold to distinguish between a rain event and dry conditions.

	POD				FAR				BS			
	DJF	MAM	JJA	SON	DJF	MAM	JJA	SON	DJF	MAM	JJA	SON
TMPA-RT	0.34	0.47	0.52	0.46	0.09	0.11	0.09	0.09	0.37	0.32	0.30	0.29
SM + LST	0.38	0.45	0.35	0.34	0.02	0.01	0.00	0.01	0.31	0.28	0.35	0.29
SM	0.34	0.42	0.29	0.31	0.03	0.01	0.00	0.01	0.34	0.30	0.38	0.31
LST	0.42	0.56	0.53	0.49	0.03	0.03	0.02	0.05	0.30	0.24	0.26	0.25

It was found that the assimilation of SM changes does negatively impact the POD and BS. Exceptions are found West of the Rocky Mountains, where the assimilation does not negatively impact the skill or even improve the skill. The same is found for the East coast, where especially in the North the skill score is increased. The FAR is positively impacted through CONUS, while the $RAPB$ clearly shows the dry bias in the SM assimilation.

Assimilation of changes in LST does improve the POD, FAR, BS and the $RAPB$ through CONUS. No distinct spatial patterns are found, while annual precipitation biases are strongly reduced compared to TMPA-RT. The highest positive impact of assimilation of LST is found for the North-West where precipitation totals are high.

Combined assimilation of SM an LST changes will show intermediate results between separate assimilation of SM and LST. The FAR is further reduced compared to SM assimilation; however, the POD remains lower than for the assimilation of only LST.

3.4 Discussion

3.4.1 Impact of event threshold

The 0 mm (Table 3.5) and 2 mm (Table 3.6) event thresholds show similar patterns concerning the seasonality of the performance. In general skill scores show a better performance throughout the season with a 2 mm threshold; which was previously also found for the year round performance (Table 3.4). The performance of the LST scenarios is not superior in terms of the BS compared to the other scenarios, which was also confirmed in Table 3.4.

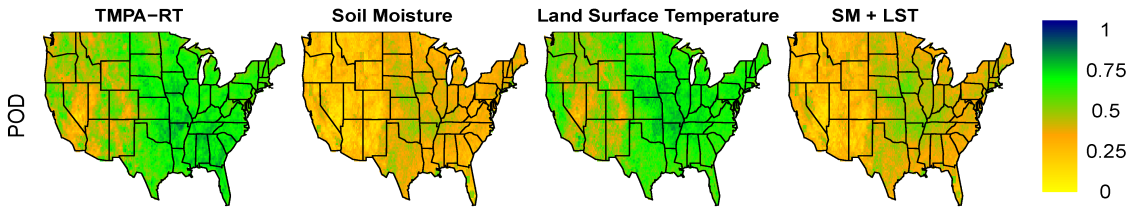

Figure 3.8 Skill scores of TMPA-RT and TMPA-RT after assimilation of soil moisture, land surface temperature or both. Skill scores are calculated based on comparison with ground-based precipitation from NLDAS-2 with a 2 mm rain threshold to distinguish between a rain event and dry conditions. Please note different colour scales compared to Figure 3.7.

Table 3.6 Skill scores of TMPA-RT and TMPA-RT after different assimilation scenarios for different seasons. Skill scores are calculated based on comparison with ground-based precipitation from NLDAS-2 with a 2 mm rain threshold to distinguish between a rain event and dry conditions.

	POD				FAR				BS			
	DJF	MAM	JJA	SON	DJF	MAM	JJA	SON	DJF	MAM	JJA	SON
TMPA-RT	0.49	0.52	0.62	0.62	0.08	0.06	0.08	0.07	0.19	0.19	0.20	0.17
SM + LST	0.44	0.34	0.31	0.35	0.04	0.01	0.01	0.01	0.14	0.13	0.13	0.10
SM	0.41	0.30	0.26	0.32	0.04	0.01	0.01	0.01	0.14	0.13	0.13	0.10
LST	0.55	0.57	0.59	0.63	0.06	0.04	0.05	0.05	0.15	0.15	0.16	0.14

As is shown in Table 3.4 the higher (2 mm) event threshold has a positive impact on the BS, which is also found in the spatial analysis. The POD for medium to high intensity rain events is increased for TMPA-RT and the LST scenario (Figure 3.8). In the FAR no significant changes in spatial patterns were found compared to the lower event threshold. The BS of the original uncorrected TMPA-RT is lower for the 2 mm threshold, and improvements are found for all the assimilation scenarios. This indicates that there is a positive impact after removing small rain events, where the scenarios that include SM data show a better performance when only medium and high intensity rain events are considered.

3.4.2 Soil moisture observations

As a result of the obvious relationship between changes in SM and precipitation, it was expected that observations of changes in SM should lead to an improved probability of rain fall detection (POD). Surprisingly, in this study this improved POD was not found for a large part of CONUS (Figure 3.7). From the synthetic experiment it was

found that the potential is high if the observed changes are accurate, so the problem is mainly caused by uncertainty and noise in the satellite retrievals.

Changes in SM were studied and it was found that the retrieved changes show great uncertainty and noise in the retrievals. From the example retrieval shown in Figure 3.6, it was found that for the South-Western swath of AMSR-E the pattern is not consistent. Although from the observed precipitation it is shown that this area should be dry, the changes in satellite retrieved SM do not show an unambiguous dry pattern. This problem is found for all sensors and for the entire assimilation period (Figures 3.9 and 3.10). Another example is given by Figure 3.11 where soil moisture retrievals often indicate a rainfall event when nothing is observed for a number of days. These higher frequency noise components (found in both space and time) will reduce the potential for reducing uncertainties in satellite precipitation observations. Additionally, these noise components in the SM retrieval produce inconsistent patterns in SM changes, when compared with observed precipitation (Figure 3.6). Although the data has been filtered to remove potential erroneous SM retrievals, noisy patterns remain visible. Most likely the majority of the satellite retrieval noise will be attributed to SM since the retrieval algorithms assume error-free radiometer-level brightness temperatures and try to estimate the SM signal from many other components in the scene, some of which are not well represented in the algorithms (e.g. landscape heterogeneity, wet lands, scattered pockets of trees and urban areas). The retrievals are not constrained to previous SM retrievals either which increase the degrees of freedom (and hence potential for noise) in the SM retrieval.

Furthermore, it is found that the changes in soil moisture simulated by the model and observed by the satellite have a different dynamic range (Figure 3.12). This indicates that changes in the satellite SM are more abrupt than the model response to similar events. The number of times a positive SM change is found for satellite-derived SM is significantly larger than for the model simulated SM. When a positive increase in SM is associated with precipitation, this indicates that satellite retrievals overestimate the percentage of rainy days by 20% compared to model simulated percentage of rain days. This could clearly impact the potential of these satellite observations to successfully retrieve rain events that are missed by TMPA-RT. If the particle generation of the data assimilation approach was not restricted to the original TMPA-RT this would lead to significant problems, with an overestimation of the number of rain events. Apart from the differences in the dynamic range of the SM changes, it was also found that satellite-derived SM changes show high noise levels for dry SM conditions. When the SM state is dry, satellite retrievals tend to show a strong increase in satellite SM changes relative to the current state, while model simulations do not suggest this pattern. This indicates that in dry conditions the satellite SM retrieval is hampered and the resulting satellite-derived SM changes are affected by a high retrieval noise. A potential solution for some of these problems is to correct the difference between modeled and observed soil moisture changes through CDF matching to match observed to modeled SM increments. Although it is recognized that this

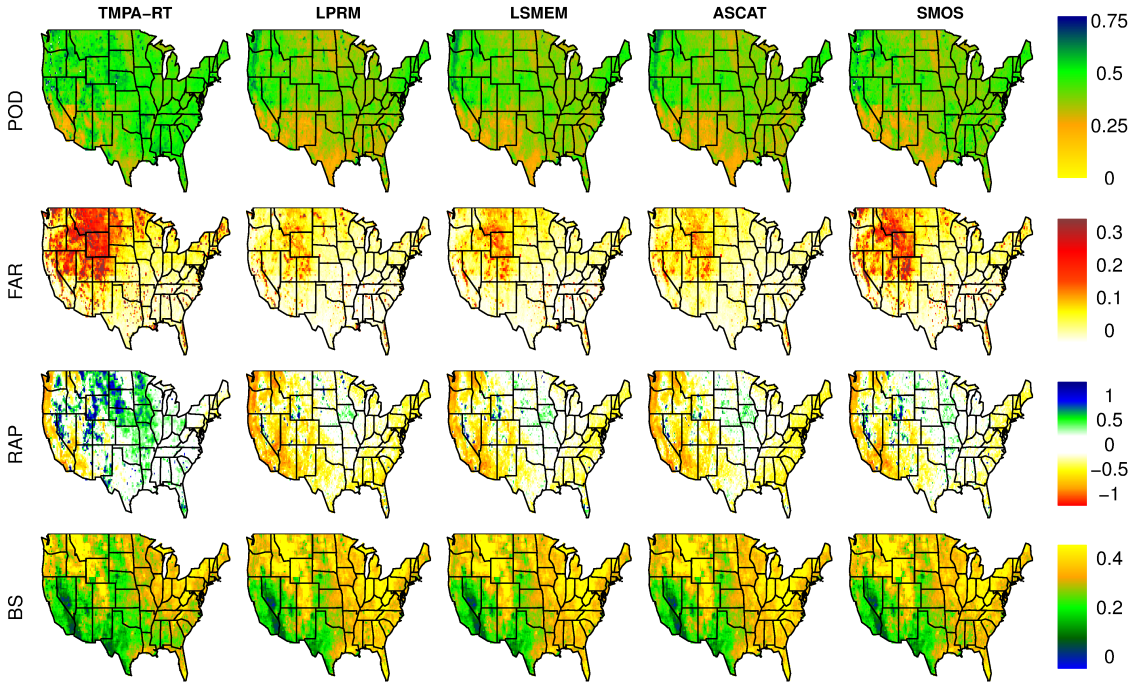

Figure 3.9 Calculated skill scores of TMPA-RT and TMPA-RT after assimilation of single sensor retrievals of soil moisture. Skill scores are calculated based on comparison with ground-based precipitation from NLDAS-2.

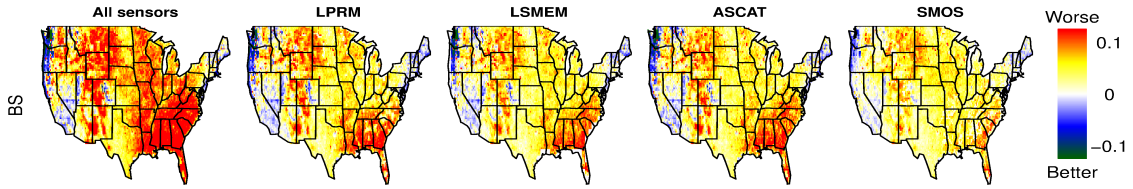

Figure 3.10 Difference in Brier scores between the original TMPA-RT and TMPA-RT after assimilation of soil moisture retrievals from all available sensors or single sensor retrievals of soil moisture.

could be a potential solution to some of the problems related to the assimilation of SM changes, this would require too much tuning of the observations. Resolving the problem of the mismatch of the SM changes in an effective and realistic manner requires additional research that is beyond the scope of this paper.

The findings on precipitation correction with SM observations from this study are contradictory to the studies of Crow and Bolten (2007); Pellarin et al. (2008); Crow et al. (2009, 2011); Brocca et al. (2013); Pellarin et al. (2013); Brocca et al. (2014), where improvements were found for some regions. Results from this study differ in the way observations are used and the spatial and temporal resolutions of the rainfall correction. In contrast with Pellarin et al. (2008, 2013), this study uses processed brightness temperatures from AMSR-E and the retrievals of SM changes that come from the LPRM and LSMEM algorithms, instead of a direct assimilation of brightness temperature. Brocca et al. (2013) use the Soil Water Index, which is a temporally smoothed soil moisture product derived from ASCAT (at 1° resolution) and performance are evaluated over 5 day aggregation periods. Brocca et al. (2014) use the soil moisture retrievals of ASCAT, AMSR-E and SMOS; however, a 5 day aggregation period is applied to improve the number of consecutive satellite observations. The studies of Crow et al. (2009, 2011) use 2-10 day average satellite-derived soil moisture increments at a coarser 1° spatial resolution. Moreover, Crow et al. (2009) use a 12 hour time shift to capture the necessary delay between precipitation and soil moisture increments and conclude that 3 day rainfall accumulation periods are approximately the finest temporal scale at which precipitation corrections are possible with satellite soil moisture from AMSR-E. All of these studies use some form of space or time aggregation (which reduces retrieval noise) or use the unprocessed brightness temperatures, which are not affected by noise attribute to the soil moisture retrieval algorithms. This suggests that satellite soil moisture retrievals are not suitable to correct satellite precipitation at the 0.25° resolution at the fine temporal resolution used in this study and should be spatially upscaled to improve the signal to noise ratio and hence contain more valuable information. Additionally, noise filtering techniques could be applied to reduce the retrieval noise (e.g. low pass filters). However, the downside of these types of techniques is that they require knowledge on future observations and are therefore difficult to apply for real-time satellite retrievals.

A second problem for the assimilation of SM changes is the difference in the penetration depth of the different sensors and the difference between the model soil moisture depth (0.1m top model layer) and the penetration depth (about 0.01 m for X-band AMSR-E). This problem should only have an impact on the actual rainfall retrieval and the effect should be less on the probability of rain detection, where SM change will only be stronger for shallower penetration depths.

Although microwave SM retrievals are known to suffer from impacts of vegetation (Parinussa et al., 2011) and topography (Engman and Chauhan, 1995) no clear patterns are found in this study. The pattern shown in Figure 3.4 and Figure 3.11 was

found all across CONUS and does not seem to be impacted by any land surface characteristics.

3.4.3 Temperature observations

In this study only changes in LST from one microwave satellite sensor have been used in the assimilation. Addition of more satellite retrieved LST products could result in a further reduction of the uncertainties in satellite precipitation. Since the LST assimilation already shows a large impact on the quality of the correction, including more sensors could have a significant impact on the reduction of the uncertainty in the satellite precipitation.

An option for additional LST observations would be LST retrievals from thermal infrared sensors (e.g. MODIS, Wan, 2008). However, thermal infrared retrievals are hampered by cloud contamination leading to a lower certainty in the retrieved LST values. Therefore, the assimilation of additional microwave retrievals (from Ka-band) could lead to a further reduction of the uncertainties in satellite based precipitation. Microwave LST retrievals are available from Special Sensor Microwave and Imager (SSMI), Tropical Rainfall Measuring Mission Microwave Imager (TMI), AMSR-E and AMSR-2. The orbits and spatial resolutions of these sensors are not identical. However, they could be of significant importance to further reduce uncertainties of satellite-derived precipitation.

3.4.4 Model and ground-based precipitation

In this study, the VIC model was implemented to transform the precipitation into changes in SM and LST. This could impact the results since the response is model specific and related to changes in land surface variables. However, VIC is capable to solve the full water and energy balance, leading to improved simulation of the land surface temperature. For this assimilation approach it is required that the Land Surface model is capable to solve the energy balance because otherwise it will not give accurate simulations of the LST changes.

Furthermore, the Northern Land Data Assimilation System phase 2 (NLDAS-2) was used as reference dataset for the quality of the assimilation. Although all ground-based observations are known to possess biases and errors, the uncertainties in the dataset will be smaller than the uncertainties found in the satellite retrieved precipitation. The results could slightly change with the use of other reference datasets. However, the difference between the ground-based observational precipitation datasets is negligible compared to the uncertainties in TMPA-RT.

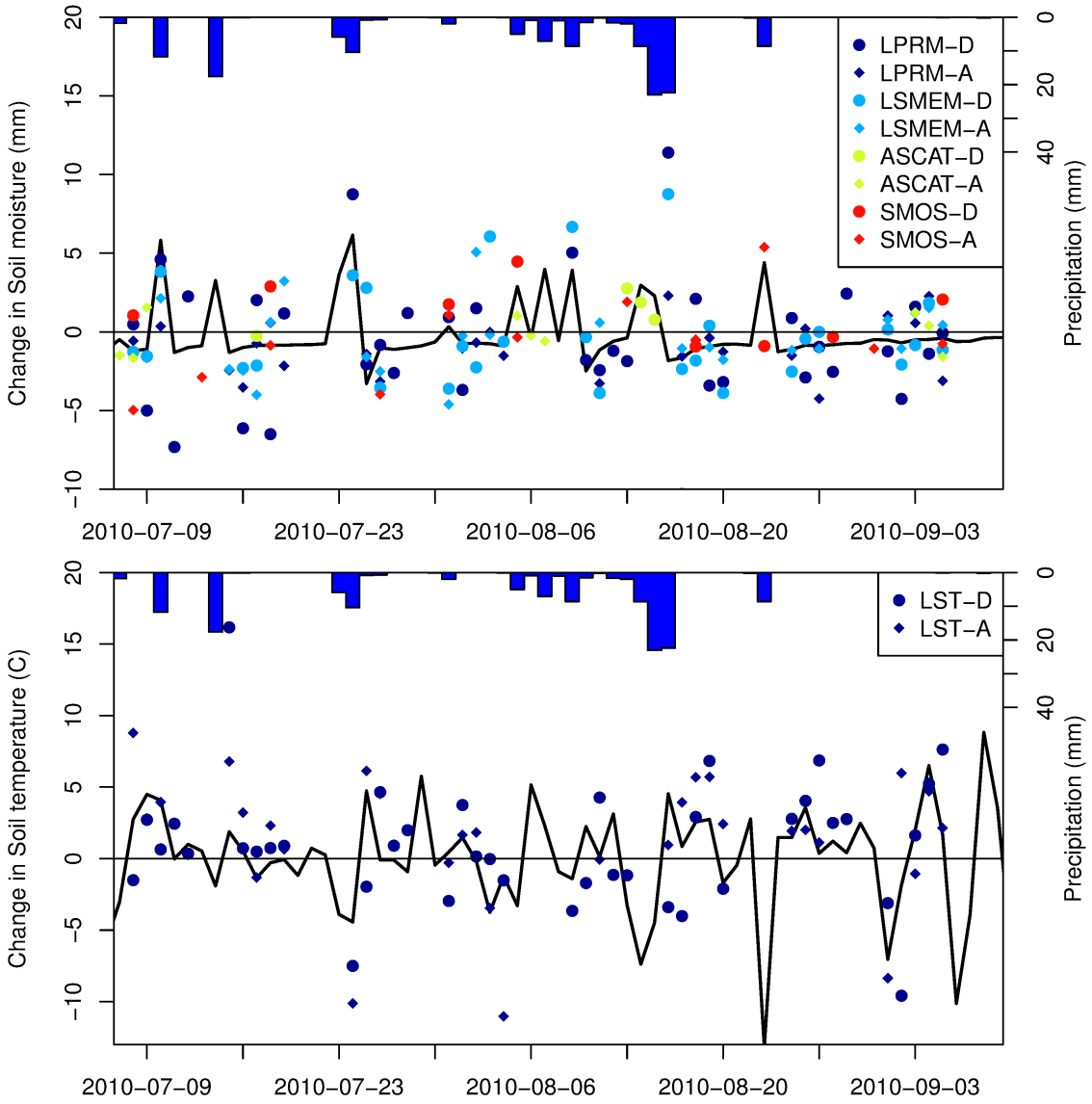

Figure 3.11 Observed (points) and modeled (line) changes in soil moisture (top panel) and land surface temperatures (bottom panel), combined with the daily precipitation (bars) for a location in Kansas State (100°W, 38°N). Changes in observed soil moisture and land surface temperatures are derived from consecutive satellite overpasses. Values are displayed at a daily time step, which could result in some temporal mismatch. Ascending (A) and Descending (D) overpasses are given separately.

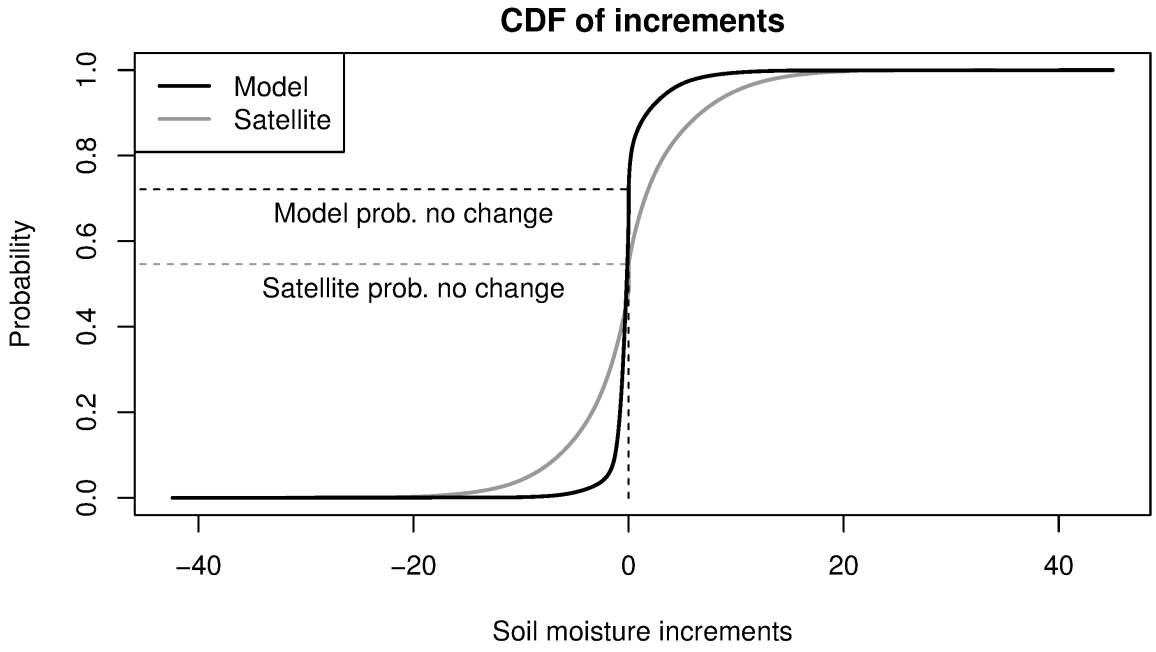

Figure 3.12 Modelled and satellite-derived changes in soil moisture after CDF matching of the original retrievals. Dashed lines indicate the probability of no or negative changes in the soil moisture state.

3.5 Conclusion

A particle filter based assimilation framework was implemented to reduce the uncertainties in satellite derived precipitation from TMPA-RT, by assimilating satellite-derived SM and LST changes over CONUS. Observations from four satellite SM algorithm and one LST algorithms have been assimilated for the period 2010-2011.

It was found that changes in SM and LST, derived from microwave remote sensing, were sensitive to ground-based precipitation observations from NLDAS-2. Additionally, the VIC model showed a high sensitivity of changes in SM and LST to precipitation.

The synthetic assimilation experiment showed the capability of the assimilation framework to reduce uncertainties in perturbed precipitation compared to the original observed precipitation. It was found that changes in synthetic observations of SM or LST could be used to improve both precipitation rates and occurrence with high accuracy. Combined assimilation of synthetic SM and LST changes showed an even higher potential to reduce uncertainties.

The assimilation framework was used to reduce uncertainties in TMPA-RT. It was found that assimilation of satellite-derived SM changes only increased the uncertain-

ties in the TMPA-RT compared to NLDAS-2 observations. This is mainly caused by noise in the retrieved SM, both in space and time. Here a better understanding of the SM error behaviors and the underlying physical mechanism is needed in order to develop a smarter and better performing SM assimilation procedure in the future. Assimilation of changes in LST significantly reduced the uncertainties within TMPA-RT, where especially the *POD* had increased from 0.45 to 0.50 on average. The false detection of rain was reduced after assimilation of SM, LST, or the combined assimilation of SM and LST. The highest impact of assimilation was found for winter and spring conditions. SM assimilation resulted in a dry bias, whereas LST assimilation resulted in more accurate annual precipitation volumes compared to TMPA-RT.

This study shows the potential of improving TMPA-RT with other satellite-based observations. TMPA-RT is now widely used for hydrological modeling, monitoring and flood and drought forecasting over sparsely gauged basins (e.g. Africa). In these types of applications, our findings could have significant implications and help improve hydrological monitoring and forecasting skills in these regions.

4 Calibration of a global hydrological model

This chapter is based on:
Wanders, N., Sutanudjaja, E. H., van Beek, L. P. H., Bierkens, M. F. P. (2014), The PCR-GLOBWB global hydrological reanalysis product, Journal of Advances in Modeling Earth Systems, submitted.

Abstract

The goal of the present work is to produce a multi-decadal "terrestrial hydrological reanalysis" dataset with retrospective and updated hydrological states and fluxes that are constrained with available in-situ river discharge measurements. By embedding the global hydrological model PCR-GLOBWB in an Ensemble Kalman Filter framework, the model parameters were calibrated based on 1495 time series of discharge observations from the GRDC. The calibrated parameters are related to the snow module, runoff-infiltration and unsaturated zone processes, as well as pre-factors to correct forcing precipitation fields for local topographic and orographic effects. The calibration covers the period 1960-2010 and the obtained posterior distributions are used to create a global hydrological reanalysis that is evaluated against 6475 discharge stations using the long-term GRDC dataset. Results show that the model parameters can be calibrated successfully. Corrections to the rainfall fields are considerable, where topography has the largest impact on the precipitation corrections. Globally the precipitation is reduced by 9.2% to 9.9×10^3 km^3 y^{-1}, indicating that the original CRU TS3.21 estimate is too wet. After calibration the $RMSE$ is reduced by 10% on average, leading to improved discharge simulations, especially under base flow situations. The final outcome is the first ensemble hydrological reanalysis product that is consistent with discharge observations, has a closed water balance (for all 48 ensemble members) and provides estimates on the uncertainty in all fluxes and storage components of the terrestrial water cycle. The new reanalysis product will be valuable for studies into atmospheric moisture recycling and the global water cycle, in general.

4.1 Introduction

Water plays a crucial role in Earth's climate, its ecosystems and its human population. Precipitation and evaporation directly interact with the climate, while the environment and human population are directly impacted by the total water avail-

ability in different storages components (e.g. snow, soil moisture, surface water or groundwater).

The impact of the terrestrial water cycle on humans and nature makes it crucial to fully understand the relationship between the different water stores and fluxes. With respect to sustainable water use and climate induced changes in water availability, it is important to have high quality estimates of the different components of the water cycle. Trend studies of the water cycle can indicate unsustainable situations or indicate changes in hydroclimatological conditions. Moreover, the different fluxes and stores of the terrestrial water cycle constitute important boundary conditions for ocean and atmospheric modelling, for the design of flood defence measures and reservoirs and for assessing human water availability.

This shows the importance of having accurate knowledge on the storage and fluxes of the terrestrial water cycle. However, the estimates of the storage and fluxes are rather different amongst studies and remain uncertain (e.g. Dirmeyer et al., 1999; Oki and Kanae, 2006; Trenberth et al., 2007, 2011). Most studies lack uncertainty estimates and the range of estimates is broad, i.e. they either consist of a deterministic single model simulation (e.g. Oki and Kanae, 2006; Trenberth et al., 2007, 2011) or are based on observations (Kinter and Shukla, 1990). Although they have the advantage that they provide estimates of uncertainty, the existing multi-model estimates are hampered by the fact that they do not take into account observational data and depend solemnly on model simulations (e.g. Dirmeyer et al., 1999; Haddeland et al., 2011). Dirmeyer et al. (1999) expresses the need for a land surface data assimilation scheme to improve the existing estimates and reduce the existing uncertainty.

In contrast to previous work, Rodell et al. (2014) used a solemnly observational based approach and an observation integrated model approach to quantify fluxes in the global water cycle for the period 2000-2010. Rodell et al. (2014) used a large set of satellite observations to close the water balance and also provided uncertainty estimates derived from the discrepancy between different observational datasets and satellite retrieval uncertainty. The observation integrated model approach used by Rodell et al. (2014) is based on a post processing optimization approach, where model simulations are constrained by observations to reduce uncertainty in flux estimates. An advantage of the applied post-processing approach is that it respects the mass balance equations and does not introduce errors in the water balance as a result of the optimization. The uncertainties in the flux and storage estimates are reduced after optimization. Although the work of Rodell et al. (2014) clearly advances the estimates of global water fluxes it does not use the observational data to constrain initial model simulation.

Pan et al. (2011) used a similar approach as Rodell et al. (2014), where additional observations were used to correct model simulations in a post-processing routine for 32 major river basins. As stated by Pan et al. (2011), the post-processing approach should lead to a *perfect* closure of the water balance. The approach is limited in

a sense that observed information is only used as post-processing for selected river basins, while it is not used to improve model performance or initial storage estimates at the global scale.

Van Dijk et al. (2014) used a Bayesian approach to reduce uncertainty in model simulations based on observations from the Gravity Recovery And Climate Experiment (GRACE). GRACE observations are directly assimilated into the model simulations, leading to improved estimates of the water storage. This Bayesian approach does lead to problems in the water balance closure, because it introduces and removes water from the storage based on the GRACE observations. Although Van Dijk et al. (2014) did not look at fluxes in the global water cycle, they do produce a reanalysis product for hydrology based on these observation integrated simulations. As mentioned before, the water balance is not closed, which limits the applicability of the reanalysis product for studies related to multiple components of the hydrological cycle and the underlying fluxes.

The objective of this study is to create an observation-integrated hydrological reanalysis dataset with a closed water balance. To fulfil this objective the global hydrological model PCR-GLOBWB (Van Beek et al., 2011) and a land surface data assimilation scheme (Ensemble Kalman Filter) were used to integrate discharge observations into the model simulations. The final outcome of this study will be the first ensemble hydrological reanalysis product that is consistent with discharge observations, has a closed water balance (for every ensemble member) and provides estimates on the uncertainty in all fluxes and storage components of the terrestrial water cycle.

4.2 Material and Methods

4.2.1 Model description

The state-of-the-art global hydrological and water resources model PCR-GLOBWB was used to simulate spatial and temporal continuous fields of discharge and storage in rivers, lakes, and wetlands at a 0.5° spatial resolution (Van Beek et al., 2011; Wada et al., 2014). In brief, the model simulates for each grid cell and for each time step (daily) the water storage in two vertically stacked soil layers and an underlying groundwater layer. At the top a canopy with interception storage and a snow cover may be present. Snow accumulation and melt are temperature driven and modelled according to the snow module of the HBV model (Bergström, 1995). The model computes the water exchange between the soil layers, and between the top layer and the atmosphere (rainfall, evaporation and snowmelt). The third layer represents the deeper part of the soil that is exempt from any direct influence of vegetation, and constitutes a groundwater reservoir fed by active recharge. The groundwater store is explicitly parameterized and represented with a linear reservoir model (Kraijenhof van de Leur, 1962). Sub-grid variability is considered by including separately short

and tall natural vegetation, open water (lakes, floodplains and wetlands), soil type distribution (FAO Digital Soil Map of the World), and the fractional area of saturated soil calculated by the Improved ARNO scheme (Hagemann and Gates, 2003) as well as the spatio-temporal distribution of groundwater depth based on the groundwater storage and the surface elevations as represented by the 1 km by 1 km Hydro1k data set (`https://lta.cr.usgs.gov/HYDRO1K/`, Verdin and Greenlee, 1996). Simulated specific runoff from the two soil layers (direct runoff and interflow) and the underlying groundwater layer (base flow) is routed along the river network based on the Simulated Topological Networks (STN30, Vörösmarty et al., 2000a) using the method of characteristic distances (Wada et al., 2014). Reservoirs and water abstraction is included in PCR-GLOBWB simulations, where the water abstraction can come from surface or groundwater (De Graaf et al., 2014). The groundwater abstraction can be divided into fossil and renewable groundwater, where the fossil groundwater is abstracted from deep groundwater aquifers that are not replenished. The abstraction rates are dynamic over time and dependent on the irrigation and none-irrigation (e.g. domestic, industry) water demand.

4.2.2 Forcing data

The required forcing data for PCR-GLOBWB consist of daily precipitation, temperature and reference potential evapotranspiration. As the original forcing data for this study, the monthly CRU TS 3.21 dataset (Harris et al., 2014) was used in combination with the daily fields of ECMWF ERA-40 (Uppala et al., 2005) and ECMWF ERA-Interim re-analysis products (Dee et al., 2011). Both ECMWF reanalysis datasets were used to downscale the monthly values of CRU TS3.21 to daily values. For downscaling in the period 1960-1978, ERA-40 (available since 1957) was used, while ERA-Interim (available since 1979) was used for downscaling in the the period 1979–2010. For an extensive explanation about the methodology used for this downscaling, the reader is referred to Van Beek (2008) and Sutanudjaja et al. (2011). In addition to this downscaling, a precipitation correction was also included based on the method of Fiedler and Döll (2007) as snow under-catch errors in a precipitation field gauge-based product of CRU TS3.21 can be large during the cold season at high latitudes.

4.2.3 Discharge data

To evaluate the performance of the PCR-GLOBWB model, discharge observations from the Global Runoff Data Centre (GRDC) were used. Stations were matched to the PCR-GLOBWB grid representation to compare simulated and observed discharge for the period 1960-2010. Discharge stations were selected when over 5 years of monthly data is available, the difference in catchment size between model and observation is

less then 10% and the station quality is sufficient according to the GRDC. These criteria resulted in a total of 6475 stations with an average record length of 28 years.

For the calibration a subset of the discharge stations from the GRDC was used, based on the quality estimate of the observations. The GRDC quality estimate was used to remove erroneous stations, thereafter the difference in catchment size between model and observation is less then 5%. This resulted in a total of 1495 reliable stations that cover 49% of the global catchments and provide observations throughout the period 1960-2010. The average data availability was 1000 stations for any given month in the simulation period.

4.2.4 Data assimilation framework

The Ensemble Kalman Filter (EnKF) is a Monte Carlo based data assimilation and model calibration approach, and especially suited for high dimensional systems (Evensen, 1994; Burgers et al., 1998; Evensen, 2003, 2009). The mode uncertainties in the EnKF are derived from the multiple ensemble members of the Monte Carlo approach. A basic assumption in the EnKF is that with enough ensemble members the ensemble spread can be used to approach the full model uncertainty of the simulation. Especially for distrubtions with large tails it is important that the number of ensemble members is sufficient to capture the full distribution. The EnKF does not require a separate model for the propogation of the model error covariance matrix, because it is computed from the ensemble spread. These properties make the EnKF highly suitable for complex spatially distributed models, with long calculation times and a large number of calibration parameters or state variables, like PCR-GLOBWB. The forward PCR-GLOBWB model is given by:

$$\Psi(t+1) = f(\Psi(t), F(t), p) \tag{4.1}$$

where $\Psi(t)$ is the state of the model at time t, $F(t)$ the model forcing at time t (e.g. precipitation, evaporation and temperature) and p are the model parameters (e.g. saturated conductivity, routing or groundwater parameters). The EnKF is applied on each monthly time step using the monthly discharge observations. The general form of the EnKF is given by Evensen (2003). It can be formalized by the model forecast (Ψ^f), given by:

$$\Psi^f = (\psi_1^f, ..., \psi_{nens}^f) \tag{4.2}$$

where $\psi_1^f, ..., \psi_{nens}^f$ are the individual model forecasts. The state error covariance matrix of the model is directly calculated from the ensemble spread using:

$$P^f = \overline{(\Psi^f - \Psi^t)(\Psi^f - \Psi^t)^T} \tag{4.3}$$

where Ψ^t is the true model state. Since the true state is not known it is assumed that:

$$P^f \approx P_e^f = \overline{(\Psi^f - \overline{\Psi^f})(\Psi^f - \overline{\Psi^f})^T} \tag{4.4}$$

where $\overline{\Psi^f}$ represents the ensemble average and it is assumed that the ensemble of model predictions is unbiased. The observations matrix, Y contains the observations and is given by:

$$Y = H\Psi^t + \epsilon \tag{4.5}$$

where H is used to transform Ψ^t to the observations and ϵ the random error in the observations. ϵ is random noise with a zero mean and a standard deviation given by R, the measurement error covariance. This leads to the general form of the EnKF:

$$\Psi^a = \Psi^f + P^f H^T (H P^f H^T + R)^{-1} (Y - H\Psi^f) \tag{4.6}$$

With the help of state-augmentation, the EnKF also allows model parameters to be estimated with each update. Since there are no observations of the parameters, only the matrix Ψ^f and measurement operator are extended to enable the parameters of Table 4.1 to be estimated. This results in updated parameters in Ψ^a which are perturbed by multiplicative white noise with a standard deviation of 0.01, to prevent ensemble deterioration. The perturbations are given by:

$$Ln(p'_t) = Ln(p) + W(0, 0.01) \tag{4.7}$$

where p'_t are the perturbed parameters and $W(0, 0.01)$ is white noise with a mean of 0 and standard deviation of 0.01 (-). These new parameters are then used to propagate the model to the next update moment using Equation 4.1.

4.2.5 Implementation of Ensemble Kalman Filter

As input for the calibration discharge observations were used to correct the model parameters. At the end of each month the difference between model simulated and observed discharge was used in Equation 4.6 to improve the estimates of the parameters. No model states were updated, since this would induce water balance errors. The prior distribution of the calibration parameters (Table 4.1) was created by:

$$p'(n) = p_0 * W(\mu_p, \sigma_p) \tag{4.8}$$

where $p'(n)$ is the prior parameterization for ensemble member (n), p_0 is the original PCR-GLOBWB parameter value and $W(\mu_p, \sigma_p)$ is derived from a normal distribution with a mean of 1 and standard deviation σ_p. For all parameters a global prefactor was applied to not over-parameterize the system, which will make it unsolvable with the limited set of discharge observations ($\approx$ 600000). When parameters are estimated for every location individually this would lead to $\approx$ 200000 parameters, whereas a basin dependent parameterization could result in an unnatural shifts in parameter values between adjacent locations. For the model parameters ($Ksat$, DDF, n) the prior estimates were generated with $\mu_p = 1.0$ and $\sigma_p = 0.1$. The precipitation was corrected using three time-dependent precipitation correction factors (c) that are given by:

$$P'(t) = P(t) * (1 + c_{uphill}(t) + c_{downhill}(t) * + c_{path}(t)) \tag{4.9}$$

where $c_{uphill}(t), c_{downhill}(t), c_{path}(t)$ are the correction factors applied to the original precipitation based on up and downhill wind direction and average slope of the terrain along the travel path of the precipitation. The precipitation correction factors are given by:

$$c_{uphill}(t) = \alpha_{uphill} * max(\cos(\pi * \frac{Asp - u_{dir}(t))}{180}), 0.0) \tag{4.10}$$

$$c_{downhill}(t) = \alpha_{downhill} * min(\cos(\pi * \frac{Asp - u_{dir}(t))}{180}), 0.0) \tag{4.11}$$

$$c_{path}(t) = \alpha_{path} * \frac{z}{Dist(t)} \tag{4.12}$$

where α_* is the calibration pre-factor (time-independent) that is calibrated based on the observations, Asp the aspect of the slope in the terrain (°), $u_{dir}(t)$ the dominant directionality of the wind for time t (derived from ERA40 and ERA-interim), z the terrain height and $Dist(t)$ the cloud travelling distance. For the initial values of α $\mu_p = 0.0$ and $\sigma_p = 0.01$ were used.

It has been frequently reported that precipitation products in mountainous regions suffer from lack of ground-based stations and have poor quality (e.g. Adam and Lettenmaier, 2003; Hijmans et al., 2005). These are the regions where the highest impact can be expected from the newly introduced correction factor. The impact of vertical movement of clouds will result in an increased specific humidity and therefore in generation of precipitation (windward conditions) or a drying of the air (leeward conditions). Hence c_{uphill} and $c_{downhill}$ have been introduced to correct for these effects, which are not captured by the small number of precipitation stations in mountainous regions. This orographic effect is strongest at the first encounter of moist air or with strong topographic terrain. However, the impact may reduce after the air has passed multiple ranges of hills or mountains. This is based on the assumption that most evaporation is generated over the ocean and transported onto the land. When air with a high specific humidity has travelled a long distance (over land) the air is more likely to have a lower specific humidity (due to losses as precipitation) and the impact of vertical movement on precipitation generation will be lower. c_{path} accounts for this process and corrects for these distance effects. Although these correction factors could be made more sophisticated, it is preferred to have simple single aspect correction factors that allow for a global time and wind direction dependent precipitation correction. This will reduce the number of parameters to be calibrated and results in a more robust model calibration. The obtained parameters and precipitation correction factors were evaluated based on the ratio between the obtained value and the spread between the realizations using the Coefficient of Variation (COV). This will provide information on the signal to noise ratio on the newly obtained parameterization. Parameters with a low COV could be deemed certain, while a high COV (especially above 1) will indicate highly uncertain parameter retrievals. The latter is the result of poor identifiability of the parameter, which in turn results either from the fact that the model is insensitive to the parameter, or from the lack of proper observations to estimate its true value.

For the assimilation of the discharge data with the Ensemble Kalman Filter (EnKF), spatial information on the measurements error covariance (R, Equation 4.6) is required. The structure of R was determined using the data quality information provided by GRDC. Discharge observations can be divided into 3 categories, namely, daily, monthly and climatology. Since the model performance is evaluated at the end of every month, monthly aggregated values were used for the assimilation scheme. Daily values were aggregated to monthly values, monthly values were used as is and the same was done for the monthly observation climatology. A holistic error model was used to determine the observation errors for each station. A 20% error was assumed for monthly aggregated daily discharge observations, where missing values are penalized with 1% per missing day (information provided by GRDC). When only the monthly discharge climatology was provided an error of 40% was imposed on the observation or the standard deviation provided by the GRDC. The error covariance between the discharge observations was set to zero since it was assumed that errors in the observations are independent, even when they are located in the same basin.

Preliminary tests showed that a total of 48 ensemble members was sufficient to obtain statistically stable parameter solutions. With the total of 48 ensemble members, the EnKF was applied to update state variables and identify parameters (Table 4.1) of the hydrological model PCR-GLOBWB. The initial model states were determined based on a fifty-year open loop simulation of PCR-GLOBWB. A fifty year period was used to ensure that the deep groundwater simulations would no longer be influenced by the initial conditions. A three-step approach was subsequently used to calibrate the hydrological model and ensure a stable, fully calibrated set of parameters. A initial calibration of 50 *years* (1960-2010) was performed, the obtained parameterization was used for a second calibration for the same 50 *years* and third calibration for the same period. The obtained parameterization after 150 *years* of calibration was used as the input for an open-loop validation simulation on which the model was validated and compared to a simulation with the standard parameterization with the same initial conditions (baseline).

The new PCR-GLOBWB parameterization and simulated monthly discharges were evaluated at 6475 stations from GRDC and compared to the baseline simulation. The model performance was evaluated in terms of correlation (r), Nash-Sutcliffe efficiency (NS, Nash and Sutcliffe, 1970), Root Mean Squared Error ($RMSE$), *bias* and Mean Absolute Error (MAE).

4.2.6 Reanalysis product

The calibrated parameters and precipitation correction factor were used in the open-loop validation simulation to create a hydrological reanalysis product for the period 1960-2010. This reanalysis product is the output of the validation simulation

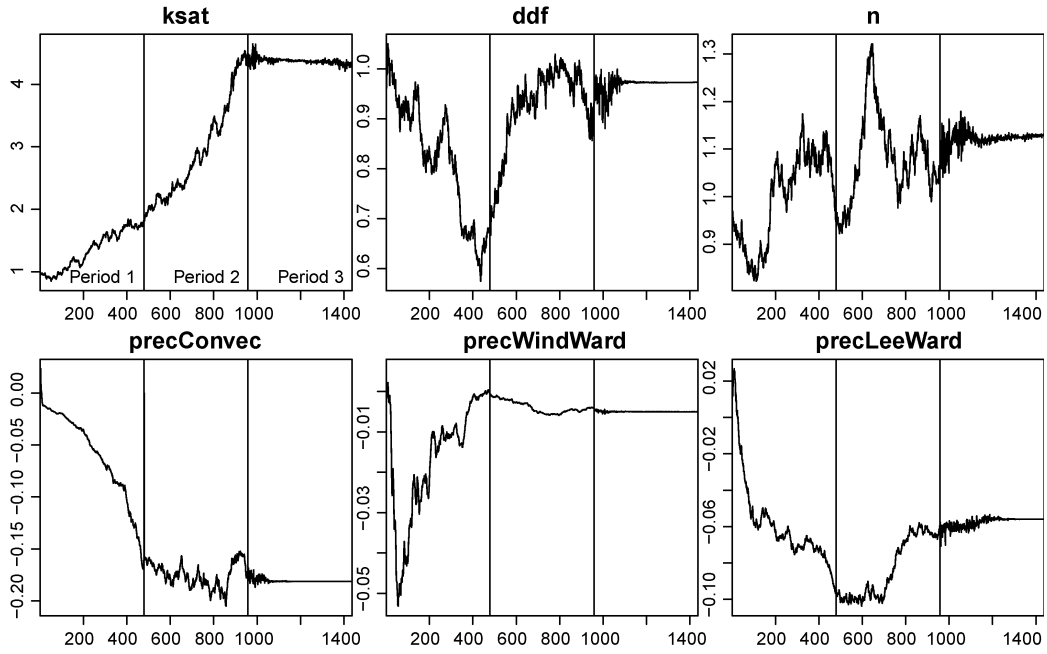

Figure 4.1 Time series of calibrated parameters, during the calibration periods. All periods use 1495 discharge observation locations for the period 1960-2010. The posterior parameters after the first calibration are used as prior for the second period and so on.

performed and contains (via the parameterization and precipitation correction) the information of all discharge observations used in the calibration procedure.

4.3 Results

4.3.1 Parameter estimation

Calibration of PCR-GLOBWB with discharge observations for the period 1960-2010 results in an adjusted parameterization of all model parameters and newly found precipitation correction factors (Table 4.1 and Figure 4.1). It was found that after calibration the model shows a slower response to precipitation as a result of a strongly increased $Ksat$ (less surface runoff, more infiltration), decreased DDF (slower snow melt) and increased n (more channel roughness). This indicates that the original model parameterization showed too strong a response to precipitation, given the observed discharge.

The precipitation correction factors show that a reduction in the original CRU TS 3.21 precipitation forcing is required to show consistency with the observed discharge totals. According to the observations the adjustments in the original CRU forcing for orographic effects are too strong for inland mountain ranges. The observations

Table 4.1 Calibration parameters and the range of their prior and posterior normal distributions. Upper half of the table gives the model parameters and bottom half the precipitation correction factors.

Parameter	description	Prior		Calibrated		
		μ	σ	μ	σ	COV
$Ksat$	Multiplier of unsaturated conductivity	1.0	0.1	4.355	0.135	0.031
DDF	Snowmelt rate	1.0	0.1	0.932	0.028	0.030
n	Manning´s roughness coefficient	1.0	0.1	1.076	0.022	0.021
α_{uphill}	Uphill precipitation	1.0	0.03	-0.004	0.0002	0.057
$\alpha_{downhill}$	Downhill precipitation	1.0	0.03	-0.062	0.004	0.070
α_{path}	Travel distance precipitation	1.0	0.03	-0.172	0.005	0.028

(and resulting calibrated correction factors) show that mountainous areas that are far inland do not enforce the same topographic effect as near-coastal mountain ranges (α_{path}). Moreover, precipitation on the leeward side of mountain ranges is overestimated leading to overestimation of discharge in these regions. It is also shown that the precipitation estimates for windward facing mountains are more accurate and hardly any correction is required compared to the original CRU forcing data.

4.3.2 Performance in selected river basins

To illustrate the impact of the precipitation correction and the calibration of the model parameters, 6 river basins have been selected to show results in more detail (Figure 4.2). It is shown that the calibration approach mainly corrects the overestimation of the discharge in some rivers (e.g. Congo, Rhine, Volta). This correction of the initial overestimation in the baseline results in a reduction of the simulation *bias* and an increase in the NS. On the other hand, r is slightly lower than for the baseline, since the temporal dynamics are slightly underestimated. However, not for all systems r is reduced as a result of calibration as can be seen for the Volta River. Due to the calibration of n and $Ksat$, the simulation of the seasonal peak in this river is significantly improved compared to the baseline. The baseline showed a significant overestimation of the length of the recession curve and an underestimation of the height of the seasonal discharge. A similar pattern in the recession curve is found for the Lena River, where the recession after the snowmelt season is more accurately modelled compared to the baseline. This behaviour could be related to the increased $Ksat$ value that allows an increased infiltration speed, leading to faster runoff generation. Rivers in the United States and Europe (e.g. Rhine, Danube, Mississippi) are less impacted by the calibration and precipitation correction; r for these rivers

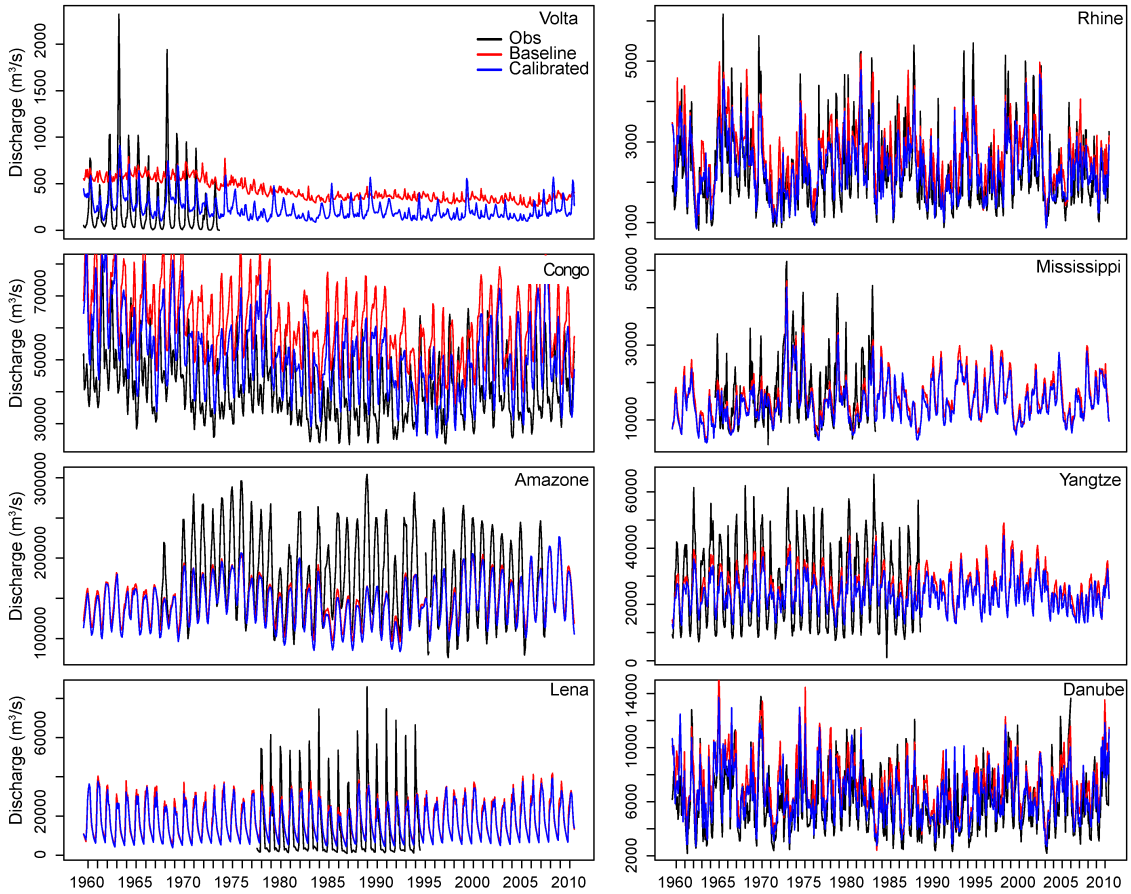

Figure 4.2 Time series of river discharge for selected rivers for the period 1960-2010.

only show a minor improvement, however the *bias*, $RMSE$ and MAE do decrease compared to the baseline. For the Congo River a significant improvement is found for all evaluation matrices. For example, the *bias* for the baseline (24020 m^3s^{-1}) was strongly reduced after calibration (13075 m^3s^{-1}) and the same was found for the $RMSE$ (26709 to 16806 m^3s^{-1}). Less so was the impact on the NS and r, where both indicated a small improvement after calibration. The selected river basins show that the impact of the EnKF optimization is most dominant in the snow-dominated and tropical regions.

4.3.3 Global discharge performance

The global average results show that the calibrated simulations outperform the baseline scenario for most skill scores with the exception of r (median baseline = 0.54, calibrated = 0.51, Figure 4.3). The NS is improved from -0.62 to -0.46, which is still negative and largely related to biases in the simulation (Figure 4.3). These biases

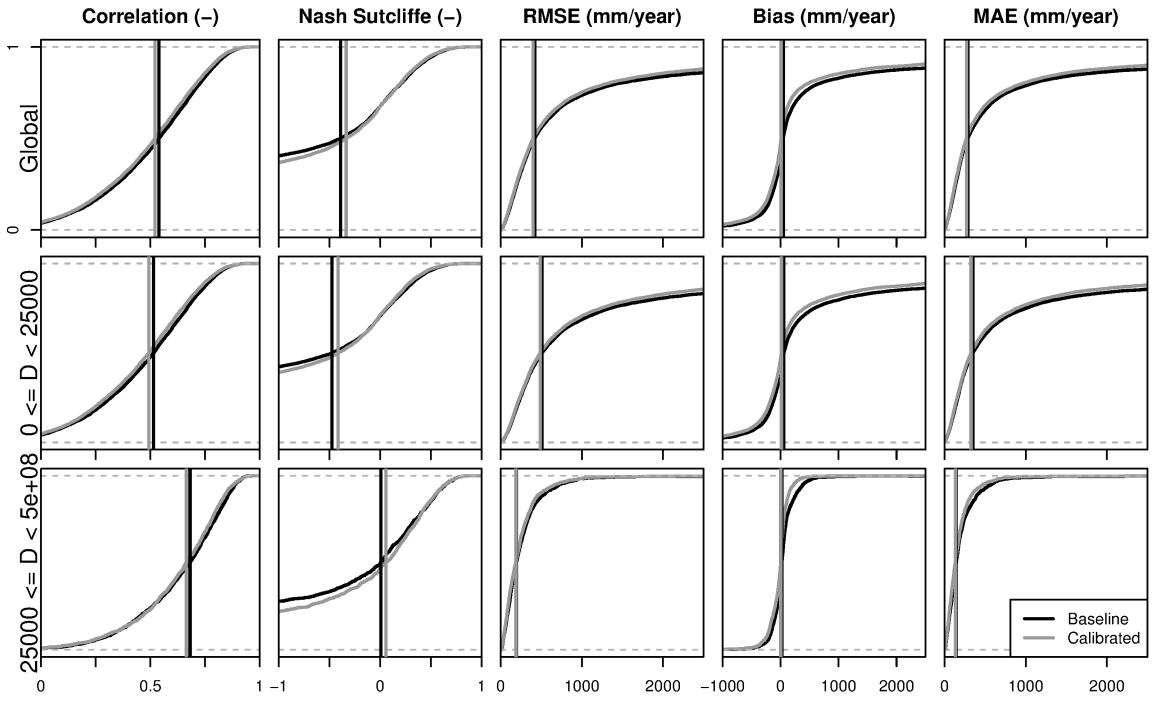

Figure 4.3 Cumulative density functions for 5 skill scores based on comparison between simulated discharge and observations of 6475 stations from GRDC. Rows show skills scores classified by catchment size (D) in km^2. Vertical lines indicate the skill score median for the baseline and calibrated discharge simulations.

have been reduced after calibration from 65.8 to 13.6 $mm\ y^{-1}$, while the $RMSE$ is reduced from 479 to 452 $mm\ y^{-1}$ and the MAE is reduced from 349 to 316 $mm\ y^{-1}$. These results indicate that major improvements have been made by adjusting the model forcing to closely match the water that discharges into the ocean. Biases are close to zero indicating that, although spatial mismatches do exist, the global estimates are more accurate than when using existing forcing data sets.
A strong improvement by calibration was found in the smaller catchments ($\leq 25000\ km^2$, second row Figure 4.3), where the NS was increased and the other skill scores were decreased. The median r was always reduced even for these small catchments, while the other skill scores suggest that the calibration mainly results in a reduction of the absolute difference between simulation and observations.

The largest improvements, also in terms of temporal dynamics, are found for the smallest catchments ($\leq$ 10000 km^2, not shown). The size of these catchments is smaller or equal to the average size of a grid cell in the PCR-GLOBWB discretization ($\approx$ 3000 km^2). This suggests that compared to the baseline scenario the new parameterization and precipitation corrections lead to significant improvements in the sub-grid simulations, mainly in poorly gauged basins.

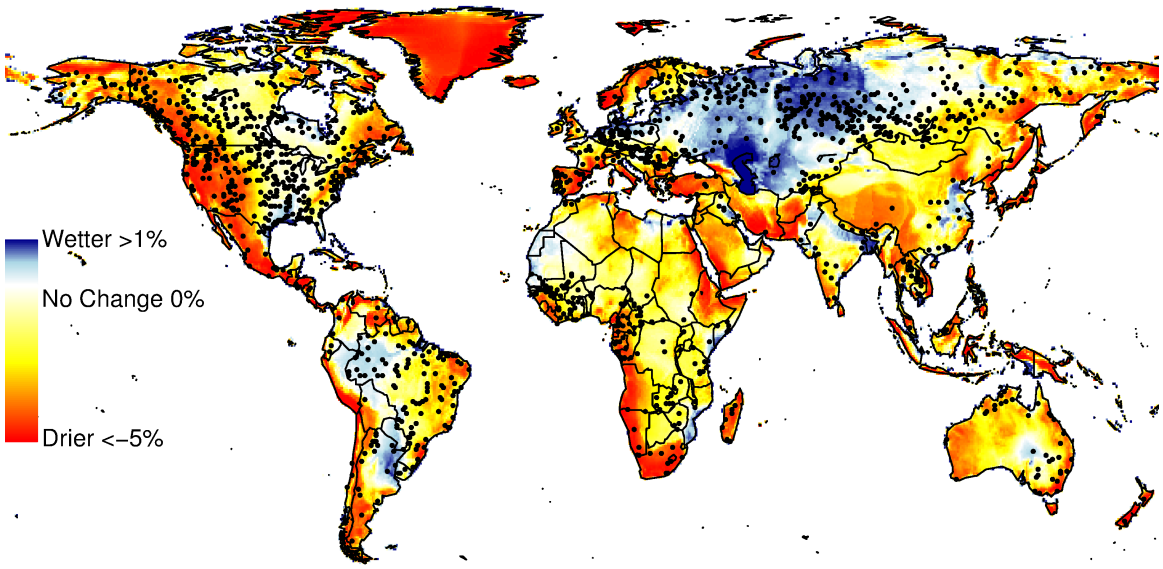

Figure 4.4 Annual average precipitation correction for the period 1960–2010 after calibration with discharge observations (black points).

The observed improvements in mainly the *bias*, $RMSE$ and MAE can be attributed to the calibration framework that is used in this study. The EnKF will reduce the error between the observations (Y) and simulation forecast (Ψ^f, Equation 4.6) based on the absolute difference between the two. Therefore, it is not surprising that the skill scores that evaluate the absolute performance in terms of ($mm\ y^{-1}$) show the largest improvements ($RMSE$, MAE and *bias*). The calibration will also affect the temporal signal and therefore the r and NS, although the objective function of the EnKF does not optimize the temporal consistency between observations and model simulation. Therefore, it is not surprising that the r is reduced, while NS is often improved since a large part of the score is impacted by the *bias* between simulation and observations.

4.3.4 Precipitation correction

In general the annual precipitation is reduced after the calibration with the discharge observations (Figure 4.4). The global annual precipitation is found to be $97.5\pm0.5\times10^3\ km^3\ y^{-1}$, with an inter-annual variability of $5.1\times10^3\ km^3\ y^{-1}$. This indicates a global reduction of $9.9\times10^3\ km^3\ y^{-1}$ based on the GRDC discharge observations compared to the original estimate of $107.4\ \times10^3\ km^3\ y^{-1}$. This reduction suggests that in the current forcing data the overestimation of precipitation is significant, which strongly impacts the simulated discharge.

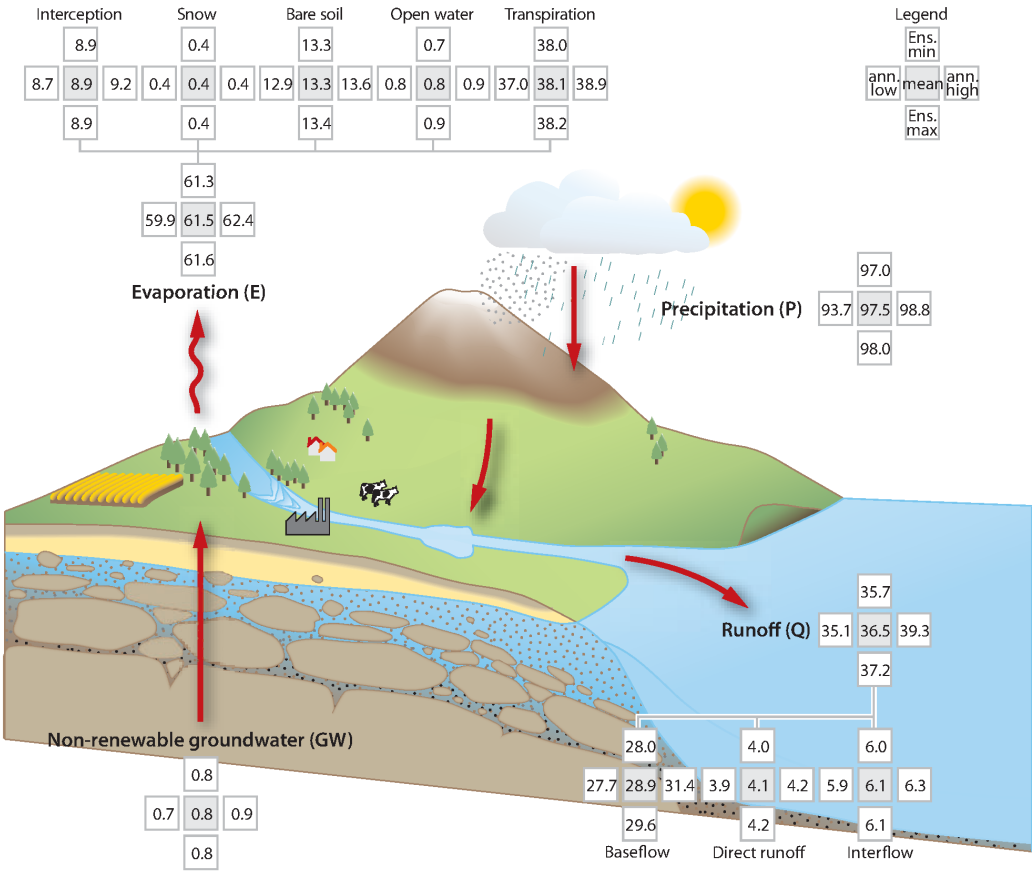

Figure 4.5 Mean annual fluxes (1.000 $km^3\ y^{-1}$) of the global terrestrial water cycle. Main flux estimates are given in bold (Precipitation, Evaporation, Non-renewable groundwater abstraction, Runoff) and decompositions of these fluxes can be found in the boxes. The legend for the boxes can be found in the topright corner. Note that the decomposition of the Runoff lacks open water evaporation, surface water abstractions and changes in reservoir and lake storage.

4.3.5 The terrestrial water cycle

Figure 4.5 shows the annual water budget for the calibrated simulation for the period 1960-2010. Both the inter-annual variability and the uncertainty in the annual mean of the 48 ensemble members can be seen. The water balance error for the PCR-GLOBWB simulation after calibration is 0.3%, which can be fully attributed to changes in the storage and numerical errors in the computer simulation (e.g. rounding errors).

The evapotranspiration is found to be $61.5 \pm 0.15 \times 10^3\ km^3\ y^{-1}$, which indicates no change compared to the baseline scenario (Table 4.2). The inter-annual variability is $2.5 \times 10^3\ km^3\ y^{-1}$ and mostly dominated by the transpiration component of the evapotranspiration (Figure 4.5). After calibration the fossil groundwater abstraction

Table 4.2 Average annual fluxes in the terrestrial water cycle derived for the baseline and calibrated scenario, for the period 1960-2010. Included are the absolute and percentile differences between the two simulations. All fluxes are given in 10^3 km^3 y^{-1}.

Flux	Baseline	Calibrated	Difference	
			Absolute	Relative (%)
Precipitation	107.4	97.5	9.9	-9.2%
Evapotranspiration	61.5	61.5	0.0	0.0%
Runoff	46.4	36.5	-9.9	-21.3%
Ground water abstraction	0.3	0.8	0.5	167%

is increased to $0.8\pm0.05\times10^3$ km^3 y^{-1}, which indicates a strong increase of 167% compared to the baseline scenario. This is mainly caused by the fact that the fossil groundwater abstraction is controlled by the evaporative demand that cannot be met, given the soil moisture status and water availability within the simulated grid cell. Because less water is available (in soil moisture and rivers) from precipitation, some of this is partly compensated by increased abstraction of fossil groundwater.

Finally, the runoff is strongly decreased (-21.3%, to $36.5\pm0.8\times10^3$ km^3 y^{-1}) compared to the baseline scenario (46.4×10^3 km^3 y^{-1}). This decrease was already found in the results for the selected river basins and induced by the strong precipitation reduction at the global scale. The global runoff ratio (Runoff/Precipitation) is found to reduce from 0.43 to 0.37, where the baseflow gives the highest contribution ($28.9\pm0.9\times10^3$ km^3 y^{-1}, 79%) to the total runoff estimates. The inter-annual variability of the discharge is relatively large (4.2×10^3 km^3 y^{-1}), when compared to the other fluxes.

4.4 Discussion and Conclusion

In this study the first ensemble hydrological reanalysis product that is consistent with discharge observations, has a closed water balance (for each ensemble member) and provides estimates on the uncertainty in all fluxes and storage components of the terrestrial water cycle is presented. The global hydrological model PCR-GLOBWB was calibrated with an Ensemble Kalman Filter (EnKF) and discharge observations from 1495 stations. The calibrated ensemble was used to simulate the terrestrial water cycle for the period 1960-2010.

4.4.1 Model calibration

The obtained results from this study clearly show that there is a potential to calibrate Global Hydrological Models (GHMs) with observational data. Although calibration is often hampered by the high dimensionality of GHMs, here the first EnKF GHM calibration is provided. The framework provided will allow for other GHMs to be calibrated with observations (e.g. discharge or satellite observations) and improve global hydrological modelling in general. The implementation of the EnKF calibration respects the closure of the water balance, which is important for many hydrological studies.

Traditionally, most calibration and validation studies focus on the observations in the Northern hemisphere and more specific Europe and the United States. Although (discharge) observations are available for other regions the quality is often deemed less or the model calibration is hampered by shorter discharge time series. As can been seen in Figure 4.4, the data availability is indeed higher for the Northern hemisphere, however some valuable observations are available in other regions. The applied calibration framework in this study allows us to include these observations and assign an appropriate (higher) error estimate to the data. With this framework even the lower quality observations are taken into account, although their relative importance on the calibration is lower. Nonetheless, the largest improvements in the global discharge simulations can be found in the snow-dominated and tropical regions. The baseline model simulations in these regions were of low quality compared to rivers in the temperate climate regions, where data availability and quality are high. However, after calibration the error in the simulated discharge in these regions is significantly reduced as a result of more realistic discharge simulations (Figure 4.2).

The applied calibration framework can be extended with additional observations for other components of the hydrological cycle (e.g. remotely sensed estimates of storage, soil moisture or snow cover). This could lead to an improved model parameterization of PCR-GLOBWB and might result in a better simulation of the terrestrial water cycle. The proposed advances are mainly hampered by the computational demand, an issue that should be resolved within the near-future as more computational power becomes available for hydrological applications.

4.4.2 Fluxes estimates

One of the main conclusions from our study is that the original CRU TS 3.21 precipitation dataset overestimates the terrestrial precipitation fluxes by 9.2%. This result is obtained after model calibration based on discharge observations from the Global Runoff Data Centre, implying that the discharge observations approach suggest that the original CRU precipitation estimates are too wet. When the newly obtained estimate of annual global runoff ($36.5 \times 10^3\ km^3\ y^{-1}$) is compared to previous studies, the differences are small (e.g. Vörösmarty et al., 2000b; Oki et al., 2001; Dai

and Trenberth, 2002; Döll et al., 2003). On the other hand, our estimate is higher than found by Oki and Kanae (2006); Haddeland et al. (2011); Rodell et al. (2014). However, it must be mentioned that Haddeland et al. (2011) report that, especially for the tropical regions, a large overestimation is observed for most model driven runoff estimates. Our calibration framework removes most of the observed bias in the tropical regions (e.g. Congo, Volta, Figure 4.2), resulting in lower annual global runoff estimates. Antartica is not included in this study, which also explains some of the differences between the estimates of this study and the work by Rodell et al. (2014). Furthermore, a 12% ($\pm 12 \times 10^3$ km^3 y^{-1}) difference amongst precipitation forcing datasets was found by Fekete et al. (2004). These forcing datasets are often used for studies related to the fluxes in the terrestrial water cycle and may be one of the biggest sources of uncertainty in the current estimates (e.g. Adam and Lettenmaier, 2003). The precipitation estimate uncertainty has a significant impact on the resulting estimate of the annual runoff. Therefore, the calibration of precipitation correction factors is a valid way to reduce the uncertainty in precipitation and resulting runoff estimates, provided that correct estimates are available for the discharge observations.

Another assumption is that only the precipitation is directly corrected in the calibration framework, while the potential evaporation estimates are not directly adjusted. The uncertainty in the evapotranspiration is reduced by the model parameters, since they control (together with the potential evaporation) the evaporative flux into the atmosphere. Since the evaporative flux is significantly smaller than the precipitation and is also impacted by other factors, the calibration of model parameters was used to constrain these fluxes. Moreover, $Ksat$ (saturated conductivity) already captures the complex feedbacks between soil moisture availability, evaporation and infiltration. This disregards the need to adjust the potential evaporation and hence reduces the dimensionality of the parameter estimation problem.

The final assumption is that the model is capable at correctly reproducing the runoff generation as a result of the provided precipitation. Because water abstractions are present in the model simulations, the reduction that was found in the total precipitation estimate is not introduced to correct absence of water abstraction in the model. Additionally, it can be shown from comparison between PCR-GLOBWB model simulations and observations that the runoff generation processes are correctly implemented in the model. Previous work by Van Beek et al. (2011) and Wada et al. (2013), showed that PCR-GLOBWB is capable of realistically reproducing monthly discharge estimates in large scale river basins. The validation provided in this work shows that this performance can be enhanced by the calibration of model parameters, leading to a further reduction of the global $RMSE$, $bias$ and MAE.

However, previous studies (e.g. Haddeland et al., 2011) have shown that differences between global hydrological models can be considerable. In this study only one global model has been used. As a consequence, the uncertainty estimates from the ensemble do not include model error and probably underestimate the actual uncertainty. This

explains the somewhat smaller uncertainty bands compared to multi-model global water balance estimates (Haddeland et al., 2011; Rodell et al., 2014). A next step should therefore consist of repeting the calibration with multiple global hydrological models, obtaining multimodel multi-ensemble estimates.

Despite the fact that only one global model was used, it is conclude that, when the obtained fluxes estimates are compared with other studies, the applied approach results in realistic simulations of the terrestrial water cycle. The improvements found in the discharge simulations suggest that the correction of precipitation fields is a valid approach to improve modelling of the terrestrial water cycle in general.

4.4.3 Reanalysis product

The improved simulation performance of PCR-GLOBWB and the fact that an observation integrated model approach was used to simulate the terrestrial water cycle, provide confidence in the new flux estimates. The multi-ensemble simulations of the terrestrial water cycle provide new insight in the uncertainty of the flux estimates. Furthermore the long time period (1960-2010) over which PCR-GLOBWB is calibrated and later used to simulate the water cycle, provides more knowledge on the inter-annual variability and makes it suitable for studies into trends and variability of the terrestrial water cycle. The ensemble mean of the 50 year simulation of all model states is provided as well as the simulations derived from every ensemble member. Hereby providing the first ensemble hydrological reanalysis product that is consistent with discharge observations, has a closed water balance (for every ensemble member) and provides estimates on the uncertainty in all fluxes and storage components in the terrestrial water cycle. This product will hopefully bring an advance in the broader field of hydrology and related research fields that are dependent on accurate estimates of the components of the terrestrial water cycle (e.g. land use changes, water availability, reservoir design, flood protection studies).

Acknowledgments

The authors would like to thank SURFsara Computing and Network Services for the use of the Cartesius system.

5 The benefits of satellite soil moisture in parameter identification

This chapter is based on:
Wanders, N., Bierkens, M. F. P., de Jong, S. M., de Roo, A., Karssenberg, D. (2014), The benefits of using remotely sensed soil moisture in parameter identification of large-scale hydrological models, Water Resources Research, 50 (8), 6874-6891, doi:10.1002/2013WR014639.

Abstract

Large-scale hydrological models are nowadays mostly calibrated using observed discharge. As a result, a large part of the hydrological system, in particular the unsaturated zone, remains uncalibrated. Soil moisture observations from satellites have the potential to fill this gap. Here the added value of remotely sensed soil moisture in calibration of large-scale hydrological models was evaluated by addressing two research questions: 1) Which parameters of hydrological models can be identified by calibration with remotely sensed soil moisture? 2) Does calibration with remotely sensed soil moisture lead to an improved calibration of hydrological models compared to calibration based only on discharge observations, such that this leads to improved simulations of soil moisture content and discharge? A dual state and parameter ensemble Kalman filter is used to calibrate the hydrological model LISFLOOD for the Upper Danube. Calibration is done using discharge and remotely sensed soil moisture acquired by AMSR-E, SMOS and ASCAT. Calibration with discharge data improves the estimation of groundwater and routing parameters. Calibration with only remotely sensed soil moisture results in an accurate identification of parameters related to land surface processes. For the Upper Danube upstream area up to 40000 km^2, calibration on both discharge and soil moisture results in a reduction by 10-30% in the $RMSE$ for discharge simulations, compared to calibration on discharge alone. The conclusion is that remotely sensed soil moisture holds potential for calibration of hydrological models, leading to a better simulation of soil moisture content throughout the catchment and a better simulation of discharge in upstream areas.

5.1 Introduction

Soil moisture plays a crucial role in the hydrological cycle, modulating evapotranspiration, overland flow and groundwater replenishment. As a consequence, an accurate simulation of discharge with hydrological models requires good quality estimates of soil moisture content. Especially in situations with a precipitation amount close to the storage capacity of the unsaturated zone, the soil moisture content has a large impact on whether overland flow will occur and the amount of overland flow generated (Merz and Plate, 1997; Penna et al., 2011). However, soil moisture content is highly variable in time and space (Western et al., 2002) and ground-observations are still limited (Dorigo et al., 2011).

Remotely sensed soil moisture provides observations with a high temporal resolution and a large spatial extent. Satellite soil moisture observations are therefore increasingly used for calibration of hydrological models and the identification of parameters related to land-surface processes (e.g. Santanello et al., 2007; Montzka et al., 2011; Sutanudjaja et al., 2013). Moreover, in areas with a low coverage of precipitation measurements, remotely sensed soil moisture can give valuable information on the spatial distribution and the intensity of precipitation events (Crow and Ryu, 2009). Thus, when used in real-time, remotely sensed soil moisture observations have the potential to increase flood forecasting accuracy (Komma et al., 2008; Hendricks Franssen et al., 2011).

Due to the large data volumes, coarse spatial resolution and its complicated error structure, the use of near real-time remotely sensed soil moisture has not yet been fully explored by hydrologists. In numerical weather forecasting and unsaturated zone modelling, the assimilation of remotely sensed soil moisture for hydrological and atmospheric simulations has showed promising results (e.g. Pauwels et al., 2001; Reichle et al., 2002; Scipal et al., 2008; Bolten et al., 2010; Brocca et al., 2010; Liu et al., 2011a; Dharssi et al., 2011; Draper et al., 2011; Brocca et al., 2012; Draper et al., 2012; De Rosnay et al., 2013). For large-scale catchments, Draper et al. (2011) assimilated remotely sensed soil moisture from the Advanced Scatterometer (ASCAT) over France to improve discharge simulations. It was concluded that the assimilation of soil moisture mainly corrected for biases in precipitation or incorrect model climatology. Several studies used in-situ observations of soil moisture or synthetic simulations of remotely sensed soil moisture to show that using these observations in model calibration could significantly change the parameter values of the model (e.g. Aubert et al., 2003; Santanello et al., 2007; Lü et al., 2011; Montzka et al., 2011). These studies were performed in catchments smaller or slightly larger than the typical resolution of microwave satellites (626-2500 km^2), and therefore do not allow to evaluate the added value of remotely sensed soil moisture for model calibration over a range of spatial scales and especially scales larger than the spatial resolution of the sensors. A recent study over a larger spatial domain by Sutanudjaja et al. (2014), used a brute force calibration of a large-scale hydrological model for the Rhine and

Meuse river basin using data from the ERS scatterometer. It was shown that, using remotely sensed soil moisture, the parameters related to the percolation through the unsaturated zone could be improved to yield a better simulation of the soil moisture content. However, discharge simulations were not improved.

The aim of this study is to investigate the benefits of multi-sensor remotely sensed soil moisture observations in parameter identification in large-scale hydrological models using detailed error estimates on satellite soil moisture observations. To achieve this aim, this research focuses on two main research questions: (i) Which parameters of hydrological models can be identified by calibration with remotely sensed soil moisture? (ii) Does calibration with remotely sensed soil moisture lead to an improved calibration of hydrological models compared to approaches that calibrate only with discharge, such that this leads to improved simulations of soil moisture content and discharge? To address these questions, the LISFLOOD (Van Der Knijff et al., 2010) large-scale hydrological model is used to simulate discharge and soil moisture for the Upper Danube catchment, which contains parts of Austria, Germany and the Czech Republic. LISFLOOD is the underlying model used in the European Flood Awareness System (EFAS) and is used in operational flood forecasting in Europe (Thielen et al., 2009; Bartholmes et al., 2009). The model is calibrated in this study using remotely sensed soil moisture observations from the Advanced Microwave Scanning Radiometer-EOS (AMSR-E), Soil Moisture and Ocean Salinity (SMOS) and ASCAT and discharge observations for the period 2010-2011. Also combinations of calibration on discharge and all satellites sensors are performed, to study the added value of the remotely sensed soil moisture when discharge observations are readily available. Error structures for the different sensors and their error cross covariance are retrieved from Chapter 2. The impact of the new calibration on the soil moisture simulations is studied and a validation on multiple discharge locations is performed. Compared to previous work, our study contains the following new elements: (i) It is the first time that real remotely-sensed data are used for calibration of a large-scale distributed hydrological model. (ii) The use of multiple sensors is new, which allows to compare the relative benefit of the different products, also compared to using discharge only. (iii) Using a probabilistic data assimilation framework for calibration and state estimation is new, in particular taking into account the full retrieval error structure and cross covariance between multiple sensors. The latter enables optimal weighting between their different information sources, potentially leading to improved calibration.

5.2 Material and Methods

5.2.1 Study area

In this study, the Upper Danube catchment up to Bratislava (catchment size 135×10^3 km^2, Figure 5.1) is used for the calibration (state updating and parameter iden-

tification) of the LISFLOOD model. The border of the Upper Danube consists of the Alps in the south and the catchment contains the northern part of Austria, the southern part of Germany, the south-eastern part of the Czech Republic and western Slovakia. Elevations range from 150 - 3150 $m.a.s.l.$. The soil mostly consists of loamy sediments and approximately 35 % of the area is covered with forest. In the catchment, daily discharge observations for 23 locations are available through the Global Runoff Data Centre (GRDC) over 2000-2011.

Meteorological input was obtained from high density interpolated ground data from various national meteorological services made available by the Joint Research Centre (Ntegeka et al., 2013). The data was interpolated with an Inverse Distance Weighting (IDW, Shepard, 1968)) approach instead of kriging, since this could generate errors if not well controlled in a real-time spatial interpolation. Time series of approximately 200 meteorological stations were used to create the spatially interpolated meteorological variables. The total precipitation over the period 2001-2011 in the catchment is approximately 920 $mm\ y^{-1}$ and total actual evapotranspiration is approximately 630 $mm\ y^{-1}$. The runoff ratio of the catchment is 0.31, where a total of approximately 290 $mm\ y^{-1}$ leaves the catchment as discharge at Bratislava, of which approximately 22 $mm\ y^{-1}$ on average is generated as surface runoff. Moreover, in the mountainous areas this amount of surface runoff is in general much higher than in the lower areas near the main stream of the Danube.

5.2.2 Hydrological model

The hydrological model LISFLOOD (Van Der Knijff et al., 2010) was used for the calibration and validation of soil moisture and discharge simulations. LISFLOOD is a hydrological rainfall-runoff-routing model running in the PCRaster modelling environment (Wesseling et al., 1996; Karssenberg et al., 2010). LISFLOOD is used in the operational EFAS of the European Commission for medium range flood forecasting of large river basins in Europe (Thielen et al., 2009; Bartholmes et al., 2009). The meteorological forcing of LISFLOOD consists of daily precipitation, daily potential evapotranspiration and the average daily temperature. The model originally consists of a vegetation layer, two layers for the unsaturated zone, one fast responding and one slow responding linear groundwater reservoir and a channel network for discharge routing (Figure 5.2). The kinematic wave equation is used for discharge routing using an hourly time step for both surface runoff to the channel network and routing within the channel network.

For this study, a number of modifications have been made to the LISFLOOD model. To enable a more detailed modelling approach of the soil moisture in the topsoil, two additional unsaturated zone layers have been added to the original LISFLOOD model, which also enables direct comparison and assimilation of each of the satellite products. The upper two layers are 2 and 3 cm thick, respectively, and the third

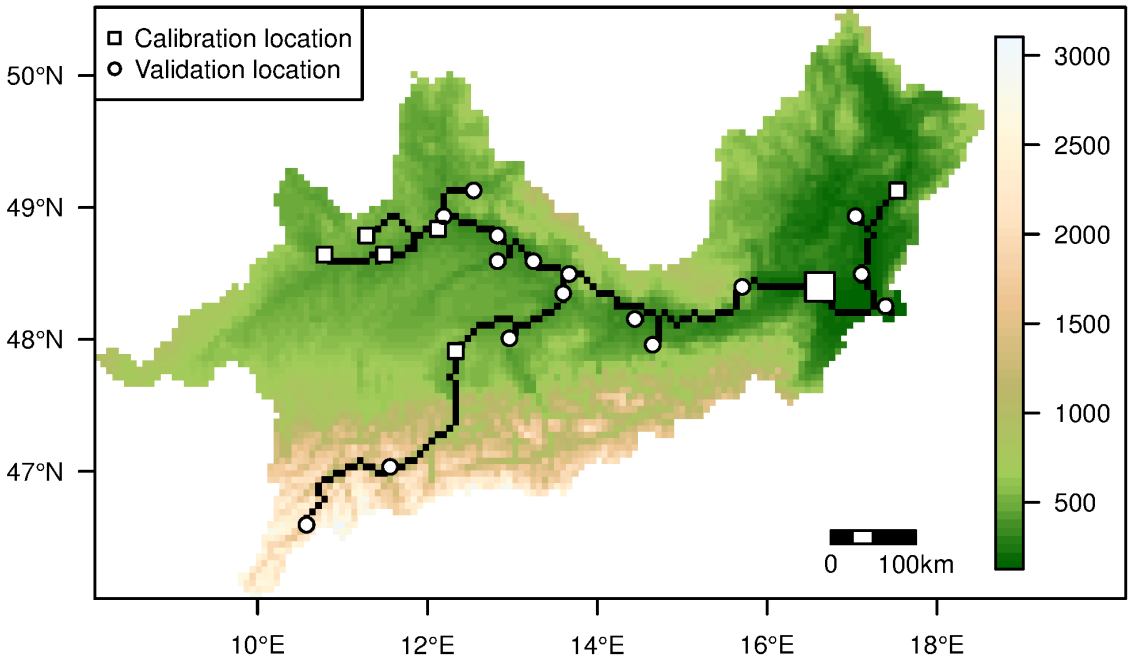

Figure 5.1 Digital elevation map of the Upper Danube catchment, colours indicate elevation (m), indicated in black is the river network, square symbols indicate locations for calibration on discharge observations, circles indicate locations for validation on discharge observations. The large square near the outlet (right) is the location used for calibration if only one discharge time series is used.

layer represents the remaining part of the rooting depth (first three layers together are hence referred to as the topsoil, Figure 5.2). The root zone is simulated using the first three layers of the unsaturated zone and evapotranspiration occurs from these layers. The evaporation for a particular layer is limited if soil moisture is below critical soil moisture conditions, in which case more water is extracted from the other soil moisture layers to compensate for the reduced evaporation. Critical soil moisture conditions are calculated from the local soil properties (Van Liedekerke et al., 2006). The abstraction per layer is linearly related to the total storage capacity of the layer. Thick layers will thus have a larger contribution to the evapotranspiration compared to thinner layers. When the entire root zone is below critical soil moisture conditions, the evaporation is limited for the entire topsoil and actual evapotranspiration will be lower than potential evapotranspiration. Bare soil evapotranspiration will occur only from the first layer of 2 cm. Via capillary rise replenishment of the root zone can occur from the subsoil. The amount of capillary rise depends on the difference in hydraulic head of two layers and the average conductivity of the layers. Sub-daily time steps are included to enable a stable performance of the soil moisture simulation, where the number of sub-daily time steps is dependent on the amount of infiltration and water storage in the unsaturated zone. For a more detailed description of the original

Table 5.1 Calibration parameters and the range of their prior normal distributions, the bottom half is only calibrated using discharge observations. T_{uz} and T_{lz} are divided into three different zones namely, steep, intermediate and flat areas. More details can be found in Section 5.2.2.

Parameter	description	unit	prior
$SnCoef$	Snowmelt rate	$mm\ d^{-1}$	0.1-10
$KSat_1$	Multiplier of unsaturated conductivity topsoil	-	0.9 - 15
$KSat_2$	Multiplier of unsaturated conductivity subsoil	-	0.9 - 22
c_{pref}	Empirical shape parameter preferential macro-pore flow	mm	0.1 - 2.3
b_{xin}	Xinanjiang shape parameter related to saturation degree	-	0.05 - 0.7
T_{uz}	Linear reservoir constant upper groundwater	d	1.5 - 40
T_{lz}	Linear reservoir constant lower groundwater	d	500 - 2500
GW_{perc}	Maximum percolation rate, upper to lower groundwater	$mm\ d^{-1}$	0.3 - 1.8
$Chan_{N2}$	Multiplier on surface roughness for surface runoff	-	0.1 - 7.2
$CalMan$	Multiplier on channel Manning´s roughness coefficient	-	0.1 - 2.0

LISFLOOD model and a full description of the equations, the reader is referred to Van Der Knijff et al. (2010).

The parameters calibrated are given in Table 5.1, combined with the range of the prior normal distribution before calibration. The same set of parameters is used to calibrate EFAS and a sensitivity analysis for each of these parameters has been performed for every new version of the LISFLOOD model (Van Der Knijff et al., 2010). Thus, the same set of parameters was subject to calibration in this study. The mean of the prior normal distribution for the model parameters is determined by the original LISFLOOD calibrated parameters. Since the distribution of parameter errors is unknown, a normal distribution with a standard deviation of 20% of the mean parameter value is used to generate ensemble member realizations for the Ensemble Kalman Filter. Realizations outside of the possible parameter range (e.g. negative saturated hydraulic conductivity) are rejected and replaced by new realizations. The prior distribution is used to determine the baseline scenario to which the other scenarios are compared and evaluated. For the reservoir constant of upper and lower groundwater (T_{uz}, T_{lz}), three spatially distributed values are identified in the calibration because groundwater response throughout the catchment may be significantly different. Therefore, the catchment is divided into three groundwater regions: locations with a terrain gradient of $\geq 15\%$ are classified as steep, areas with a gradient between 5 and 15% are classified as intermediate and areas with gradients $\leq 5\%$ are classified as the flat areas. The division in groundwater regions is made since in the mountainous (steep) areas aquifers are shallow and groundwater response will be faster compared to the flat lowland areas.

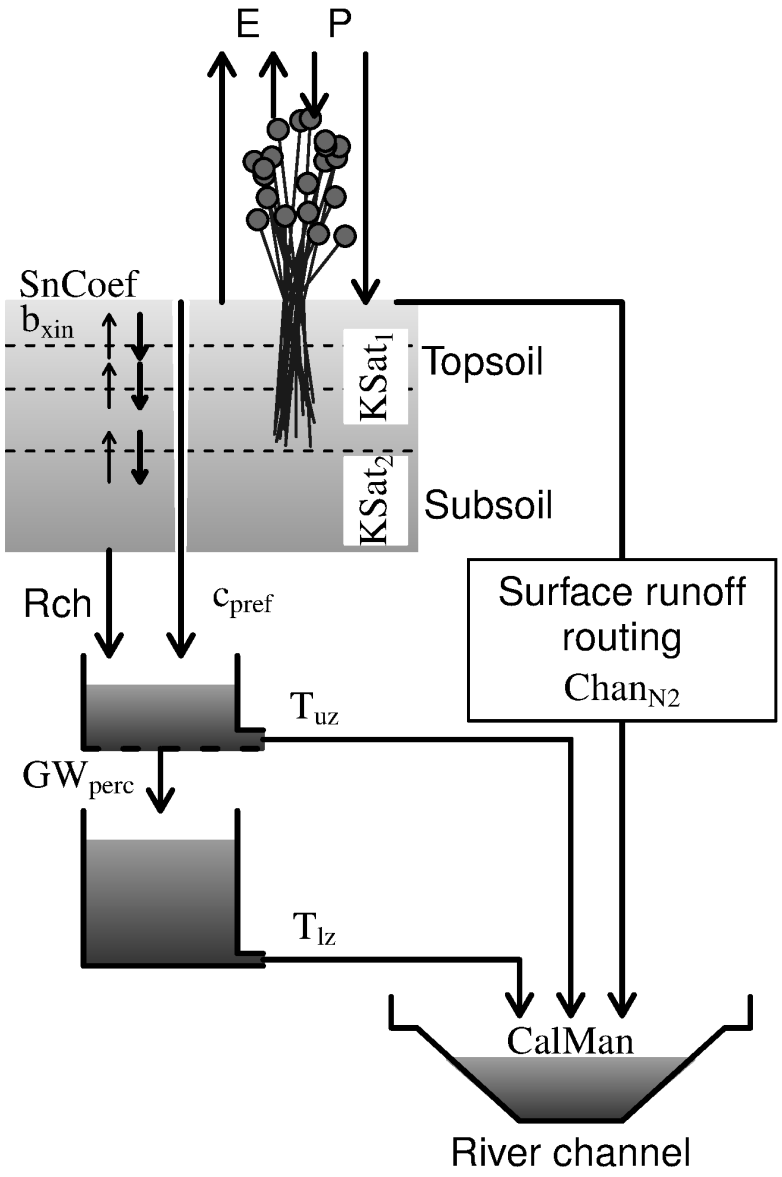

Figure 5.2 LISFLOOD model set-up, precipitation (P), evaporation (E), snowmelt coefficient ($SnCoef$), Xinanjiang shape parameter (b_{xin}), saturated conductivity of the topsoil ($KSat_1$), saturated conductivity of the subsoil ($KSat_2$), empirical shape parameter preferential macro-pores flow (c_{pref}), recharge from the unsaturated zone to the groundwater (Rch), maximum percolation rate from upper to lower groundwater (GW_{prec}), reservoir constant upper groundwater (T_{uz}), reservoir constant lower groundwater (T_{lz}), surface runoff roughness coefficient ($Chan_{N2}$), Channel Manning´s roughness coefficient ($CalMan$).

5.2.3 Data

Satellite data

Remotely sensed soil moisture data from three satellites is used, namely SMOS, ASCAT and AMSR-E (Table 5.2). SMOS is the first dedicated soil moisture satellite using fully polarized passive microwave signals at 1.41 GHz (L-band) observed at multiple angles (Kerr et al., 2012). The observation depth of SMOS is up to 5 cm with a spatial resolution of 35 - 50 km depending on the incident angle and the deviation from the satellite ground track. SMOS retrievals which are potentially contaminated with Radio Frequency Interference (RFI) have been removed.

AMSR-E is a multi-frequency passive microwave radiometer (6.9 GHz, C-band) and is used for soil moisture retrievals. The spatial resolution of AMSR-E is between 36 and 54 km with an observation depth of 2 cm and a revisit time of 3 $days$. Several algorithms estimating surface soil moisture from AMSR-E observations exist (e.g. Njoku et al., 2003; Owe et al., 2008; Pan et al., 2014). The Land Parameter Retrieval Model (LPRM), which was used for this study and the LPRM soil moisture products have been validated against in situ observations (e.g. Wagner et al., 2007; De Jeu et al., 2008; Draper et al., 2009), models (e.g. Loew et al., 2009; Crow et al., 2010; Bisselink et al., 2011) and other satellite products (e.g. Wagner et al., 2007; Dorigo et al., 2010).

ASCAT uses active microwave at a frequency of 5.3 GHz (C-band) to determine the soil moisture content (Wagner et al., 1999; Naeimi et al., 2009). ASCAT uses a change detection method (Naeimi et al., 2009) and data is provided relative to the soil moisture content of the wettest (field capacity) and driest (wilting point) measured conditions (Wagner et al., 1999). The spatial resolution of ASCAT is around 25 km, the observation depth is 2 cm and the temporal resolution equals a revisit time of 3 $days$.

All satellite soil moisture products are used on an equal area Discrete Global Grid product (DGG). For the SMOS and ASCAT soil moisture retrieval time series, a DGG is available. AMSR-E data was projected on the DGG of SMOS using the nearest neighbour approach. The DGG of ASCAT has a resolution of 12.5 km, while the the SMOS DGG uses a slightly lower resolution of 15 km.

Although the passive microwave satellite missions, SMOS and AMSR-E, give absolute soil moisture values in $m^3\ m^{-3}$, all satellite data were converted to relative soil moisture. The relative soil moisture values are calculated compared to the model climatology, to remove systematic biases between observations and model simulations. The converted satellite values $\theta_{s,new}$ in $m^3\ m^{-3}$ used for calibration are calculated by:

$$\theta_{s,new} = \frac{\theta_s - \theta_{s,5}}{\theta_{s,95} - \theta_{s,5}}(\theta_{FC} - \theta_{WP}) + \theta_{WP} \tag{5.1}$$

Table 5.2 General sensor properties relevant for this study. Satellite errors are derived from Chapter 2.

	SMOS	ASCAT	AMSR-E
Frequency (GHz)	1.41	5.3	6.9
Microwave type	Passive	Active	Passive
Spatial resolution (km)	35-50	25	36-54
Max revisit time (days)	3	3	3
Observation depth (cm)	0-5	0-2	0-2
Descending overpass (h)	6:00 PM	9:30 AM	1:30 AM
Observation error ($m^3\ m^{-3}$)	0.057	0.051	0.049
Number of observations (-)	92000	223000	81000

where θ_s are the observed satellite soil moisture values (m^3m^{-3} or -), $\theta_{s,95}$ and $\theta_{s,5}$ are the $95th$ and $5th$ percentiles of satellite soil moisture values per DGG location respectively (m^3m^{-3} or -), θ_{FC} and θ_{WP} are field capacity and wilting point of the modelled soil moisture values (m^3m^{-3}). The average model values, θ_{FC} and θ_{WP}, are calculated using the model average over the support unit of the satellite retrieval.

Frozen soils, snow accumulation and RFI hamper the soil moisture retrieval due to changes in the dielectric constant when water freezes. Therefore, retrievals done with (1) an air temperature below $4°C$, (2) simulated snow accumulation and (3) the presence of RFI (mainly for SMOS), (4) a retrieval uncertainty for SMOS (DQX) of $\geq$ 0.04 m^3m^{-3}, were not used in the calibration. Retrievals under one of the above conditions will be unreliable and would lead to incorrect calibration of the hydrological model. The temperature data was derived from the observed data and snow conditions were derived from the model simulation.

5.3 Cross-variograms of errors in remotely sensed soil moisture products

To calculate the spatial correlation between the satellite errors of different sensors cross-variograms of the errors have been calculated using the data from Chapter 2. The semivariance of the measurements is calculated by computing the distance between two individual observations. The fitted cross-variogram is used to derive the semivariance for these observations. This procedure is repeated for all possible combinations of the satellite observations. Cross-variograms of the error show that the error for the different satellite products is correlated up to a maximum distance of 150 km (Figure 5.3).

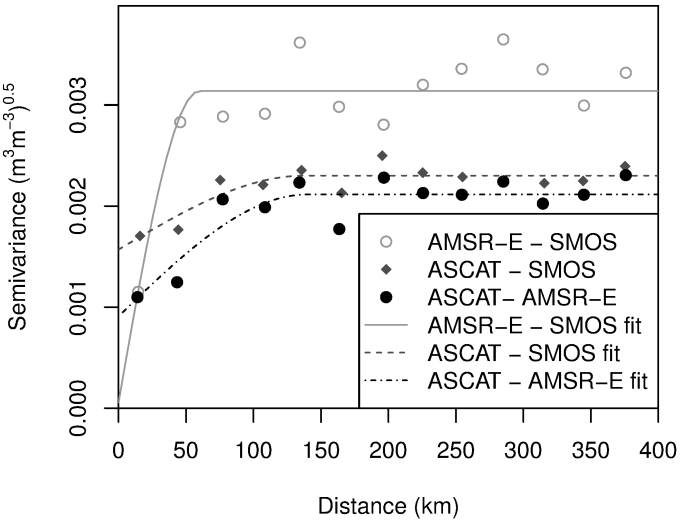

Figure 5.3 Cross-variograms of the bin-average time dependent satellite product error calculated for three satellite soil moisture products and a unsaturated zone model, for the period January 2010 - June 2011 over Spain derived from Chapter 2.

Discharge data

The Upper Danube catchment contains 23 locations where daily discharge observations are available. Time series of discharge are available from January 2000 until December 2011. Using a split sample approach the model parameters are calibrated using 7 stations and validated against 16 stations which are situated throughout the catchment of the Upper Danube (Figure 5.1). Calibration and validation stations are selected such that they are equally distributed over the catchment and are situated in both small streams and the main stream of the Upper Danube.

5.3.1 Data assimilation

The Ensemble Kalman Filter (EnKF) is a Monte Carlo based approach which is highly suitable for data assimilation and model calibration in high dimensional systems (Evensen, 1994; Burgers et al., 1998; Evensen, 2003, 2009), like the LISFLOOD model. Due to the Monte Carlo approach the model uncertainties in the EnKF can be calculated from the ensemble spread. In order to reduce calculation time, it is assumed that the ensemble spread is sufficiently large to simulate the true uncertainty of the simulation. When the ensemble size is too low, the tails of the distribution are most likely not simulated correctly and ensemble uncertainty is underestimated. An advantage of the EnKF is that it does not require propagation of the error covariance matrix as the standard Kalman Filter would require. This eliminates the need for a complex forward error model which needs to be run parallel to the model

simulations. Compared to the 4DVAR (Le Dimet and Talagrand, 1986) assimilation technique, the advantage is that there is no need for an adjoint state model to invert the model state into the period before assimilation. In contrast to the particle filter (Van Leeuwen, 2009), the EnKF can be used with a lower number of members, because the risk of particle collapse and ensemble deterioration is not as high as for the particle filter. These properties of the EnKF make it highly suitable for complex spatially distributed models, with long calculation times, a large number of calibration parameters and state variables. The EnKF has been successfully applied for flood forecasting with assimilation of discharge observations (e.g. Weerts and El Serafy, 2006; Clark et al., 2008; Komma et al., 2008; Camporese et al., 2009; Pauwels and De Lannoy, 2009; Mendoza et al., 2012; Rakovec et al., 2012; McMillan et al., 2013). Additionally, the current EnKF set-up can be used to do forecasts in an operational flood forecasting framework, without changing the model set-up and preserving the model uncertainties as was done in Chapter 6.

With a total of 300 ensemble members, the EnKF is applied to update state variables and identify parameters (Figure 5.4 and Table 5.1) of the hydrological model LISFLOOD (Figure 5.2). The perturbation of each parameter has been described in Section 5.2.2, while the initial model states are determined based on a ten-year open loop simulation of LISFLOOD with the perturbed parameters. A ten year period is used to ensure that the deep groundwater simulations would no longer be influenced by the initial conditions. The forward LISFLOOD model is given by:

$$\Psi(t+1) = f(\Psi(t), F(t), p) \tag{5.2}$$

where $\Psi(t)$ is the state of the model at time t, $F(t)$ the model forcing at time t (e.g. precipitation and evaporation) and p are the model parameters. The EnKF is applied on each daily time step using observations from remote sensing (AMSR-E, SMOS and ASCAT) and discharge observations. The general form of the EnKF is given by Evensen (2003). It can be formalized by the model forecast (Ψ^f), given by:

$$\Psi^f = (\psi_1^f, ..., \psi_{nens}^f) \tag{5.3}$$

where $\psi_1^f, ..., \psi_{nens}^f$ are the individual model forecasts, for each of the $nens$ ensemble members. Ψ^f is a $nstate \times nens$ matrix where $nstate$ is the number of model states. The state error covariance matrix of the model is directly calculated from the spread between the different ensemble members using:

$$P^f = \overline{(\Psi^f - \Psi^t)(\Psi^f - \Psi^t)^T} \tag{5.4}$$

where Ψ^t is the true model state $nstate \times nens$ matrix. Since the true state is not known it is assumed that:

$$P^f \approx P_e^f = \overline{(\Psi^f - \overline{\Psi^f})(\Psi^f - \overline{\Psi^f})^T} \tag{5.5}$$

where $\overline{\Psi^f}$ represents the ensemble average and it is assumed that the ensemble of model predictions is unbiased. The observations matrix, Y, is a $nobs \times nens$ matrix

containing the observations, where *nobs* is the number of observations. Y is given by:

$$Y = H\Psi^t + \epsilon \tag{5.6}$$

where H is a $nobs \times nstate$ transforming Ψ^t to the observations and ϵ the random error in the observations. ϵ is random noise with a zero mean and an standard deviation given by R, the measurement error covariance ($nobs \times nobs$ matrix). In this study, H ensures a spatial match between the satellite observations and modelled soil moisture from the model. This leads to the general form of the EnKF:

$$\Psi^a = \Psi^f + P^f H^T (HP^f H^T + R)^{-1}(Y - H\Psi^f) \tag{5.7}$$

Apart from state-augmentation, the EnKF also allows model parameters of the LISFLOOD model to be estimated in the same update moment. Since there are no observations of the parameters, matrix Y remains the same. However, the matrix Ψ^f and measurement operator are extended with 14 rows to enable the parameters of Table 5.1 to be estimated at the update moment. This results in updated parameters in Ψ^a which are perturbed with white noise with a standard deviation of 0.01, to prevent ensemble collapse. The perturbations are given by:

$$Ln(p'_t) = Ln(p) + W(0, 0.01) \tag{5.8}$$

where p'_t are the perturbed parameters and $W(0, 0.01)$ is white noise with a mean of 0 and standard deviation of 0.01 (-).

A relaxation factor β of 0.7 is used for the parameter updating, to prevent strong updates of Ψ^a as a result of erroneous measurements which could result in non-feasible updates of parameters. Additionally, a β of 0.7 ensures that observations at the end of the calibration still can impact the parameter calibration. If no relaxation factor is applied, the estimated uncertainty of the model predictions (P^f) is small compared to R and no updates would occur anymore at the end of the calibration period. This is particularly important because some observations get more abundant over time due to an improvement in the algorithms of the remotely sensed soil moisture. Especially in a scenario where multiple observations are used (e.g. discharge and multiple satellites) this will ensure that all observations contribute to the calibration. A β of 0.7 was selected as the best value, to ensure convergence of the parameters and allows all sensors to be used in the parameter estimation. The introduction of β results in a modified form of Equation 5.7 for parameter updating:

$$\Psi^a_p = \beta\Psi^f_p + (1 - \beta)P^f H^T (HP^f H^T + R)^{-1}(Y - H\Psi^f_p) \tag{5.9}$$

where Ψ^a_p and Ψ^f_p are the parameter analysis and parameter forecast, respectively. This theoretical framework has been successfully applied in other studies to estimate both state and parameters (e.g. Tong et al., 2012).

Due to small sample sizes and a small number of observations, spurious correlations could occur. This would result in update of parameters that have no physical relation

with the observations. To avoid the effects of these unwanted updates of parameters, the covariance between the observations and these parameters is set to zero. This is done for the parameters at the bottom half of Table 5.1. Given the relations defined in the model structure, it is not possible that the satellite observations contain information on the values of these parameters.

The soil moisture and discharge observations are used to correct the states in the model using Equation 5.7. The soil moisture observations are directly used in the data assimilation system to correct the soil moisture content of the different layers. The error covariance between the different soil layers is calculated from Equation 5.5. Discharge observations are used to correct the groundwater states. Since the discharge observations are strongly related to the groundwater, they contain a large amount of information on the groundwater storage and can be used to correct the groundwater simulations. Other advantages of the correction of the groundwater is that the update will have a larger impact on discharge simulations for the next timestep, while updating the river water levels will only result in an improvement in the discharge simulation for a short period (up to 6 days maximum for the Upper Danube).

For the assimilation of the satellite data with the Ensemble Kalman Filter (EnKF), spatial information on the measurements error covariance (R, Equation 5.7) is required. The structure of R is determined using the data of Chapter 2 over Spain as obtained using high resolution modelling of the unsaturated zone. From this study, the relative errors of each satellite product were determined as well as the spatial correlation of the errors of the satellites. Because Chapter 2 did not include the spatial correlation between the satellite errors of different sensors, the cross-variograms between sensors were additionally calculated using the same dataset (Appendix 5.3). The error covariance between the discharge observations is set to zero while the error for the discharge observations is assumed to be 30% of the discharge (e.g. Di Baldassarre and Montanari, 2009). It is also assumed that there is no error covariance between the satellite observations and discharge observations.

5.3.2 Scenarios

To test if the Ensemble Kalman Filter calibration framework is capable to calibrate known parameters and reproduce these results with different prior distributions, a synthetic dataset was used for a calibration experiment. Using known parameters, a synthetic dataset was produced and used as synthetic observations for parameter estimation and state updates. Both discharge and synthetic satellite observations are reproduced with the synthetic experiment. The framework was tested with the assimilation of one synthetic discharge observation in combination with multi-sensor synthetic soil moisture observations for a period of two years. The errors assumed for the synthetic observations are identical to those of the real observations. For the

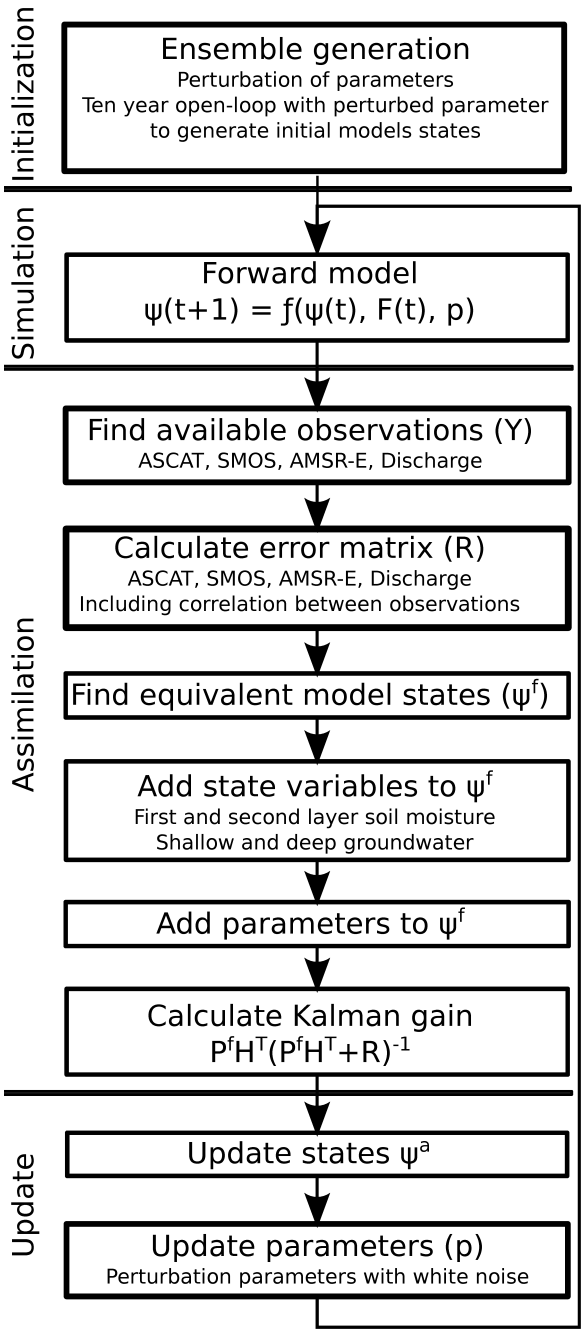

Figure 5.4 Flowchart of data assimilation scheme.

synthetic discharge a 30% error and an error of 0.05 m^3m^{-3} for all of the synthetic ASCAT, AMSR an SMOS observations are assumed. ASCAT and AMSR-E synthetic observations are created from the 0-2 *cm* soil moisture layer, while SMOS synthetic observations are generated from the average of the two first soil moisture layers (0-5 *cm*). A total of 300 ensemble members is used for the synthetic experiment, which is identical to the number used for the calibration of other scenarios. It was tested whether calibrated parameters are found to be identical to the parameter set used to create the synthetic dataset.

After the synthetic experiment, a sensitivity analysis was performed on the LISFLOOD model to enable better interpretation of the results. This sensitivity experiment is complementary to the normal sensitivity analysis of LISFLOOD, which is described by Van Der Knijff et al. (2010). Since the LISFLOOD was modified for the assimilation of remotely sensed soil moisture, this new sensitivity analysis is required. All parameters (Table 5.1) were modified by taking the 90% and 110% of the prior mean. The discharge and soil moisture dynamics as well as the absolute levels of these variables have been related to all calibration parameters of the model. The variance is computed for each of these variables to estimate the dynamic behaviour, while the absolute levels are computed by taking the long term mean.

After these initial experiments, observations of three microwave satellites and seven discharge time series were used to estimate the parameters of the LISFLOOD model for the Upper Danube area using the Ensemble Kalman Filter. Different calibration scenarios were tested, each using different observations or combinations of observations. This is done to obtain understanding of the influence of the observations on the retrieved parameters and their capacity to estimate the parameters. A detailed description of the calibrated parameters, updated state variables, total number of observations and the total number of scenarios can be found in Table 5.3. The calibration scenarios included are:

1. One satellite soil moisture product, either ASCAT, AMSR-E or SMOS.
2. Discharge observations, either one or seven locations (Figure 5.1).
3. Discharge observations (one or seven locations) and one satellite soil moisture product.
4. Discharge observations (one or seven locations) and all satellite products.

The individual scenarios were calibrated for a two year period (2010-2011). This period was chosen because of the availability of all three microwave soil moisture satellite products. When all three satellite products are used, ASCAT and AMSR-E are directly compared to 0-2 *cm* simulated soil moisture and SMOS is compared to the weighted-average of the two first simulated soil moisture layers (0-2 and 2-5 *cm*). The updates of the two soil moisture layers are dependent on the specific uncertainty

of the satellite observation and the uncertainty in the modelled soil moisture. The satellite observations are directly compared to the simulated soil moisture at their specific penetration depth to reduce errors in the assimilation.

The calibrated parameters found at the end of the calibration period for the different scenarios were used to simulate discharge for the period 2000-2009 as a validation of the model. All 300 members from the ensemble found by calibration were used in the validation to determine the uncertainty in the simulated discharge and soil moisture. No assimilation of observations was performed during the validation, to only validate the performance of the calibrated model without data assimilation. From this ensemble, the ensemble mean discharge and soil moisture were calculated and compared with the observed discharge and soil moisture. The performance of the soil moisture simulations was evaluated with time series of AMSR-E (2002-2009) and ASCAT (2007-2009). These time periods were selected because these data are not used during the calibration of the LISFLOOD model and are therefore considered to be independent, although it is acknowledged that independent observations would have been better. The performance of the calibration scenarios was also compared with a simulation using the prior distributions of parameters (baseline scenario).

In the validation, the Root Mean Square Error (RMSE) of the discharge and soil moisture simulations was calculated by:

$$RMSE = \sqrt{\frac{\sum_{t=1}^{T}(Z_{mod}(t) - Z_{obs}(t))^2}{T}} \tag{5.10}$$

where Z_{mod} is the modelled ensemble mean discharge or soil moisture and Z_{obs} is the observed discharge or soil moisture, T is the total number of observations (-), approximately 3.600 for discharge and between 81.000 and 396.000 for the satellite observations (dependent on the scenario). To enable comparison between discharge time series of different stations, the $RMSE$ of a station is standardized on the average discharge of the station ($\overline{Q_{obs}}$) using:

$$SRMSE = \frac{RMSE}{\overline{Q_{obs}}} \tag{5.11}$$

where $SRMSE$ is the Normalized Root Mean Square Error (-) of the discharge location and $\overline{Q_{obs}}$ is the average observed discharge ($m^3 s^{-1}$).

5.4 Results

5.4.1 Calibration on synthetic dataset and sensitivity analysis

The synthetic calibration experiment was repeated six times using 300 ensemble members and different realizations of the prior distribution showing consistent results for

Table 5.3 Detailed description of the calibration scenarios. Scenario names indicate the assimilated data, the number of observations are divided between remotely sensed soil moisture observations. Calibrated parameters are either soil parameters (Soil), including $SnCoef$, $KSat_1$, $KSat_2$, c_{pref} and b_{xin}. Finally, the updated state variables are given, where Topsoil indicates the first two layers of the LISFLOOD model and GW both ground water reservoirs of the LISFLOOD model.

Scenario	Number of observations		Calibrated	Updated
	Soil moisture	Discharge	parameters	state variables
No assimilation	0	0	None	None
ASCAT	81000	0	Soil	Topsoil
AMSR-E	223000	0	Soil	Topsoil
SMOS	92000	0	Soil	Topsoil
All satellites	396000	0	Soil	Topsoil
1 discharge station	0	730	All	Topsoil & GW
7 discharge stations	0	5000	All	Topsoil & GW
ASCAT + 1 discharge station	81000	730	All	Topsoil & GW
AMSR-E + 1 discharge station	223000	730	All	Topsoil & GW
SMOS + 1 discharge station	92000	730	All	Topsoil & GW
All satellites + 1 discharge station	390000	730	All	Topsoil & GW
ASCAT + 7 discharge stations	81000	5000	All	Topsoil & GW
AMSR-E + 7 discharge stations	223000	5000	All	Topsoil & GW
SMOS + 7 discharge stations	92000	5000	All	Topsoil & GW
All satellites + 7 discharge stations	396000	5000	All	Topsoil & GW

every repetition. Parameters used to produce the synthetic data set were within the 95% confidence interval of the calibrated parameter distributions (Figure 5.5), with the exception of GW_{perc}. This is caused by the low sensitivity of the model to changes in this parameter compared to changes in T_{lz}. The synthetic discharge could be reproduced with a $SRMSE$ of 0.06 at the outlet of the Upper Danube. From these results, it is concluded that the EnKF calibration framework shows a consistent performance and could be used with confidence to calibrate scenarios based on satellite and discharge observations. The framework can be used with confidence to calibrate large-scale hydrological models and distributed land-surface models in general.

The results of the sensitivity analysis are presented in Table 5.4 and show that the soil moisture is very sensitive to, in decreasing order of importance, c_{pref}, b_{xin}, $KSat_1$, $SnCoef$ and $KSat_2$. The parameters in the bottom half of Table 5.1 do not have any impact on the soil moisture simulation and hence it is justified to assume no

Table 5.4 The dependency of mean soil moisture (Θ), variance in soil moisture ($var(\Theta)$), mean discharge (Q) and the variance in discharge ($var(Q)$) to changes in individual parameters ($\Delta\alpha$).

	$\frac{\Delta\Theta}{\Delta\alpha}$	$\frac{\Delta var(\Theta)}{\Delta\alpha}$	$\frac{\Delta Q}{\Delta\alpha}$	$\frac{\Delta var(Q)}{\Delta\alpha}$
$SnCoef$	265	0.040	2638	-0.001
$KSat_1$	-415	0.142	-14068	-0.030
$KSat_2$	3	0.001	1	0.002
c_{pref}	1835	-0.087	-8891	0.103
b_{xin}	1600	-0.163	13419	0.090
T_{uz}	0.0	0.0	484	0.064
T_{lz}	0.0	0.0	9115	0.001
GW_{perc}	0.0	0.0	-2649	0.069
$Chan_{N2}$	0.0	0.0	-6	-0.008
$CalMan$	0.0	0.0	-11	0.032

correlation between these parameters and soil moisture observations during the data assimilation.

The discharge dynamics and total discharge volumes are sensitive to changes in all parameters (Table 5.1). The largest sensitivity of the total runoff is to $KSat_1$, b_{xin}, T_{lz}, c_{pref}, GW_{prec} and $SnCoef$ (in decreasing order of importance). Part of the impact of the parameters related to overland flow is caused by the contribution of surface runoff to the total discharge. Additionally, the evapotranspiration rate largely determines the total discharge volume of the catchment. Evapotranspiration is controlled by the infiltration rate of soil moisture through the unsaturated zone and hence is strongly related to b_{xin} and $KSat_1$. Discharge dynamics are sensitive to c_{pref}, b_{xin}, GW_{perc}, T_{uz}, $CalMan$, $KSat_1$, $Chan_{N2}$ and $KSat_2$.

5.4.2 Parameter identification

The calibrated parameters for all calibration scenarios show that including more discharge and soil moisture observations, leads to decreased spread in the calibrated parameters (Figure 5.6). Including multiple discharge observation time series instead of one leads to a better identification of parameters (Figure 5.6) as is expected from the increased amount of information given to the calibration framework.

When both discharge and soil moisture observations are used for the parameter estimation and state updates of the LISFLOOD model, parameters related to land surface processes, e.g. saturated hydraulic conductivity, are better identified, result-

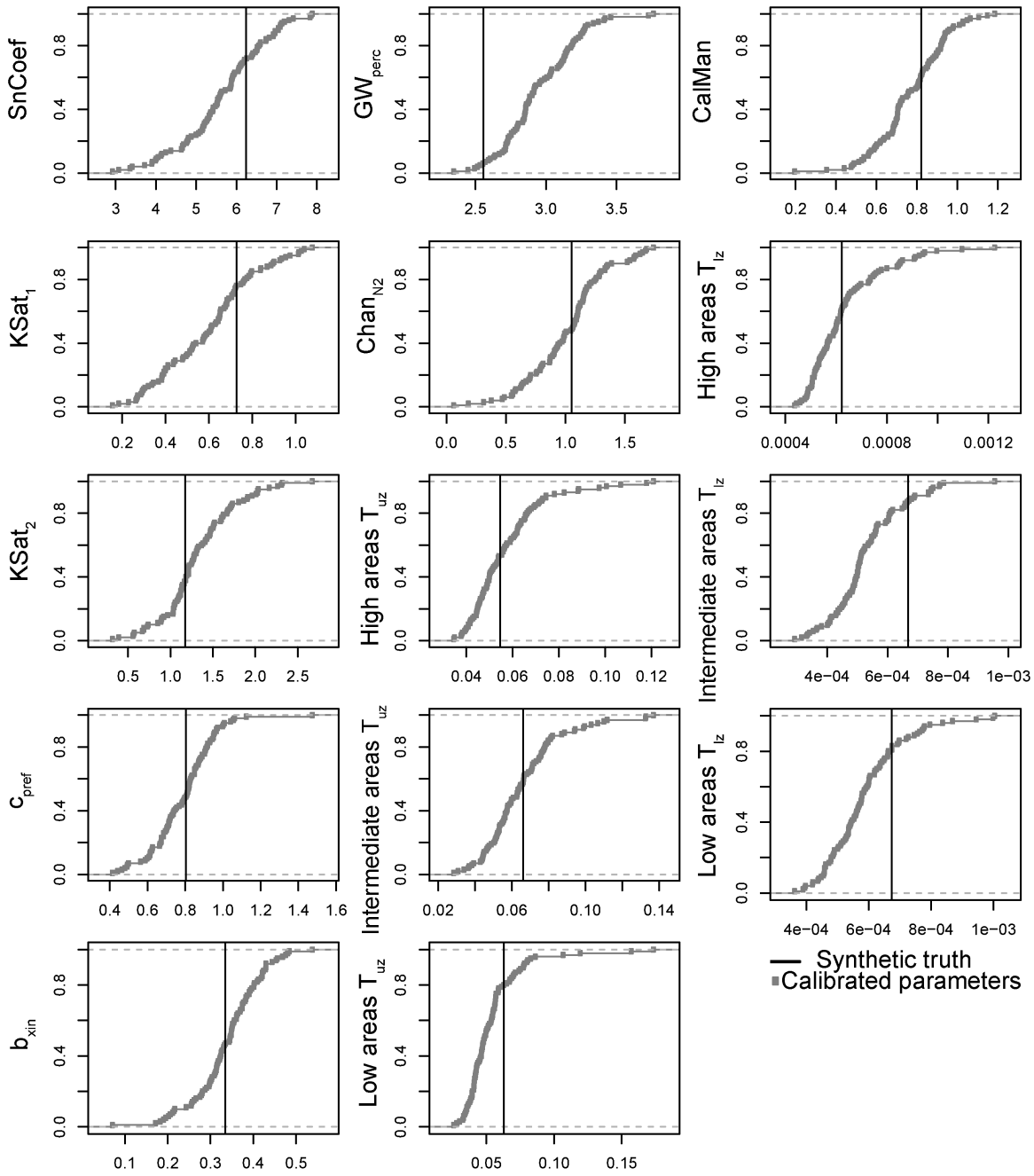

Figure 5.5 The calibrated parameter distributions for the synthetic experiment used in the simulation of discharge in the LISFLOOD model. In black the parameter set used to create the synthetic dataset is shown, grey indicates the calibrated parameter set based on the synthetic data. With the exception of GW_{perc} all parameters are within the 95% confidence interval of their true values used to generate the synthetic data. Description of the parameters is given in Table 5.1.

ing in posterior parameter distributions with a low uncertainty (Figure 5.6). The uncertainty of surface parameters calibrated with only discharge observations is significantly higher compared to the calibration with both soil moisture and discharge observations. This confirms that discharge observations contain less information on processes related to the unsaturated zone than soil moisture observations and are more informative regarding processes in the groundwater system and channel routing. Satellite observations will contribute to the calibration and contain information on land-surface processes that cannot be inferred from discharge observations. When soil moisture observations are added to the calibration, some small changes can be found in the groundwater parameters. This is related to the fact that some parameters impact both discharge and soil moisture simulations (e.g $KSat_1$ and b_{xin}). When these parameters are modified, also other parameters impacting discharge should be modified to compensate for changes in the input from the soil moisture, to correctly simulate the discharge in the catchment.

The uncertainty found in calibrated parameters by calibration with ASCAT is lower than with AMSR-E or SMOS soil moisture (not shown), which could be caused by the smaller error in the ASCAT soil moisture product used in the data assimilation system (Chapter 2) or higher spatial resolution of the ASCAT product. For this study, it was assumed that the error structure of Chapter 2 is identical to the error structure of the microwave remote sensing observations for the Upper Danube, which could also impact the results. Additionally, the number of observations used for the calibration with ASCAT is also significantly higher than for calibration with either AMSR-E or SMOS (Table 5.2). This result is not dependent on the addition of discharge observations. More research in required to see if this result is also valid for other areas and independent of model structure and calibration framework.

5.4.3 Discharge simulation

Time series for the validation of the discharge at the outlet of the Upper Danube show that without the EnKF data assimilation, the discharge is on average underestimated for both peak flows and baseflow (Figure 5.7). In all calibration scenarios, the estimation of discharge is improved compared to the no calibration scenario; especially the base flow has increased to levels more similar to those observed during low flow periods. Depending on the different satellites used for the calibration, the $SRMSE$ is decreased by $\approx 10\%$ compared to no calibration (Figure 5.8 and 5.9). The improvement in discharge simulation is the largest for AMSR-E and lower for ASCAT and SMOS. Although parameter uncertainties are smaller for ASCAT, calibration did not necessarily lead to better discharge simulations. For SMOS, the performance could be hampered by the relatively large number of missing data (masked). This is due to RFI, which has a big impact on the data quality of SMOS in this region (Dall'Amico et al., 2012). The error of SMOS satellite retrievals used in this study is

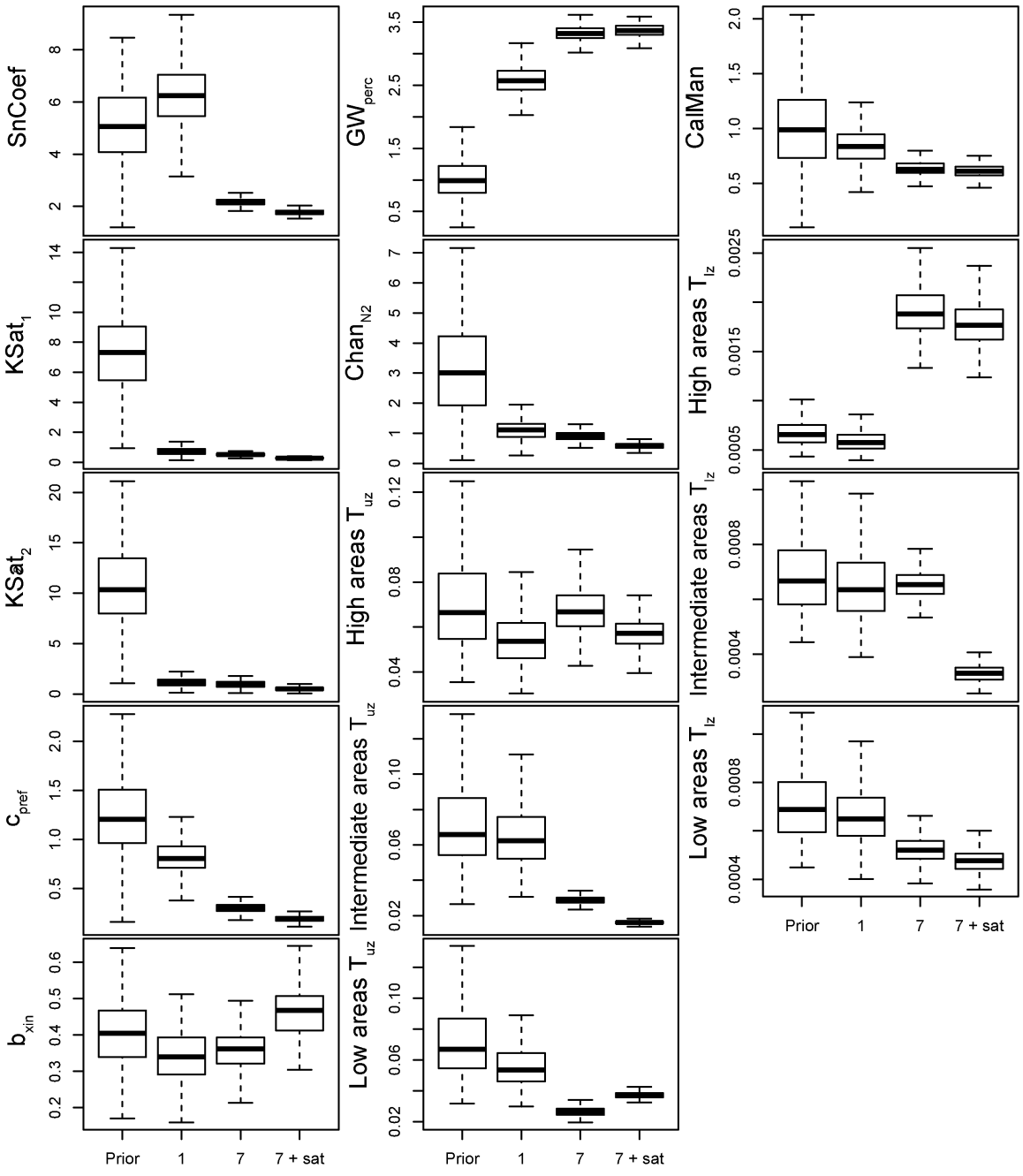

Figure 5.6 The calibrated parameter distributions for three different calibration scenarios and the prior parameter estimations used in the simulation of discharge in the LISFLOOD model. Prior is based on expert knowledge and used as prior for the other scenarios, 1 is calibration on one discharge station close to the outlet (Fig 5.1), 7 is calibration based on 7 stations distributed across the catchment and 7 + sat is calibration based on 7 discharge stations and remotely sensed soil moisture by three microwave satellite sensors (SMOS, AMSR-E and ASCAT). Description of the parameters is given in Table 5.1.

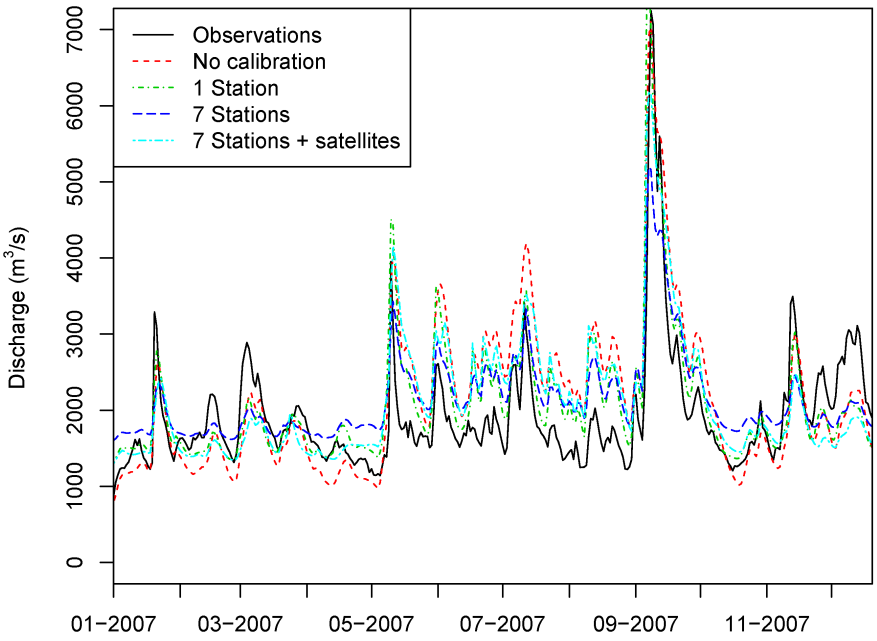

Figure 5.7 Time series of ensemble mean discharge at the outlet of the Upper Danube Catchment, for multiple calibration scenarios: observed indicates the observed discharge time series. Calibration scenarios are: No calibration, a simulation using the prior distribution of parameters based on expert knowledge, 1 station is calibration on one discharge station (Fig 5.1), 7 stations is calibration based on 7 stations and 7 station + satellites is calibration based on 7 discharge stations and remotely sensed soil moisture by three microwave satellite sensors (SMOS, AMSR-E and ASCAT).

also relatively large compared to the other two satellites, which in combination with a reduced number of observations leads to a decreased performance in the calibration.

For the simulation of discharge at the catchment outlet, the calibration on only one station shows a lower $SRMSE$ (Equation 5.11) compared to calibration on more discharge observations, or calibration on both discharge and satellite observations (Figure 5.8). This is caused by the fact that the discharge location used for calibration on only one station is situated close to the catchment outlet (large square in Figure 5.1). Therefore, calibration parameters are only adjusted to give the best simulation of the discharge at the outlet as possible, while other calibration scenarios also aim at satisfying other calibration criteria. The average $SRMSE$ for all validation locations (Figure 5.1) is reduced when the LISFLOOD model is calibrated using seven discharge observations compared to only calibration on one discharge observation (Figure 5.9). This decrease is found for all scenarios that include seven discharge locations, with or without the addition of satellite observations. This leads to the conclusion that increasing the number of discharge locations will not necessarily increase the accuracy of discharge simulations at the outlet. However, it will result in a better simulation of

the distribution of runoff and thereby improve overall discharge simulation throughout the catchment. Overall, the discharge simulation for the validation period is improved by $\approx 15\%$ compared to calibration only on discharge at the outlet, as shown by a decrease in the $SRMSE$ (Figure 5.9).

Throughout the catchment, the calibration with remote sensed soil moisture improved discharge simulation in the upstream part of the catchment (t-test at the 95% confidence level). However, no catchment above 40000 km^2 showed any significantly improved discharge simulation as a result of calibration on one or multiple sources of remotely sensed soil moisture. Calibrations with seven discharge locations and either ASCAT, AMSR-E, SMOS or a combination of satellites is compared to a scenario with only calibration on seven discharge locations (Figure 5.10). Only locations where the discharge is decreased or increased by more than 5% are shown. From this spatial comparison it is concluded that discharge simulations are improved in the upstream areas when soil moisture is added to the calibration.

Compared to calibration with only discharge, calibration with discharge and satellite data does improve discharge simulations for smaller catchments. From these results, it is concluded that adding satellite data to the calibration will mostly improve the overall discharge results in situations when no discharge data are available for calibration. In these situations, satellite observations lead to small improvements of discharge simulations.

5.4.4 Soil moisture simulation

Soil moisture simulation of the LISFLOOD model after calibration on discharge or satellite observations is compared with time series of AMSR-E (2002-2009) and ASCAT (2007-2009). After calibration an improvement is found compared to the soil moisture simulation with the prior distribution. Compared to observed AMSR-E and ASCAT data, the average $RMSE$ is reduced from 0.24 (prior distribution) to 0.058 m^3m^{-3} after calibration on multi-sensor satellite observations. However, no difference could be found between the different scenarios, using one or multiple satellite products. When the scenarios are compared spatially some distinct patterns are found. The improvements for calibration with ASCAT and AMSR-E are mainly found in the mountainous areas as can be seen in Figure 5.10. This could be related to the relatively poor model simulation of the unsaturated zone in these regions in the scenario without calibration, leading to a large improvement. Additionally, in these regions the observation error of ASCAT and AMSR-E is lower than for SMOS (Chapter 2). The combination of these two factors leads to large improvements in mountainous areas, which would normally not be expected because of the low quality of remotely sensed soil moisture retrievals in these areas. Calibration on SMOS data only improves soil moisture in the lowland regions, which could be related to the increased observation depth of the SMOS satellite compared to the other sensors. If all

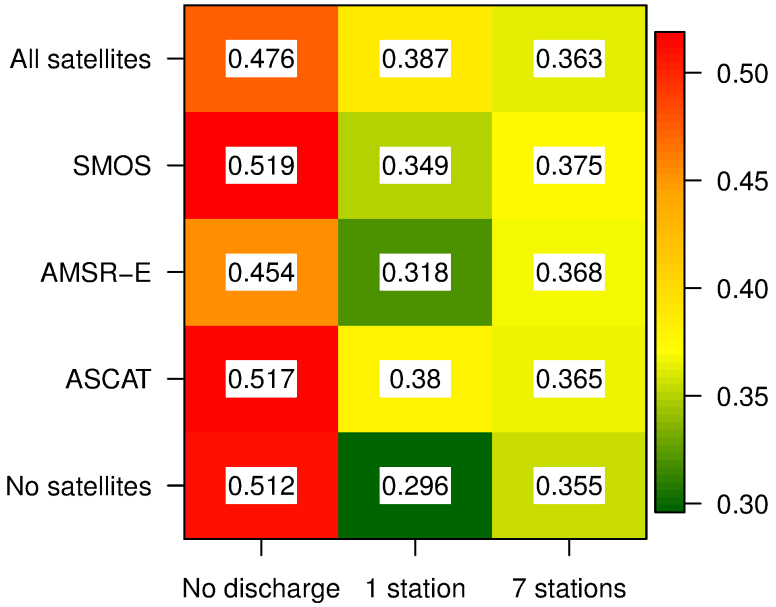

Figure 5.8 Cross table with the Normalized Root Mean Square Error of the ensemble mean discharge at the outlet of the Upper Danube catchment using 15 different calibration scenarios. Columns indicate calibration without using discharge, 1 discharge location close to the outlet or 7 discharge locations distributed throughout the catchment. Rows indicate calibration on soil moisture, without using any data or using either data from the ASCAT, AMSR-E or SMOS satellite or a combination of all three sensors (All satellites).

satellite data are used at the same time to calibrate the LISFLOOD model, simulated soil moisture patterns are improved for large parts of the catchment, without favouring specific regions. This is caused by the fact that single satellite improvements are compensated by other sensors and a more widespread improvement is the result.

As all parameters are spatially lumped (with exception of T_{uz} and T_{lz}), calibration will result in improvements for some areas, while the simulation deteriorates for other regions of the Upper Danube. Due to the large number of parameters, it is not feasible to include a calibration of spatially distributed parameters with the given number of ensemble members, i.e. this would lead to numerical problems for the calibration framework and unidentifiable model parameterizations.

5.5 Discussion and Conclusion

The LISFLOOD hydrological model was calibrated for the Upper Danube catchment using discharge observations and remotely sensed soil moisture from three different space-borne sensors. An Ensemble Kalman Filter with augmented state was used to

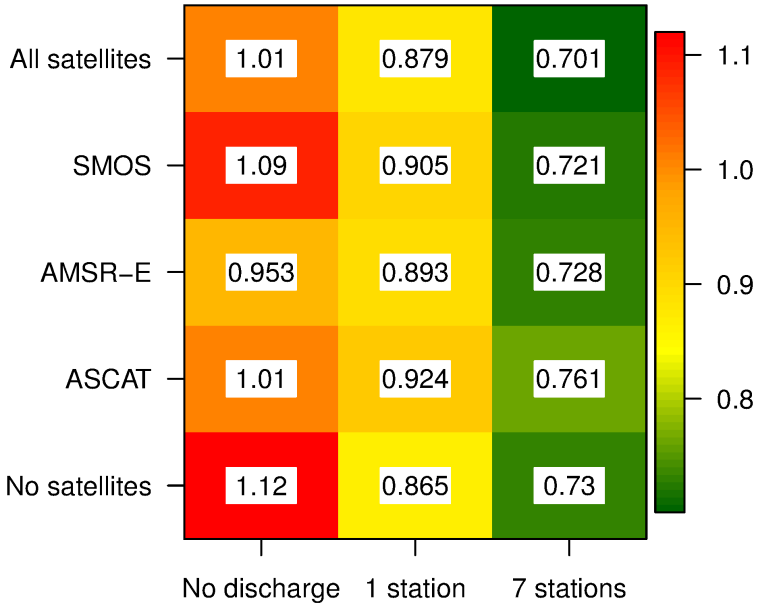

Figure 5.9 Cross table with the average Normalized Root Mean Square Error of the ensemble mean discharge at all validation locations of the Upper Danube catchment (Fig 5.1) using 15 different calibration scenarios. Columns indicate calibration without using discharge, 1 discharge location close to the outlet or 7 discharge locations distributed throughout the catchment. Rows indicate calibration on soil moisture, without using any data or using either data from the ASCAT, AMSR-E or SMOS satellite or a combination of all three sensors (All satellites).

estimate parameters of the LISFLOOD model for a period of two years (2010-2011). In total 10 model parameters were calibrated and used for a validation over a period of 10 years (2000-2009).

The Ensemble Kalman Filter was successfully used to calibrate the model on a synthetic dataset with known parameters and state variables. All parameters could be successfully identified using synthetic observations of discharge and satellite soil moisture. It is concluded that the Ensemble Kalman Filter can be used with confidence to calibrate spatially distributed hydrological models and estimate both state variables and parameters.

Parameters of the LISFLOOD model were identified with reduced uncertainty when soil moisture data was assimilated into the hydrological model. Especially parameters related to land-surface processes showed a strong decrease in parameter uncertainty compared to calibration without soil moisture data. Parameters related to groundwater and routing were better calibrated using one or multiple discharge observations. When more discharge observations were introduced to the calibration framework, un-

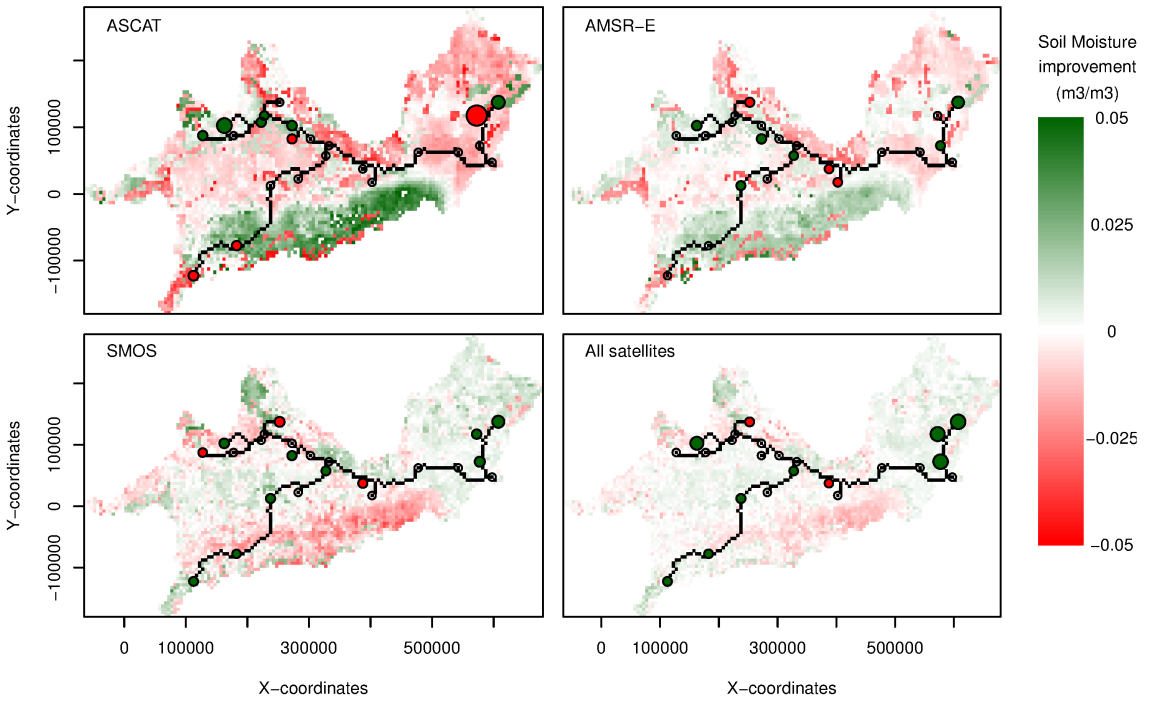

Figure 5.10 Comparison between calibration on 7 discharge locations and calibration based on these discharge locations and remotely sensed soil moisture. Colours indicate the improvement in the soil moisture simulations for the validation period, circles indicate whether any improvement is found for the ensemble mean discharge simulation, size of the circle indicates the relative improvement in the discharge simulations and blank circles are locations with a less than 5% change compared to the calibration on 7 discharge locations. ASCAT is a comparison between the calibration on only discharge and discharge combined with remotely sensed soil moisture observations from ASCAT (similar for AMSR-E and SMOS). All satellites show a comparison between the calibration on only discharge and discharge combined with all three remotely sensed soil moisture observations.

certainties in parameters, uncertainties in groundwater and routing parameters were reduced.

The use of remotely sensed soil moisture significantly improved the model performance compared to parameters estimated with expert knowledge. However, the results of this study show that the contribution of remotely sensed soil moisture to the improvement of discharge is limited for large catchments. No catchment above 40000 km^2 showed any improved discharge simulations as a result of calibration on one or multiple sources of remotely sensed soil moisture.

On average small improvements in soil moisture simulations were found for all scenarios that included soil moisture assimilation. Soil moisture simulations are mostly improved for ASCAT and AMSR-E in areas with large relief, where the relative importance of fast runoff processes is larger compared to the topographically flat areas.

SMOS showed a different pattern, with improvements in soil moisture simulation mainly observed in flat areas, and SMOS showed relatively smaller improvements in soil moisture simulations. When all three sensors were combined, locally improvements were more averaged out, while on average, simulations of soil moisture throughout the catchment were improved. Compared to soil moisture simulation with the prior distribution of parameters, all calibration scenarios with remotely sensed soil moisture significantly improved soil moisture simulations.

Compared to calibration with only discharge, calibration with addition of satellite data does improve discharge simulations for smaller catchments. In contrast to Lee et al. (2011), in this study only an improvement was found for discharge simulations in small sized catchments. This small improvement in upstream discharge is also in line with work of Brocca et al. (2010). However, Brocca et al. (2010) and Lee et al. (2011) both used assimilation of soil moisture during the validation period, which could lead to different results. Sutanudjaja et al. (2014) calibrated a hydrological model on soil moisture observations, and also found minor improvements in discharge simulations for a large catchment.

It is concluded that remotely sensed soil moisture improves the calibration of the LISFLOOD hydrological model for small catchments, while for larger catchments, above 40000 km^2, this increase in model performance is negligible due to the large relative importance of groundwater and channel routing.

Increasing the number of discharge observations, will improve catchment average discharge simulations, which confirms previous work by Rakovec et al. (2012). Moreover, the error in the discharge simulation at the outlet will not decrease by adding more discharge observations, which is mainly caused by the fact that it is easier to fit a single discharge time series than discharge series at multiple locations simultaneously. This finding is contradictory to Rakovec et al. (2012), which might be the result of a larger catchment size in this study. This larger catchment will result in significantly longer travel times of the water, interference of man-made structure and additionally, a larger grid resolution of the hydrological model. All these factors could cause the difference between this study and work of Rakovec et al. (2012).

The addition of soil moisture in the calibration further improves discharge simulations in the upstream areas of the Upper Danube. Additionally the soil moisture simulation is improved for large parts of the catchment. This leads to the conclusion that a more realistic portrayal of the catchment's hydrology (i.e. being right for the right reason) will thus be achieved by using multiple discharge time series and remotely sensed soil moisture in model calibration.

A point of attention is the availability of discharge and precipitation data for this catchment. The precipitation network in this catchment is very dense, leading to low uncertainties in interpolated precipitation for the Upper Danube. As suggested by Crow and Ryu (2009), remotely sensed soil moisture could be used to correct for

uncertainties in precipitation or other meteorological forcing data. Thus, the assimilation of remotely sensed soil moisture for parameter estimation in more sparsely gauged regions could potentially result in larger improvements in discharge and soil moisture simulations than observed in this study.

Acknowledgments

EC-JRC is acknowledged for being able to work with the Danube model set-up.

6 Remotely sensed soil moisture for improving flood forecasting

This chapter is based on:
Wanders, N., Karssenberg, D., de Roo, A., de Jong, S. M., and Bierkens, M. F. P. (2014), The suitability of remotely sensed soil moisture for improving operational flood forecasting, Hydrology and Earth System Sciences, 18, 2343-2357, doi:10.5194/hess-18-2343-2014.

Abstract

The added value of assimilated remotely sensed soil moisture for the European Flood Awareness System (EFAS) was evaluated and its potential to improve the prediction of the timing and height of the flood peaks and low flows. EFAS is an operational flood forecasting system for Europe and uses a distributed hydrological model (LISFLOOD) for flood predictions with lead times up to 10 days. For this study, satellite-derived soil moisture from ASCAT, AMSR-E and SMOS is assimilated into the LISFLOOD model for the Upper Danube basin and results are compared to assimilation of discharge observations only. To assimilate soil moisture and discharge data into the hydrological model, an Ensemble Kalman Filter (EnKF) is used. Information on the spatial (cross-) correlation of the errors in the satellite products is included to ensure increase performance of the EnKF. For the validation, additional discharge observations, not used in the EnKF, are used as an independent validation dataset. Our results show that the accuracy of flood forecasts is increased when more discharge observations are assimilated; the Mean Absolute Error (MAE) of the ensemble mean is reduced by 35%. The additional inclusion of satellite data results in a further increase of the performance: forecasts of base flows are better and the uncertainty in the overall discharge is reduced, shown by a 10% reduction in the MAE. In addition, floods are predicted with a higher accuracy and the Continuous Ranked Probability Score ($CRPS$) shows a performance increase of 5-10% on average, compared to assimilation of discharge only. When soil moisture data is used, the timing errors in the flood predictions are decreased, especially for shorter lead times, and imminent floods can be forecasted with more skill. The number of false flood alerts is reduced when more observational data is assimilated into the system. The added values of the satellite data is largest when these observations are assimilated in combination with distributed discharge observations. These results show the potential of remotely sensed soil moisture observations to improve near-real time flood forecasting in large catchments.

6.1 Introduction

Floods are extreme hydrological events caused by excessive water availability and may cause large economical, societal and natural damage. One example is the summer 2013 flood in central Europe producing historical high water levels in large parts of the Danube and Elbe catchments, causing a total estimated economic loss of 23 billion Euro (Aon Benfield, 2013). Due to their increasing impact on society, forecasting of these extreme events has become more important to increase preparedness and improve the response to and prevention of floods. This requires an increasing need to develop accurate and reliable flood forecasting systems. National forecasting systems have been developed in for example England (National Flood Forecasting System), Germany (Hochwasservorhersagezentral), Netherlands, Germany and Switzerland (FEWS-Rhine & Meuse), Czech Republic (CHMI-IWSS), Sweden (SMHI) and most other countries in Europe. For transboundary river basins, national forecasting systems are often lacking skill and transboundary forecasting systems are preferred. To fulfil this need, the European Commission developed the European Flood Awareness System (EFAS) for flood forecasting up to a lead times of 10 days for the European continent (Thielen et al., 2009). Additionally, EFAS will contribute to understanding of flood events on a transboundary scale and will support international crisis management at the European level.

Flood forecasts are made for multiple basins, using distributed hydrological modelling. Systems like EFAS are highly dependent on the meteorological forcing provided as well as the pre-storm initial conditions of the catchment (Nester et al., 2012; Alfieri et al., 2013). To improve estimates of initial conditions data assimilation techniques have the potential to update incorrect model states with observational data to obtain the best possible estimate of the current status of the hydrological system. Discharge data is often used in these data assimilation frameworks, because it contains the integrated information of all other hydrological states (e.g. Vrugt et al., 2006; Clark et al., 2008; Rakovec et al., 2012). However, it is difficult to obtain these measurements in real-time in a way they can be used in EFAS. Observations might not be available in real-time, quality control cannot be done in real-time or local data providers are unfortunately not willing to share the information. Measurements of hydrological states other than discharge are rarely used for estimating the model's initial state while these may be of considerable value. In particular, measurements of the pre-storm soil moisture conditions could potentially improve flood forecasting systems, since initial soil moisture conditions are expected to have a large impact on the flood peaks during a storm event. The soil moisture content determines the amount of water which can still be stored in the unsaturated zone or percolate to the saturated zone and thereby influences the precipitation required to generate overland flow. However, field observations at continental scale are not available due to the limited number of observational networks and their low spatial support. Remotely sensed soil moisture retrievals from the microwave domain could potentially fill the need for soil moisture

observations at the large spatial scales. Observations are globally available and revisit times per sensor are between 1 and 3 days depending on latitude. An additional advantage is that the data is available within 3 hours after observed and the satellites have a global coverage, while single discharge observations are only valid for the catchment scale.

Multiple studies have used remotely sensed soil moisture to improve discharge simulations in small catchments ($\leq$ 1000 km^2) and to correct for errors in pre-storm soil moisture conditions (Pauwels et al., 2001; Scipal et al., 2008; Brocca et al., 2010; Chen et al., 2011; Brocca et al., 2012; Matgen et al., 2012). These studies show that assimilation of these data improved the simulation of flood events and especially the height of the flood peak. For large-scale catchments, Draper et al. (2011) assimilated remotely sensed soil moisture from ASCAT over France to improve discharge simulations. It was concluded that the assimilation of soil moisture mainly corrected for biases in precipitation or incorrect model climatology. However, the potential to improve flood forecasts was not studied at the large-scale. The previously mentioned studies mainly focussed on the potential gain for flood forecasting, when only observations from a single sensor are assimilated. This potential can be increased by making use of soil moisture retrieved by multiple sensors, thereby increasing the quality and quantity of the observations. However, the added value of combined assimilation of data from multiple sensors for operational flood forecasting at large-scale remains unknown. Moreover, it is equally important to take into account that assimilation of remotely sensed soil moisture can lead to significant difference in the parametrization of the hydrological model (e.g. Santanello et al., 2007; Sutanudjaja et al., 2014) and this will also impact the potential gain from the assimilation of observations of other hydrological variables. Additionally the added value of the remotely sensed soil moisture compared to the assimilation of discharge observations has not been studied so far. Therefore, more research is required, especially in large-scale catchments using conjunctively multi-sensor remotely sensed soil moisture observations and discharge data.

The aim of this study is to determine the benefits of the assimilation of multi-sensor soil moisture observations in operational flood forecasting systems in large scale catchments. To achieve this aim, this research focuses on three main research questions: (i) Does the assimilation of remotely sensed soil moisture lead to increased forecasting skills in terms of forecast uncertainty and forecast bias compared to assimilation of discharge observations? (ii) Does the assimilation of remotely sensed soil moisture increase the lead times at which floods can be accurately predicted? (iii) Is it possible to reduce the number of false flood alerts with the use of remotely sensed soil moisture? These research questions are answered using the EFAS model setup, which enables a proper validation of the results in the context of a real operational system. Results of assimilating remotely sensed soil moisture are compared with assimilation of discharge data only. Also, the impact of the number of discharge observations and the benefit of the assimilation of remotely sensed soil moisture for a model calibrated

on discharge are investigated. These analyses enable a more detailed evaluation of the potential gain of the assimilation of remotely sensed soil moisture for operational flood forecasting. As a test-basin the Upper Danube catchment is selected which is one of the largest catchments in Europe containing a large number of locations with time series of discharge. Satellite data from three microwave sensors (ASCAT, AMSR-E and SMOS) is used in the assimilation framework to increase the number of observations and the potential benefits of these observations for the flood prediction.

6.2 Material and Methods

6.2.1 Study area

The study area is the Upper Danube catchment upstream of Bratislava (catchment size $135 \cdot 10^3$ km^2, Figure 6.1). The border of the Upper Danube is formed by the Alps in the South and the catchment contains the northern part of Austria, the southern part of Germany, the South-eastern part of the Czech Republic and western Slovakia. Elevations range from 150 - 3150 m above sea level. In the catchment, daily discharge observations for 23 locations are available through the Global Runoff Data Centre (GRDC), which enable validation and assimilation (Figure 6.1). With a split-sample approach discharge observations used for assimilation will not be used for validation to assure an independent validation of the improvements in the flood forecasting after the assimilation.

6.2.2 European Flood Awareness System

The European Flood Awareness System was developed in 2003 by the European Commission at the Joint Research Centre in Ispra and is being improved since. In 2012 EFAS became an operational service aiming to provide flood forecasts up to 10 days in advance over the European continent (`www.efas.eu`). At the core of the EFAS system is the hydrological model LISFLOOD which was originally developed by De Roo et al. (2000), later improved by Van Der Knijff et al. (2010) and running in the PCRaster modelling environment (Wesseling et al., 1996; Karssenberg et al., 2010). LISFLOOD was specifically developed for discharge simulations of large scale river basins. The model consists of a vegetation layer, two layers to simulate the unsaturated zone, two linear reservoirs to represent fast and slow responding groundwater systems and a channel network for discharge routing.

In this study, the original two-layer representation of the unsaturated zone (De Roo et al., 2000; Van Der Knijff et al., 2010) was replaced by a new unsaturated zone model component that uses four layers (Figure 6.2). This enables a more detailed representation of the soil moisture in the topsoil and results in modelled soil moisture that is directly comparable to the soil moisture observations retrieved from remotely

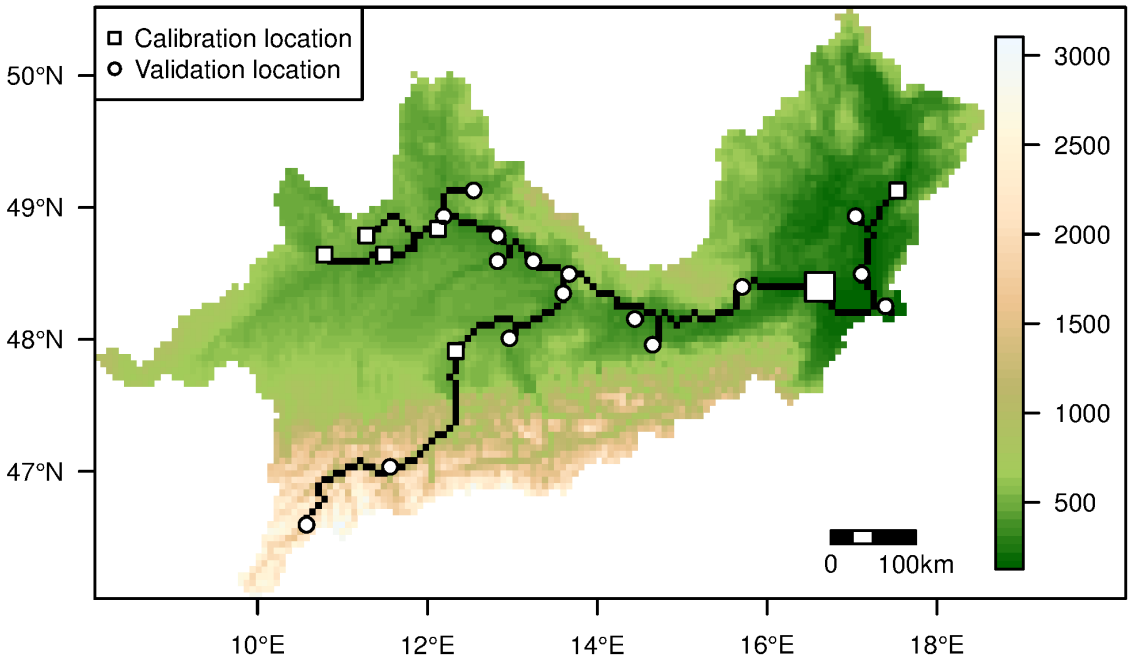

Figure 6.1 Digital elevation map of the Upper Danube catchment, colours indicate elevation (m), indicated in black is the river network, square symbols indicate locations for calibration on discharge observations, circles indicate locations for validation on discharge observations. The large square near the outlet (right) is the location used for calibration if only one discharge time series is used ($Q1$ and $Q1_{sat}$).

sensed soil moisture. The layers have been added in the topsoil and possess a depth equal to the typical penetration depth of microwave sensors. The new model set-up consists of unsaturated zone layers of 2 and 3 *cm* thick, respectively, the third layer represents the remaining part of the rooting depth (the topsoil, Figure 6.2). The root zone is simulated using the topsoil and evapotranspiration occurs from these layers. The evaporation for a particular layer is limited if soil moisture is below critical soil moisture conditions, in which case more water is extracted from the other soil moisture layers to compensate for the reduced evaporation. The abstraction per layer is linearly related to the total storage capacity of the layer. Thick layers will thus have a larger contribution to the evapotranspiration compared to thinner layers. When the entire root zone is below critical soil moisture conditions the evaporation is limited for the entire topsoil and actual evapotranspiration will be lower than potential evapotranspiration. Bare soil evapotranspiration occurs only from the first layer of 2 *cm*. Via capillary rise replenishment of the root zone can occur from the fourth unsaturated zone layer (the subsoil). The amount of capillary rise depends on the difference in hydraulic head between two layers and the average conductivity of the layers. The first layer will also largely impact the amount of surface runoff in the LISFLOOD model. The soil wetness of the first layer determines the infiltration

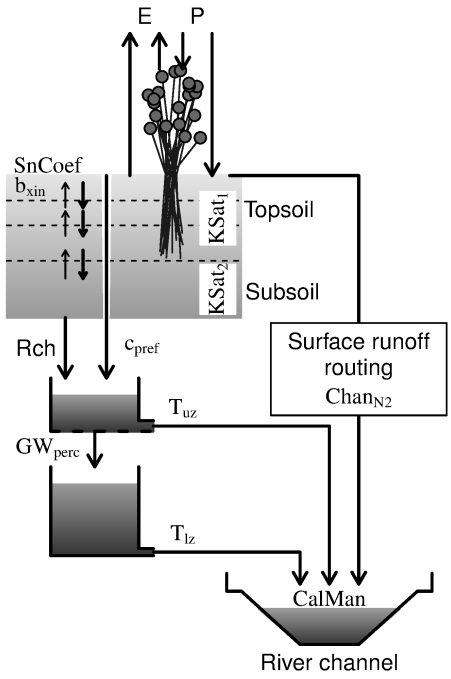

Figure 6.2 LISFLOOD model set-up, with fluxes; precipitation (P), evaporation (E), recharge from the unsaturated zone to the groundwater (Rch). The calibration parameters of the model are: snowmelt coefficient ($SnCoef$), Xinanjiang shape parameter (b_{xin}), saturated conductivity of the topsoil ($KSat_1$), saturated conductivity of the subsoil ($KSat_2$), empirical shape parameter preferential macro-pore flow (c_{pref}), maximum percolation rate from upper to lower groundwater (GW_{prec}), reservoir constant upper groundwater (T_{uz}), reservoir constant lower groundwater (T_{lz}), surface runoff roughness coefficient ($Chan_{N2}$), channel Mannings roughness coefficient ($CalMan$).

capacity of the unsaturated zone and when the infiltration capacity is exceeded by rainfall or snowmelt this will generate overland flow. Sub-daily time steps are included to enable a stable performance of the soil moisture simulation, where the number of sub-daily time steps is dependent on the amount of potential infiltration and water storage in the unsaturated zone.

In order to use the best calibrated model for the study area, the hydrological model LISFLOOD was calibrated for the Upper Danube. For the calibration, soil moisture and discharge observations were used to calibrate the most sensitive model parameters. The parameters which were calibrated were related to the snow accumulation, infiltration and percolation through the unsaturated zone, the groundwater system and routing of discharge (Figure 6.2). A dual state and parameter Ensemble Kalman filter was used to calibrate LISFLOOD for the Upper Danube. A total of 300 members was used to estimate all parameters of the model over the period 2010-2011. The period was selected because satellite data from multiple sensors is available for this period. This resulted in calibrated parameters with distributions defined by 300

realizations of parameter sets, which could be used for hydrological simulations. The use of these parameter distributions allows to account for the uncertainty in the initial conditions and for different hydrological responses to identical meteorological inputs. More detailed information on the probabilistic model calibration set-up can be found in Chapter 5.

The meteorological forcing of EFAS consists of daily precipitation, daily potential evapotranspiration and the average daily temperature. EFAS uses meteorological forcing from the 51 members of the European Centre for Medium-Range Weather Forecasting Ensemble Prediction System (ECMWF-EPS). This results in 51 hydrological forecasts for every 12 hours at midday and midnight. The new set-up of EFAS which uses 300 realizations of parameter sets, differs from the original EFAS set-up which uses one parameter set. Additionally, the new set-up also uses a set of initial hydrological conditions which are forced with identical meteorological forcing. The original EFAS set-up only uses one parameter set and one initial hydrological condition for all meteorological forecasts. The EFAS setup used here will allow accounting for the uncertainty in the initial conditions which can be an important factor in flood forecasting.

Throughout the manuscript the term EFAS will be used when talking about the entire forecasting system, i.e. the combination of meteorological forcing, hydrological model and resulting flood forecasts. The term LISFLOOD will be used when the focus is specifically on the data assimilation or the hydrological model.

6.2.3 Data

Satellite and discharge data

Remotely sensed soil moisture data from three satellites is used, namely SMOS, ASCAT and AMSR-E. A detailed description of the the satellite properties can be found in Section 5.2.3 of this thesis.

All satellite soil moisture products are used on an equal area Discrete Global Grid product (DGG). For the SMOS and ASCAT soil moisture product a DGG is available (Bartalis et al., 2006a), while for the AMSR-E product a DGG is not available. Therefore, the AMSR-E data was projected on the DGG of SMOS using the nearest neighbour approach, because both satellites have roughly the same spatial resolution. The DGG of ASCAT uses equally spaced areas of 12.5 km while the other DGG uses a slightly lower resolution of 15 km between points.

Although both SMOS and AMSR-E, give absolute soil moisture values in m^3m^{-3}, all satellite data was converted using a rescaling approach. This was done to prevent suboptimal data assimilation as a result of biases between the model and satellite dynamic range. These biases can reduce the quality of the data assimilation scheme

resulting in a poor model performance. Similar to Section 5.2.3, the converted satellite values $\theta_{s,new}$ in m^3m^{-3} used for assimilation are calculated by:

$$\theta_{s,new} = \frac{\theta_s - \theta_{s,5}}{\theta_{s,95} - \theta_{s,5}}(\theta_{FC} - \theta_{WP}) + \theta_{WP} \tag{6.1}$$

where θ_s are the observed satellite soil moisture values, $\theta_{s,95}$ and $\theta_{s,5}$ are the $95th$ and $5th$ percentiles of satellite soil moisture values respectively (-), θ_{FC} and θ_{WP} are field capacity and wilting point of the modelled soil moisture values (m^3m^{-3}). θ_{FC} and θ_{WP}, are dependent on the soil texture and are averaged over the spatial resolution of the satellite observation.

Discharge data

The Upper Danube catchment contains 23 locations where daily discharge observations are available (Figure 6.1). Time series of discharge are available from January 2000 until December 2011. Using a split sample approach the discharge of 7 stations was used for data assimilation into the forecasting system, while the other 16 stations were only used for validations of the forecasts. This approach is similar to the experimental set-up of Lee et al. (2012) and Rakovec et al. (2012), who used multiple interior discharge stations for validation and assimilation. Assimilation and validation stations are selected such that they are equally distributed over the catchment and are situated both in small rivers and the main Upper Danube river. This will allow to evaluate the impact of the data assimilation at different catchment sizes within the Upper Danube catchment.

6.2.4 Data assimilation

Identical to Chapter 5, the EnKF is applied to update state variables of the hydrological model. The LISFLOOD model is given by:

$$\Psi(t+1) = f(\Psi(t), F(t), p) \tag{6.2}$$

where f is the set of model equations, i.e. the model structure, representing the hydrological processes that lead to change in the system state over time, $\Psi(t)$ is the state of the model at time t, $F(t)$ the model forcing at time t (i.e. precipitation, evaporation and temperature) and p are the model parameters. The EnKF is applied on each daily time step using observations from remote sensing (when available, AMSR-E, SMOS and ASCAT) and discharge observations. If no observations of any kind are available no update will be performed. When only a limited number of observations are available these will be used to update the model. The general form of the EnKF (Evensen, 2003) is given by:

$$\Psi^a = \Psi^f + P^f H^T (H P^f H^T + R)^{-1} (Y - H\Psi^f) \tag{6.3}$$

where Ψ^a is the analysis of Ψ^f, the model forecast, P^f the error covariance matrix of the model, R is the measurement error covariance, H is the measurement operator which relates the model states Ψ to the satellite or discharge observations Y. The observations Y can be described by:

$$Y = H\Psi^t + \epsilon \tag{6.4}$$

where the true model state (Ψ^t) is transformed to the Y, using the measurement operator (H) and random noise ϵ with a zero mean and a measurement error. The state error covariance matrix of the model prediction is calculated from the ensemble spread:

$$P^f = \overline{(\Psi^f - \Psi^t)(\Psi^f - \Psi^t)^T} \tag{6.5}$$

where Ψ is the model state vector and the superscripts f and t represent the forecast and true state, respectively. Since the true state is not known it is assumed that:

$$P^f \approx P_e^f = \overline{(\Psi^f - \overline{\Psi^f})(\Psi^f - \overline{\Psi^f})^T} \tag{6.6}$$

where $\overline{\Psi^f}$ represents the ensemble average and it is assumed that the ensemble of model simulations is sufficient to represent the true state. The EnKF is implemented in the PCRaster modelling environment (Karssenberg et al., 2010).

For the assimilation of the satellite data with the Ensemble Kalman Filter (EnKF), spatial information on the measurement error covariance (R, Equation 6.3 and 6.4) is required. The structure of R is determined from estimates of Chapter 2 over Spain, obtained by using high resolution modelling of the unsaturated zone. From this study the errors of each satellite product were determined (diagonal terms of R) as well as the spatial correlation of the errors of the satellites and the covariance between the errors of different sensors (off-diagonal terms of R).

All observations are assimilated as daily averages, since this is the same temporal resolution as the meteorological forcing. Following Di Baldassarre and Montanari (2009), the error covariance between the discharge observations is set to zero with a 30% error on the discharge observations. No covariance is assumed between the satellite soil moisture and discharge observations..

6.2.5 Assimilation and ensemble hindcasting

In this study, observed satellite and discharge data for December 2010 - November 2011 are used in a hindcasting experiment for the Upper Danube. Only one year was selected to test the procedure since all satellite products are available for this time period with sufficient data quality. After the selected time period the AMSR-E sensor was shut down and before the selected period the quality of the SMOS observations was still below the potential maximum quality due to RFI contamination.

A data assimilation procedure was used to create a reanalysis time series of all state variables which are used as starting point for the hindcast (t_0). Model states are updated with the observations and used to have a better estimate of initial conditions at t_0. Figure 6.3 provides a flowchart that shows the full hindcasting procedure described below. The 300 parameter realizations from the probabilistic calibration were used to generate the reanalysis time series. As meteorological forcing for the analysis, observed time series of daily precipitation, daily potential evapotranspiration and the average daily temperature were used. Observations are interpolated between meteorological stations with an inverse distance interpolation. For every time step up till t_0, observed state variables, remotely sensed soil moisture and/or discharge (depending on the scenario), are assimilated into the model. Assimilation is done on a daily time step, since information on the exact time of the discharge observations is largely unknown. Additionally, the model uses meteorological input with a temporal resolution of one day. Parameters are not updated in the assimilation. Thus, the same set of 300 parameter sets is used to generate the 300 ensemble members between analysis steps with the EnKF.

At t_0, the start of the hindcast, the forward model (Equation 6.2) is used for the hindcasting of discharge and other state variables. After t_0, the daily forcing from the ECMWF-EPS is used to drive the model simulation. The hindcast is evaluated based on the observed discharge for the hindcasting period. Like in EFAS, hindcasts are done at midday and midnight based on the latest simulations of the ECMWF-EPS leading to a total of 730 hindcasts. In the original forecasts from EFAS only one set of initial conditions is used, thereby neglecting the uncertainty in the initial conditions. In this experiment, 300 possible realizations of the initial conditions are available from the reanalysis. For each hindcast the 51 members of the ECMWF-EPS are used twice with random realizations from the 300 members of the reanalysis to create $n = 102$ realizations per hindcast. In this approach different meteorological forcing and initial conditions are used for each hindcast to have a better estimate of the forecast uncertainty. A four month simulation was performed using all 300 members in combination with all 51 meteorological forecasts. An analysis of the probability density functions of each hindcast showed that a total of 102 realizations showed no significant differences with a simulation consisting using all possible ($51 \times 300 = 15300$) realizations (for lead times up to 10 days). The significance was tested with a non-parametric Kolmogorov-Smirnoff test, which showed that distributions created with 102 realizations and 15300 realizations are identical ($p = 0.05$). In another set of runs, it was shown that using fixed initial conditions for the hydrological state leads to significantly different distributions. The same holds for fixing the meteorological forecast for all 300 ensemble members which results in a significantly different probability density function compared to the run created with 15300 realizations. With this exercise it is concluded that both the uncertainty in initial states as well as the forcing uncertainty need to be taken into account, but that it suffices to use a subset of the possible realizations to model this joint uncertainty. Hence, to reduce calculation times 102 realizations per hindcast were used in all scenarios. Calculation times

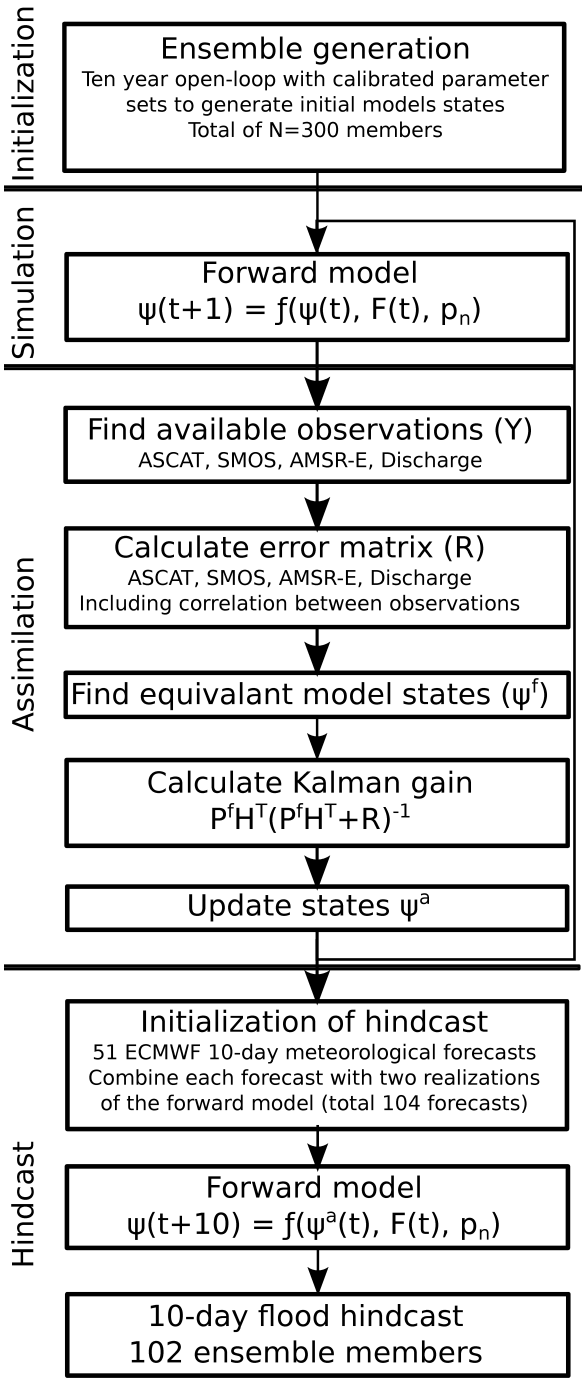

Figure 6.3 Flowchart of the hindcasting procedure including initialization of the model and the construction of the reanalysis time series.

Table 6.1 Hindcasting scenarios for the EFAS system including abbreviations and assimilated data used to create a re-analysis time series from which hindcasts were initiated. The calibration indicates the data used in Chapter 5 to calibrate the hydrological model.

	Hindcast		Calibration
Scenario	# of discharge stations	Satellite data	Data for calibration
$Q0$	0 stations	None	None, expert knowledge
$Q0_{sat}$	0 stations	All satellite data	Satellite data
$Q1$	1 stations	None	1 discharge observation
$Q1_{sat}$	1 stations	All satellite data	1 discharge station & satellite data
$Q7$	7 stations	None	7 discharge stations
$Q7_{sat}$	7 stations	All satellite data	7 discharge stations & satellite data
$Q7_{noDA}$	None	None	7 discharge stations
$Q7_{satDA}$	None	All satellite data	7 discharge stations

for this new assimilation system are low. For a 10-day forecast with 102 members for the Upper Danube the required calculation time is 120 seconds on a 8-core machine with 2.26 GHz processors and 24 GB RAM.

6.2.6 Scenarios

The different scenarios used are given in Table 6.1 as well as the data used in the assimilation before the hindcasting was done. The parametrization was calibrated for the Upper Danube for the period 2010-2011 and was used to create analysis time series for each scenario. The calibration was based on the observations available for the reanalysis, so if both discharge and satellite data were available these were also used for the calibration of the hydrological model (Table 6.1).

Two additional scenarios have been included (bottom half of Table 6.1) to show the performance of the hindcasts in case of limited or no data availability. Both scenarios have been calibrated on discharge and use assimilation of satellite observations or no data.

6.2.7 Evaluation

The evaluation of each hindcast was done based on coefficient of variation (COV), Continuous Ranked Probability Score ($CRPS$, Hersbach, 2000), Mean Absolute Error (MAE), Brier Score (BS, Brier, 1950) and the number of false and true positive

flood alerts. These scores were calculated for each lead time separately to evaluate the quality of the hindcast for different lead times.

To assess the spread of the ensemble of simulated discharges, the coefficient of variation was determined with:

$$COV = \frac{1}{T}\sum_{t=1}^{T}\frac{\sigma_{Q_{mod}(t)}}{\overline{Q_{mod}(t)}} \tag{6.7}$$

where $\sigma_{Q_{mod}(t)}$ and $\overline{Q_{mod}(t)}(m^3d^{-1})$ are the standard deviation and the mean of the ensemble of modelled discharge at time t, respectively, and T is the number of time steps (days) in the reanalysis period.

The $CRPS$ (Hersbach, 2000) was used to calculate whether the uncertainty of the forecast is correct and not over- or underestimated. The $CRPS$ is given by:

$$CRPS = \frac{1}{T*N}\sum_{t=1}^{T}\sum_{n=1}^{N}\int_{x=-\infty}^{x=\infty}(CDF_n^f(x,t) - CDF_n^o(x,t))^2 dx \tag{6.8}$$

where $CDF_i^f(x,t)$ is the cumulative density function of the hindcast at time t for ensemble member n, $CDF_i^o(x,t)$ is the cumulative density function of the observation at time t for ensemble member n. $CDF_i^o(x,t)$ is given by a Heaviside function, with a step from 0 to 1 probability at the observed value. The $CRPS$ is standardized by $\overline{Q_{obs}}$ for each validation location to enable a comparison between stations with a different magnitude of discharge.

To calculate if the hindcasts were biased the MAE was calculated using the ensemble mean of the forecast. The MAE is given by:

$$MAE = \frac{1}{T}\sum_{t=1}^{T}\frac{|\overline{Q_{mod}(t)} - Q_{obs}(t)|}{\overline{Q_{obs}}} \tag{6.9}$$

where $\overline{Q_{mod}(t)}$ and $Q_{obs}(t)$ (m^3d^{-1}) are the average hindcasted discharge and observed discharge at time t, respectively, and $\overline{Q_{obs}}$ is the average discharge over the evaluation period. COV, $CRPS$ and MAE were used to evaluate the performance of each scenario and to determine the quality of each hindcasting scenario. Scores were standardized to enable a comparison between upstream and downstream stations without correcting for differences in discharge volumes. In addition, these scores were determined per lead time separately to enable a better comparison between the different scenarios and also to determine the flood forecasting performance of EFAS for different lead times.

To test the accuracy of the flood alerts (both timing and height of the flood peak), the Brier score is calculated for different flood thresholds and different lead times. The Brier score was calculated by:

$$BS = \frac{1}{T}\sum_{t=1}^{T}(sgn(Q_{mod}(t)) - sgn(Q_{obs}(t))) \tag{6.10}$$

where $sgn(Q_{mod}(t))$ and $sgn(Q_{obs}(t))$ are binary values indicating flood event (1) or no flood event (0) for model and observation, respectively. The Brier score can be calculated for different thresholds of discharge and different lead times. In this study two threshold levels were used, namely the 80^{th} and 90^{th} percentile of the discharge (Q_{80}, Q_{90}). Exceedance of these arbitrary levels will not necessarily cause flood situations, however to allow for evaluation of hindcasts these high discharge events were used. Furthermore the number of false positives (flood forecast, no flood observed), missed events (no flood forecasted, flood observed) and correctly forecasted (flood forecasted, flood observed) were calculated for each hindcasting scenario for the Q_{80} and Q_{90}. This resulted in 1035 and 2070 time steps with floods exceeding Q_{90} and Q_{80} respectively divided over 10 to 18 flood events on average over the 16 validation locations.

6.3 Results

6.3.1 Reanalysis

To analyse the performance of the reanalysis the COV (Equation 6.7) is used to determine the uncertainty after the assimilation of the observations (Figure 6.4 and Table 6.2). In the $Q0$ scenario, the model is not calibrated and no data is assimilated into the reanalysis to correct for incorrect model states. The uncertainty in the model simulation is large with a COV of 0.25. Uncertainty even increases during extreme flood events, reducing the potential to use a model calibrated on expert knowledge without data assimilation for flood forecasting. The assimilation of three different satellite products ($Q0_{sat}$) results in a reduction of the COV of the discharge simulation to 0.136 compared to 0.25 for $Q0$ (Figure 6.4). This reduction is caused by the assimilation procedure, which constrains the model to follow the observations and hence the spread between ensemble members is reduced. Soil moisture observations do not contain information on groundwater and routing processes, hence they impact the discharge simulation only indirectly via surface runoff and percolation to the groundwater from the unsaturated zone. This results in the fact that the discharge simulations are not necessarily improved by assimilation of remotely sensed soil moisture observations.

Two scenarios were created where only discharge is assimilated into the model, namely $Q1$ and $Q7$. For $Q1$ only discharge from the outlet was used and for $Q7$, additional discharge observations (Figure 6.1) upstream were assimilated into the model. The assimilation of additional observation data reduces the COV to 0.08 for $Q1$ and to 0.04 for $Q7$, which is for both scenarios lower than for $Q0$ (Table 6.2). $Q1$ shows a small positive bias in the selected time period compared to the discharge observations. However, on average the bias does not exist for the entire entire simulation period and no systematic bias exists between the simulation and the observations.

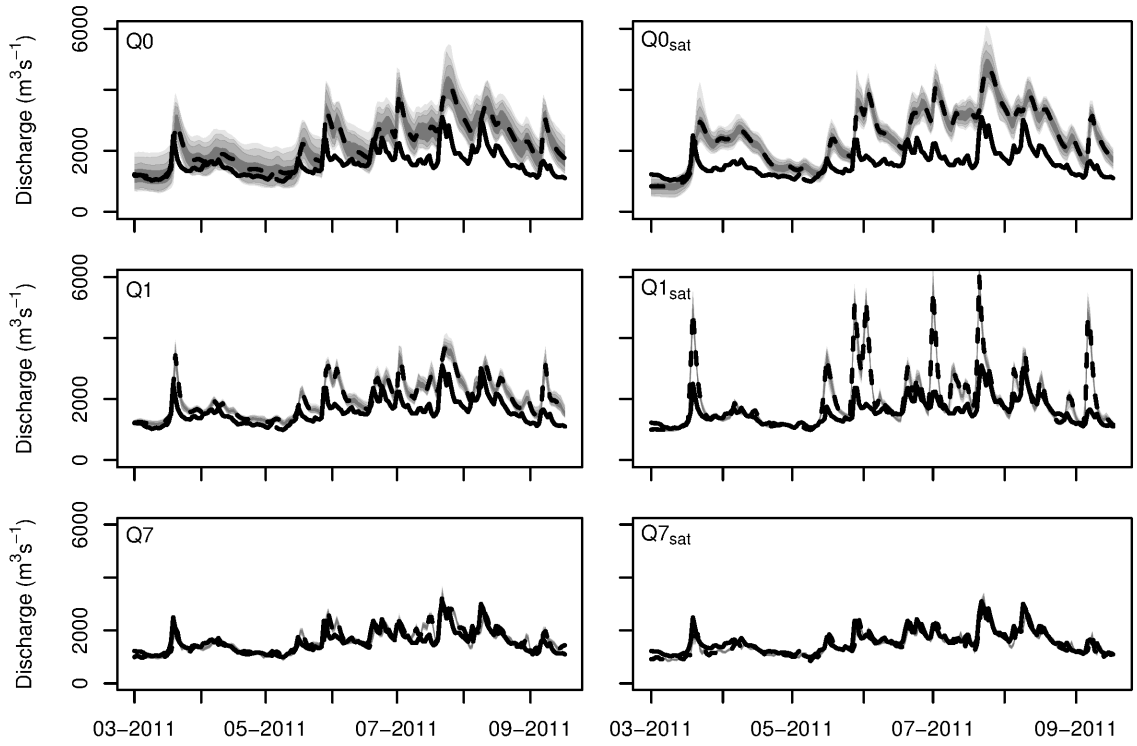

Figure 6.4 Reanalysis time series of discharge at the outlet of the Upper Danube catchment (Figure 6.1) for part of the hindcasting period. In grey are all model realizations, the ensemble mean is given by the dotten black line and the solid black line gives the observed discharge value. The different assimilation scenarios are indicated on the left; for explanation of scenarios see Table 6.1. The different assimilation scenarios are indicated in the top left corner of each plot.

Finally, two scenarios where both discharge and remotely sensed soil moisture observations are assimilated into the model ($Q1_{sat}$ and $Q7_{sat}$) were evaluated. In these scenarios the uncertainty is reduced compared to most other scenarios. However, peak discharge for $Q1_{sat}$ is overestimated, while baseflow simulations are better compared to $Q1$. Improved simulations are also observed with $Q7_{sat}$ compared to $Q7$ and the problem with overestimated peak discharge is gone $Q7_{sat}$ (Figure 6.4). An example time series is provided to show the impact of the satellite observations in the $Q7_{sat}$ scenario (Figure 6.5).

It must be mentioned that additional discharge data has a larger impact on the reduction of the uncertainty, than assimilation of remotely sensed soil moisture. Remotely sensed soil moisture enables a better simulation of the base flow compared to assimilation of discharge observations only. The reduction in uncertainty of the discharge simulations with the assimilation of remotely sensed soil moisture shows that this

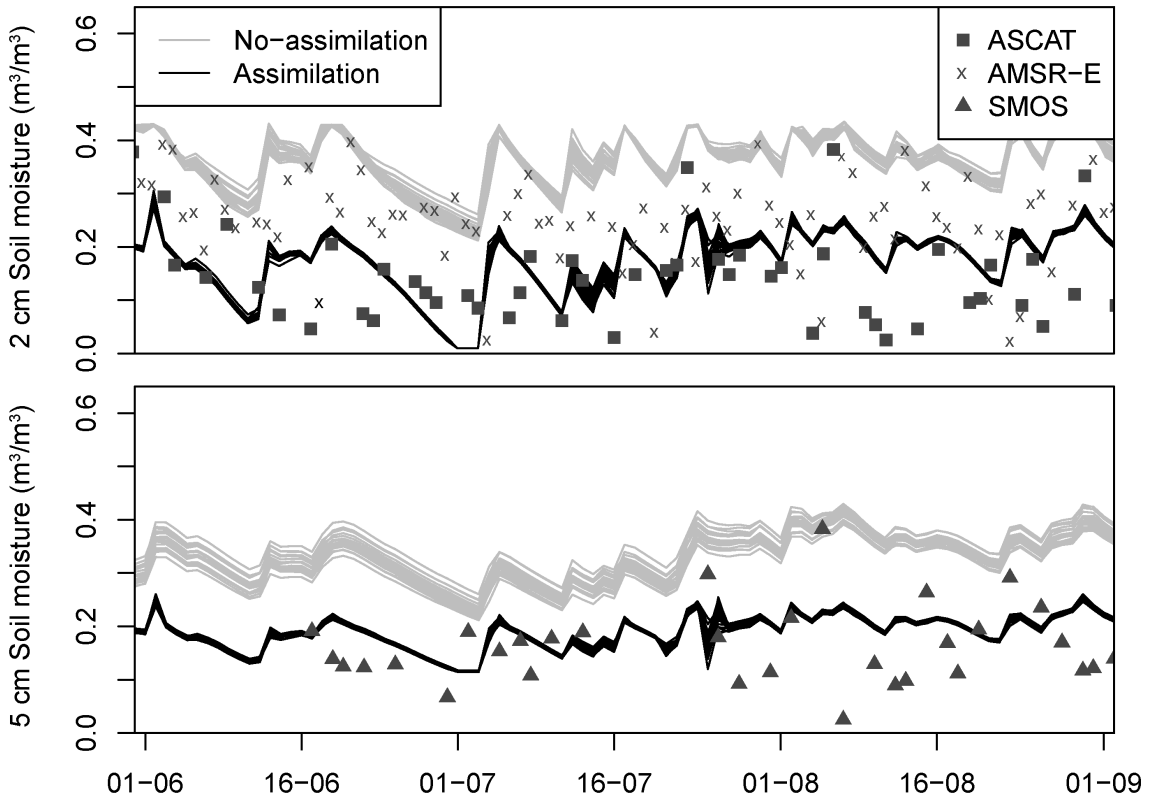

Figure 6.5 Example time series (14°E, 48°N) of simulated soil moisture for $0-2$ *cm* (upper panel) and the simulated soil moisture for $0-5$ *cm* (lower panel) for the analysis period, $Q7_{sat}$ scenario. Observations of remotely sensed soil moisture are shown from three different sensors. Jumps in the time series at assimilation moments indicate the update of model states according to the observations.

method has a high potential in sparsely gauged river basins to reduce uncertainties in simulate discharges.

6.3.2 Hindcasting performance

The hindcast performance of each scenario was evaluated using the $CRPS$ (Equation 6.8) and the MAE (Equation 6.9). In general the uncertainty in the hindcast is reduced when more data is assimilated into the system, leading to a better hindcast simulation (Figure 6.6). When more discharge data is assimilated, the uncertainty is more strongly reduced than with the assimilation of only remotely sensed soil moisture data (Figure 6.4 and 6.6). This is also confirmed by the $CRPS$ score for the different scenarios (Figure 6.7), where the decrease in $CRPS$ is strongest when more discharge data is used (Table 6.2). In general the $CRPS$ increases with increasing lead times for all scenarios with the exception of $Q1_{sat}$. Due to the larger spread for longer lead

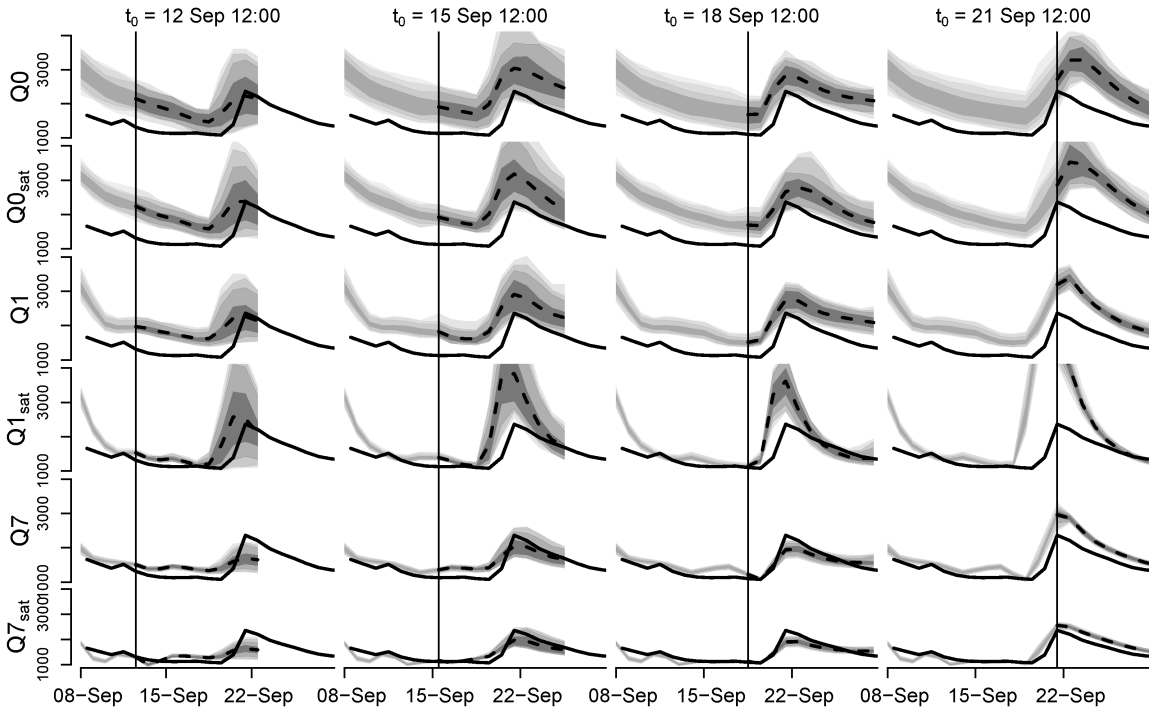

Figure 6.6 Example forecast time series of discharge at the outlet of the Upper Danube catchment (Figure 6.1) for part of the hindcasting period. In grey are all model realizations, the ensemble mean is given by the dashed line and solid black line gives the observed discharge value. Each column of figures gives the hindcast for a particular time, indicated by the vertical line.

times (Figure 6.6) the $CRPS$ will increase, because forecasts with high uncertainty are penalized. The $CRPS$ for $Q1_{sat}$ is the highest, indicating that this scenario has the lowest hindcasting skill of all scenarios (Figure 6.7 and Table 6.2). This is caused by the overestimation of most flood events, which results in a high $CRPS$. When more discharge data is assimilated ($Q0$ compared to $Q1$ and $Q7$) the $CRPS$ is reduced throughout the catchment for most locations including the outlet near Bratislava. When a combination of discharge data and satellite data is assimilated ($Q7_{sat}$), the quality of the hindcast is highest (Figure 6.6).

The MAE (Equation 6.9) is calculated for all scenarios for different lead times and locations (Figure 6.8). Compared to the scenario without assimilation of observations ($Q0$), only the scenarios where multiple discharge stations are assimilated ($Q7$ and $Q7_{sat}$) show an increase in performance. The best performance is generated by $Q7_{sat}$, which shows a low bias compared to the observed discharge. For $Q1_{sat}$ the MAE is relatively low, especially when compared to the $CRPS$. This is mainly caused by the accurate discharge simulation in base flow periods, resulting in a low MAE.

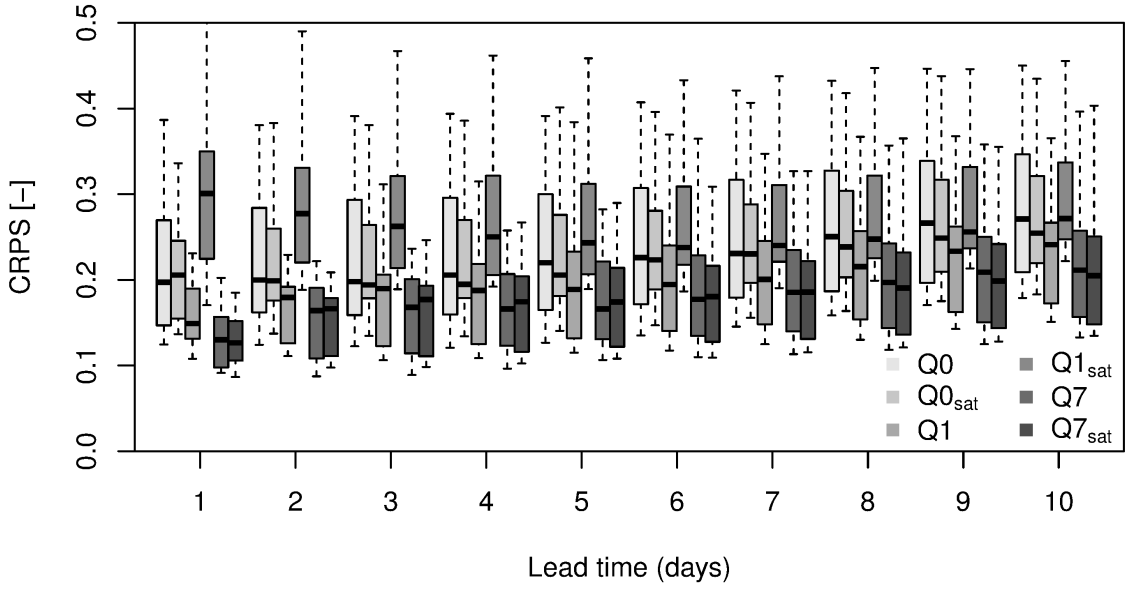

Figure 6.7 Continuous Ranked Probability Scores ($CRPS$) for different forecasting times for the European Awareness Flood System (EFAS). Each box only contains the $CRPS$ for the 16 validation locations for a period of 1 year with two forecasts per day.

Table 6.2 Average skill scores for different hindcast scenarios for the EFAS system. Scores are averaged over different forecasting times and for different locations with discharge observations in the Upper Danube (Figure 6.1).

Scenario	COV	$CRPS$	MAE	$BS\ Q_{90}$	$BS\ Q_{80}$
$Q0$	0.272	0.328	0.620	0.130	0.257
$Q0_{sat}$	0.161	0.252	0.791	0.220	0.363
$Q1$	0.084	0.203	0.702	0.168	0.314
$Q1_{sat}$	0.075	0.306	0.508	0.084	0.177
$Q7$	0.049	0.186	0.382	0.038	0.166
$Q7_{sat}$	0.047	0.182	0.309	0.029	0.096
$Q7_{noDA}$	0.055	0.187	0.385	0.042	0.173
$Q7_{satDA}$	0.053	0.183	0.384	0.040	0.160

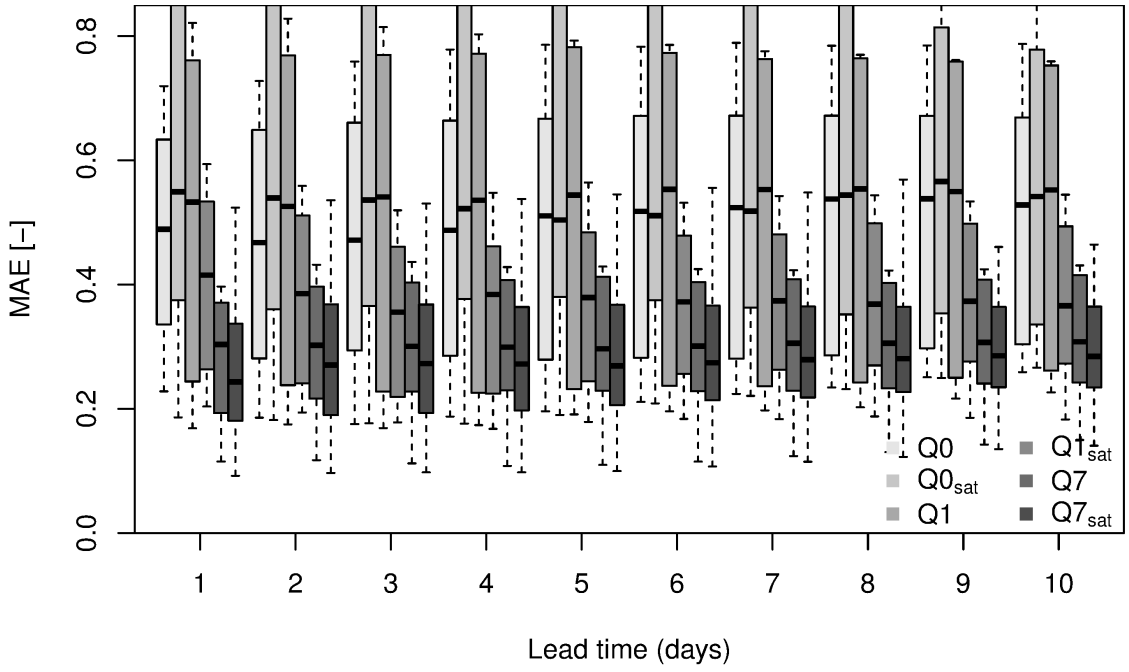

Figure 6.8 Mean Absolute Error (MAE) for different forecasting times for the European Awareness Flood System (EFAS). MAE is standardized by dividing the MAE through the mean discharge. Each box only contains the MAE for the 16 validation locations for a period of 1 year with two forecasts per day.

6.3.3 Flood hindcasting skill

The performance of each scenario was evaluated using the BS (Equation 6.10) and the number of false positive flood alerts. Due to the large spread within the ensemble the $Q0$ in general has a low forecasting skill (Table 6.2). This is shown by the relatively high BS (Figure 6.9) and the large number of false positive forecasts (Figure 6.10). Almost all flood events are correctly captured also for long lead times, which is caused by the overestimation of discharge in general (Figure 6.6). The overestimation of discharge also causes the high number of false positive flood forecasts, where around 90% of the exceedances of the threshold are incorrect and no flooding occurs. Compared to $Q0$ the forecasting skill for $Q0_{sat}$ is decreased, shown by an increasing BS and a higher number of false positives. The high number of false positives is the result of an even higher overestimation of the peak discharge in this scenario (Figure 6.6), which results in false flood alerts. The number of missed and correctly forecasted floods remains the same. The BS and the number of false positives for $Q1$ and $Q7$ is considerably lower than for $Q0$. $Q7$ also has a better hindcast skill than the $Q1$ caused by the increased number of observations used in the assimilation framework. The improved forecasting skill is also found in the BS for both $Q1_{sat}$ and $Q7_{sat}$ (Figure 6.9), which are for both scenarios lower than without the assimilation of remotely sensed soil moisture. For $Q1_{sat}$ this is mainly caused by an increased

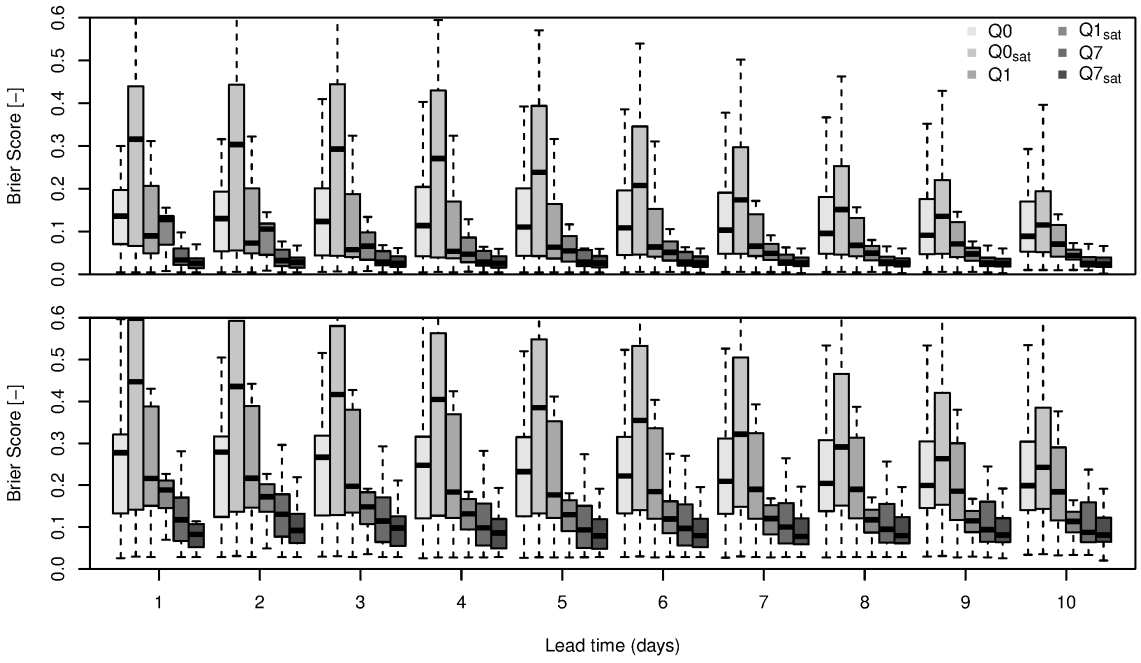

Figure 6.9 Brier Score (BS) for different forecasting times for the European Flood Awareness System (EFAS) in the Upper Danube (Figure 6.1). Each box only contains the BS for the 16 validation locations for a period of 1 year with two forecasts per day. The Brier scores for the 90% threshold (top) and the 80% threshold (bottom) are given. A total of 1035 and 2070 time steps (90^{th} and 80^{th} percentile, respectively) with flooding were observed for the Upper Danube

performance in the upstream areas of the catchment, while $Q7_{sat}$ shows an improved performance throughout the catchment. The number of false positive flood forecasts is reduced by 70% compared to the scenarios with only discharge assimilation, while the number of missed and correctly forecasted floods remains the same. This leads to the conclusion that even when the simulation of discharge throughout the catchment is used and discharge simulations are of a high quality, adding satellite data will lead to an improvement in the forecasting skills of the hydrological model.

6.3.4 Hindcasting performance with limited assimilation

Two additional scenarios have been evaluated were the model was calibrated on discharge observations alone and either remotely sensed soil moisture is assimilated ($Q7_{satDA}$) or no observations are assimilated ($Q7_{noDA}$) in the reanalysis period (Table 6.2). The reanalysis for $Q7_{noDA}$ shows the largest spread in the reanalysis (indicated by a large COV), while with the assimilation of remotely sensed soil moisture ($Q7_{satDA}$) this uncertainty is reduced. However, the uncertainties remain larger than for scenarios $Q7$ and $Q7_{sat}$, where in both cases discharge data has been assimilated.

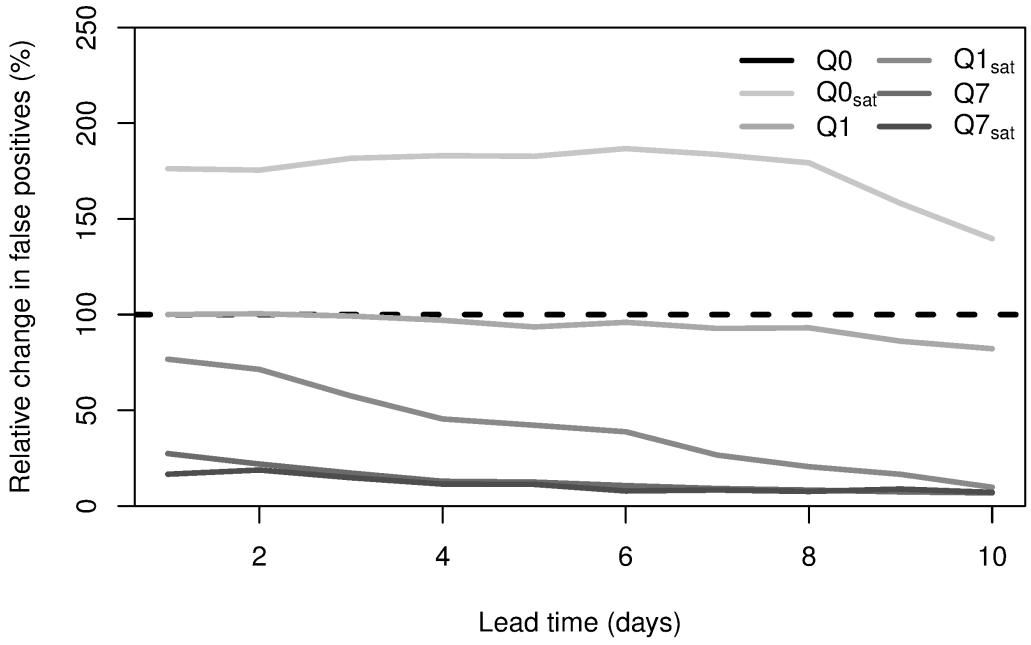

Figure 6.10 Relative changes in false positive flood alerts for the 90^{th} percentile threshold, compared to no assimilation scenario ($Q0$) for different forecasting times. A total of 1035 time steps with flooding were observed for the Upper Danube.

The uncertainty in the hindcasting performance ($CRPS$) is reduced for $Q7_{satDA}$ compared to $Q7$ and almost equal to joint assimilation of discharge and soil moisture ($Q7_sat$). This indicates that the more accurate representation of the soil moisture will reduce the uncertainty in model simulations and hence hindcasts. For both $Q7_{noDA}$ and $Q7_{satDA}$ the MAE does not show an increased performance, indicating that the bias is not reduced compared to $Q7$ nor $Q7_{sat}$.

As expected, the hindcast skills scores (BS) are reduced when the satellite data is used in the assimilation compared to no assimilation. Compared to $Q7$ and $Q7_{sat}$ the hindcast skill for the extreme events are not increased. However, compared to $Q7$ and $Q7_{noDA}$ the assimilation of satellite data ($Q7_{satDA}$ and $Q7_{sat}$) will increase the hindcast skill for the less severe floods (BSQ_{80}).

In general, the assimilation of remotely sensed soil moisture will increase the simulation of discharge. However, the discharge simulation performance for the extreme events is less impacted by the assimilation of soil moisture observations. The assimilation of soil moisture observations results in a better estimate of the initial soil moisture conditions and estimate of discharge ($CRPS$), mainly for the intermediate discharge rates. In extreme events with high precipitation totals the relative importance of pre-storm soil moisture conditions is reduced. Assimilation of discharge has the largest impact on the uncertainty in the hindcast, which will have an impact

on the ensemble spread. Joint assimilation of soil moisture and discharge observations, combining the advantages of both types observations, leads to improved initial conditions and consequently high hindcasting skills, especially for the extreme events (BSQ_{90}). The low uncertainty as a result of discharge assimilation with the improved estimate on the soil moisture state in the catchment leads to increased hindcasting performance.

6.4 Conclusions

In this study the added value of remotely sensed soil moisture in an operational flood forecasting system was evaluated. The gain from assimilation of soil moisture observations is compared to assimilation of only discharge and the combination of discharge and soil moisture observations. EFAS was used for a hindcasting experiment in the Upper Danube. Hindcasts were made for a period of one year and the results compared for six different scenarios.

The assimilation of remotely sensed soil moisture has an impact on the simulation of discharge, as shown by other studies (e.g. Pauwels et al., 2001; Brocca et al., 2010, 2012; Draper et al., 2011). However, in this study the impact is not only limited to small catchments with a spatial extent close to or smaller than the satellite resolution but also works for larger catchments.

We show that the assimilation of remotely sensed soil moisture improves the flood forecasting, especially when used in combination with assimilation of distributed discharge observations. The uncertainty in the discharge simulations is reduced and biases in the simulation are reduced when satellite data is assimilated. In scenarios where only discharge from the outlet is used in combination with satellite observations, the peak discharges are generally overestimated. Although this will result in a less accurate simulation of discharge it will not impact the quality of the forecasting of the flood events.

Floods are better predicted when soil moisture data is assimilated into EFAS in combination with discharge observations. The number of false alerts is reduced compared to scenarios when remotely sensed soil moisture observations are not used. Although the gain of using more discharge observations remains larger, soil moisture observations improve the quality of the flood alerts, both in terms of timing and in the exact height of the flood peak.

Two additional scenarios were studied, where only calibration of the hydrological model was used and no assimilation or assimilation of only satellite data. These scenarios were created to study the added value of the assimilation compared to only calibration of the hydrological model. It was found that the COV, $CRPS$, MAE and BS are all reduced by the assimilation of remotely sensed soil moisture compared to

no assimilation. However, assimilation of discharge reduces uncertainties more than assimilation of remotely sensed soil moisture. Simulations without data assimilation tend to have biases in the simulation and a larger ensemble spread than scenarios with data assimilation, while the reduced uncertainty resulting from assimilation will lead to a increased reliability of flood forecasts. These results show that the assimilation of soil moisture will result in an increased performance compared to not assimilating observations. This is important for ungauged basins, where satellite data is available and discharge observations are not available or not available in near-real time. Additionally these results show the added value of assimilation of observations into the EFAS system, compared to the current set-up.

In conclusion, the uncertainty in the flood forecasts is reduced when discharge observations and satellite data are assimilated into the hydrological model of the EFAS system for the Upper Danube. The addition of remotely sensed soil moisture to existing discharge observations reduces the number of false positive flood alerts and thereby increases the reliability of the flood awareness system. Although the number of the data available via satellite retrievals still remains a challenge in an operational system, the potential benefits could lead to a significant reduction in the false flood alerts, possibly also for other catchments. This will reduce the number of unnecessary precautions taken by the responsible governments and increase the confidence and willingness to act upon these flood alerts.

Acknowledgements

EU-JRC is acknowledged for being able to work with the Danube model set-up. GRDC and ECMWF are acknowledged making their data publicly available. Jutta Thielen is acknowledged for her constructive review of the manuscript.

Part II

Assessment of drought definitions

7 Comparison of frequently used drought indicators

This chapter is based on:
Wanders, N., van Loon, A. F., van Lanen, H. A. J. (2014), Uncover the real drought, Geophysical Research Letters, under review.

Abstract

Drought is caused by a prolonged deficit in available water and has a major impact on natural and social resources. Possible impacts of drought are crop losses, famine, fatalities, power black outs and degraded ecosystems. These severe socio-economic impacts show the need to carefully monitor drought conditions using the appropriate drought indicators. The indicators should consider differences in drought-generating processes resulting in drought in different domains of the terrestrial water cycle. The objective of this study is to determine which indicators can be used for monitoring drought in each domain of the terrestrial water cycle. A selection of frequently used indicators for different drought types (e.g. SPI for different accumulation periods, PDSI, threshold approach) was used to investigate their potential to monitor drought on a global scale. Correlations (r) between indicators were calculated for the major climates and for the whole globe to quantify the unique information content of each indicator and their interchangeability to be used for different drought types. It was found that indicators used for precipitation drought show low correlations ($r = 0.1 - 0.65$), although most of them are calculated in a similar way (e.g. SPI-1 and SPI-3). Indicators for soil moisture drought show even lower similarity ($r = 0.25$), while indicators for streamflow drought show the highest correlation ($r = 0.5 - 0.95$). Additionally, meteorological drought indicators are not capable to correctly describe soil moisture drought ($r = 0.0 - 0.7$) nor streamflow drought ($r = 0.0 - 0.75$). These findings have implications for drought monitoring systems: (i) for each drought type, which is associated with one or more impacted sectors, a different indicator should carefully be identified; (ii) drought indicators that are designed to monitor the same drought type (e.g. meteorological) should also be carefully identified because these show large discrepencies in their anomalies and hence drought detection. Correlation between drought indicators also depends on climate type. In particular snow-dominated climates need indicators that address snow accumulation and melting. In addition, studies on trends in drought or projections of future drought should be specific on the drought type to reduce the current confusion in how drought has developed or will develop.

7.1 Introduction

Drought is caused by a prolonged deficit in the available water and has a major impact on both natural and societal hydrological resources (Wilhite, 2000; Tallaksen and Van Lanen, 2004; Mishra and Singh, 2010; Sheffield and Wood, 2011). Due to the large spatial and long temporal extent of drought events, they tend to have a large economic damage, e.g. $2.2 billion for the still ongoing California drought (2014) in the United States alone (Howitt et al., 2014). This drought is caused by lack of precipitation in three consecutive years, leading to a significant reduction of the water levels in some of the major rivers and reservoirs affecting shipping and energy production. Agriculture is even more heavily impacted resulting in job loss for thousands of agricultural workers. A similar situation occurred in the United Kingdom in 2012. Due to very low rainfall in the winter of 2011/2012 most reservoirs were not replenished by spring 2012 leading to restrictions on water use (Marsh and Parry, 2012).

These examples clearly show that drought can affect all domains of the hydrological cycle and can mitigate from on impacted sector to another. Three major drought types that refer to different parts of the hydrological cycle are identified, namely, meteorological, soil moisture/agricultural and hydrological drought. Depending on the type of drought the impacts on society and nature are different (Figure 7.1). This emphasizes the need to monitor drought throughout the hydrological cycle, to be able to pro-actively respond to possible impacts. To facilitate the monitoring of drought, indicators are used to monitor and determine the severity of drought events.

Most drought indicators aim to subtract the normal seasonal variation in water availability or water state from the climatological variations and thereby quantify extreme events and thus drought. However, the large number of different drought indicators (e.g. Keyantash and Dracup, 2002) results in uncertainty of which indicators could be used under which circumstances and for what purpose. It is obvious that this will lead to confusion about which indicator to use for which impact. Expert knowledge is required to monitor drought with the correct indicators. Mostly, the focus of drought monitoring is put on precipitation and soil moisture drought, while the impact of drought on various sectors goes beyond these domains of the hydrological cycle (Figure 7.1). The World Meteorological Organization advices to the use one single drought indicator that derives drought conditions from anomalies in precipitation (World Meteorological Organization, 2009). However, an important unknown remains if one single indicator would suffice to monitor drought conditions relevant to all possible impacted sectors. Which indicator would fullfill this goal and would this indicator provide valuable information on drought conditions for all relevant potential impacted sectors (Figure 7.1).

The objective of this study is to investigate: (i) intrachangeability of drought indicators used for different drought types (ii) interchangeability of drought indicators

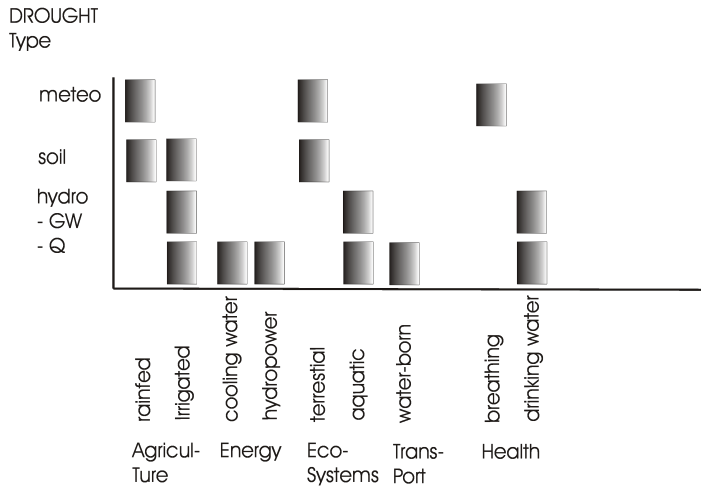

Figure 7.1 Different types of drought and their impact on society and nature.

used for the same drought type (iii) dependency of this intrachangeability and interchangeability on climatology. A conceptual hydrological model was used to simulate time series of hydrological variables to determine different drought indicators. Time series of these indicators were compared on a global scale.

7.2 Material and Methods

7.2.1 Hydrological model

A conceptual hydrological model (Van Lanen et al., 2013) was used to simulate the catchment response to meteorological forcing. The model was used to simulate the hydrological cycle at a global scale with a resolution of 0.5° for the period 1958-2002. The model incorporates snow, soil moisture and groundwater modules that enable the simulation of the hydrological response of the 0.5° grid cell. Using a lumped approach, the model generates time series of snow accumulation, soil moisture, groundwater and discharge. The precipitation, temperature and potential evapotranspiration data that are required as forcing were derived from the WATCH reanalysis dataset (Weedon et al., 2011). The conceptual model uses a fixed catchment parameterization which reflects a sandy-loam soil with an intermediate groundwater response time. The model has been successfully applied in previous studies (Van Lanen et al., 2013; Van Loon et al., 2014). The conceptual model allows for isolation of the climatic signal from the signal due to differences in catchment characteristics. This allows to focus on differences between drought indicators, only with respect to different climate types.

Table 7.1 Indicators under study and their properties.

Indicator	Drought type	Period	Abbr.	Reference
Effective Drought Index	Meteorological	365 days	EDI	(Byun and Wilhite, 1999)
Standardized Precipitation Index	Meteorological	1 month	SPI-1	(McKee et al., 1993)
Standardized Precipitation Index	Meteorological	3 month	SPI-3	(McKee et al., 1993)
Standardized Precipitation Index	Meteorological	6 month	SPI-6	(McKee et al., 1993)
Standardized Precipitation Index	Meteorological	12 month	SPI-12	(McKee et al., 1993)
Standardized Precipitation Index	Meteorological	24 month	SPI-24	(McKee et al., 1993)
Palmer Drought Severity Index	Soil moisture	-	PDSI	(Palmer, 1965)
Threshold level method	Meteorological	1 month	MAP	(Yevjevich, 1967)
Threshold level method	Soil moisture	1 month	MAS	(Yevjevich, 1967)
Threshold level method	Hydrological	1 month	MAQ	(Yevjevich, 1967)
Total Storage Deficit Index	Hydrological	-	TSDI	(Yirdaw et al., 2008)
Groundwater Resource Index	Hydrological	-	GRI	(Mendicino et al., 2008)

7.2.2 Drought indicators

Drought in all parts of the hydrological cycle were evaluated using a selection of 12 frequently used drought indicators (Table 7.1). These indicators cover all drought types and strongly vary in calculation procedure and input data required. These drought indicators were applied to detect drought conditions in the hydrological simulations. The exact calculation procedure is given in Section 7.3. Here the SPI-12 and SPI-24 are classified as meteorological drought indicators, however, these are often used as proxy for soil moisture or meteorological drought (Seneviratne et al., 2012).

For drought indicators that require only precipitation as input, the time series of the WATCH reanalysis dataset were used (Weedon et al., 2011). All indicators were derived on a monthly time step and normalized time series for each indicator were calculated. For more information about the calculation procedure of each drought indicator the reader is referred to the individual papers mentioned and Section 7.3.

Indicators were evaluated based on the correlations between indicators that should indicate similar drought types or could be used to monitor similar impacts (Figure 7.1). The correlation between two meteorological drought indicators (e.g. EDI and SPI-1) is referred to as interchangeability. The correlation between indicators of different drought types (e.g. SPI-1 for meteorological and GRI for hydrological drought) is referred to as intrachangeability. Additionally, the impact of climate types according to the Köppen-Geiger classification was evaluated, to see if a dependency exists between the correlation and the climate type.

7.3 Drought indicator calculation

7.3.1 Effective Drought Index

A method to identify meteorological drought on a daily time scale is the Effective Drought Index (EDI). It was developed by Byun and Wilhite (1999) to calculate daily water accumulation with a weighting function of time passage. Daily rain- and snowfall data from time series of 30 years or more are used for the calculation of the EDI. These long series are needed to transform the EDI values into a reliable normal distribution (Kim et al., 2009). Most drought indices have their limitations because they are based on a monthly time step (Byun and Wilhite, 1999; Kim et al., 2009), while the EDI has a daily time step. The EDI is a standardized index, which makes it possible to compare EDIs from different climatic regions. The use of the EDI has been tested in several drought studies (Byun and Wilhite, 1999; Smakhtin and Hughes, 2007; Kim et al., 2009).

7.3.2 Standardized Precipitation Index

The Standardized Precipitation Index (SPI) was developed by McKee et al. (1993). The SPI calculation is done with monthly precipitation, which is fitted to a two parameter gamma probability distribution. This distribution is then transformed into a normal distribution (Redmond, 2000; Keyantash and Dracup, 2002; Naresh Kumar et al., 2009). The SPI is designed to quantify the precipitation deficits for multiple timescales (Keyantash and Dracup, 2002). McKee et al. (1993) suggest to calculate the SPI for 3-, 6-, 12-, 24-, and 48 month time scales. The longer timescales are sometimes used as proxies of streamflow and groundwater drought. Because of the normalized distribution, wetter and drier climates can be represented and compared in the same way. A disadvantage of the SPI is the need for long time series of observed data, and the possibility of trends in precipitation during this period. The National Drought Mitigation Centre in the United States has daily updates of the SPI for the United States. SPI has gained importance in recent years as a potential drought indicator and is being used more frequently for assessment of drought intensity in many countries (e.g. United States, Korea, and Australia) as mentioned by Vincente-Serrano et al. (2004), Wilhite et al. (2005) and Wu et al. (2006). The World Meteorological Organization (2009) has recommended the SPI as the best suitable indicator for meteorological drought. The SPI is a commonly used indicator across the world.

7.3.3 Palmer Drought Severity Index

The Palmer Drought Severity Index (PDSI) was developed by Palmer (1965) to provide an index based on drought severity, that allowed the comparison of drought with

different time and spatial scales. Palmer (1965) based his index on the supply-on-demand concept of the soil water balance. The PDSI takes into account precipitation, evapotranspiration, and soil moisture, although it is still classified by many authors as a meteorological drought indicator. In the United States the PDSI is regarded the most prominent index for meteorological and soil moisture drought (Alley, 1984; Keyantash and Dracup, 2002; Wells et al., 2004). The PDSI is based on a generic two-layer soil model. For both layers soil moisture storage is calculated based on observed meteorological conditions. In this research the PDSI is considered a soil moisture drought indicator, because of the simulated soil moisture content. Several limitations of the PDSI have been reported by Alley (1984). The most important limitation is that the beginning and end of a drought or wet spell are not clearly defined and only based on Palmer's study (Palmer, 1965). The two-layer approach is a simplification and may not be an accurate representation of the actual situation. In colder climates, accumulation of snow and frozen ground are not represented by the index (Dai et al., 2004). The PDSI is used for drought research on a global scale in studies done by Dai et al. (2004); Sheffield and Wood (2007); Sheffield et al. (2009); Dai (2013); Sheffield et al. (2012). In the United States the National Climatic Data Centre has maps from 1895 till present of monthly PDSI values.

7.3.4 The threshold method

The threshold method or truncation level method originates from the theory of runs developed by Yevjevich (1967) and has been widely used (Smakhtin, 2001). With the threshold method, different drought characteristics can be determined (e.g duration and deficit volume) (Tallaksen et al., 1997; Hisdal et al., 2004; Fleig et al., 2006; Tallaksen et al., 2009). The method is based on a threshold. When streamflow or another hydrometeorological variable is below this threshold it is considered a drought situation (Dracup et al., 1980; Hisdal et al., 2004).

7.3.5 Total Storage Deficit Index

The Total Storage Deficit Index (TSDI) was developed by Yirdaw et al. (2008) for drought characterization in the Canadian Prairie. In their study, they combined the TDSI with water storage anomalies from Gravity Recovery And Climate Experiment (GRACE) satellite observations and streamflow measurements. A study of Agboma et al. (2009) used the TSDI in combination with the Variable Infiltration Capacity (VIC) model. The TSDI uses precipitation, evapotranspiration, and discharge from the basin outlet. The anomalies in total amount of water stored in the catchment are an indicator for drought. Since no further research has been done on the TSDI, only the experiences results from Yirdaw et al. (2008) and Agboma et al. (2009) are available. So far, the TSDI is not used on a global scale.

7.3.6 Groundwater Resource Index

For the calculation of groundwater drought, the Groundwater Resource Index (GRI) can be used. This index, developed by Mendicino et al. (2008), was tested in Calabria, Italy. The GRI is based on a normal distribution of the simulated groundwater storage in at a site. Since the GRI is a very new drought indicator, the performance of the GRI has only been tested by Mendicino et al. (2008) with 40-years of simulated data. The simulated data were generated by a hydrological model which used: precipitation, air temperature, and air pressure data as driving force. They compared the GRI with the SPI of 6-, 12-, and 24-months. They found that the GRI was a better indicator for drought in the Mediterranean area than the SPI.

7.3.7 Sensitivity analysis

A sensitivity analysis was done to assess the robustness of the model parameterization with respect to the generated time series of soil moisture, discharge and derived drougth indicators. The sensitivity analysis by Van Lanen et al. (2013) showed that hydrological drought characteristics derived from simulated discharge, did not change significantly with changes in parameterization. However, here the robustness of the model with respect to different drought indicators was evaluated. The sensitivity of the soil moisture and discharge simulations to changes in the parameterization was evaluated for a temperate climate (with seasonal snow impact). The relative difference in the variance and the mean of the soil moisture and discharge are related to the changes in parameterization. Thereafter, drought characteristics are calculated with different drought indicators and via correlation indicators the time series are compared with the baseline scenario (sandy-loam soil with an intermediate groundwater response time) .

7.4 Results

7.4.1 Sensitivity analysis of hydrological model

From the local sensitivity analysis, it was found that the parameterization of the conceptual model has a minor impact on the simulated drought indicators and hence it hardly influences the comparison between indicator time series. The impact on the correlations between drought indicators is less than 0.005 for all indicators under study for all locations. This clearly shows that the impact of the model parameterization on the conclusions of this study is negligible.

7.4.2 Analysis of spatial patterns in drought indicators

An example of the drought conditions in Africa in August 1984 is shown for all indicators under study, indicating the severity of the drought conditions and to explore differences between drought indicators (Figure 7.2). It is clear that although the 1984 drought in Africa is known to be severe (Van Huijgevoort et al., 2012; Wada et al., 2013), not all indicators show this signal. There is a strong disagreement amongst the drought indicators on the spatial pattern of the drought and the severity. Although not all indicators have been developed to monitor the same drought type, similarities in the spatial patterns should be visible between indicators of the same type. Certainly most indicators of the same type use similar input data. This example of a spatial drought pattern clearly shows that when this drought was monitored with a single indicator, the impact assessment of the natural hazard, could be significantly different relative to monitoring with another drought indicator of the same type. Since the textitreal drought situation is unknown no comparison could be made with the *real* drought situation; however, a better agreement on the spatial pattern of the same type should occur.

7.4.3 Interchangeability of drought indicators

The correlation between drought indicators used for different drought types (intra-changeability) is lower than the correlation for indicators within a drought type (interchangeability, Figure 7.3). It is striking to see that meteorological drought was characterized differently by the seven relevant indicators used in this study (EDI, MAP, SPI-1,3,6,12,24), resulting in the lowest median correlations over all climates ($r = 0.1 - 0.65$). Because these indicators use only precipitation time series, the cause of the low correlation can fully be alloted to the way in which precipitation time series are transformed to meteorological drought. These indicators were expected to have a high correlation because they should represent drought conditions for the same impacts. This could be partly caused by the way indicator calculations deal with this highly dynamic time series of precipitation.

The low average correlations ($r = 0.25$) found between the two soil moisture indicators (PDSI and MAS) are a result of the different ways in which soil moisture drought is defined. Especially in situations with snow accumulation the way in which the drought identification was performed is of high importance. For example, PDSI does not account for snow or delayed soil moisture availability as a result of snow melt, which results in different drought characteristics compared to MAS.

The interchangeability of three hydrological drought indicators (GRI, TSDI, MAQ) is high compared to the other drought types ($r = 0.5 - 0.95$, also seen in Figure 7.2). This indicates that one indicator might already suffice to correctly characterize hydrological drought events and their impacts (in contrast to meteorological or soil moisture drought). The fact that hydrological drought indicators show the highest

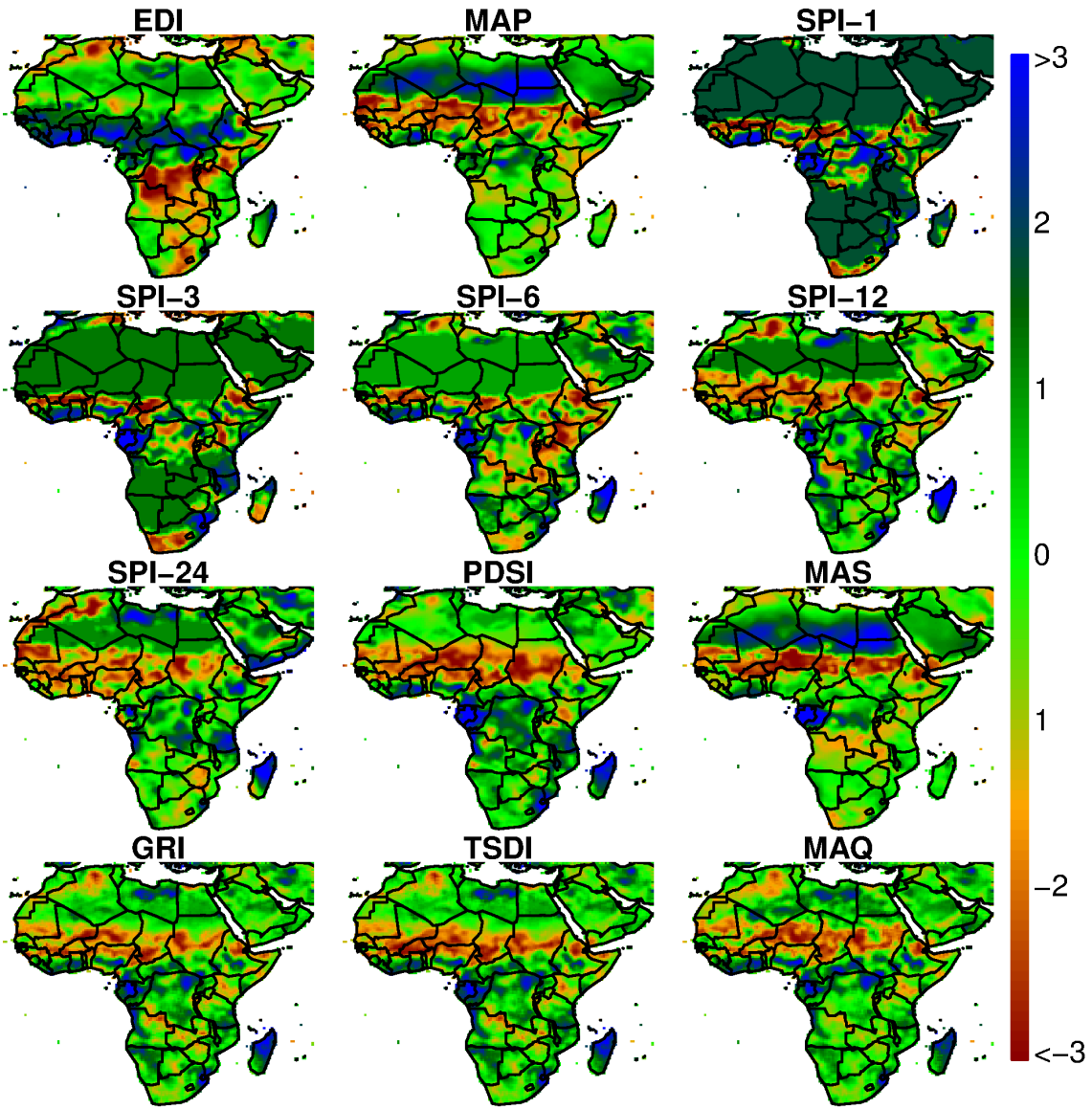

Figure 7.2 Drought conditions over Africa in August 1984 for selected drought indicators under study. Colours indicate the normalized drought severity, where negative numbers show more severe drought conditions and positive numbers more wetness.

interchangeability could be related to the fact that the dynamics in groundwater and discharge time series is low compared to precipitation or soil moisture time series. This low dynamic behaviour results in a reduced impact of any smoothing or aggregation in the drought indicator calculation and as a result leads to higher correlations and agreement in the identification of drought events. Hydrological drought events often have long duration, whereas meteorological drought events are often short.

7.4.4 Intrachangeability of drought indicators

The potential intrachangeability of drought indicators is even lower than the interchangeability, which is to be expected when indicators are supposed to monitor different domains of the hydrological cycle (Figure 7.3). Meteorological drought indicators show low intrachangeability with soil moisture ($r = 0.0 - 0.7$) and hydrological drought indicators ($r = 0.0 - 0.75$). The highest correlations of meteorological drought indicators with indicators of other drought types are found for the EDI, SPI-3, SPI-6 and SPI-12, while the indicators with short or very long aggregation periods (MAP, SPI-1 and SPI-24), clearly show low potential intrachangeability. The indicators with a short aggregation period do not have memory to accurately reproduce soil moisture of hydrological drought conditions.

Soil moisture indicators show an intermediate intrachangeability with meteorological drought indicators ($r = 0.0 - 0.7$) and hydrological drought indicators ($r = 0.1 - 0.65$), where the PDSI shows the highest intrachangeability with meteorological drought indicators.

The results suggest that substitutes (meteorological drought indicators that should approximate another drought type) cannot be used to study different drought types. For example, the intrachangeability of drought indicators is always lower than the interchangeability found for each of the three hydrological drought indicators. This indicates, for instance, that differences amongst hydrological drought indicators are smaller than for differences between hydrological drought indicators and possible substitutes, e.g. SPI-12 or SPI-24 ($r = 0.3 - 0.7$). Although computational effort and complexity of the calculations might be decreased by selection of a substitute for all drought types, this does not provide useful information for impacted sectors. For example, when the SPI is used to monitor hydrological drought (for reasons of data availability), this leads to different drought severity patterns (see Figure 7.2).

An impact of snow accumulation is found for the snow-affected (D) and polar (E) climate where the intrachangeability of meteorological and hydrological drought indicators is lower than for other climate types. Similar to the result obtained for meteorological drought indicators, the intrachangeability between soil moisture and hydrological drought indicators is hampered in snow-affected (D) and polar (E) climate regions. This clearly illustrates that snow should be accounted for in these regions, when soil moisture or hydrological drought is considered. In snow affected

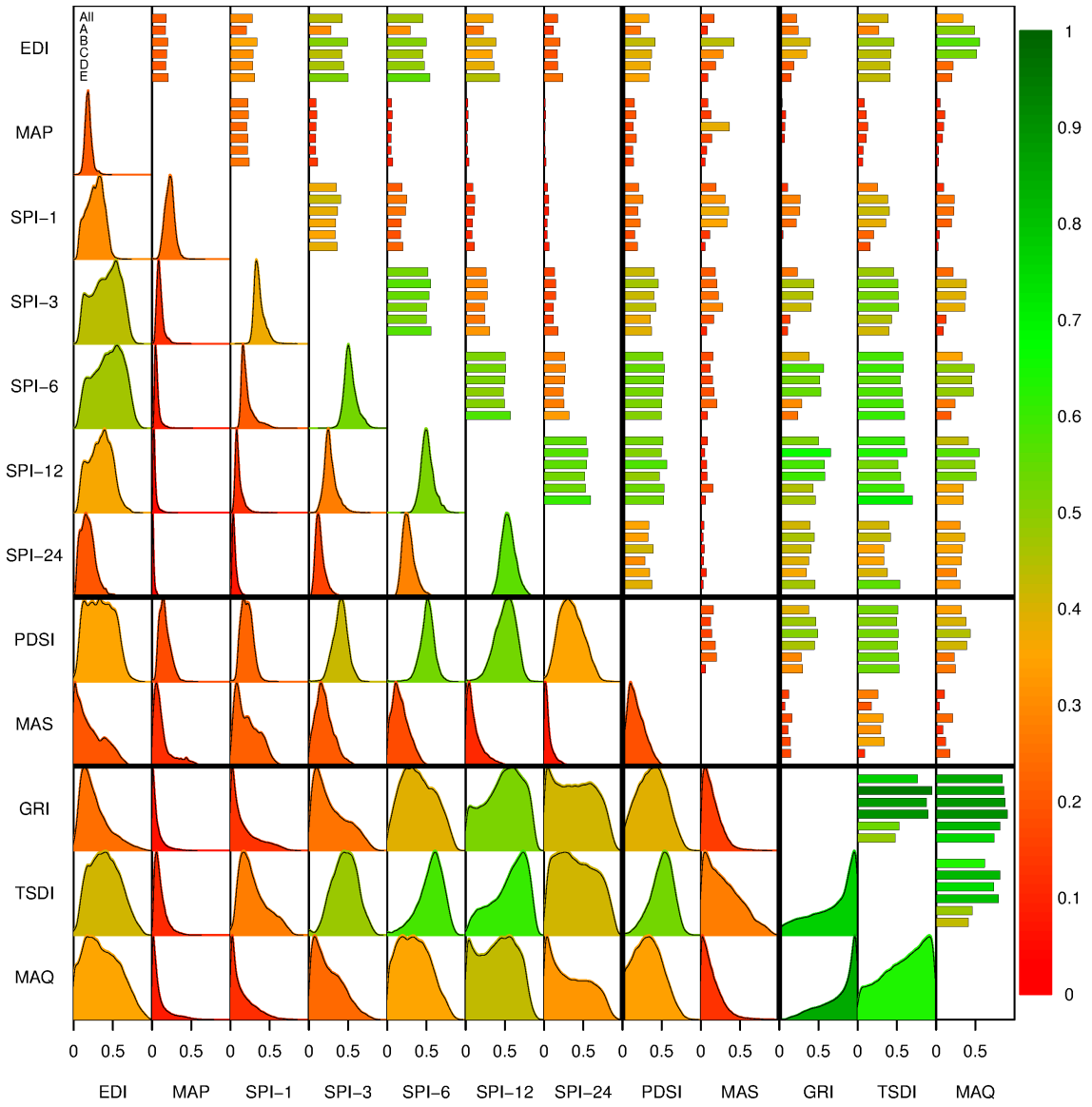

Figure 7.3 Correlations between indicators for the period 1958-2002, where the colours of bars and histograms indicate median correlations between indicators. The colours of each global correlation distribution (below diagonal) indicate the global median of the correlations, where no distinction is made between climate types. Bar plots (above diagonal) indicate the median of the globe (All), tropical (A), desert (B), temperate (C), Snow (D) and Polar (E) climate type (upper left cell gives sequence of climate types for the histograms). Different drought types as defined in Table 7.1 are separated by thick lines.

(D) climates, snow melt can end drought events by increased water availability in spring, which could lead to different behaviour of indicators that either include snow accumulation or not. Moreover, a meteorological drought in winter is not directly visible in groundwater or discharge (Van Loon and Van Lanen, 2012). Especially, indicators that do not include snow accumulation and snow melt are highly affected by this and show low correlations in these snow-affected regions. In the desert climate (B) all indicators are affected by long periods with no precipitation or recharge. In these regions the definition of a drought remains challenging and should be done with care in order not to confuse drought and aridity (i.e normal climatic conditions). Intrachangeabilityality of drought indicators is higher in the tropical (A) and temperate (C) climate regions than in the dry and cold climates (B, D and E).

7.5 Discussion and Conclusions

The low correlations between drought indicators (Figure 7.3) show that it is very important to select the correct indicator for monitoring, forecasting and predicting a drought relevant for an impacted sector. Since drought impacts are related to different domains of the hydrological cycle (Figure 7.1), no single indicator can be used to monitor all impacts. Additionally, the different spatial patterns between indicators for a known drought event show the need to be cautious when using a single drought indicator to identify drought conditions even for one drought type (Figure 7.2). The example for a drought over Africa shows that the indicator used to characterize drought should be dependent on the impact under study.
Time series of different drought indicators are often used to derive trends in drought characteristics. However, intercomparison of the outcome of these drought studies should be done with extreme caution since indicators used might not capture the same type of drought and are therefore not to be compared. Caution is also advisable when one particular drought indicator is calculated for different lag-times or in different ways (e.g. the PDSI Dai, 2013; Sheffield et al., 2012). Trend analysis based on a single indicator creates the illusion that the phenomenon drought is studied in general, but the drought is not captured by one indicator and consequently only the trend for some impacts is studied. Single indicator studies can be used to capture trends in a single type of drought (e.g. meteorological or hydrological), although this should also be done with care since using a different indicator could lead to different results (see interchangeability potential, Section 7.4.3).
There was an attempt and a request from policy-makers to identify a universal drought indicator to enable global drought monitoring and enable global risk assessment (World Meteorological Organization, 2009). However, researchers should not try to fulfil this quest to one ultimate drought indicator, since such an indicator can never cover the full width of the multi-faced drought phenomenon. Every impact requires a different type of indicator and although some impacts can be studied with the same indicator, this is certainly not a standard procedure. The performance of an

indicator is also dependent on climate type, indicating that the desire for one global indicator certainly cannot be fulfilled.
For monitoring the propagation of drought through the hydrological cycle it is important that drought indicators are calculated in a similar way for all domains of the hydrological cycle (Van Loon and Van Lanen, 2012).
A distinction can be made between indicators used for drought awareness usually on a large scale (e.g. the European Drought Observatory, Sepulcre-Canto et al., 2012) and indicators for operational practices on a river basin scale (e.g. Andreu et al., 2009). Indicators for public awareness could be dimensionless and do not require a direct connection with an impacted sector. For example, the SPI with different accumulation periods can be used to monitor anomalies throughout the hydrological cycle, since it gives an indication on the duration and severity of the drought. Indicators like the SPI are, however, not applicable to calculate drought deficits since only standardized anomalies are provided. The SPI or similar indicators can be used to increase public drought awareness due to their easy interpretation. Similar calculation procedures as the SPI have been applied to other hydro-meteorological time series to study drought propagation in for example runoff (Standardized Runoff Index, Shukla and Wood, 2008) and groundwater (Standardized Groundwater Index, Bloomfield and Marchant, 2013). For operational purposes, however, a threshold approach would be more suitable, since it can directly be translated into drought deficits or water shortages. The threshold approach is easily applicable throughout the hydrological cycle and therefore suitable for propagation studies (e.g. Peters et al., 2003, 2006; Tallaksen et al., 2009; Van Loon and Van Lanen, 2012; Van Loon et al., 2014). The calculated deficits are not very informative for the general public unless standardised, e.g. by the mean flow.
The results of this study should impact the way in which drought should be monitored and forecasted. Since indicators are not interchangeabilityal, different indicators are required for different impacts. Additionally, studying drought in snow-affected regions should be done with more care and a realistic representation of snow accumulation should be included in indicators used for these regions (Staudinger et al., 2014). In this study, it is shown that drought indicators show large differences in drought identification and therefore drought indicators should be related to the impacted sector under study. Drought indicators are hardly inter- and intrachangeabilityal and therefore a careful selection of the drought indicator is required. Using a single indicator to study global trends for all drought types is impossible and unrealistic.

Acknowledgments

This research contributed to the European Union (FP7) funded Integrated Project DROUGHT-R&SPI (contract no. 282769). It is part of the programme of the Wageningen Institute for Environment and Climate Research (WIMEK-SENSE) and it supports the work of the UNESCO-IHP VIII FRIEND-Water programme.

8 Hydrological drought under a changing hydrological regime

This chapter is based on:
Wanders, N., Wada, Y., van Lanen, H. A. J. (2015), Global hydrological droughts in the 21^{st} century under a changing hydrological regime, Earth System Dynamics, 6, 1-15, doi:10.5194/esd-6-1-2015.

Abstract

Climate change very likely impacts future hydrological drought characteristics across the world. Here, the impact of climate change on future low flows is quantified and associated hydrological drought characteristics on a global scale using an alternative drought identification approach that considers adaptation to future changes in hydrological regime. The global hydrological model PCR-GLOBWB was used to simulate daily discharge at 0.5° globally for 1971–2099. The model was forced with CMIP5 climate projections taken from five GCMs and four emission scenarios (RCPs), from the Inter-Sectoral Impact Model Intercomparison Project. Drought events occur when discharge is below a threshold. The conventional variable threshold (VTM) was calculated by deriving the threshold from the period 1971–2000. The transient variable threshold (VTM_t) is a non-stationary approach, where the threshold is based on the discharge values of the previous 30 years implying the threshold to vary every year during the 21st century. The VTM_t adjusts to gradual changes in the hydrological regime as response to climate change. Results show a significant negative trend in the low flow regime over the 21st century for large parts of South America, southern Africa, Australia and the Mediterranean. In 40–52 % of the world reduced low flows are projected, while increased low flows are found in the snow dominated climates. In 27 % of the global area both the drought duration and the deficit volume are expected to increase when applying the VTM_t. However, this area will significantly increase to 62 % when the VTM is applied. The mean global area in drought, with the VTM_t, remains rather constant (11.7 to 13.4 %), compared to the substantial increase when the VTM is applied (11.7 to 20 %). The study illustrates that an alternative drought identification, considering adaptation to an altered hydrological regime, has a substantial influence on future hydrological drought characteristics.

8.1 Introduction

Drought has large socio-economic and environmental impacts, e.g. on food (rainfed agriculture, irrigation), energy (hydropower, release of cooling water), water-borne transport, ecosystem services, wild fires, greenhouse gas emissions (e.g. Wilhite, 2000; Tallaksen and Van Lanen, 2004; Sheffield and Wood, 2011). The 2011 drought in the Horn of Africa caused large famine across the region, leaving hundreds of thousands of people in need of assistance and many were regrettable fatalities (United Nations, 2011; Sida et al., 2012). Drought-related heat waves and forest fires caused almost 80000 deaths in Europe in 2003. Overall losses were estimated to be about 5000 billion Euro over the period 1998–2009 (EEA, 2010). IPCC describes in the Special Report on EXtremes (IPCC-SREX) that droughts will intensify in the 21st century in certain seasons and areas (e.g. many European regions, parts of North America, Central America, southern Africa) as result of climate change (Seneviratne et al., 2012). Society needs to be better prepared to ensure future water, food and energy security (e.g. Romm, 2011; Van Vliet et al., 2012; Bourzac, 2013). The severe impacts of large-scale droughts show the need to improve understanding of droughts on continental and global scales, particularly to increase credibility of future drought projections.

Drought is induced by below-normal precipitation and/or temperature anomalies, which also propagate to reduce soil moisture. For management of groundwater and surface water, however, more relevant is the further propagation into hydrological drought (e.g. Van Loon and Van Lanen, 2012). Despite the need for hydrological drought information, most large-scale future drought studies focus either on precipitation or soil moisture (e.g. Burke et al., 2006; Sheffield and Wood, 2008; Sheffield et al., 2012; Dai, 2013; Orlowsky and Seneviratne, 2013; Trenberth et al., 2014). Few studies deal with assessments of large-scale future hydrological drought (e.g. Forzieri et al., 2014; Prudhomme et al., 2014). The limitation of these studies are, however, that most of them only use one emission scenario that is based on the previous generation (i.e. CMIP3) of global circulation models (GCMs) and the previous scenario projections (i.e. IPCC SRES). Furthermore, Forzieri et al. (2014) only assesses future drought for one continent (i.e. Europe) at high spatial resolution, rather than spanning the whole globe. An exception is the recent study by Prudhomme et al. (2014), which describes projections of hydrological drought across the world obtained from a comprehensive multi-model ensemble (five GCMs and seven global hydrological models or GHMs) using most recent climate models (CMIP5) and four emission scenarios (i.e. RCPs). All studies on large-scale future hydrological drought, so far, used the so-called threshold method (e.g. Hisdal et al., 2004; Fleig et al., 2006) and drought characteristics in the 21st century are identified by using the threshold of the control or historical period (e.g. 1971–2000). However, one may argue if such a stationary approach is suitable for all impact assessments. An updated (transient) threshold for a moving reference period that reflects changes in the hydrological regime over time

might be more appropriate to assess such impacts. Vidal et al. (2012) explored the use of a changing drought index for future drought in France. A transient threshold assumes adaptation to long-term changes in the hydrological regime. It is also more in line with the drought definition (Tallaksen and Van Lanen, 2004) being a deviation from normal conditions (i.e. normal implies decadally updated 30 year averages according to the World Meterological Organization guidelines), although the consequences of such a statistically-constructed metric for real-world applications need careful investigation (e.g. World Meteorological Organization, 2007; Arguez and Vose, 2010) and should consider if drought-impacted sectors can cope with the changes in the hydrological regime.

The objective of this study is to assess the impact of climate change on future hydrological drought across the globe under a changing hydrological regime, here represented using a transient threshold over the spatially-distributed river discharge. The paper is innovative by using: (i) a gradually-changing, spatially-distributed threshold to adapt to changing hydrological regime, (ii) the latest version of climate models from CMIP5 climate projections, and (iii) the number of emission scenarios: four RCPs (2.6, 4.5, 6.0, 8.5).

The paper starts with a brief description of the global hydrological model, forcing data, drought identification approach and the trend analysis, which are followed by the description of the temporal evolution of the spatially-distributed threshold for the river discharge over the 21st century. Next, future drought duration and drought intensity obtained with the transient threshold method, reflecting a changing hydrological regime, are presented and intercompared with the non-transient threshold approach that is derived from the control period (fixed historical period). Results are followed by a discussion that intercompares the outcome of this study with existing assessments of future hydrological drought. It also addresses uncertainty aspects (e.g. variability among GCMs and RCPs), sensitivity of the threshold values applied (Q_{80}, Q_{90}), and the impact of the combined effect of the change in the simulated water availability (hydrological regime) and in the drought characteristics. Eventually, conclusions and recommendation are given.

8.2 Material and Methods

8.2.1 Model simulation of streamflow

The state-of-the-art global hydrological and water resources model PCR-GLOBWB was used to simulate spatial and temporal continuous fields of discharge and storage in rivers, lakes, and wetlands at a 0.5° spatial resolution (Wada et al., 2010, 2013, 2014; Van Beek et al., 2011). In brief, the model simulates for each grid cell and for each time step (daily) the water storage in two vertically stacked soil layers and an underlying groundwater layer. At the top a canopy with interception storage and

a snow cover may be present. Snow accumulation and melt are temperature driven and modelled according to the snow module of the HBV model (Bergström, 1995). To represent the rain-snow transition over sub-grid elevation dependent gradients of temperature, 10 elevation zones were distinguished in each grid cell based on the HYDRO1k Elevation Derivative Database, and re-scaled the 0.5° grid temperate fields with a lapse rate of 0.65°C per 100 m. The model computes the water exchange between the soil layers, and between the top layer and the atmosphere (rainfall, evaporation and snowmelt). The third layer represents the deeper part of the soil that is exempt from any direct influence of vegetation, and constitutes a groundwater reservoir fed by active recharge. The groundwater store is explicitly parametrized and represented with a linear reservoir model (Kraijenhof van de Leur, 1962). Sub-grid variability is considered by including separately short and tall natural vegetation, open water (lakes, floodplains and wetlands), soil type distribution (FAO Digital Soil Map of the World), and the area fraction of saturated soil calculated by the Improved ARNO scheme (Hagemann and Gates, 2003), as well as the spatio-temporal distribution of groundwater depth based on the groundwater storage and the surface elevations as represented by the 1 km by 1 km Hydro1k data set (`https://lta.cr.usgs.gov/HYDRO1K/`). Simulated specific runoff from the two soil layers (direct runoff and interflow) and the underlying groundwater layer (base flow) is routed along the river network based on the Simulated Topological Networks (STN30) (Vörösmarty et al., 2000a) using the method of characteristic distances (Wada et al., 2014).

The PCR-GLOBWB model and model outputs have been extensively validated in earlier work. Simulated mean, minimum, maximum, and seasonal flow (all at monthly temporal step), monthly actual evapotranspiration, and monthly total terrestrial water storage were evaluated respectively against 3613 GRDC observations (`http://www.bafg.de/GRDC`) ($r^2 \sim 0.9$ and slope ~ 0.9 to 1.1 respectively for each monthly flow), the ERA-40 reanalysis data, and the GRACE satellite observations, in earlier work (Van Beek et al., 2011; Wada et al., 2012, 2014), and generally showed good agreement with them.

In brief, the PCR-GLOBWB model has been evaluated with r^2, slope and the root mean square error ($RMSE$) against 3613 GRDC stations with drainage areas larger than 2500 km^2, that is roughly equivalent to one grid cell (0.5°). These stations contain the long-term statistics of mean, minimum, and maximum discharge with sufficient data record (more than 10 years of monthly data), to evaluate our modelled streamflow. Because of the coarse spatial resolution of the model (0.5), the upstream drainage area of some stations, particularly the smaller ones, cannot be represented accurately, thus they have not been included in our model evaluation. Notwithstanding, this data set provides a good starting point to evaluate the skill of the model to simulate discharge variations within and between years for varying catchment sizes and regions. In addition, in Wada et al. (2014), the monthly streamflow has also been evaluated with r^2, slope, and NashSutcliffe model efficiency coefficient (NS).

Table 8.1 GCMs (Global Climate Models) used in this study.

GCM	Organization
HadGEM2-ES	Met Office Hadley Centre
IPSL-CM5A-LR	Institute Pierre-Simon Laplace
MIROC-ESM-CHEM	JAMSTEC, NIES, AORI (The University of Tokyo)
GFDL-ESM2M	NOAA Geophysical Fluid Dynamics Laboratory
NorESM1-M	Norwegian Climate Centre

The reader is referred to Van Beek et al. (2011) and Wada et al. (2014) for the detailed descriptions of the validation exercises.

The model has also been applied to simulate low flow conditions and associated hydrological drought events at a global scale (Wada et al., 2013) and simulated drought deficit volumes and drought frequency were extensively validated against those derived from observed streamflow (from GRDC stations) (Wada et al., 2013) over regions where drought has a major impact on the hydrology. The comparison showed that the model performance is good for simulating low flow conditions across regions with different climatic conditions. In addition, the model has been tested to simulate different drought conditions using different percentile threshold levels (Q_{70}, Q_{80}, and Q_{90}) and the performance remains good. These previous modeling exercises led to the conclusion that the PCR-GLOBWB model is suited to reproduce low flow conditions and that the model can adequately simulate hydrological drought events across the globe. Uncertainties that are inherent to the model and the intercomparison with existing studies or models are discussed in Section 8.4.

The model was forced with daily fields of precipitation, reference (potential) evapotranspiration and temperature taken from five global climate models (GCMs; see Table 8.1) and four underlying emission scenarios (here accounted for by using four Representative Concentration Pathways or RCPs; see Table 8.2). The newly available CMIP5 climate projections were obtained through the Inter-Sectoral Impact Model Intercomparison Project (Warszawski et al., 2014). The GCM climate forcing was bias-corrected on a grid-by-grid basis (0.5° grid) by scaling the long-term monthly means of the GCM daily fields to those of the observation-based WATCH climate forcing for the overlapping reference climate 1960–1999 (Hempel et al., 2013). Potential evapotranspiration was calculated with the bias-corrected GCM climate forcing with the method of Hamon (Hamon, 1963). The resulting bias-corrected transient daily climate fields were used to force the model over the period 1971–2099 with a spin-up, reflecting a climate representative prior to the start of the simulation period. The result of each GCM is treated equally and no weight was given to a particular GCM

Table 8.2 Overview of representative concentration pathways (RCPs) (Van Vuuren et al., 2011). Radiative forcing values include the net effect of all anthropogenic greenhouse gases and other forcing agents.

RCPScenario
2.6 Peak in radiative forcing at $\sim 3.1\ W\ m^{-2}$ ($\sim 490 ppm\ CO_2$ equivalent) before 2100 and then decline (the selected pathway declines to 2.6 $W\ m^{-2}$ by 2100)
4.5 Stabilization without overshoot pathway to 4.5 $W\ m^{-2}$ ($\sim 650 ppm\ CO_2$ equivalent) at stabilization after 2100
6.0 Stabilization without overshoot pathway to 6 $W\ m^{-2}$ ($\sim 850 ppm\ CO_2$ equivalent) at stabilization after 2100
8.5 Rising radiative forcing pathway leading to 8.5 $W\ m^{-2}$ ($\sim 1370 ppm\ CO_2$ equivalent) by 2100

based on the performance against historic climate. As a result, 20 (5 GCMs by 4 RCPs) projections of future daily streamflow were produced.

8.2.2 Drought calculation

Hydrological drought characteristics (e.g. drought duration and deficit volume) were derived from simulated time series of daily discharge (Q) using the variable threshold level approach (Yevjevich, 1967; Tallaksen et al., 1997; Hisdal et al., 2004). In this study the Q_{90} ($m^3\ s^{-1}$) was derived from the flow duration curve, where the Q_{90} is the threshold which is equalled or exceeded for 90 % of the time. This threshold has been selected to study the impact of severe drought conditions and have been used in multiple studies where drought is studied (e.g. Fleig et al., 2006; Parry et al., 2010).

The drought state is given by:

$$Ds(t,n) = \begin{cases} 1 & \text{for } Q(t) < Q_{x,n}(t,n) \\ 0 & \text{for } Q(t) \geq Q_{x,n}(t,n) \end{cases} \tag{8.1}$$

where $Q_x(t,n)$ is the x percentile threshold $Ds(t,n)$ is a binary variable indicating if a location or grid cell (n) is in drought at a given time t. The drought duration for each event at n is calculated with:

$$Dur_{i,n} = \sum_{t=S_i}^{L_i} Ds(t,n) \tag{8.2}$$

where $Dur_{i,n}$ is the drought duration (d) of event i at n, S_i the first time step of a event i and L_i the last time step of the event. The deficit volume per time step was

defined by:

$$Def(t,n) = \begin{cases} Q_x(t,n) - Q(t,n) & \text{for } Ds(t,n) = 1 \\ 0 & \text{for } Ds(t,n) = 0 \end{cases} \tag{8.3}$$

where $Def(t,n)$ is the daily deficit volume of drought i ($m^3\ s^{-1}$) at n. The total drought deficit volume for each drought event was calculated with:

$$Def_i(n) = \sum_{t=S_i}^{L_i} Def(t,n) \tag{8.4}$$

where $Def_i(n)$ is the total deficit volume of the drought event i ($m^3\ s^{-1}$) at n. The deficit volume is the cumulative deviation of the discharge from the threshold over the duration of a drought event. If the $Q_x(t,n)$ equals $0\,m^3\ s^{-1}$ by definition a drought will not occur since $Ds(t,n)$ will remain zero (Eq. 8.1). If $Q_x(t,n)$ equals $0\,m^3\ s^{-1}$ for more than 50 % of the time, no drought characteristics were calculated for this cell. These cells were excluded from the analysis, since frequent zero discharge situations are part of the local climate (i.e. aridity) and are not manifestation of hydrological drought condition or occurrence (Chapter 9).

The total area in drought (AID) at a given time t was calculated by:

$$AID(t) = \frac{\sum_{n=1}^{N} \mathrm{Ds}(t,n)}{N} \tag{8.5}$$

where $AID(t)$ is the total area in drought, N (–) is the total number of cells in the area (e.g. continent, Köppen–Geiger climate region) or all grid cells (globe) except those arid regions that were excluded from the analysis. The $AID(t)$ can range between 0 and 1, where 0 indicates that there is no cell in the area in drought and 1 indicates that all cells in the area are in drought.

8.2.3 Variable threshold approach

In this study, two variable threshold approaches were used. The first approach uses the non-transient calculation of the variable threshold level method, where monthly values of Q_x are calculated from the aggregated daily values of $Q(t)$ over a fixed 30 year period (usually 1971–2000). Thereafter, the monthly values of Q_x are smoothed with a moving average window of 30 days, resulting in the conventional variable threshold (VTM, Van Loon and Van Lanen, 2012; Van Lanen et al., 2013; Prudhomme et al., 2014; Van Loon et al., 2014), that was used in the few studies so far on future hydrological drought.

However, present climatology can significantly change over the future period under climate change. This will result in an altered hydrological regime. This could have

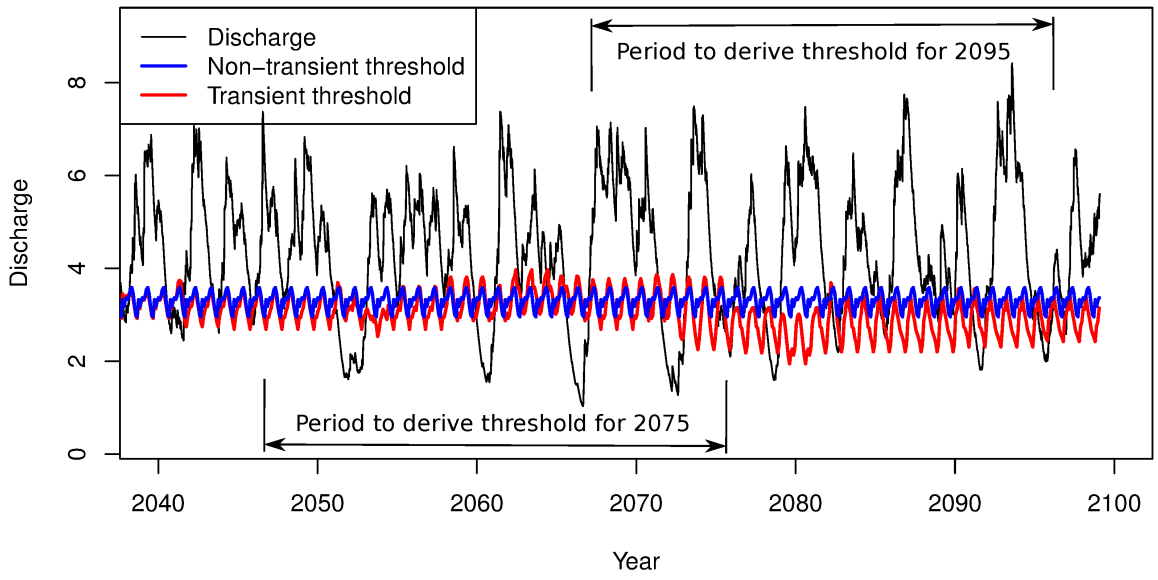

Figure 8.1 Example time series with schematic overview of the non-stationary variable threshold (VTM), which is constant over the 21st century, and the stationary variable threshold (VTM_t) that considers the gradually-changing future hydrological regime.

a significant impact on the detection of drought events, leading to the misrepresentation of drought events as reported by Van Huijgevoort et al. (2014). Areas which become gradually dryer, will be constantly in drought, whereas the opposite will happen in regions with increased low flows. Hydrological regime shifts (e.g. earlier snow melt peak) could have a similar impact, where the threshold is not adjusted to the new hydrological conditions. Therefore, the transient variable threshold (VTM_t) is proposed, where monthly values of Q_x are calculated from the aggregated daily values of $Q(t)$ of the previous 30 years (Figure 8.1). The monthly values of Q_x are derived from the discharge climatology of the past 30 years instead of a threshold based on a historic period (1971–2000). The monthly Q_x is smoothed with a moving average window of 30 days, resulting in the variable threshold (VTM_t).

The difference between the VTM and VTM_t can be seen in Figure 8.1. Both thresholds have been applied to the complete time series of river discharges for the period 2000–2099 and drought events were calculated.

8.2.4 Trend analysis

To study the trends in future drought thresholds, time series of 130 years of simulated river discharges were used. A linear regression was used to study the directionality of the changes and the robustness of those changes. These analyses were performed for each cell separatly to study the effect of regime shifts (e.g. due to shifts in snow

melt peaks). The robustness in the spatially-distributed trends of the threshold was investigated per season for an ensemble of five GCMs, four RCPs and only statistically significant ($p < 0.05$) trends were taken into account. For each cell the trend was calculated over the three months belonging to the season for each of the 20 ensemble members. If for a certain season 16 out of 20 ensemble members showed the same trend direction it was assumed to be a robust decrease or increase. If 13 to 15 members had the same direction then the trend is classified as a possible decrease of increase, while for a lower number than 13, no trend was supposed to occur.

Relative trends in drought characteristics were determined by comparing the average drought characteristics for the period 1971–2000 to the period 2070–2099. Per year the number of droughts, number of drought days and total drought deficit were calculated. Yearly statistics were used since drought events often last for more than one month and therefore it would result in large fluctuations in monthly drought statistics. The robustness in the trends in drought characteristics was studied by comparing the outcome from the multiple GCM simulations for each RCP scenario. If for one RCP, all 5 GCMs pointed in the same direction it was assumed to be robust, while if the GCMs showed more discrepancy the changes were deemed not to be robust. This resulted in 3 classes, robust (5 GCMs agree), likely (4 GCMs agree) and plausible (3 GCMs agree). The classification was done per grid cell for both the robustness of the trend in average drought duration and the trend in the average deficit volume. These were per grid cell combined in a bivariate classification.

8.2.5 Köppen–Geiger climate classification

The impact of changes in temperatures and precipitation patterns has been evaluated with the Köppen–Geiger climate classification (Geiger, 1954, 1961). For all combinations of RCPs and GCMs the Köppen–Geiger climate type has been determined for each cell. Climate classification has been done for each year in the period 2000–2099, where the previous 30 years have been used to calculated the climatology. Changes in climate types have been evaluated for major and minor climate types, for each RCP–GCM combination separately. After the climate types have been determined for each RCP–GCM combination separately, the dominant climate type for each RCP is determined from the 5 GCMs. Since climatology is discrete classification no averaging was applied between the GCM climate types. The dominant climate type was used as the ensemble mean RCP climatology and used in further analyses.

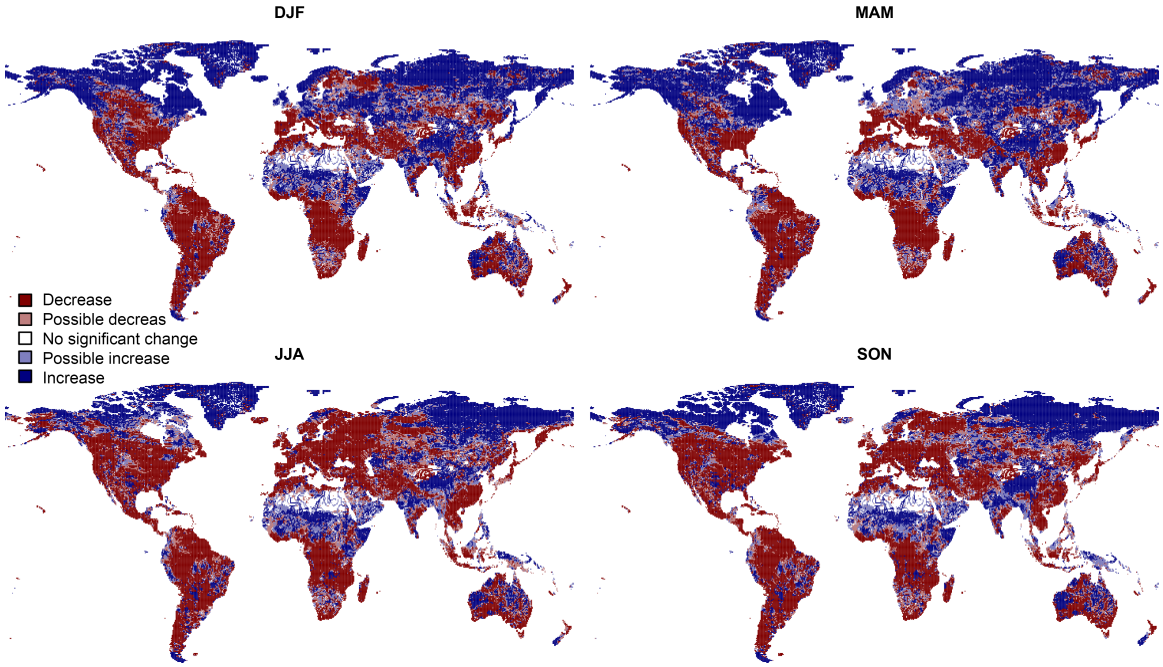

Figure 8.2 Average trends in the transient Q_{90} threshold in the four seasons derived from simulation with PCR-GLOBWB. Trends are aggregated over 3 month periods for an ensemble of 20 members consisting of 4 RCPs and 5 GCMs. An increase or decrease is significant when over 16 ensemble members show similar trends. When over 13 ensemble members agree on the directionality of the change, the trend is deemed possible.

8.3 Results

8.3.1 Trends in future low flow regimes

Global trends in the transient variable threshold (VTM_t) were studied for each RCP separately and for the ensemble of five GCMs (Figure 8.2). When VTM_t decreases, the long-term low flow regime is reduced in that location and drought characteristics were calculated against the reduced low flows. For the average over all RCP scenarios, 40–52 % of the world will face decreasing low flows (VTM_t for Q_{90}). However, regional variability is large. As expected, RCP2.6 shows the smallest area with a decrease in low flows globally (40 % of the world), while for RCP8.5 the decrease in the threshold is more severe (52 %). Difference in these trends are larger among continents and climate types (Figure 8.3) than among the GCMs; the latter in general show high agreement on the directionality of the change. For the equatorial and warm temperate climate (A and C) the low flows will decrease in 62–77 % of the area, while for the snow and polar climates (D and E) the low flows will increase in 54–90 % of the area (depending on RCP scenario). In these colder regions the increased low flows are mainly due to larger snowmelt and increased precipitation. However, a seasonal shift

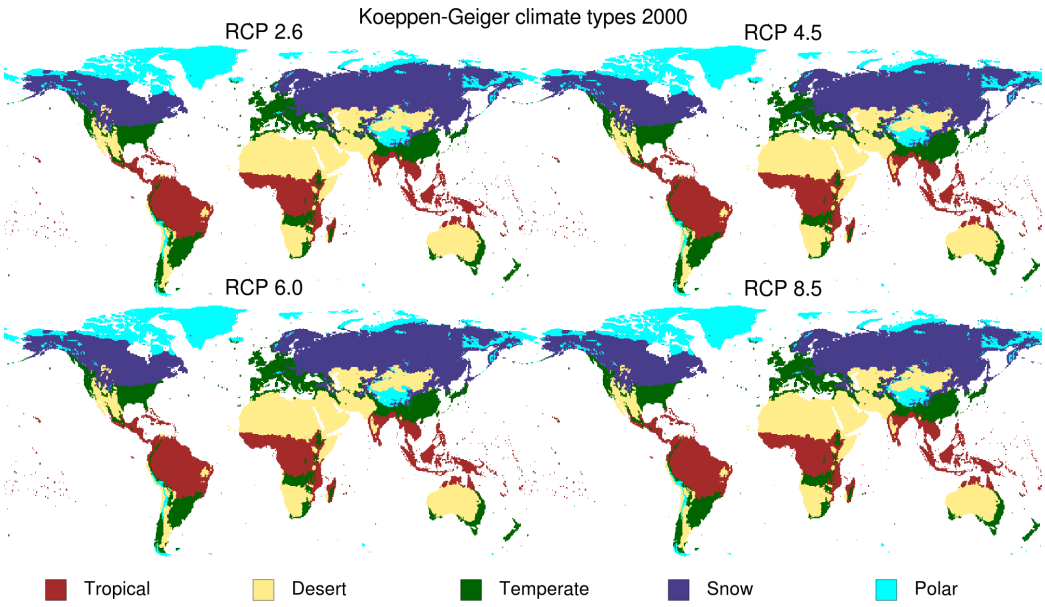

Figure 8.3 Global map of Köppen–Geiger climate types for 2000.

in low flows was observed for these regions where the snowmelt will occur earlier in the season under a warmer climate. This leads to reduced low flows late in summer, which was observed by the decreasing trend in July to September for most of the Northern Hemisphere (Figure 8.2).

Decreasing low flows were observed in: South America, southern Africa, Australia and the Mediterranean area. For the summer months also North America and Europe are largely effected by a decreasing trend. As expected, the decrease in low flows is most severe for the highest emission scenario (RCP8.5), while the trends are less obvious for the lowest emission scenario (RCP2.6). However, all RCPs agree on where in the world the low flows will decrease (e.g. decrease in variable threshold).

8.3.2 Comparison in drought characteristics under a non-transient and transient hydrological regime

Drought characteristics, i.e. drought duration and deficit volume, were calculated with the VTM_t for Q_{90} for all RCP scenarios and for all GCMs. Model agreement in the direction of the change is high and distinct patterns are visible in the results (Figure 8.4). Globally the agreement between the GCMs is high especially for the snow dominated climate (D), the Mediterranean and South America. Four possible cases have been distinguished in the bivariate distribution of the drought duration and the deficit volume: (i) an increase in both drought duration and deficit volume in 27 % of the world (RCP8.5), (ii) increase in duration and decrease in deficit (11 %),

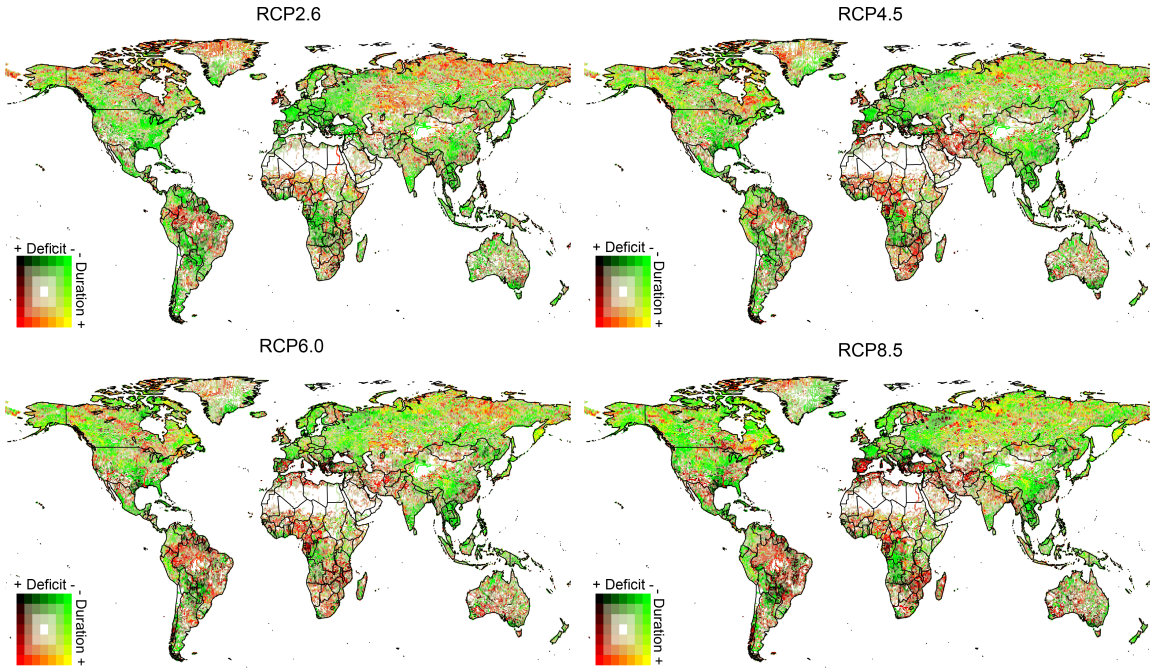

Figure 8.4 Average trends in drought duration and drought deficit volume, derived with a transient Q_{90} threshold from discharge simulation of PCR-GLOBWB. Maps indicate the changes per RCP for a ensemble of 5 GCMs. Colours indicate the robustness of the trend where the darkest colours are robust (5 GCMs agree), thereafter likely (4 GCMs agree) and plausible (3 GCMs agree). A white colour indicates areas where no drought characteristics were calculated.

(iii) decrease in duration and increase in deficit (17 %), and (iv) a decrease in both drought characteristics (38 %). The remaining part shows no trends of characteristics could not be calculated.

Significant different trends in drought duration and deficit volume were obtained when instead of a gradually-changing hydrological regime (VTM_t) a stationary regime (VTM) was assumed (Figures 8.4 and 8.5). Large parts of the world, especially the Southern Hemisphere, show significant increases in both drought duration and deficit volumes. Only the snow affected climates show a decrease in both duration and deficit volume. There is also a better agreement that the trends in the duration and deficit volume point in the same direction than for VTM_t. An increase in both drought duration and deficit volume is found for 62 % of the world (RCP8.5). The areas covered by the other three cases are: (i) increase in duration and decrease in deficit (4 %), (ii) decrease in duration and increase in deficit (6 %), and (iii) decrease in both drought characteristics (25 %). The differences between Figures 8.4 and 8.5 clearly show that the use of a different threshold approach (VTM_t compared to VTM), which reflects whether a non-stationary or a stationary hydrological regime was assumed, has a significant impact on the obtained drought characteristics.

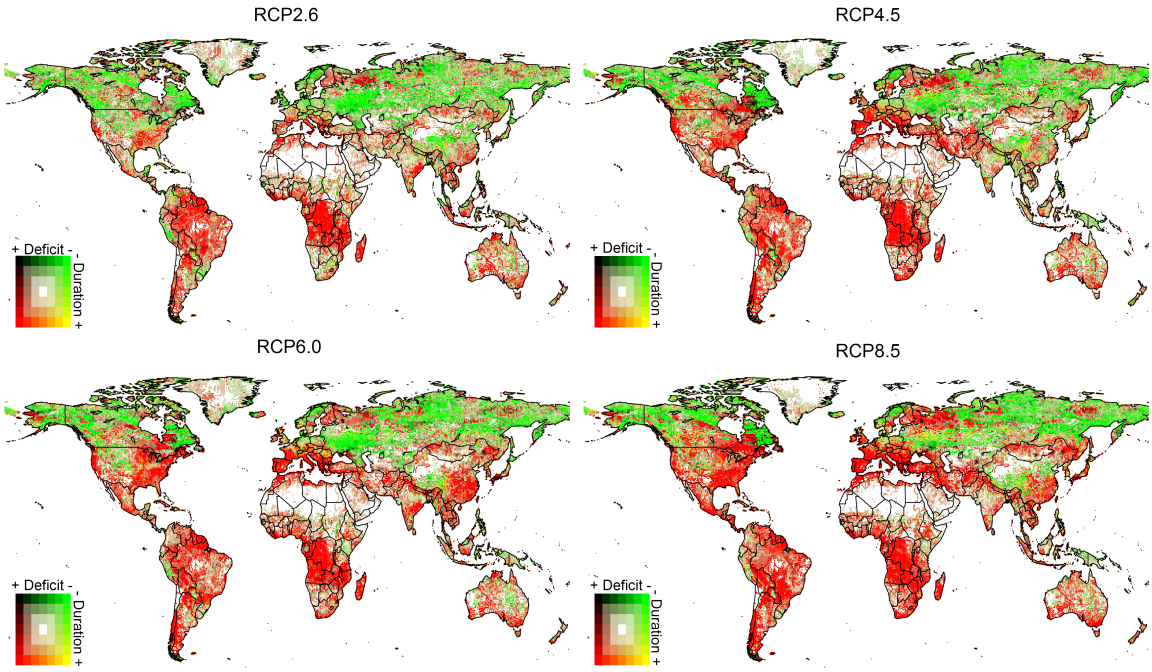

Figure 8.5 Average trends in drought duration and drought deficit volume, derived with the non-transient Q_{90} threshold from discharge simulation of PCR-GLOBWB. Maps indicate the changes per RCP for a ensemble of 5 GCMs. Colours indicate the robustness of the trend where the darkest colours are robust (5 GCMs agree), thereafter likely (4 GCMs agree) and plausible (3 GCMs agree). A white colour indicates areas where no drought characteristics were calculated.

8.3.3 Trends in drought characteristics under a non-stationary hydrological regime

With the VTM_t for all RCPs in large parts of the snow dominated climate a trend was found towards longer droughts, although the low flows have increased (Figures 8.2 and 8.4). This is partly due to the decreased length of the snow accumulation season and partly due to the shift in the snowmelt peak. Trends in the deficit volume in these areas are not so pronounced. Precipitation totals for these regions show an increase of 30–100 mm in annual precipitation for the period 2070–2099 compared to 1971–2000 (Warszawski et al., 2014). The annual temperature shows an increase of 2–5 $^\circ$ C depending on RCPs when the above-mentioned periods were compared. This confirms the observed earlier snowmelt peak and increased water availability in these regions. The snowmelt peak comes earlier in the year leading to drier soil moisture and groundwater conditions in summer.

For the Mediterranean, the savannah areas of Africa and Middle East, the increase in drought duration is larger for most scenarios (except RCP2.6). The threat is even higher due to the decrease in water availability during low flow conditions (Figure 8.2).

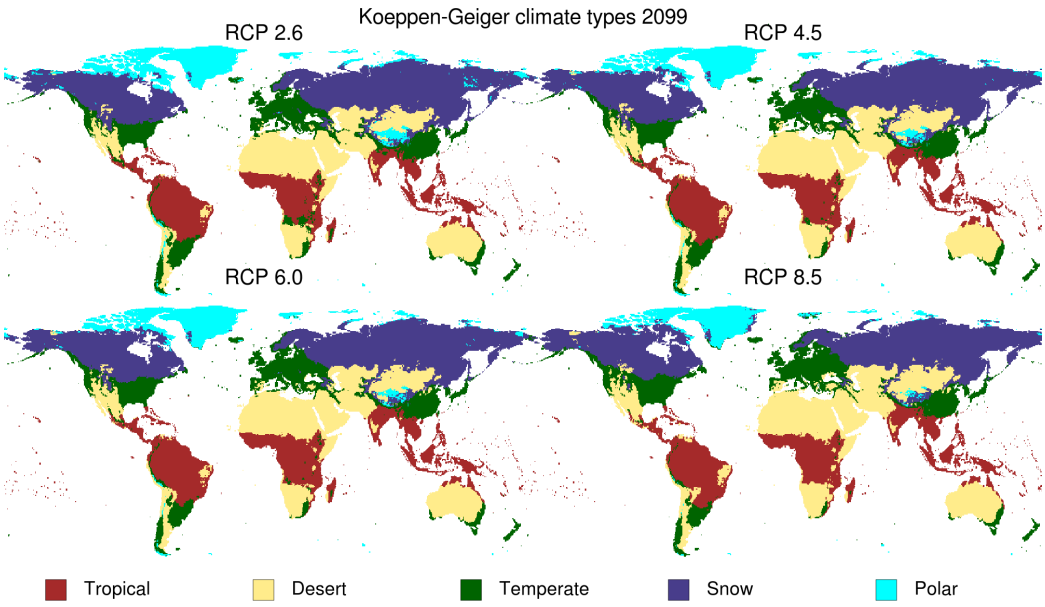

Figure 8.6 Global map of Köppen–Geiger climate types for 2099.

In these regions water scarcity is a known problem which could be intensified by increased drought durations. The same pattern was found for the interior of Australia, where drought duration is projected to increase and low flows to decrease. However, the impact is less due to a lower population density in the region. For these drier areas, temperature rise will be limited to 0.5–3.5 ° C, while annual precipitation will decrease by 35–90 mm.

For South America the decrease in annual precipitation is limited to 12–60 mm, while temperature increase is low (1.2–3.5 ° C) compared to global averages (1.5–4.5 ° C). However, drought duration in the eastern part of the continent shows a strong increase. In the wetter regions of the Amazon Basin this will likely not cause significant impacts. However, the drier regions in Eastern Brazil could be affected as the agricultural areas (mostly irrigation) are located there.

8.3.4 Köppen–Geiger climate classification

As a result of changes in temperature and precipitation patterns the KppenGeiger climate classification for a certain location may change in the 21st century. The area and location of temperate (C) and polar (E) major climate types are most affected by the changing climate (Table 8.3 and Figures 8.3 and 8.6). Global coverage of both climate types will reduce mostly due to increasing temperatures (E) and decrease in annual precipitation (C). On the other hand the tropical (A), desert (B) and snow (D) climate types will increase in global coverage in 2070–2099 compared to 1971–2000.

Table 8.3 Average fraction of changed major Köppen–Geiger climate types between 2000 and 2099 based on 5 GCMs and 4RCPs.

Original Climate type	New Climate type A	B	C	D	E
A	0.975	0.025	0.000	0.000	0.000
B	0.009	0.989	0.001	0.001	0.000
C	0.128	0.091	0.781	0.000	0.000
D	0.000	0.025	0.104	0.871	0.000
E	0.000	0.027	0.025	0.343	0.605

Regions where changes are largest can be found in: polar regions in the Northern Hemisphere (E to D), around the Sahara (C to B) and Gobi desert (E to B), Eastern Europe (D to C) and the tropics (C to A). Although not used further in this paper the changes in area and location of minor climate types are significant, especially in the temperate (C) and snow (D) minor climate types. The area of the minor climate types shows a shift from colder climate types (within the major climate type) to warmer climate types.

8.3.5 Trends in area in drought (AID)

The total area in drought has been calculated for Q_{90} with the transient (VTM_t) and the non-transient (VTM) variable threshold approach. For the VTM_t also an approach with transient adjusted climatology was applied to account for changes in the AID when location shift from one major climate type to another. This has been done for the globe and the five Köppen–Geiger major climate regions. The temporal evolution of the mean and uncertainty of the 20 ensemble members (5 GCMs and 4 RCPs) are given in Figure 8.7. The mean global area in drought is projected to increase from 11.7 to 13.4 % under a gradually-changing hydrological regime (VTM_t) (Figure 8.7). The uncertainty (one standard deviation) among the members by the end of the 21st century is about 1.9 %. When a stationary hydrological regime was assumed (VTM), then the increase of the global area in drought was substantially larger. The mean area is expected to grow from 11.7 to 19.5 %. The spread among members also is projected to be substantially larger by the end of the 21st century, i.e. 5 % under a stationary hydrological regime.

The area in drought of the tropical (A) climate is expected to grow more than the global increase over the 21st century (Figure 8.7). The mean area in drought for the tropical climate will remain steady around 16.7 % for the non-stationary hydrological

regime (VTM_t), whereas it is projected to double (16.7 to 32.6 %) by the end of the century for a stationary hydrological regime (VTM). The difference between the adjusted climate type and the fixed climate types is minor at the end of the 21st century, 16.6 % compared to 16.4 % (dynamic climate types). The spread among the members for the tropical climate is about 3.9 % at the start of the century and is similar for the VTM_t and VTM, but differences in spread are larger by the end of the century when a stationary hydrological regime (VTM_t) was supposed rather than a non-stationary regime (VTM) (5.5 and 8.5 %, respectively).

The difference in area in drought between the VTM_t and VTM approaches among the Köppen–Geiger major climates is smallest for the polar (E) climates (Figure 8.7), which is caused by the increased water availability. The mean area in drought is projected to remain constant (around 10.0 %) under a non-stationary hydrological regime (VTM_t), and is expected to only slightly decrease under a stationary regime (VTM) (10.2 to 6.7 %). In contrast to the other climates, the spread by the end of the 21st century is smaller when a stationary hydrological regime was supposed (i.e. 3.5 % for the VTM_t approach and 2.3 % for the VTM approach).

The impact of a changing climate is minor as can clearly be seen from Figure 8.7. Only minor differences can be found between the transient and stable climate classification results. This suggests that the impact of changes in major climate types is limited on the AID.

8.4 Discussion

8.4.1 Implication of transient threshold approach

This study uses a newly developed transient threshold, which is based on the discharge climatology of the previous 30 years. This approach has implications on how changes in drought characteristics are evaluated. For some applications the absolute water availability is important, where a particular demand of available water should be met (e.g. energy production from reservoirs or drinking water supply). However, it is questionable whether these demands could be seen as a drought. They are related to water availability and demand, which is more a matter of water scarcity, since it deals with the imbalance between the available water and the demand (European Union, 2007a). Drought only deals with natural conditions and is not driven by any type of demand. Therefore, sectors that have a human induced water demand are not considered with the transient threshold and these sectors should work with a conventional fixed threshold approach. This threshold describes the water demand that should be met to prevent imbalance between demand and supply.

When looking at natural conditions and extremes in these conditions, processes like ecosystems and agriculture are included in the transient threshold approach. Climate

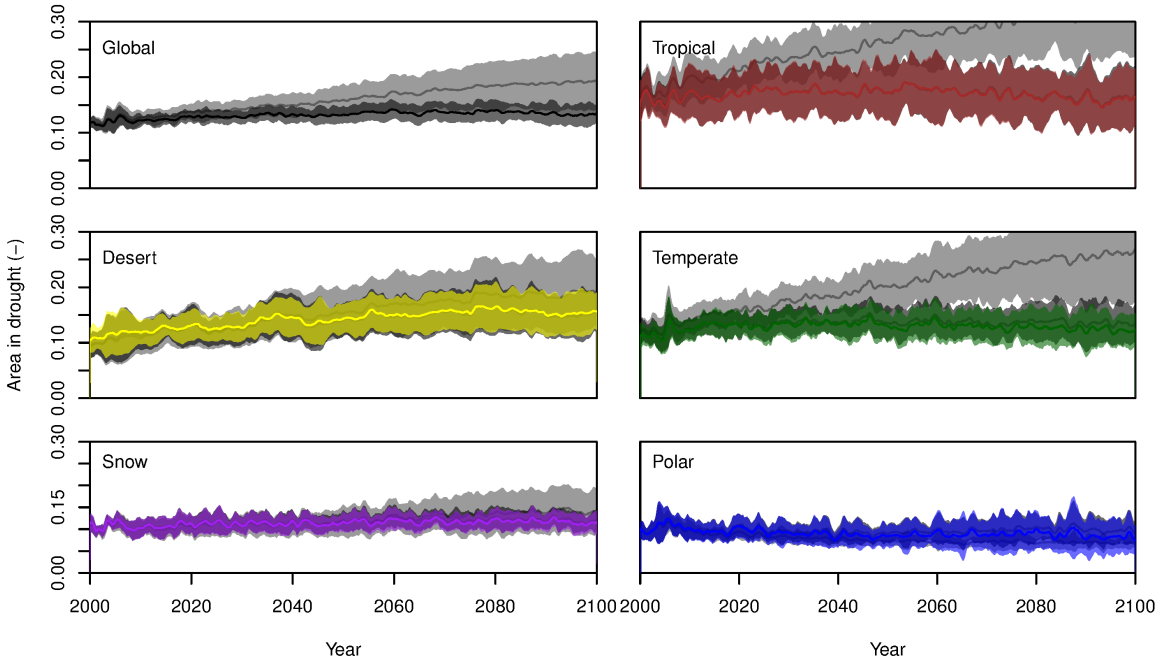

Figure 8.7 Projected evolution of ensemble mean area (solid line) and the spread in hydrological drought in the 21st century derived from simulation with PCR-GLOBWB, forced by an ensemble of 20 scenarios consisting of four RCPs and five GCMs. The evolution is given for the globe and for the five major Köppen–Geiger climatic regions. The coloured lines present the evolution under a changing hydrological regime with changing climate types per cell (transient variable threshold, VTM_t), dark gray without a changing climate per cell with the VTM_t and light gray the evolution under a stationary hydrological regime (non-transient variable threshold, VTM).

change will induce changes in ecosystems (Fischlin et al., 2007) and require changes in agricultural management (European Union, 2009). These sectors will slowly adapt to the changes in climatology, leading to higher or lower water availability depending on where you are at Earth and hence other crops or ecosystems. When the sectors get used to the new conditions and a below normal water availability event will occur (i.e. drought) the effects can be significantlt different than without a changing climate. To illustrate, one can picture a semi-arid region where agriculture is heavily impacted by water limiting conditions. When this region is permanently receiving more water (e.g. rain), this will result in a change to crops that require more water and are more productive and profitable. If this area is hit by a drought event the crop losses will be high due to fact that farmers have changed to the more water demanding crops. This will result in higher productivity in the wetter, but then normal years and bigger losses in drought years, which will impact the local economy and residents. For the ecosystems a similar situation will occur, since nature will seek for an optimal situation relative to the available resources. Animals and plants that can deal with semi-arid conditions will be replaced by more successful species which fully utilize the increased

availability of water resources. These animals and plants will be heavily impacted in drought conditions since they require more water and other resources, which will increase the drought vulnerability of the ecosystem. When the fixed threshold would have been applied this interaction between nature/humans and the availability of resources would not be taken into account and hence not captured by the analyses of future hydrological drought. For conditions that deal with a fixed demand or a demand that is not driven by water availability this is no problem. However, in conditions where the water resources are limiting the transient threshold will give a more realistic portrayal of the potential impact of future hydrological drought.

This statement does not only apply to changes in future hydrological drought but it will also impact climate impact assessments of frequently used drought indicators like the Standardized Precipitation Index (SPI, McKee et al., 1993) and Palmer Drought Severity Index (PDSI, Palmer, 1965). For the calculation of these indicators the distribution of events is used to assess anomalies. However, the distribution of a 30-year period will change with a changing climate and what is a anomaly in the current condition could be seen as normal in 50 years. Therefore, it is proposed not only to apply the transient approach on drought assessments that study hydrological drought with the threshold approach. The transient approach should be applied more widely to all type of drought assessments ranging from normalized indicators like the SPI or PDSI to drought indicators like the threshold level approach. It is argued that a combined transient and non-transient approach would cover all potential drought impacts and would provide a more realistic portrayal of future drought under a changing climate.

8.4.2 Intercomparison with existing studies on large-scale future hydrological drought

This study showed that in more than half of the world (about 60 % of the land area) hydrological drought frequency is projected to increase by the end of the 21st century even by considering that the hydrological regime will change. The average drought duration and deficit volume each are expected to increase on around 30 and 40 % of the globe. Chapter 9 reports in the global analysis on future hydrological drought using a conceptual hydrological model and 3 GCMs (SRES A2 scenario), a decrease of the number of days in drought, pointing at a lower drought frequency and an increase of the average drought duration and deficit volume of the remaining drought events. The characteristics they found cannot directly be compared because these refer to magnitudes rather than to affected areas (this study) and they used another threshold (Q_{80}) and the non-transient variable threshold approach (VTM, i.e. stationary hydrological regime). However, there seems to be some disagreement in at least the drought frequency. Repetition of our drought analysis with Q_{80} and the VTM led to a lower area (40 %) with an increased drought frequency, whereas the area with longer drought events and larger deficit volumes increased by about 52 and

56 %, which indicates agreement in the direction of change of hydrological drought when the same methodology was applied.

Forzieri et al. (2014) used a large-scale hydrological model and 12 GCMs (SRES A1B scenario) to conclude that low flows in the 2080s are expected to become more extreme in large parts of Europe during the period without frost. Exceptions are Scandinavia, the Baltic countries and northern Russia. They used the Q_{80} and the VTM for their analysis. In our study the area in Europe with a higher future drought frequency varied from about 75–85 % (RCPs 6.0 and 8.5), which seems to be in line with their study. The area with a higher future average drought deficit volume, however, is about 30–35 % (see also Figure 8.4), which appears to disagree with their conclusion. Repetition of our drought analysis with Q_{80} and the VTM led to a larger area (55–70 %) with an increased deficit volume, which agrees more with their outcome.

Prudhomme et al. (2014) explored future hydrological drought using seven global hydrological models (GHMs) and the same GCMs and RCPs as this study. They show that the increase of the global area in drought depends on the RCP, models (GCM, GHM, in particular if the CO_2 effect is included) and the temporal scale (annual, season). The mean increase varies from about 4 % under RCP2.6 to 13 % under RCP8.5. The spread in increase is large with a maximum increase of about 25 %. They used the Q_{90} and the VTM for their analysis. Their results correspond well with our study, but only when using a non-stationary hydrological regime (Figure 8.5). Clearly, the increase of global area in hydrological drought is smaller, if the variable threshold is based on a transient hydrological regime (VTM_t).

Intercomparison of future hydrological drought from this study against existing similar studies showed that the outcome points more or less in the same direction, if the same methodology is applied. However, it also shows the large influence of assumptions on projected drought characteristics, such as a transient variable threshold derived from a changing hydrological regime that is introduced in this study vs. the non-transient variable threshold derived from a stationary hydrological regime that has been used in the few existing future hydrological drought studies so far.

Van Huijgevoort et al. (2014) describe that it is not straightforward to determine future hydrological drought with the VTM derived from observations in the past. This can lead to unintended future drought events (short-lived, very high deficit volume) for climates and hydrological systems with a sharp rise in the hydrograph (e.g. cold climates with pronounced snow melt, monsoon climates) that will face a regime shift. The VTM_t method proposed in this study implicitly handles this impact of a regime shift.

When the transient threshold decreases (Figure 8.2) it implies that the low flows are reduced in that location. When these reduced low flows coincide with an increase in drought duration and deficit volume this will have a large impact on the water availability under drought (15 % of the world). This poses enormous challenges to

society and nature to adapt, especially in developing countries, which usually are very vulnerable.

8.4.3 Uncertainty

Differences between projected temperature and precipitation with GCMs and RCPs used (Tables 8.1 and 8.2) are large (e.g. Warszawski et al., 2014). Clearly, these differences influence future hydrological drought, as illustrated by Chapter 9 and Prudhomme et al. (2014). The spread in the projected temporal evolution of the global area in hydrological drought, as shown in Figure 8.7, also illustrates the impact of different climate drivers. In particular, the spread is large for the Tropical climate and Desert climate. Prudhomme et al. (2014) conclude that the model structure of the hydrological models substantially contributes to uncertainty in future hydrological drought, particularly if the rather hard predictable response of plants to a changing CO_2 concentration (i.e. CO_2 effect) is implemented. The PCR-GLOBWB model used in this study, is one of the seven hydrological models that contributed to the ISI-MIP project (Warszawski et al., 2014); the CO_2 effect is not included. The model has proven to reasonably capture hydrological characteristics (Wada et al., 2013).

Another source of uncertainty is the drought identification methodology that should be defined by the drought-impacted sectors. These sectors determine the magnitude of the threshold level to be used (e.g. Q_{80} instead of Q_{90}) and whether a fixed threshold (constant through the whole period) or a variable threshold method should be applied. Similarly, these sectors determine if a VTM_t for the variable threshold approach, should be chosen for the assessment of future drought that considers a gradually changing hydrological regime in the future or that a VTM should be taken that is based on a stationary hydrological regime derived from historical observations. Table 8.4 shows that the global area with increased average hydrological drought duration is hardly affected by the selection of the magnitude of the threshold level (maximum difference in % change is 1 %). Differences for the average deficit volume are slightly larger (maximum difference in % change of global area with increased deficit volume is 4 %). Differences are substantially larger whether the VTM_t or the VTM was applied. The difference in change of area in hydrological drought with increased drought duration is 13 % for RCP2.6 and 18–19 % for the other RCPs. The difference in change for the drought deficit volume is 9 % for RCP2.6, 13 % for RCP4.5 and 6.0, and 17 % for RCP8.5. As expected, it appears that the difference in projected change of global area in hydrological drought between the two variable threshold methods is larger for the more extreme RCPs.

Table 8.4 Change in global area (%) with increased hydrological drought duration and drought deficit volume: % change derived from 30 year averages of future (2070–2099) against reference (1971–2000) for two variable threshold methods (VTM_t and VTM) and two thresholds Q_{80} and Q_{90}.

Drought identification method	RCP	% of world with Increased drought duration		Increased drought deficit	
		Q_{80}	Q_{90}	Q_{80}	Q_{90}
Transient (VTM_t)	2.6	33	33	42	38
	4.5	32	32	41	38
	6.0	35	34	43	40
	8.5	33	33	40	39
Non-transient (VTM)	2.6		46		47
	4.5		50		51
	6.0		52		53
	8.5		54		56

8.5 Conclusions

In this study future hydrological drought that considers adaptation to a gradually-changing hydrological regime has been studied. An ensemble of 5 General Circulation Models (GMCs) and 4 Representative Climate Pathways (RCPs) has been used as meteorological forcing for the global hydrological model PCR-GLOBWB. Daily discharge has been simulated for the period 1971–2099 and drought in discharge was detected using two threshold level approaches. The conventionally applied variable threshold (VTM) was calculated by deriving the threshold from the period 1971–2000 and subsequently the VTM was used for the period 2000–2099 to identify future drought characteristics (stationary approach). As an alternative, the transient variable threshold (VTM_t) was proposed, which is based on the discharge values of the previous 30 years, where the threshold will vary over time (non-stationary approach). The VTM_t reflects changes in the hydrological regime as response to climate change. The VTM_t is supposed to provide more realistic future hydrological drought characteristics when the impacted sectors are able to adapt to gradual changes in the hydrological regime. The Q_{90} (discharge that is equalled or exceeded 90 % of the time) has been used both for the VTM and VTM_t.

Results based on the VTM_t show that low flows are projected to become lower in 40–52 % of the world (dependent on the RCP). In the equatorial and warm temperate (A and C) climates the low flows will decrease in 62–77 % of the area, while for the snow and polar (D and E) climates the low flows will decrease in 10–46 % of the

area. The small decrease in low flows for the snow affected climates is mainly due to increased precipitation leading to higher low flows. A regime shift was also found, where snow melt will occur earlier in the season due to higher temperatures, leading to drier conditions during the summer. Droughts were identified relative to these altered low flow conditions when applying the VTM_t.

Future hydrological drought characteristics strongly depend on whether the impact of adaptation to a gradually changing hydrological regime due to climate change is considered (VTM_t) or not (VTM). The global area with an increase of both duration and deficit volume is only 27 % (RCP8.5) by the end of the 21st century by using the VTM_t, whereas this is substantially larger (62 %) when the VTM is applied. The area with a decrease of both the duration and the deficit volume is larger when the VTM_t was used rather than the VTM (38 and 25 %, respectively). The global area in drought is also strongly affected by whether the VTM_t or VTM is applied. The mean global area with drought in discharge is projected to increase by only a few per cent (11.7 to 13.4 %) when using the VTM_t, but it is expected to become about 20 % (RCP8.5) when the stationary approach was applied (VTM). The spread in projected areal increase among ensemble members also is substantially smaller when the VTM_t is used instead of the VTM.

Results show that although the VTM_t has been used, drought duration and deficit volume is expected to increase in large parts of South America, southern Africa and the Mediterranean. In 15 % of the world a negative trend in low flows is found in combination with an increase in drought duration and deficit volume, which points at a likelihood of severe future water stress.

The study demonstrates that an alternative way to identify hydrological drought that considers adaptation to an altered hydrological regime caused by climate change, has a significant influence on future hydrological drought characteristics. For sectors that can deal with gradual changes in the hydrological regime the transient variable threshold (VTM_t) is an alternative approach to calculate drought characteristics.

Acknowledgements

This work has been supported by the framework of ISI-MIP funded by the German Federal Ministry of Education and Research (BMBF) (Projectfunding reference number: 01LS1201A). This research was undertaken as part of the European Union FP7 Collaborative project DROUGHT-R&SPI (grant 282769). The research is part of the programme of the Wageningen Institute for Environment and Climate Research (WIMEK-SENSE), and it supports the work of the UNESCO-IHP VII FRIEND-Water programme.

Part III

Uncertainty in projections of hydrological drought

9 Future discharge drought across climate regions

This chapter is based on:
Wanders, N., van Lanen, H. A. J. (2015), Future discharge drought across climate regions around the world modelled with a synthetic hydrological modelling approach forced by three General Circulation Models, Natural Hazards and Earth System Sciences, in press.

Abstract

Hydrological drought characteristics (drought in groundwater and streamflow) likely will change in the 21^{st} century as a result of climate change. Magnitude and directionality of these changes and their dependency on climatology and catchment characteristics, however, is largely unknown. In this study a conceptual hydrological model was forced by downscaled and bias-corrected outcomes from three General Circulation Models for the SRES A2 emission scenario (GCM forced models), and the WATCH Forcing re-analysis dataset (reference model). The threshold level method was applied to investigate drought occurrence, duration and deficit volume. Results for the control period (1971-2000) show that the drought characteristics of each GCM forced model reasonably agree with the reference model for most of the climate types, suggesting that the climate model's results after post-processing produce realistic outcome for global drought analyses. For the near future (2021-2050) and far future (2071-2100) the GCM forced models show a decrease in drought occurrence for all major climates around the world and increase of both average drought duration and deficit volume of the remaining drought events. The largest decrease in hydrological drought occurrence is expected in cold (D) climates where global warming results in a decreased length of the snow season and an increased precipitation. In the dry (B) climates the smallest decrease in drought occurrence is expected to occur, which probably will lead to even more severe water scarcity. However, in the extreme climate regions (desert and polar), the drought analysis for the control period showed that projections of hydrological drought characteristics are most uncertain. On a global scale the increase in hydrological drought duration and severity in multiple regions will lead to a higher impact of drought events, which urges water resources managers to timely anticipate on the increased risk on more severe drought in groundwater and streamflow and to design pro- active measures.

9.1 Introduction

Drought are caused by situations with less than normal natural water availability. They occur in all components of the hydrological cycle and occur across all climate regions throughout the globe (Wilhite, 2000; Tallaksen and Van Lanen, 2004; Mishra and Singh, 2010; Sheffield and Wood, 2011). On a global scale drought is one of the most severe natural hazards, with large environmental and socio-economic impacts, and more attention is require to be better prepared for the future water, food and energy security (Romm, 2011; Van Vliet et al., 2012). The recent summer drought in Russia and Central United States (National Oceanic and Atmospheric Administration, 2012) were the most severe on record. The 2011 drought in the Horn of Africa caused large famine across Djibouti, Ethiopia, Kenya and Somalia (United Nations, 2011). In Europe almost 80000 people died due to drought-related heat waves and forest fires; overall losses were estimated to be as high as 4940 billion Euro over the period 1998-2009 (EEA, 2010). Seneviratne et al. (2012) report that there is medium confidence that since the 1950s some regions of the world have experienced longer and more severe drought (e.g. southern Europe and West Africa) and that drought will intensify in the 21^{st} century in some seasons and areas (e.g. many European regions, parts of North America, Central America, southern Africa) as result of climate change. Lack of long, updated time series of observed hydrological data (e.g. Hannah et al., 2011; Stahl et al., 2012), multiple definitions and drought-generating processes (e.g. Van Loon and Van Lanen, 2012), and the incapability of models to include all these processes (e.g. Gudmundsson et al., 2012; Haddeland et al., 2011; Prudhomme et al., 2011) impede our ability to instil strong confidence in the assessment of past and future drought across the world. High-impact large-scale drought, like the recent drought in Russia, United States and Africa, show the need to improve understanding of drought on continental and global scales, particularly to provide an improved assessment of climate change impact on drought.

Most global drought studies and near-real time drought monitoring programs focus on meteorological drought (in particular SPI, McKee et al., 1993), since meteorological data are widely available on a global scale. Other research has focused on soil moisture drought on global scale (e.g. Dai et al., 2004; Sheffield and Wood, 2007; Sheffield et al., 2009; Dai, 2011; Orlowsky and Seneviratne, 2013). Global soil moisture drought have been often examined (e.g. Dai et al., 2004; Dai, 2011; Sheffield et al., 2012) with the Palmer Drought Severity Index (PDSI Palmer, 1965), which is calculated from a simple soil water balance, with the threshold method in combination with a more comprehensive model (e.g. Sheffield and Wood, 2007; Sheffield et al., 2009) or through anomalies (e.g. Orlowsky and Seneviratne, 2013). For water resources, it is particularly relevant how meteorological and soil moisture drought propagate into hydrological drought (e.g. Peters et al., 2003; Tallaksen et al., 2009; Van Loon and Van Lanen, 2012). At large scales, Global Hydrological Models (GHMs) are used to produce runoff time series, which are then used for hydrological drought assessment. At the

continental scale, Andreadis et al. (2005) investigated runoff drought in the United States and Prudhomme et al. (2011) studied European runoff drought. Forzieri et al. (2014) project for the A1B scenario that future drought in streamflow will increase in many European regions, except for North and Northeast Europe. Corzo Perez et al. (2011b) and Van Huijgevoort et al. (2012) show hydrological drought characteristics at the global scale. These large-scale studies investigate which characteristics (frequency, scale, duration, severity) of past hydrological drought are captured with the GHMs to explore their potential to assess future continental and global drought. Recently, the WATCH (WATer and global CHange) project concluded a comprehensive multi-model analysis (e.g. Haddeland et al., 2011) that tested GHM performance against historic low runoff (e.g. Gudmundsson et al., 2012; Stahl et al., 2012) and drought (e.g. Prudhomme et al., 2011). Corzo Perez et al. (2011b) made a first attempt to use the outcome from the WATCH model suite to assess future hydrological drought across the globe (three General Circulation Models (GCMs), two scenarios, multiple hydrological models).

A detailed impact assessment on the importance of climate and catchment structure on drought occurrence is complicated since GHMs have a complex model structure with a large number of internal and external feedback mechanisms. To investigate the relative importance of climate and catchment structure on hydrological drought, Van Lanen et al. (2013) used a synthetic hydrological modelling approach to study the effects of these factors on hydrological drought characteristics on a global scale. The approach involved a conceptual hydrological model that was applied to a set of possible realizations of catchment characteristics (synthetic catchments) in combination with precipitation and evapotranspiration data from different climates around the globe. With this set-up Van Lanen et al. (2013) examined the relative importance of the physical catchment structure and meteorological forcing data (i.e. precipitation and evapotranspiration). They conclude that the physical catchments structure (i.e. the responsiveness of the groundwater system and soil type) has a similar impact on drought characteristics as climatology. However, the effects of climate change with respect to future hydrological drought across the world is largely unknown and difficult to study (Corzo Perez et al., 2011b).

The objective of this study is to examine the impact of climate change on hydrological drought at a global scale. Following the approach of Van Lanen et al. (2013) a synthetic hydrological model was used to model discharge time series at randomly selected locations in various climate regions around the world. Three GCMs provided model forcing data to the hydrological model and simulated drought were compared against those derived from a reanalysis data (WATCH) forced model over the period 1971-2000 to explore uncertainty due to GCM forcing. Thereafter the effect of climate change was studied by the inter-comparison of modelled discharge time series and associated drought characteristics against the control period (1971-2000) for all GCM scenarios and the periods 2020-2050 and 2070-2100. The results allow a discussion on the projected impact of climate change on hydrological drought char-

acteristics, including uncertainty, which, in addition to impacts on meteorological and soil water drought characteristics, provide key information for planning of future water resources.

9.2 Forcing data

9.2.1 WATCH Forcing Data

The WATCH Forcing Data (WFD) consist of time series of meteorological variables (e.g. rainfall, snowfall, temperature, wind speed) and are a product of the EU-FP6 project WATCH (WATer and global CHange). The WFD are derived from bias-corrected ECMWF ERA-40 reanalysis data (Uppala et al., 2005), which have a sub-daily, 1° resolution. For the WFD these data have been downscaled to 0.5° and temperature and specific humidity were bias corrected for elevation difference between the ERA-40 grid and WFD grid (Weedon et al., 2010, 2011). Bias corrections were applied to the daily temperature cycle and average temperature values using the CRU 2.0 data (Mitchell and Jones, 2005) and to the number of "wet" days using the CRU data, while precipitation totals were corrected with the GPCCv4 dataset (Schneider et al., 2008). The CRU grid was used for the projection of the WFD, resulting in a total of 67420 land points at $0.5° \times 0.5°$ resolution. The WFD for the period 1971-2000 have been used as a reference forcing dataset in this study. The WFD were successfully used in multiple hydrological studies (e.g. Corzo Perez et al., 2011a; Haddeland et al., 2011; Harding et al., 2011; Prudhomme et al., 2011; Gudmundsson et al., 2012; Stahl et al., 2012; Van Vliet et al., 2012; Van Huijgevoort et al., 2013; Van Loon et al., 2014). In this study the WFD were used to identify the reference hydrological situation for every selected location, with the synthetic hydrological modelling approach.

9.2.2 General Circulation Models

In this study the output from three coupled atmosphere-ocean GCMs for the SRES A2 scenario (Nakićenović and Swart, 2000) has been used. The SRES A2 scenario includes extensive emission of carbon dioxide and slow adaptation by the global population, leading to severe changes in future climatology. Through the EU-WATCH project simulation outcome from three GCMs was available on a global scale and used for this study. The GCMs included are ECHAM5 (Roeckner et al., 2003; Jungclaus et al., 2006), CNRM3 (Royer et al., 2002; Salas-Mélia, 2002) and IPSL (Hourdin et al., 2006; Madec et al., 1998; Fichefet and Maqueda, 1997; Goosse and Fichefet, 1999). Additional GCM simulations from other projects were not used since these used other bias correction approaches and data than the three GCMs selected for this study. Each GCM provides meteorological forcing for the period 1960-2100. The

Table 9.1 Three IPCC AR4 GCMs and their properties.

Centre	GCM	Horizontal res.	Vertical res.
MPI	ECHAM5/MPIOM T63	$\approx 1.9° \approx 200\ km$	31 Layers
CNRM	CNRM-CM3 T42	$\approx 2.8° \approx 300\ km$	45 Layers
IPSL	IPSL-CM4	$3.75° \times 2.5° \approx 300\ km$	19 Layers

period 1971-2000 was used as control period. The same procedure as for the WFD was applied in WATCH to downscale each GCM to the higher resolution 0.5° grid of the WFD. The WFD were used to determine the bias correction required for rainfall, snowfall, minimum, mean and maximum air temperature for the control period. The procedure is described in more detail by Piani et al. (2010a,b); Chen et al. (2011); Haerter et al. (2011). More detailed information on the GCMs can be found in Table 9.1. The data from the GCMs were used as meteorological input data for the synthetic hydrological modelling approach to produce discharge time series and associated drought characteristics for: (i) the control period (1971-2000), and (ii) the periods 2021-2050 and 2071-2100 to intercompare obtained drought characteristics against those derived from the reference model (1971-2000).

The advantages of this mini-ensemble is that the bias correction was performed by experts in the field both for the control period (Piani et al., 2010a,b; Haerter et al., 2011) using the WFD dataset (Weedon et al., 2010, 2011) to correct the models and for the future (Hagemann et al., 2011; Chen et al., 2011). This resulted in consistent downscaled and bias-corrected GCM data for 1963-2100. The period 1963-1970 was used to initialize the hydrological model and make sure that the groundwater and discharge simulations where no longer influenced by the initial conditions. Although this mini-ensemble most likely under samples the climate variability, the advantage of having a long initialization period and a validated bias correction is deemed more important.

9.3 Model framework

9.3.1 Model description

The synthetic hydrological model, is a lumped conceptual hydrological model, which consists of reservoirs for snow cover, soil moisture and groundwater (Figure 9.1). The model concept is a simplified representation of the natural system that simulates daily fluxes and state variables. The synthetic hydrological model generates time series of potential realizations for soil moisture storage and groundwater discharge

without use of specific local catchment information apart from meteorological forcing (synthetic catchments). The simulations do not claim to provide actual site specific soil moisture storage and groundwater discharge, but rather give a possible realization of these variables given the local meteorological data (e.g. Van Lanen et al., 2013; Van Loon et al., 2014). The water balance of the modelled soil moisture is given by:

$$SS(t) = SS(t-1) + P_{ra}(t) + Q_{sn}(t) - E_{act}(t) - Q_s(t) \tag{9.1}$$

where, SS is the soil moisture storage (mm), P_{ra} the rainfall ($mm\ d^{-1}$), Q_{sn} the snow melt ($mm\ d^{-1}$), E_{act} the actual evapotranspiration ($mm\ d^{-1}$) and Q_s is recharge generated by percolation through the unsaturated zone ($mm\ d^{-1}$). The model is forced with daily temperature, precipitation and potential evapotranspiration to enable snow accumulation, soil moisture, actual evapotranspiration and discharge simulations. Estimates of daily evapotranspiration were calculated using the Penman-Monteith reference evapotranspiration (McMahon et al., 2013). The potential evapotranspiration was calculated from daily temperature (minimum, mean, maximum), air pressure and wind speed (Allen et al., 2006). The daily mean temperature was also used in the snow-module for snow accumulation and melt, following the widely-accepted approach of the HBV-model (Seibert, 2002). Precipitation is simulated as snow when air temperature is below a pre-defined threshold, snow melt only occurs above the threshold temperature and is simulated with the degree-days approach (Clyde, 1931; Collins, 1934). The snow water balance of the snow module is given by:

$$Sn(t) = Sn(t-1) + P_{sn}(t) - Q_{sn}(t) \tag{9.2}$$

where Sn is the snow storage (mm) and P_{sn} is snowfall ($mm\ d^{-1}$). The groundwater recharge ($mm\ d^{-1}$) is given by:

$$R_{ch}(t) = Q_s(t) + Q_b(t) \tag{9.3}$$

where $Q_s(t)$ is recharge generated by unsaturated zone ($mm\ d^{-1}$) and $Q_b(t)$ is recharge generated by bypass in the unsaturated zone ($mm\ d^{-1}$). The percolation through the unsaturated zone is given by:

$$\begin{array}{ll} Q_s(t) = SS(t) - SS_{FC} & \text{if } SS(t) \geq SS_{FC} \\ Q_s(t) = (\frac{SS(t)-SS_{CR}}{SS_{FC}-SS_{CR}})^{b_{xin}} Ksat & \text{if } SS_{CR} \leq SS(t) \leq SS_{FC} \\ Q_s(t) = 0 & \text{if } SS(t) \leq SS_{CR} \end{array} \tag{9.4}$$

where $SS(t)$ (mm) is the soil moisture content at time t (d), b_{xin} is a shape parameter derived from the soil retention curve ($-$), $Ksat$ is the unsaturated hydraulic conductivity at field capacity ($mm\ d^{-1}$), SS_{CR} and SS_{FC} (mm) are the critical and field capacity soil moisture content, respectively. The bypass to the groundwater ($Q_b(t)$) is 50% of the rainfall above 2 mm, when the soil is below SS_{CR} to simulate flow through the macropores of the unsaturated zone. A soil with an intermediate soil moisture supply capacity was selected to simulate the response of the unsaturated zone (Van Lanen et al., 2013). This soil has a total supply capacity of 125 mm where

about 75 mm is readily available for evapotranspiration. The water balance of the groundwater system is given by:

$$SG(t) = SG(t-1) + R_{ch}(t) - Q_{out}(t) \tag{9.5}$$

where SG is the groundwater storage (mm) and Q_{out} is the groundwater discharge ($mm\ d^{-1}$). The Q_{out} is calculated with the De Zeeuw-Hellinga approach (Kraijenhof van de Leur, 1962; Ritzema, 1994):

$$Q_{out}(t) = Q_{out}(t-1) * e^{\frac{-1}{j}} + R_{ch}(t) * (1 - e^{\frac{-1}{j}}) \tag{9.6}$$

where j is the groundwater response parameter (d), which can be derived from data on the aquifer transmissivity, storativity and the distance between rivers. The j-value in this study was fixed to 250 d, which corresponds to an intermediate-responding groundwater system. The groundwater discharge is hereafter called discharge ($Q = Q_{out}$). The ability of the synthetic model to reproduce observed streamflow was demonstrated by Tijdeman et al. (2012). The synthetic model was evaluated against observed drought characteristics of four contrasting catchments in Europe. It was shown that the model is capable to correctly simulate hydrological drought characteristics. The Nash-Sutcliffe (NS, Nash and Sutcliffe, 1970) for the selected catchments was between 0.35 - 0.75, with an improved performance for the low-flow conditions (NS 0.35 - 0.85). For a more detailed description of the synthetic hydrological modelling approach or the validation results, the reader is referred to Tijdeman et al. (2012); Van Lanen et al. (2013); Van Loon et al. (2014).

9.3.2 Drought identification

Hydrological drought characteristics (e.g. drought duration and deficit volume) were derived from simulated time series of daily discharge (Q) using the threshold level approach (Yevjevich, 1967; Tallaksen et al., 1997; Hisdal et al., 2004). In this study the Q_{80} ($mm\ d^{-1}$) was derived from the flow duration curve, where the Q_{80} is the threshold which is equalled or exceeded for 80% of the time. The Q_{80} has been used in multiple studies where drought is studied (e.g. Fleig et al., 2006; Parry et al., 2010). A monthly threshold was applied, where the Q_{80} is derived for every month of the year. With a moving average window of 30-days the threshold was smoothed, resulting in the variable monthly threshold used for this study (Van Loon and Van Lanen, 2012). The Q_{80} obtained from the reference period was also used for the future period to enable drought identification in the period 2000-2100, relative to 1971-2000. Similar to Chapter 8 the drought state is given by:

$$Ds(t,n) = \begin{cases} 1 & \text{for } Q(t,n) < Q_{80}(t,n) \\ 0 & \text{for } Q(t,n) \geq Q_{80}(t,n) \end{cases} \tag{9.7}$$

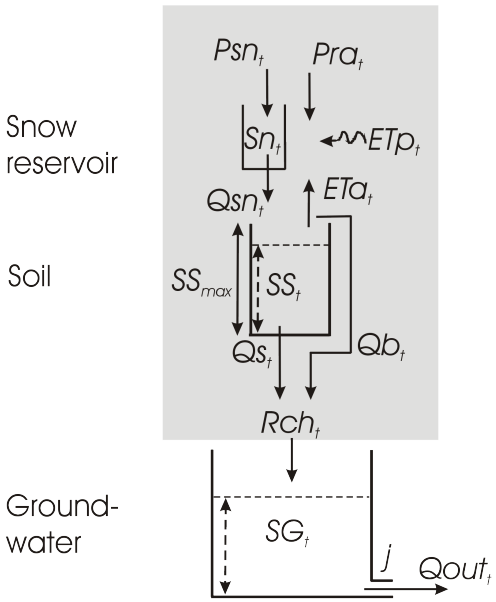

Figure 9.1 Model set-up of the synthetic hydrological model used in this study. The model consists of three partitions, Snow, Soil and Groundwater. P_{sn} snowfall, P_{ra} rainfall, ET_p potential evapotranspiration, ET_a actual evapotranspiration, S_n snow storage, SS soil storage, SS_{max} maximum soil storage, Q_{sn} snow melt, Q_s recharge to the groundwater from the unsaturated zone, Q_b bypass flow, R_{ch} total recharge to groundwater, SG groundwater storage, j groundwater response parameter, Q_{out} groundwater discharge and t is the time index.

where $Ds(t)$ is a binary variable indicating if a location is in drought at time t. The drought duration for each event was calculated with:

$$Dur_i = \sum_{t=S_i}^{L_i} Ds(t) \tag{9.8}$$

where Dur_i is the drought duration (d) of event i, S_i the first time step of an event i and L_i the last time step of the event. The Percentage Drought per Year (PDY) was used in this study as a measure of drought occurrence that enables a comparison between the simulated discharge time series of different time periods (e.g. 2021-2050 relative to 1971-2000). The PDY was calculated by:

$$PDY = \frac{\sum_{t=1}^{T} Ds(t) * 365}{T} \tag{9.9}$$

where PDY is the fraction of the total simulation period that a location is in drought ($d\ y^{-1}$) and T is the total number of timesteps. Please note that PDY=73 $d\ y^{-1}$ for the control period 1971-2000 by definition. The deficit volume was defined by:

$$Def(t,n) = \begin{cases} Q_{80}(t,n) - Q(t,n) & \text{for } Ds(t,n) = 1 \\ 0 & \text{for } Ds(t,n) = 0 \end{cases} \tag{9.10}$$

where $Def(t)$ is the daily deficit volume of drought i (mm). The total drought deficit volume for each drought event was calculated with:

$$Def_i = \sum_{t=S_i}^{L_i} Def(t) \tag{9.11}$$

where Def_i is the total deficit volume of the drought event i (mm). The deficit volume is the cumulative deviation of the discharge from the threshold over the duration of a drought event. Furthermore, the standardized deficit volume (d) was obtained with:

$$StDef_i = \frac{Def_i}{\overline{Q}} \tag{9.12}$$

where $StDef_i$ is the deficit volume of event i (d) divided by $\overline{Q}$, the mean yearly discharge $(mm\ d^{-1})$. $StDef_i$ was introduced to enable a comparison across the globe between locations with different flow magnitudes. Since the deficit volume (Def_i) is highly correlated to the discharge, the obtained $StDef$ provides the drought severity relative to the local hydrological situation. The $StDef$ can be interpreted as the number of days that the mean yearly discharge is missing. The drought duration and standardized deficit volume are hereafter referred to as the duration and deficit volume. If the Q_{80} equals 0 $mm\ d^{-1}$ for more than 20% of the time, no drought characteristics were calculated since by definition a drought will not occur (Equation 9.7). These locations were excluded from the analysis, since frequent zero discharge situations are part of the local climate (i.e. aridity) and are not a situation with below normal water availability. When a drought is already present at the beginning of a simulation period or still present at the end no valid average characteristics could be obtained and therefore the drought event was excluded from the analysis to avoid including incomplete drought events in the statistics.

9.3.3 Similarity Index

The Similarity Index (SI) was introduced as a measure to examine changes in drought characteristics (Van Lanen et al., 2013). Bivariate probability distributions (Wand and Jones, 1995) were used to find relations between drought duration (Equation 9.8) and deficit volume (Equation 9.12). The bivariate probability distributions were compared for different time periods and their joint occurrence was evaluated with the SI. The area of the 90% probability mass of the bivariate probability distribution field was calculated and used for further evaluation. Both low and high extreme values of Dur_i and Def_i were excluded, since the focus of this study is not on changes in the most extreme drought conditions. The similarity index (SI) quantifies the degree of

overlap (%) between two 90 % $Dur - StDef$ probability fields as follows:

$$\begin{aligned} SI &= \frac{R1 \cap R2}{R1} \cdot 100 \\ R1 &= \sum_{x=1}^{m} \sum_{Y=1}^{n} MR1(m,n) \qquad \text{if } MR1(m,n) = 1 \\ R1 \cap R2 &= \sum_{x=1}^{m} \sum_{Y=1}^{n} MR1(m,n) \text{if } MR1(m,n) = 1 \text{ and } MR2(m,n) = 1 \end{aligned} \tag{9.13}$$

where $R1$ is the 90 % $Dur - StDef$ probability field of realization of period 1 (e.g. 1971-2000), $R1 \cap R2$ is the coinciding 90 % $Dur - StDef$ probability fields of realizations of period 1 and 2 (e.g. 1971-2000 and 2021-2050, respectively), m and n indicate probable realizations of Dur_i and Def_i. $MR1$ and $MR2$ are matrices, $MR1$ contains the conditional probabilities of realization of period 1, and $MR2$ the field of realization of period 2. $MR1(m,n)$ and $MR2(m,n)$ are binary quantities where 1 equals a value within, and 0 a value outside the 90 % $Dur - StDef$ probability field of realizations 1 and 2, respectively. In this study $m \cdot n$ was set at $150 \cdot 150$ and physical limits of Dur and $StDef$ where fixed to 1296 (d) and 256 (d), respectively. By definition the SI can range between 0% (no joint occurrence) to 100% (complete joint occurrence). For a more detailed description of the SI the reader is referred to Van Lanen et al. (2013).

9.3.4 Selection of evaluation locations

For a global evaluation of the change in drought duration and deficit volume as result of climate change, locations (i.e. WATCH cells) were randomly selected around the world. The Köppen-Geiger climate classification (Köppen, 1900; Geiger, 1954, 1961) was used to ensure that sufficient locations were selected in all different major climate regions. The five climate types distinguished in this study are: Equatorial (A), Arid (B), Warm temperate (C), Snow (D) and Polar climates (E). The global map with Köppen-Geiger climate classification was recalculated based on the WFD, to obtain correct positioning of climate regions (Figure 9.2). Van Lanen et al. (2013) found that 1495 locations were sufficient to adequately include world's climates and the same locations were also used for this study (21 locations were excluded due to large numbers of no flow conditions). They show that at least 30 randomly selected locations are required per major climate region to obtain reliable general drought characteristics. The selected locations were distributed over the climate types A, B, C, D and E as follows: 16%, 21%, 16%, 34% and 13%, which reflect differences in area of major climate regions.

9.3.5 Impact assessment of climate change

To examine the impact of climate change on characteristics of discharge drought, the synthetic hydrological modelling approach was used and forced with meteorological

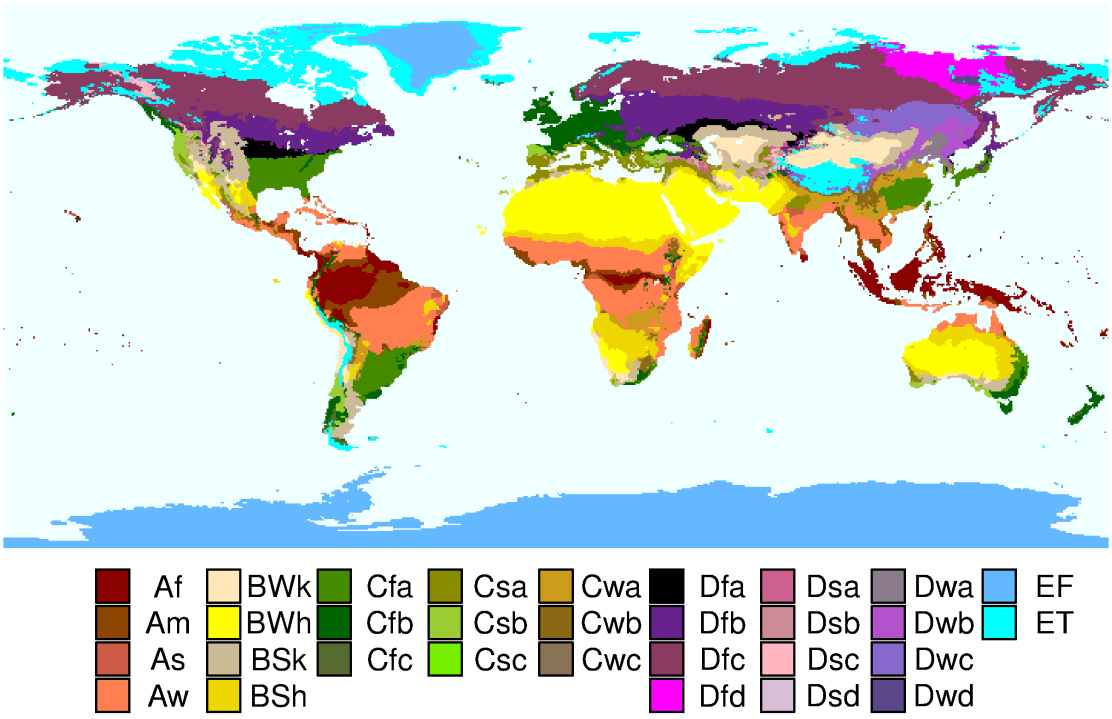

Figure 9.2 The Köppen-Geiger climate classification, based on the climatology of the WATCH Forcing Data (1958-2001).

data from three GCMs (GCM forced) over the period 1960-2100. This period was divided into three evaluation periods, namely 1971-2000, 2021-2050, 2071-2100. An eleven year warm-up period (1960-1970) was applied for the hydrological model to remove biases resulting from the initial conditions. The monthly Q_{80} was derived over the period 1971-2000 to determine the variable threshold (Section 9.3.2). The 1971-2000 threshold was applied to the two other future periods, to enable calculation of the drought characteristics (D and $StDef$, Equations 9.8 and 9.12), and to determine the effect of climate change relative to the period 1971-2000. The effect of climate changes on drought duration and deficit volume was studied for all different major climate regions. The discharge drought characteristics of each GCM forced hydrological model over the control period (1971- 2000) were compared against the characteristics derived from the model forced with the WFD for the same period (reference model) to explore uncertainty due to GCM forcing. Ideally, there should be only minor differences in drought characteristics between the characteristics derived from discharge simulated with the GCM forcing and the simulation with the WFD, since the control periods of each GCM are bias corrected to match the WFD (Piani et al., 2010a,b; Haerter et al., 2011; Chen et al., 2011; Hagemann et al., 2011). The changes in drought characteristics were evaluated for the period 2021-2050 and 2071-2100 by comparing against the control period of each GCM forced hydrological model. For the evaluation the SI was calculated for all major climate types and used to determine the changes

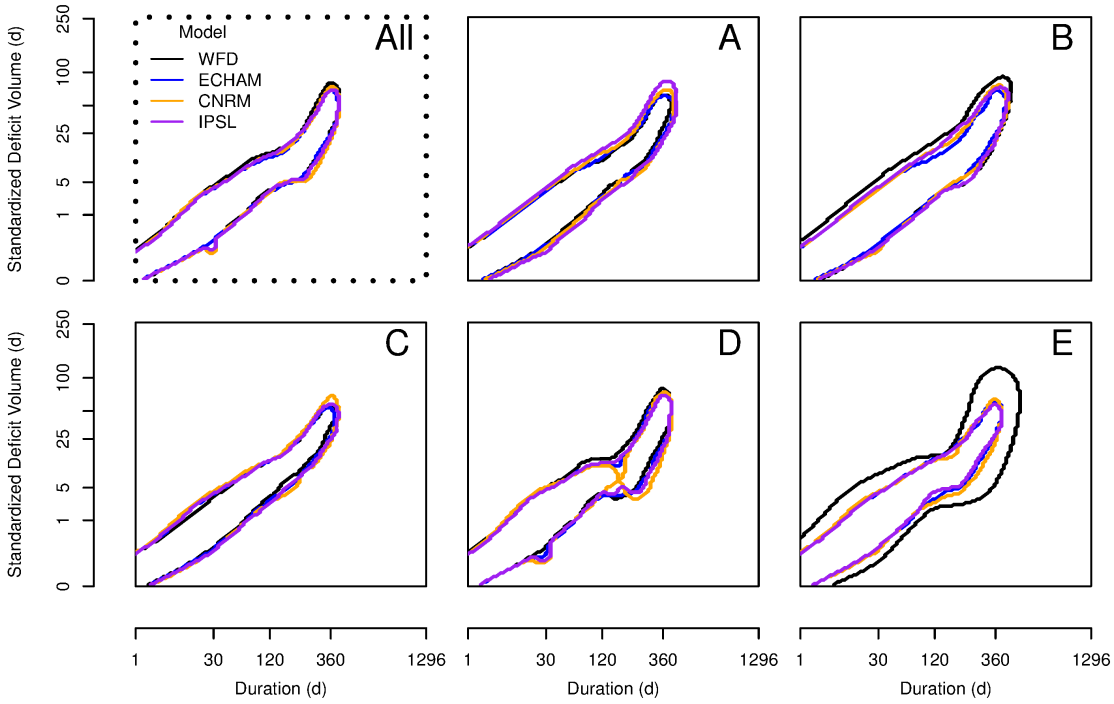

Figure 9.3 Bivariate probability functions for two hydrological drought characteristics (duration and standardized deficit volume) for all climate types (All) and individual major climate types, Equatorial (A), Arid (B), Warm temperate (C), Snow (D) and Polar climates (E) obtained from simulations of the synthetic hydrological model, using meteorological forcing by the WATCH Forcing Data (WFD, reference) and General Circulation Models; ECHAM, CNRM and IPSL.

in drought duration and deficit volume as a result of a changing climate. For the seasonal analysis of changes in drought deficit volumes, the season for the location at the Southern hemisphere has been transposed to match the Northern hemisphere climatology.

9.4 Results

9.4.1 Control period

Hydrological drought derived from discharge time series that were simulated with the synthetic hydrological modelling approach using re-analysis data (WFD) as meteorological forcing (reference model) were the benchmark in this study. The hydrological drought characteristics were intercompared for the control period from 1971-2000 with those obtained from the same hydrological model that was forced with downscaled and bias-corrected outcome from three GCM forced models.

Table 9.2 Similarity Index (SI) between the reference model with meteorological forcing from the WATCH Forcing Data and models with meteorological forcing from three General Circulation Models (ECHAM, CNRM, IPSL) for the control period (1971-2000). SI is given for all major climates, Equatorial (A), Arid (B), Warm temperate (C), Snow (D) and Polar climates (E) and averaged over all climates.

	WFD					
	A	B	C	D	E	All
ECHAM	100	75	99	92	67	91
CNRM	100	82	100	87	73	94
IPSL	100	85	98	90	65	93

The bivariate density distributions obtained for the control period for all three GCM forced models show large similarity with the reference model for all climate types (Figure 9.3). However, some deviations occur for the polar (E) and arid (B) climate types where the GCM forced models show less spread in the drought characteristics than the reference model. In the snow dominated (D) climate type a division between short duration and long multi-year drought events was found. This is caused by the fact that groundwater storage is not replenished in the winter season. Below zero temperatures in the following summer prevent snowmelt and groundwater recharge and hence drought conditions will not lift. When summer temperatures are too low to generate enough snow melt to replenish the groundwater, this drought will continue over the next winter. If the drought continues over winter this will automatically result in a multi-year drought and hence long drought durations (Van Loon et al., 2014). Overall the GCM forced models show a large resemblance to the reference model throughout the climate regions, especially for the less extreme climate types. This is also illustrated through the Similarity Index (SI, Equation 9.13) when the GCM forced models are compared against the reference model (Table 9.2). For example, the SI for the A-climate is 100%, which means that the bivariate distribution of drought duration and deficit volume for the 3 GCM forcing datasets is identical to the WFD forcing. The SI for the C-climate is almost 100%, and for the D-climate around 90%. For the B-climate the SI is still 75% or more, whereas for the E-climate the SI is above 60%.

The average drought duration and deficit volume for the major climates and averaged over all climates show that the GCM forced models are in good agreement with the reference model with some mismatch in the extreme arid and polar climate types (Figure 9.4 and 9.5). The results from Table 9.3 support the SI findings (Figure 9.3 and Table 9.2) that the GCMs are capable to produce realistic meteorological forcing for hydrological drought assessment under most climate conditions, but show difficulties in desert and polar climates. The drought duration derived from the GCM

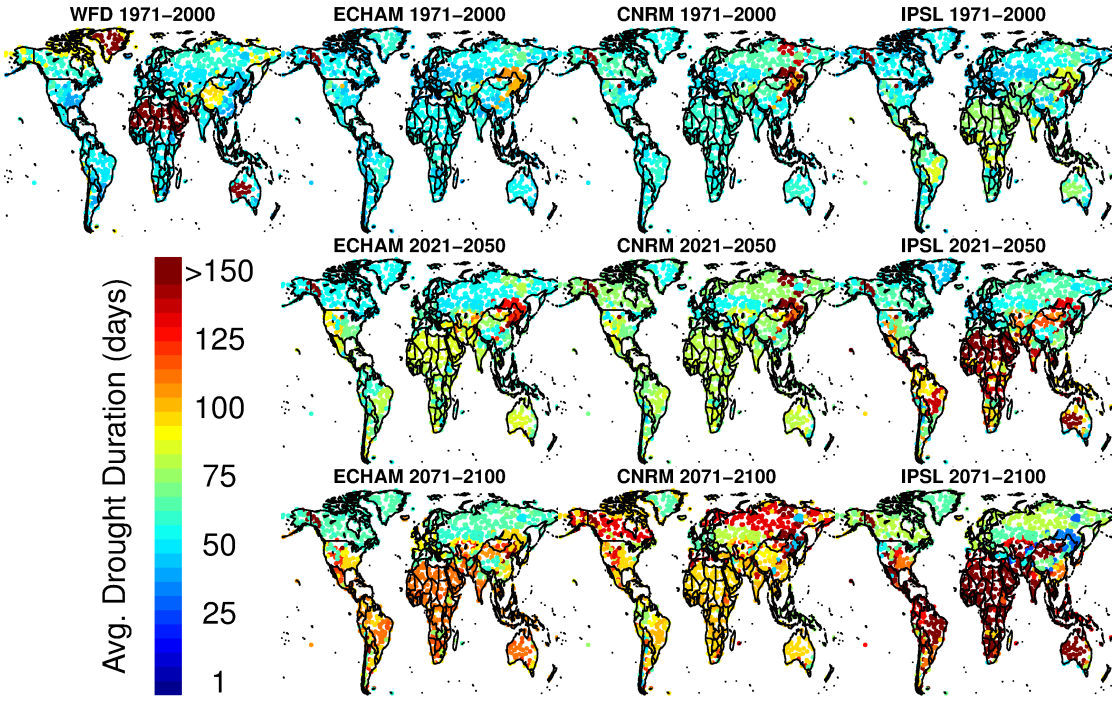

Figure 9.4 Spatial distribution of average hydrological drought duration for different time periods, obtained from simulations of the synthetic hydrological model, using meteorological forcing by the WATCH Forcing Data (WFD) and three General Circulation Models, ECHAM, CNRM and IPSL.

forced models for the A, C and D major climate types deviates less than 10% from the duration obtained for the reference model (Table 9.2, IPSL for the A climate type is an exception). For the B and E climates the deviation is larger, in particular for the latter (up to more than 50%). The deficit volume shows a similar pattern but relative deviations are larger because of smaller magnitude (Table 9.2). Uncertainties in the differences are low (Table 9.3), increasing the confidence that GCMs can correctly reproduce hydrological drought characteristics for the control period.

The monthly drought deficits for the control period for all three GCM forced models show large similarity with the reference model derived from the WFD (Figure 9.6). The GCM forced simulation show identical patterns with respect to the monthly distribution of the drought deficits. An exception is found for the polar (E) climate type, where the drought deficit volume in summer is overestimated by the GCM forced simulations.

The deviation of the GCM forcings from the reference situation that are found are most likely caused by the bias correction applied to GCM forcing data. Bias correction is applied to the number of rain days and total precipitation volumes. However, the frequency, co-occurrence and magnitude of precipitation is not bias-corrected.

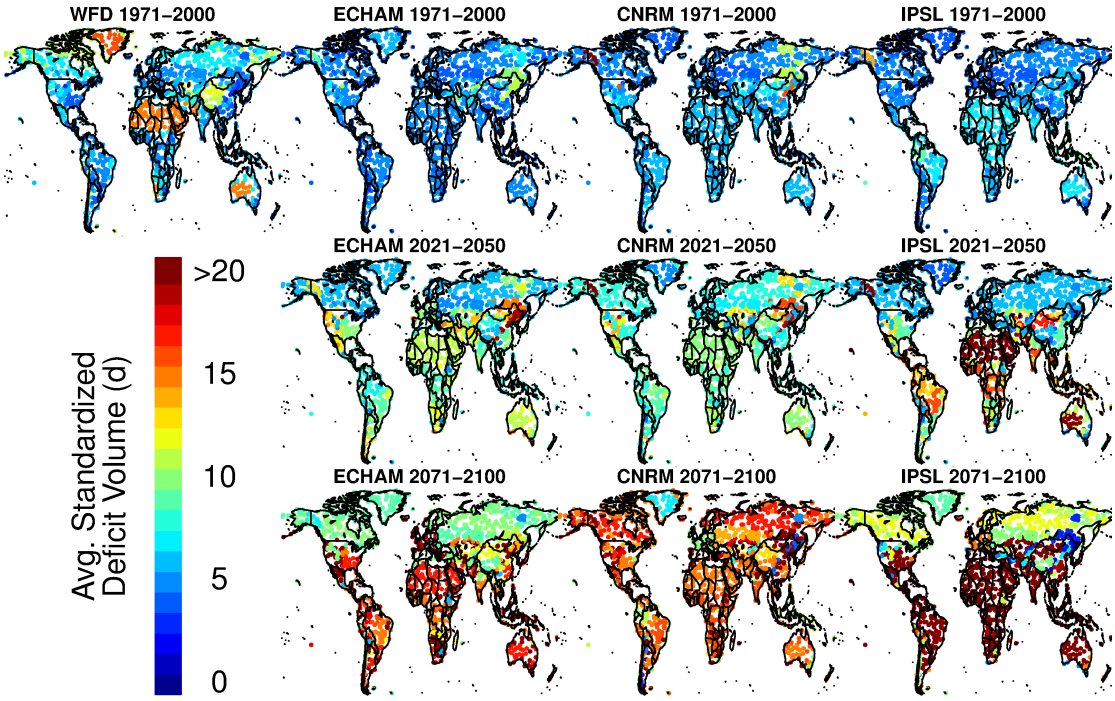

Figure 9.5 Spatial distribution of average standardized deficit volume for different time periods, obtained from simulations of the synthetic hydrological model, using meteorological forcing by the WATCH Forcing Data (WFD) and three General Circulation Models, ECHAM, CNRM and IPSL.

Since the precipitation is corrected using a fitted gamma-distribution these second order statistics are not included in the bias correction. This could (especially in a dry climate) have a significant impact on the drought characteristics, where little rainfall could end a drought event. In the polar climate, the interaction between precipitation amounts and temperatures is of significant importance with respect to ending of drought events. If the forcing of the GCM would have exactly the same statistical properties as the WFD, no differences would occur in drought characteristics. Therefore, it is concluded that the statistical properties of the precipitation and temperature are not fully matched for the polar climates and to a lesser extent for the B-climate, which significantly impacts the drought characteristics in these climates.

9.4.2 Future period

All GCM forced models show a decrease in the number of hydrological drought throughout climate types (Figure 9.7, upper row, note logarithmic scale). This decreasing number of drought is associated with an increase in the duration by 143 to 157% for all GCM forced models in 2071-2100 (Figure 9.7 and 9.8, second row, Table 9.4). The most severe drought also show a very strong increase relative

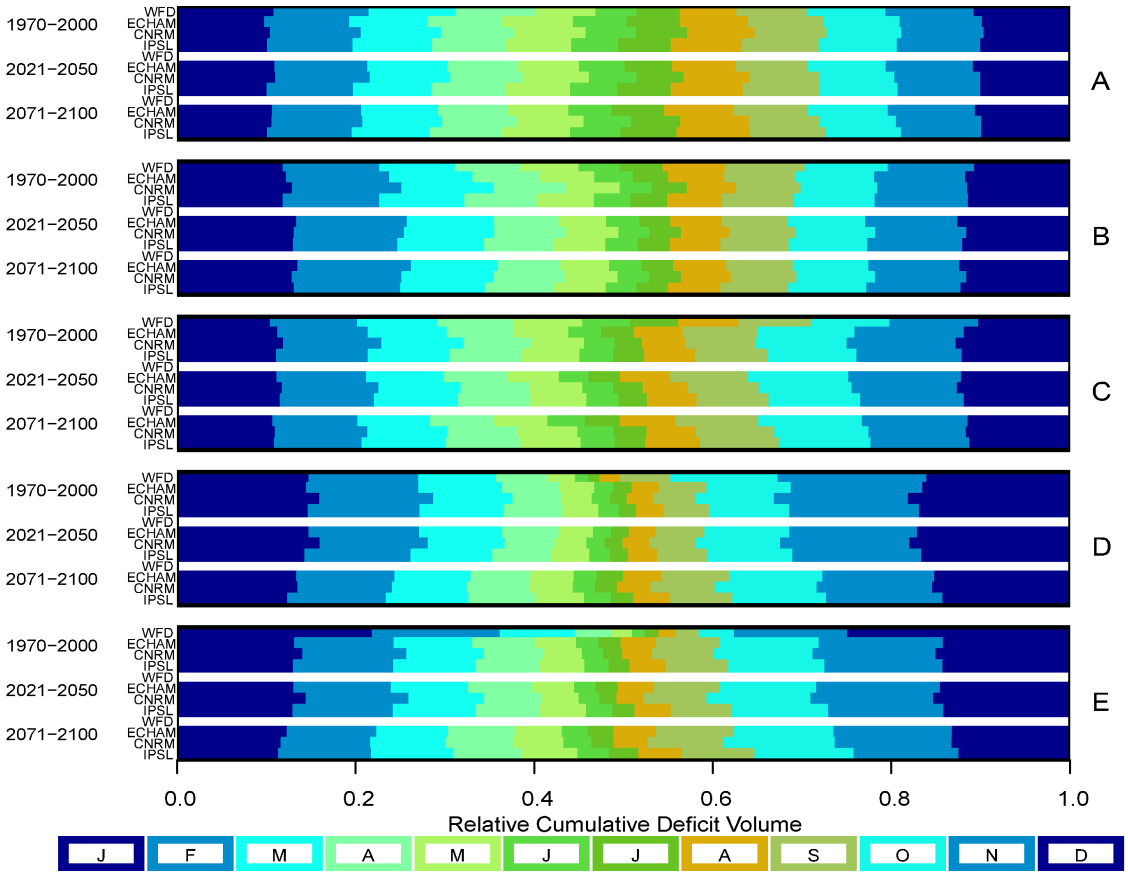

Figure 9.6 Monthly distribution of the annual total cumulative deficit volume over the year, obtained from simulations of the synthetic hydrological model, using meteorological forcing by the WATCH Forcing Data (WFD) and General Circulation Models, ECHAM, CNRM and IPSL. Results are shown per analysis period and for each major climate type separately.

to the control period and the spread in duration between locations strongly increases (Figure 9.7). The overall effect of climate change on the PDY over the two future periods shows a decreasing trend (Figure 9.7, third row). The total time a location is in drought decreases by 67 to 74% in 2071-2100 (Table 9.4), indicating that the locations are less in drought throughout the 30 year period (Figure 9.8). The deficit volume shows an overall increase of slightly over 200% in 2071-2100 (Table 9.4, Figure 9.5), which indicates that although drought are less frequent, the severity in both duration and deficit volume increases for the remaining events. Uncertainties in the estimated relative changes are low, 2 - 5% for duration and 1 - 5% for the PDY, (Table 9.4), with the exception of the deficit volume (4 - 64%). This indicates that it is more difficult for the ensemble of GCMs to indicate changes in deficit volumes with high certainty.

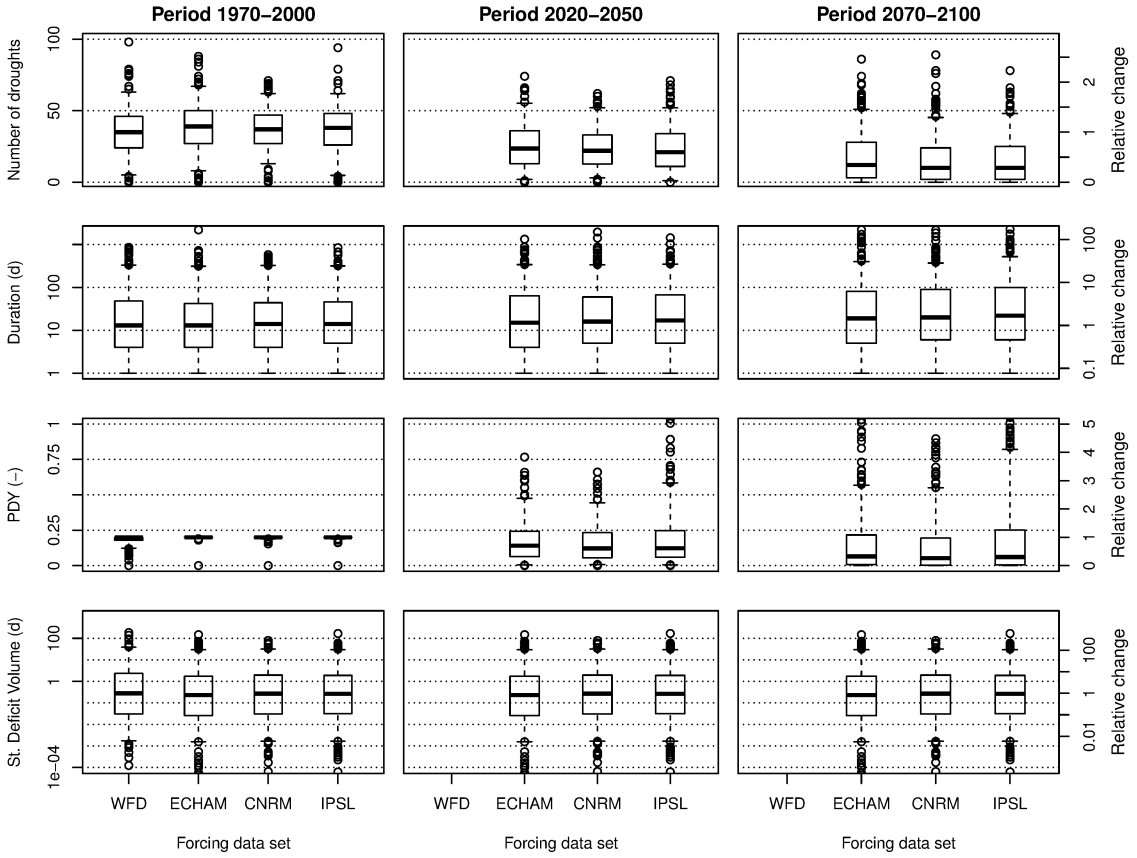

Figure 9.7 Distribution of three discharge drought characteristics obtained from a synthetic hydrological model using meteorological forcing from the WATCH Forcing Data (reference model) and three models with meteorological forcing from General Circulation Models (ECHAM, CNRM and IPSL) for the control period (1971-2000). Row one indicates the number of hydrological drought per evaluation period, row two the average drought duration, row three the percentage of the year in drought and the last row gives the average standardized deficit volume.

Table 9.3 Absolute average hydrological drought characteristics for the control period (1971-2000), including relative difference for the three GCMs, relative to the WATCH Forcing Data and the standard deviation of the relative difference. Characteristics are provided for Equatorial (A), Arid (B), Warm temperate (C), Snow (D) and Polar climates (E).

		WFD	ECHAM		CNRM		IPSL	
		Abs.	Abs.	Rel.	Abs.	Rel.	Abs.	Rel.
Duration (d)	A	54.3	57.3	106 ± 3%	59.5	110 ± 3%	70.7	130 ± 10%
	B	79.4	57.4	72 ± 3%	63.1	79 ± 3%	66.5	84 ± 4%
	C	50.2	49.3	98 ± 3%	54.6	109 ± 3%	51.4	102 ± 3%
	D	57.1	56.5	99 ± 4%	57.0	100 ± 12%	55.5	97 ± 6%
	E	105.0	48.8	46 ± 4%	51.8	49 ± 6%	47.2	45 ± 4%
	All	66.7	59.8	90 ± 2%	69.0	103 ± 4%	66.6	100 ± 2%
Standardized deficit volume (d)	A	5.31	4.58	86 ± 5%	5.25	99 ± 5%	6.61	124 ± 6%
	B	8.44	4.89	58 ± 4%	5.85	69 ± 4%	5.47	65 ± 4%
	C	4.73	4.26	90 ± 5%	5.01	106 ± 5%	4.13	87 ± 5%
	D	5.61	4.82	86 ± 4%	4.43	79 ± 11%	4.14	74 ± 5%
	E	10.89	4.08	37 ± 4%	4.24	39 ± 6%	3.64	33 ± 4%
	All	6.58	5.05	77 ± 2%	5.94	90 ± 4%	5.24	80 ± 2%

The projected changes in the median of discharge drought characteristics (duration, deficit volume and PDY) for each major climate type are included in Table 9.4. The duration increases relative to the control period in all major climate regions, where the period 2071-2100 is more affected than 2021-2050 (Table 9.4). The strongest increase occurs for the equatorial and arid climates, where duration increases up to 181% for IPSL (Table 9.4). For the snow and polar climate (D, E) the increase in duration is smaller (114-138%) and lower than for the warmer A, B and C climates.

The PDY is projected to decrease throughout the 21^{st} century (Figure 9.8, Table 9.4). However, changes vary throughout climate regions. Averaged over all climates by the end of the century, median PDY will decrease to 26-33% relative to the control period, leading to an average of $\approx$ 22 $d\ y^{-1}$. For the equatorial climate (A) the direction of the change is not uniform. The IPSL forced model shows an increase for the equatorial climate (A) in 2071-2100 (128%), while both ECHAM and CNRM show that the PDY will decrease throughout all climate types (74% and 44%). For the other climate regions the direction of the change is uniform and shows a decrease in the PDY. For the snow climate, the changes are largest, the total PDY reduces to 5-8% relative to the control period, leading to an average PDY of $\approx$ 5 $d\ y^{-1}$ by the end of the 21^{st} century.

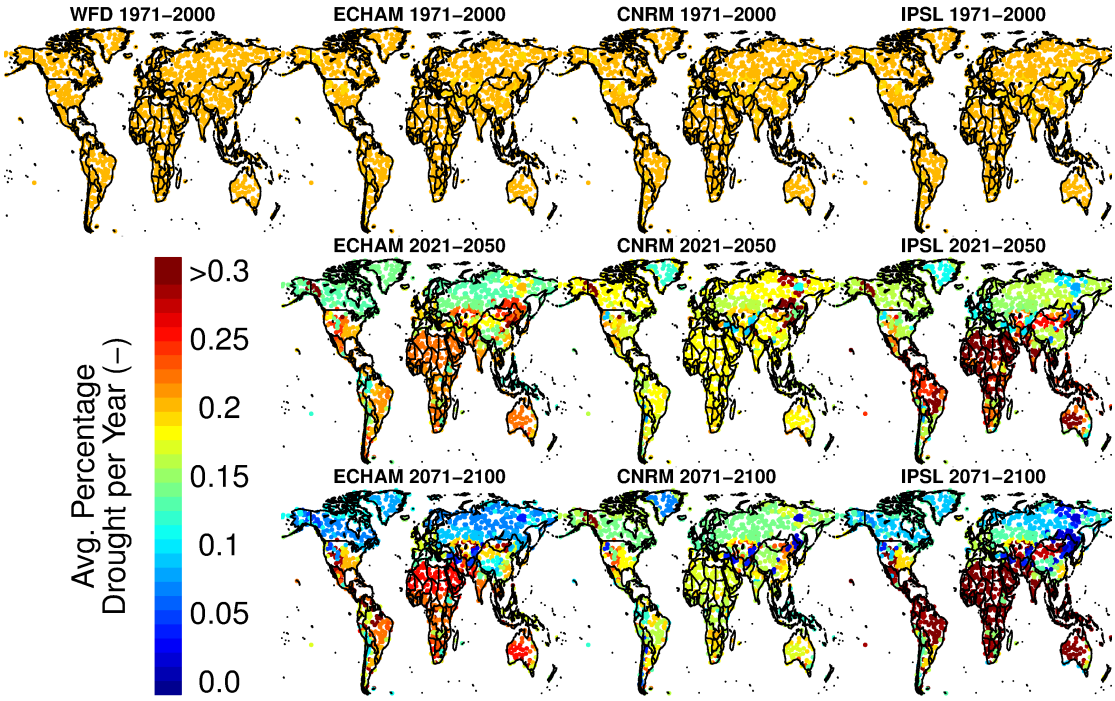

Figure 9.8 Spatial distribution of average Percentage Drought per Year for different time periods, obtained from simulations of the synthetic hydrological model, using meteorological forcing by the WATCH Forcing Data (WFD) and General Circulation Models, ECHAM, CNRM and IPSL.

A substantial increase was found for the deficit volume for all climate regions in both future periods, where the mean deficit volume clearly increases over the century (Figure 9.5, Table 9.4). This increase is strongest for the A, B and C climates, where the ranges increase by 217 to 327%, leading to median deficit volumes between 9.24 and 21.6 d, i.e. 9.24 and 21.6 times the mean discharge.

Seasonal changes in the relative importance of the drought deficit are small, with the exception of the polar (E) and snow dominated (D) climate types (Figere 9.6). In these regions a shift to more spring and summer dominated drought are projected. This is caused by shifts in the snowmelt season due to temperature rise (as a result of climate change), resulting in a lower water availability in late spring and summer (development towards warm snow season drought, Van Loon and Van Lanen, 2012). This effect is not found in the other major climate, since the discharge seasonality in the regions is not dominated by snow accumulation and melt periods. Although locally, the changes in the drought seasonality might be severe, on a global scale no changes have been found as a result of changes in climatology (e.g. shifts in precipitation patterns).

For all future GCM forced models the 90% probability fields were calculated and the changes relative to the control period are presented using the SI (Table 9.5). All

Table 9.4 Changes in median of drought characteristics (% relative to control period, 1971-2000, including standard deviation) for climate types: Equatorial (A), Arid (B), Warm temperate (C), Snow (D) and Polar climates (E).

		2021-2050			2071-2100		
		ECHAM	CNRM	IPSL	ECHAM	CNRM	IPSL
Duration (d)	A	142 ± 4	138 ± 4	131 ± 12	175 ± 7	169 ± 5	181 ± 15
	B	142 ± 4	133 ± 3	144 ± 6	175 ± 6	160 ± 4	181 ± 12
	C	133 ± 4	123 ± 3	115 ± 5	150 ± 7	162 ± 6	162 ± 7
	D	107 ± 7	93 ± 15	100 ± 11	129 ± 8	121 ± 29	114 ± 12
	E	100 ± 4	108 ± 16	108 ± 8	123 ± 6	138 ± 23	131 ± 7
	All	115 ± 3	114 ± 6	121 ± 5	146 ± 3	143 ± 9	157 ± 6
PDY ($d\ y^{-1}$)	A	81 ± 5	75 ± 4	112 ± 5	74 ± 4	44 ± 4	128 ± 5
	B	95 ± 4	81 ± 3	98 ± 4	89 ± 4	56 ± 3	99 ± 4
	C	78 ± 4	65 ± 4	49 ± 3	41 ± 4	40 ± 3	22 ± 4
	D	57 ± 3	49 ± 3	47 ± 2	8 ± 3	5 ± 3	8 ± 2
	E	61 ± 4	53 ± 4	52 ± 3	22 ± 4	19 ± 4	25 ± 4
	All	70 ± 2	61 ± 1	62 ± 2	33 ± 2	26 ± 1	30 ± 2
Standardized deficit volume (d)	A	193 ± 7	194 ± 7	182 ± 25	301 ± 18	317 ± 13	327 ± 40
	B	206 ± 9	179 ± 7	218 ± 16	305 ± 15	268 ± 12	310 ± 64
	C	164 ± 10	145 ± 7	134 ± 9	217 ± 21	220 ± 20	247 ± 22
	D	131 ± 8	103 ± 18	117 ± 11	144 ± 12	152 ± 36	126 ± 25
	E	115 ± 7	128 ± 20	115 ± 8	147 ± 14	170 ± 35	167 ± 18
	All	155 ± 4	139 ± 7	146 ± 8	206 ± 7	214 ± 12	222 ± 22

models indicate that changes occur with a similar magnitude for all major climate types. For example, the SIs obtained with the ECHAM forced model show that 19% of drought characteristics (duration and deficit volume) of events in 2021-2050 (averaged over all climates), did not occur in the control period. This percentage increases up to 31% by the end of the century. The strongest decrease in SI (i.e. largest change) was found in the equatorial, arid and warm temperate climates (A, B, C) where SI values can be as low as 60%. The same pattern was found for the snow climate (D), however, changes in SI are smaller.

9.5 Discussion

Most global drought projections address meteorological or soil moisture drought. Dai (2013) has investigated global soil moisture drought up to 2010 and states that the

Table 9.5 Similarity Index (SI) for the near (2021-2050) and far (2071-2100) future, compared to the control period (1971-2000) derived from a synthetic hydrological model forced with three General Circulation Models. SI is given for all major climates, Equatorial (A), Arid (B), Warm temperate (C), Snow (D) and Polar climates (E) and averaged over all climates.

GCM	Period	A	B	C	D	E	All
ECHAM	2021-2050	77	71	73	84	84	81
ECHAM	2071-2100	63	60	64	70	73	69
CNRM	2021-2050	78	82	85	88	81	87
CNRM	2071-2100	64	71	68	64	68	71
IPSL	2021-2050	73	71	83	87	86	82
IPSL	2071-2100	60	58	63	73	71	68

PDSI changes derived from observed weather records are consistent with model predictions, which would indicate severe and extended global drought in the 21st century resulting from either decreased precipitation and/or increased evaporation. Sheffield et al. (2012) argue that the increase in global soil moisture drought since the 1980s is overestimated because the PDSI was computed with a too simple evapotranspiration model, which has consequences of how to interpret the impact global warming on global drought changes. Orlowsky and Seneviratne (2013) use meteorological drought (SPI) and soil moisture drought (anomaly) to illustrate that there will be both wetting regions in the 21^{st} century (e.g. East and South Asia, Sahel, Central North America, Central Europe) and drying regions (e.g. Australia, South Africa, Central America, Amazon, Mediterranean). Seneviratne et al. (2012) conclude that there is medium confidence that in some regions across the world duration and intensity of meteorological or soil moisture drought will increase and elsewhere the confidence level is low because of definitional differences or model disagreement. Land surface processes and properties (e.g. groundwater flow and storage, stream-aquifer interaction, Van Lanen et al., 2004; Van Loon et al., 2012) make meteorological or soil moisture drought projections not straightforwardly applicable to hydrological drought.

Hydrological drought projections, which are of paramount importance for assessments of future water resources, are still limited. GCMs and Regional Climate Models (RCMs) are somewhat simplified to include all relevant land surface processes and properties, hence usually lack adequate soil and aquifer storage processes (Stahl et al., 2011). Hydrological drought projections are often associated with change in annual runoff or river flow (e.g. Arnell, 2003; Milly et al., 2005). Off-line approaches on a global scale use large-scale hydrological models in combination with forcing from either GCMs or RCMs. Intermediate approaches are needed to downscale and bias correct the climate model forcing (Haddeland et al., 2011), which is a challenging

process (e.g. Sperna Weiland et al., 2010; Hagemann et al., 2011), in particular for the future climate (Chen et al., 2011). Very few attempts have been made so far to derive hydrological drought characteristics at the global or continental scale under future climate. Forzieri et al. (2014) project an increase in deficit volume of river flow for vast areas of Europe, except the Scandinavian countries and North Russia. Hirabayashi et al. (2008) and Feyen and Dankers (2009) project a substantial increase in the number of drought days (PDY) or flow deficit volume for the period 2071-2100 in some regions, whereas in contrast, wide areas will benefit from a decrease in drought days. An increase in number of drought days in general is not in line with the modelling experiment in this study, whereas an increase in deficit volume is supported (Table 9.4). In Chapter 10 an increased water availability in the colder snow dominated climate types was found, which is in line with the findings of this study. Corzo Perez et al. (2011b) analysed future drought for two time domains (2021-2050 and 2071-2100), two emission scenarios (A2 and B1), 3 downscaled and bias-corrected GCMs, and 5 large-scale hydrological models. The number and spatial distribution of drought events did not clearly show a consistent change. The limited number of global studies on future hydrological drought still makes projections uncertain.

In the control period 1971-2000, differences occur between hydrological drought characteristics (Figure 9.3) derived from discharge time series simulated with meteorological forcing from downscaled and bias-corrected outcomes from three Global Circulation Models (GCM forced models). For example, the duration and deficit volume averaged over all climates varies from 60 to 69 d and 5.05 to 5.94 d, respectively, for the three GCM forced models (Table 9.3). The main reason for this is GCM model uncertainty, caused by the differences in model structures (Chen et al., 2011; Haerter et al., 2011). Differences in hydrological drought characteristics among GCM forced models are more similar than the differences between characteristics derived from the GCM forced models and characteristics that were obtained using re-analysis data as meteorological forcing (reference model). Exceptions are the B and E climates (Tables 9.2 and 9.3). For the A, C and D climates differences in drought duration of GCM forced models against the reference model vary from 0-30%, whereas for the deficit volume the range is 1-26% (Figure 9.4 and 9.5). Differences in drought characteristics between GCM forced models and the reference model are mostly negative, implying that the drought duration and standard deficit volume are smaller when GCM forcing was used instead of re-analysis data. Differences in drought characteristics against the reference model are not always mono-directional for a particular climate (e.g. drought duration for the C climate). The above-mentioned differences are a measure for climate model uncertainty. Most large-scale studies, which explore hydrological impact of climate change, compare simulated and observed annual river flow to assess model fitness as a basis for projections (e.g. Arnell, 2003; Milly et al., 2005). Other studies also focus on low-water availability and include minimum flow or flow deficits to investigate future drought (e.g. Feyen and Dankers, 2009; Forzieri et al., 2014). Few large-scale studies test hydrological model performance by comparing GCM forcing against observed forcing. Sperna Weiland et al. (2010) are such

an exception. They conclude that bias-corrected GCM-forcing should be used with caution for global hydrological impact studies in which persistence is relevant, like for drought. Another example is Corzo Perez et al. (2011b), who confirm that for a control period no clear patterns can be found in differences between hydrological drought characteristics derived from GCM-forced hydrological models and the same models forced with re-analysis data.

Global annual precipitation totals are projected to increase throughout the 21^{st} century, although locally annual precipitation might decrease (Solomon et al., 2007). Precipitation increase is most prominent in the equatorial and polar climates, resulting in an increase in discharge (Solomon et al., 2007), which was confirmed by the data from GCMs that was used for this study. Therefore, in the 21^{st} century the historic Q_{80} (1971-2000) was exceeded for more than 80% of the time in our study, hence the PDY decreased both in the near and far future (Table 9.4).

It was noticed that for the equatorial climate the impact of climate change is not unambiguous. Two GCM forced models (ECHAM, CNRM) indicate a decrease in total drought occurrence (PDY) relative to the control period (19-25% for 2012-2050 and 36-56% for 2071-2100), while one GCM forced model (IPSL) indicates a small increase (12% for 2012-2050 and 28% for 2071-2100) in total drought occurrence (A climate, Table 9.4). The main reason for the model disagreement is an increase in precipitation projected by ECHAM and CNRM and a decrease by IPSL in most of the selected locations for the A climate leading to higher and lower discharge, respectively.

The three GCMs project increasing annual temperatures leading to a decreased length of the snow accumulation period in cold climates (D- and E-climates), which have great impact on river flow (e.g. Wilson et al., 2010), and consequently on drought occurrence (PDY, D climates, Table 9.4). For instance, duration of rain-to-snow-season drought as identified by Van Loon and Van Lanen (2012) will decrease due to later precipitation as rain in autumn or earlier rain in spring, leading to, quicker snow melt peak. It was found that the combined effect of increased precipitation and shorter snow accumulation periods causes a strong decrease in total drought duration (i.e. PDY). Feyen and Dankers (2009) report on a decrease in drought severity (i.e. 7-day minimum flow and deficit volume during the frost period) in the cold European climates. Classical rainfall drought, however, will become more severe due to lower summer flows in some regions, e.g. southern and eastern Norway (Feyen and Dankers, 2009; Wilson et al., 2010; Wong et al., 2011; Stahl et al., 2011), which is supported by this study, where the remaining drought in the far future last 14-29% longer and are 26-52% more severe.

A large portion of the globe is covered by snow dominated and polar climates (D and E, Figure 9.2). While the impact of climate change on hydrological drought may be most severe for the snow dominated regions (D and E-climates), the societal impact is expected to be relatively low. In these regions the population density is low and the projected changes have a positive impact on the water availability. Projected

changes are far more likely to have a significant impact on the tropical and desert climates (A and B-climate). In these regions vulnerability to drought is higher while the drought resilience is lower compared to other regions in the world. Therefore, the forecasted increase in severity and duration of drought should be seen as events which could severely impact the region. These changes could lead to forced immigration, putting pressure on adjacent regions usually also scarce in water already. Uncertainty in projections for these regions should challenge policy makers and stakeholders to take appropriate decisions for drought adaptation measures.

9.6 Conclusions

With a synthetic hydrological modelling approach the impact of climate change on drought occurrence and severity was studied. Drought characteristics, namely drought duration, standardized deficit volume and percentage of drought occurrence per year were calculated for the time period 1960-2100. Three different General Circulation Models (ECHAM, CNRM, IPSL) were used as meteorological forcing to simulate possible effects of climate change on drought (GCM forced models). The A2 emission scenario was used to explore the most severe outcome for the three GCM forced models. Obtained drought characteristics were compared against the drought characteristics obtained from simulations of the hydrological model forced with meteorological data from the WATCH Forcing Data, which was used as a reference dataset in this study (reference model). Comparison was performed for the control period 1971-2000 and the deviations of each GCM forced model from the reference model were calculated. On a global scale drought duration found for the reference model and the GCM forced models were in the same order of magnitude, while the standardized deficit volume was underestimated compared against the reference model. It was concluded that the GCM forced models produce realistic meteorological forcing for future hydrological drought assessment, but have difficulties to capture the more extreme arid and polar climates. This issue is most likely caused by the bias correction, which only corrects for numbers of rain days and total precipitation volumes. However, it does not take into account second order statistics like the sequence of rainfall events, the co-occurrence and magnitude of specific events. These second order statistics could have significant impact on the duration and severity of drought events.

The effects of climate change were studied for two periods, namely 2021-2050 and 2071-2100 and compared relative to the control period. From the analysis it is concluded that average drought duration and standardized deficit volume will increase as a result of climate change. However, the total drought duration and number of drought will decrease since on a global scale the total water availability will increase due to increased precipitation totals.

On a global scale the average duration of drought events will increase by a factor 1.5 in the far future (2071-2100), where this increase is most severe in the equatorial and arid climate types. Overall the total drought duration (PDY) decreases to 26-33% relative to the control period, where the decrease is most striking in the snow climates. Increasing temperatures cause a decrease in winter drought and snow accumulation, combined with increased precipitation, leading to a very strong decrease in total drought duration (5-8% relative to the control period). Global average drought standardized deficit volume increases by slightly more than 2 times for the period 2071-2100, which suggests that drought severity will increase as a result of changes in the climate.

Projections of global hydrological drought, which are essential for future water resources management, are still very limited. This study advances knowledge on future hydrological drought. Averaged over all climates the GCM forced hydrological models produces similar changes in discharge drought. Some spread is found among the models, but the directionality is similar. In general, the synthetic hydrological modelling approach shows that hydrological drought occurrence (i.e. total days in drought per year) is projected to decrease over the 21^{st} century, particularly in the temperate and cold climate regions. On the contrary, average drought duration and deficit volume of the remaining drought are expected to substantially increase. The most critical impacts are projected for the already water scarce arid climates (B climates), where drought occurrence will not decrease that much and average duration and deficit volume of remaining drought events will increase more than in other climates. However, in this climate, model uncertainty is largest.

Acknowledgements

The authors would like to thank Graham Weedon (UK MetOffice) for supplying the WATCH Forcing Data. The work done by Cui Chen, Jan Haerter and Stefan Hagemann (Terrestrial Hydrology Group, Max Planck Institute for Meteorology, Hamburg, Germany), Jens Heinke (Potsdam Institute for Climate Impact Research, Potsdam, Germany) and Claudio Piani (Abdus Salam International Centre for Theoretical Physics, Trieste, Italy) to downscale and bias correct the climate output from the three GCMs (daily data, 1960-2100) was very much appreciate. This research has been financially supported by the EU-FP6 Project WATCH (contract 036946), the EU-FP7 Project DROUGHT-R&SPI (contract 282769). This research supports the work of the UNESCO-IHP VIII FRIEND-Water programme.

10 Human and climate impacts on hydrological drought

This chapter is based on:
Wanders, N., Wada, Y. (2014), Human and climate impacts on the 21^{st} century hydrological drought, Journal of Hydrology, in press, doi:10.1016/j.jhydrol.2014.10.047.

Abstract

Climate change will very likely impact future hydrological drought characteristics across the world. Here, the impact of human water use including reservoir regulation and climate change on future low flows and associated hydrological drought characteristics was quantified on a global scale. The global hydrological and water resources model PCR-GLOBWB is used to simulate daily discharge globally at 0.5° resolution for 1971-2099. The model was forced with the latest CMIP5 climate projections taken from five General Circulation Models (GCMs) and four emission scenarios (RCPs), under the framework of the Inter-Sectoral Impact Model Intercomparison Project. A natural or pristine scenario has been used to calculate the impact of the changing climate on hydrological drought and has been compared to a scenario with human influences. In the latter scenario reservoir operations and human water use are included in the simulations of discharge for the 21^{st} century. The impact of humans on the low flow regime and hydrological drought characteristics has been studied at a catchment scale. Results show a significant impact of climate change and human water use in large parts of Asia, Middle East and the Mediterranean, where the relative contribution of humans on the changed drought severity can be close to 100%. The differences between Representative Concentration Pathways (RCPs) are small, indicating that human water use is proportional to the changes in the climate. Reservoirs tend to reduce the impact of drought by water retention in the wet season, which in turn will lead to increased water availability in the dry season, especially for large regions in Europe and North America. The impact of climate change varies throughout the season for parts of Europe and North-America, while in other regions (e.g. North-Africa, Middle East and Mediterranean), the impact is not affected by seasonal changes. This study illustrates that the impact of human water use and reservoirs is nontrivial and can vary substantially per region and per season. Therefore, human influences should be included in projections of future drought characteristics, considering their large impact on the changing drought conditions.

10.1 Introduction

Climate change is expected to increase drought intensity and frequency worldwide as a result of changes in precipitation patterns and rising temperature (Burke et al., 2006; Lehner et al., 2006; Feyen and Dankers, 2009; Dai, 2011, 2013; Prudhomme et al., 2014; Trenberth et al., 2014). Drought is generally related to meteorological extremes and is induced by below-normal precipitation (Wilhite and Glantz, 1985; Wilhite, 2000; Mishra and Singh, 2010). Lack of precipitation causes meteorological drought and agricultural drought over the region, but further propagates into hydrological drought via the drainage network (Tallaksen et al., 1997; Sheffield and Wood, 2007; Tallaksen et al., 2009; Sheffield et al., 2012; Van Loon et al., 2014). Various studies analysed the severity, frequency and trends of hydrological droughts using large-scale hydrological models that enable the analysis of drought over continental to global scales (Hisdal et al., 2001; Fleig et al., 2006; Feyen and Dankers, 2009; Tallaksen et al., 2009; Corzo Perez et al., 2011b; Van Huijgevoort et al., 2013, 2014; Alderlieste et al., 2014). However, the anthropogenic impact on drought is generally less well known and such impact has rarely been explored. Notable exceptions are recent studies by Dai (2011, 2013) and Sheffield et al. (2012), who indicated that anthropogenic global warming is likely responsible for intensifying meteorological droughts, primarily due to enhanced evaporative demand and altered monsoon circulation over regions such as Africa and Asia. Another exception by Wada et al. (2013) showed that human water consumption substantially intensifies the magnitude of hydrological droughts regionally by 10-500%, and it alone increases global drought frequency by 30%. However, no study has yet provided a comprehensive overview of human and climate impacts on future hydrological drought at the global scale. Prudhomme et al. (2014) provided future projections of hydrological drought based on a large ensemble of five Global Climate Models (GCMs) from the latest CMIP5 (Coupled Model Intercomparison Project Phase 5), four emission scenarios or Representative Concentration Pathways (RCPs) and seven Global Hydrological Models (GHMs). Yet, they considered only the effect of climate on hydrological drought using the streamflow simulated under natural or pristine conditions such that anthropogenic influence (e.g., irrigation and reservoir regulation) on resulting drought is not explicitly incorporated.

The severe impacts of large-scale droughts have historically shown the need to improve understanding of drought mechanisms so that our society can be better prepared (Trenberth et al., 1988; Gleick, 2000; Andreadis et al., 2005; Seager, 2007; Gleick, 2010; Pederson et al., 2012). Thus, providing a comprehensive overview of future drought projections considering both human and climate impacts is a vital step, ensuring future water and food security. Here, for the first time a full global analysis of the impact of human activities (irrigation and reservoir regulation, Wada et al., 2013) and climate change on hydrological drought is presented. Streamflow is simulated under both natural or pristine conditions and under conditions including human

influences using the global hydrological and water resources model PCR-GLOBWB (Van Beek et al., 2011; Wada et al., 2011a,b, 2014) with five GCMs from the latest CMIP5 and four emission scenarios (here represented by RCPs 2.6, 4.5, 6.0 and 8.5). Human-induced change are incorporate by including human water use for irrigation and reservoir regulation parameterized by the latest extensive global reservoir data set (GRanD, Lehner et al., 2011). Another innovative aspect of this study is that a transient spatially-distributed threshold or Q_{90} (30-year window) was applied, identifying drought characteristics that reflects changes in the hydrological regime over time (Chapter 8), while most studies used the threshold calculated over the control or historical period (e.g., 1971-2000). A transient threshold assumes adaptation to long-term changes in the hydrological regime as the drought is defined by a deviation from normal conditions (i.e. normal implies decadally updated 30-year averages according to the WMO guidelines) (World Meteorological Organization, 2007; Arguez and Vose, 2010). Our study stands out from earlier work by presenting for the first time the human impact on future hydrological droughts using the latest multi-model climate projections and multi-emission scenarios.

Section 10.2 of this paper presents a brief description of the global hydrological and water resources model PCR-GLOBWB, climate forcing data, the drought identification method and the simulation protocol. In Section 10.3 the simulation results are presented and the human and climate impacts on future hydrological drought are evaluated globally and per river basin. Section 10.4 discusses the advantages and the limitations of our approach and the associated uncertainties, and provides conclusions from this study.

10.2 Material and Methods

10.2.1 Model simulation of streamflow

The state-of-the-art global hydrological and water resources model PCR-GLOBWB was used to simulate spatial and temporal continuous fields of discharge and storage in rivers, lakes, and wetlands at a 0.5° spatial resolution (Wada et al., 2010; Van Beek et al., 2011; Wada et al., 2014). In brief, the model simulates for each grid cell and for each time step (daily) the water storage in two vertically stacked soil layers and an underlying groundwater layer. At the top a canopy with interception storage and a snow cover may be present. Snow accumulation and melt are temperature driven and modelled according to the snow module of the HBV model (Bergström, 1995). To represent the rain-snow transition over sub-grid elevation dependent gradients of temperature, 10 elevation zones were distinguished in each grid cell based on the HYDRO1k Elevation Derivative Database (`https://lta.cr.usgs.gov/HYDRO1K/`), and the 0.5° grid temperate fields are down-scaled with a lapse rate of $0.65°C$ per 100 m. The model computes the water exchange between the soil layers, and between

Table 10.1 GCMs (Global Climate Models) used in this study.

GCM	Organization
HadGEM2-ES	Met Office Hadley Centre
IPSL-CM5A-LR	Institute Pierre-Simon Laplace
MIROC-ESM-CHEM	JAMSTEC, NIES, AORI (The University of Tokyo)
GFDL-ESM2M	NOAA Geophysical Fluid Dynamics Laboratory
NorESM1-M	Norwegian Climate Centre

the top layer and the atmosphere (rainfall, evaporation and snowmelt). The third layer represents the deeper part of the soil that is exempt from any direct influence of vegetation, and constitutes a groundwater reservoir fed by active recharge. The groundwater store is explicitly parameterized and represented with a linear reservoir model (Kraijenhof van de Leur, 1962). Sub-grid variability is considered by including separately short and tall natural vegetation, open water (lakes, floodplains and wetlands), soil type distribution (FAO Digital Soil Map of the World), and the area fraction of saturated soil calculated by the Improved ARNO scheme (Hagemann and Gates, 2003) as well as the spatio-temporal distribution of groundwater depth based on the groundwater storage and the surface elevations as represented by the 1 km by 1 km Hydro1k data set. Simulated specific runoff from the two soil layers (direct runoff and interflow) and the underlying groundwater layer (base flow) is routed along the river network based on the Simulated Topological Networks (STN30, Vörösmarty et al., 2000a) using the method of characteristic distances (Wada et al., 2014).

The PCR-GLOBWB model and model outputs have been extensively validated in earlier work. Simulated mean, minimum, maximum, and seasonal flow, monthly actual evapotranspiration, and monthly total terrestrial water storage were evaluated against 3600 GRDC observations (`http://www.bafg.de/GRDC`) ($R^2 \sim 0.9$), the ERA-40 reanalysis data, and GRACE satellite observations, respectively in earlier work (Van Beek et al., 2011; Wada et al., 2012, 2014), and generally showed good agreement. Simulated drought deficit volumes were also validated against those derived from observed streamflow (from GRDC stations) for major river basins of the world (Wada et al., 2013). The comparison generally showed reasonable agreement for most of the basins, which leads to the conclusion that PCR-GLOBWB can adequately reproduce low flow conditions and associated drought events across the globe.

The model was forced with daily fields of precipitation, reference (potential) evapotranspiration and temperature taken from five GCMs (Table 10.1) and four underlying emission scenarios (here accounted for by using four RCPs (Table 10.2). The newly available CMIP5 climate projections were obtained through the Inter-Sectoral Impact Model Intercomparison Project (Warszawski et al., 2014). The GCM climate forcing

Table 10.2 Overview of representative concentration pathways (RCPs) (Van Vuuren et al., 2011). Radiative forcing values include the net effect of all anthropogenic greenhouse gases and other forcing agents.

RCP	Scenario
2.6	Peak in radiative forcing at ∼3.1 $W\,m^{-2}$ (∼490 $ppm\ CO_2$ equivalent) before 2100 and then decline (the selected pathway declines to 2.6 $W\,m^{-2}$ by 2100).
4.5	Stabilization without overshoot pathway to 4.5 $W\,m^{-2}$ (∼650 $ppm\ CO_2$ equivalent) at stabilization after 2100
6.0	Stabilization without overshoot pathway to 6 $W\,m^{-2}$ (∼850 $ppm\ CO_2$ equivalent) at stabilization after 2100.
8.5	Rising radiative forcing pathway leading to 8.5 $W\,m^{-2}$ (∼1370 $ppm\ CO_2$ equivalent) by 2100

was bias-corrected on a grid-by-grid basis (0.5° grid) by scaling the long-term monthly means of the GCM daily fields to those of the observation-based WATCH climate forcing for the overlapping reference climate 1960-1999 (Hempel et al., 2013). Potential evapotranspiration was calculated with the bias-corrected GCM climate forcing with the method of Hamon (Hamon, 1963). The resulting bias-corrected transient daily climate fields were used to force the model over the period 1971-2099 with a spin-up, reflecting a climate representative prior to the start of the simulation period. The results of each GCM are treated equally and no weight was given to a particular GCM based on the performance against historic climate. As a result, 20 projections (5 GCMs with 4 RCPs) of future daily streamflow were produced.

10.2.2 Drought calculation

Hydrological drought characteristics (e.g. drought duration and deficit volume) were derived from simulated time series of daily discharge (Q) using the variable threshold level approach (e.g. Yevjevich, 1967; Dracup et al., 1980; Tallaksen et al., 1997; Hisdal et al., 2004; Fleig et al., 2006; Tallaksen et al., 2009; Wanders et al., 2010). In this study the Q_{90} ($m^3 s^{-1}$) was derived from the flow duration curve, where the Q_{90} is the threshold which is equalled or exceeded for 90% of the time. This threshold has been selected to study the impact of severe drought conditions and has been used in multiple studies where drought is studied for future and current hydrological conditions (e.g. Fleig et al., 2006; Parry et al., 2010; Van Loon et al., 2014).

The drought state is given by:

$$Ds(t,n) = \begin{cases} 1 & \text{for } Q(t,n) < Q_x(t,n) \\ 0 & \text{for } Q(t,n) \geq Q_x(t,n) \end{cases} \tag{10.1}$$

where $Q_x(t,n)$ is the threshold which is equalled or exceeded for x percent of the time and $Ds(t,n)$ is a binary variable indicating if a location or grid cell (n) is in drought at a given time t. The drought duration for each event at n is calculated with:

$$Dur_{i,n} = \sum_{t=S_i}^{L_i} Ds(t,n) \tag{10.2}$$

where $Dur_{i,n}$ is the drought duration (d) of event i at n, S_i the first time step of a event i and L_i the last time step of the event. An event starts when $Q(t,n) < Q_x(t,n)$ and ends when $Q(t,n) \geq Q_x(t,n)$. The deficit volume per time step was defined by:

$$Def(t,n) = \begin{cases} Q_x(t,n) - Q(t,n) & \text{for } Ds(t,n) = 1 \\ 0 & \text{for } Ds(t,n) = 0 \end{cases} \tag{10.3}$$

where $Def(t,n)$ is the daily deficit volume of drought i (m^3s^{-1}) at n. The total drought deficit volume for each drought event was calculated with:

$$Def_i(n) = \sum_{t=S_i}^{L_i} Def(t,n) \tag{10.4}$$

where $Def_i(n)$ is the total deficit volume of the drought event i (m^3s^{-1}) at n. The deficit volume is the cumulative deviation of the discharge from the threshold over the duration of a drought event. The intensity of all drought events is calculated with:

$$Int(n) = \sum_{i=1}^{I} \frac{Def_i(n)}{Dur_i(n)} \tag{10.5}$$

where the total drought deficit is divided by the total drought duration of location n, for all drought events I, to obtain the total drought intensity $(m^3s^{-1}d^{-1})$. The intensity enables comparison of the drought impact for a location under different scenarios. If the $Q_x(t,n)$ equals 0 m^3s^{-1} by definition a drought will not occur since $Ds(t,n)$ will remain zero (Equation 10.1). If $Q_x(t,n)$ equals 0 m^3s^{-1} for more than 50% of the time, no drought characteristics were calculated for this cell, although some techniques exist to deal with these extreme situations (Van Huijgevoort et al., 2012). In this study these locations were excluded from the analysis, since frequent zero discharge situations are part of the local climate (i.e. aridity) and are not a manifestation of hydrological drought conditions or occurrence.

10.2.3 Transient variable threshold approach

Most studies that evaluate future changes in hydrological drought use the Variable Threshold level Method (VTM), to derive drought characteristics (e.g. Prudhomme et al., 2014; Alderlieste et al., 2014; Forzieri et al., 2014). In this study, the transient Variable Threshold level Method approach (VTM_t) was used that was developed in Chapter 8. The VTM_t was calculated from the daily values of Q_x derived from simulated discharge of the previous 30-year period ($x = 90$, in this study). For each month daily discharge values of the last 30-year period are binned and the Q_x is calculated. Thereafter, the monthly values of Q_x were smoothed with a moving average window of 30-days, resulting in the variable threshold (VTM_t). The VTM_t is expected to adapt to changes in the hydrological regime, based on the simulation of the previous 30-year period, while the standard VTM does not change over time and is normally derived from a control period (typically 1970-2000). Present climatology can significantly change over the future period under human and climatological influences. This will result in an altered hydrological regime and therefore the VTM_t was used when future hydrological drought characteristics were calculated. This requires that the VTM_t is calculated every day and dependent on the climatology of the last 30 years for the entire future period (Chapter 8). Changes in the VTM_t will also indicate changes in the low flow regime in the 21^{st} century. This approach is different from the more traditional non-transient threshold that is calculated from a control period and that will not adapt to changes in the hydrological regime. Figure 10.1 indicates, in a theoretical example, the difference between the traditional non-transient threshold and the transient threshold. It shows that the threshold will gradually change, since the VTM_t was derived from the discharge of the previous 30-year period, instead of a extrapolation of the threshold based on the discharge from a control period.

10.2.4 Assessment of climate and human impact

To assess the impact of climatic changes on hydrological drought characteristics for the 21^{st} century, two periods were compared. The first period runs from 1971-2000 (control period, ctrl) and the second period runs from 2070-2099 (future period). For both periods a scenario with natural conditions (pristine) was considered to derive hydrological droughts. In this scenario no human impacts were included and only climate change affects the changes in hydrological drought characteristics. To evaluate the impact of climate change, the changes (in percent) in the low flow regime have been calculated by:

$$dVTMclim_t = \frac{VTMfuture_t - VTMctrl_t}{VTMctrl_t} \times 100 \tag{10.6}$$

where $dVTMclim_t$ is the change in the low flow regime, $VTMctrl_t$ and $VTMfuture_t$ are the transient variable thresholds for the control and future period, respectively. Thereafter, the VTM_t was used to calculate the drought characteristics, for both the

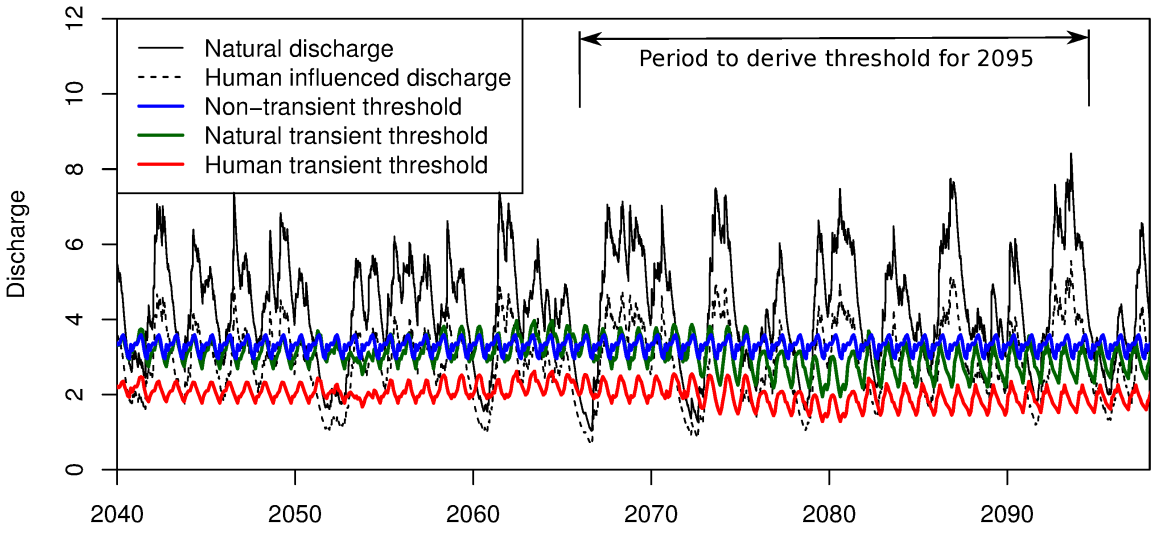

Figure 10.1 Example time series of threshold calculation for different scenarios. The traditional non-transient threshold is derived from the natural discharge for a control period (typically 1970-2000). The natural transient threshold is derived from the natural discharge of the previous 30-year period. The human transient threshold is derived from the human influenced discharge of the previous 30-year period.

periods. The changes for the future period in the ensuing deficit volumes calculated compared to the control period is thus an indication of the impact of climate change on hydrological drought. The relative climate impact on the deficit volume is given by:

$$dDef_{clim} = \frac{Def_{future} - Def_{ctrl}}{Def_{ctrl}} \times 100 \tag{10.7}$$

where $dDef_{clim}$ is the relative impact of climate change on the drought deficit volume, Def_{ctrl} and Def_{future} are the drought deficit volumes for the control and future period, respectively.

To assess the impact of human water use and reservoirs on projected changes in hydrological drought characteristics for the 21^{st} century, two scenarios have been used. The pristine scenario has been compared to a scenario with human influences (human). In the scenario with human influences, water is abstracted according to the local water demand and associated reservoir operations are included (Wada et al., 2014). Reservoirs are located on the drainage or river network based on the newly available and extensive Global Reservoir and Dams Dataset (GRanD, Lehner et al., 2011) that contains 6,862 reservoirs with a total storage capacity of 6,197 km^3. The reservoirs were placed over the river network based on the year of their construction. Water is abstracted from surface water (river discharge, reservoirs and lakes) and groundwater, part of it comes back to the river network as return flow and part of

it is consumed. Human water use was calculated for the irrigation sector only, since comprehensive sets of socio-economic projections are not yet available consistently across all RCPs under SSPs (Shared Socioeconomic Pathways), which can be used to estimate industrial and domestic water use. Irrigation water use was simulated with PCR-GLOBWB per unit crop area based on the surface water balance (surface water layer for paddy rice) and the soil water balance (soil moisture deficit in the root zone calculated from the difference between the water content at field capacity and the water content at wilting point) (Wada et al., 2014). Irrigated areas were obtained from the MIRCA2000 data set (Portmann et al., 2010). The losses during water transport and irrigation application were included in the calculation based on daily evaporative and percolation losses per unit crop area. Current land use and population density are constant over time since only limited sets of socio-economic data and no future irrigated area projections are available for the 21^{st} century. Meteorological forcing from five different GCMs with four RCPs have been used to project discharge for the 21^{st} century for both the pristine and human scenario. Effects on projected discharge have been studied, where the changes per RCP were calculated using the ensemble mean of all GCMs. Thereafter, the relative impact of each scenario on the projected changes in hydrological drought has been studied by comparing both scenarios.

For both scenarios the transient threshold (VTM_t) was calculated and compared (see Figure 10.1 for the example). By making a comparison between both thresholds (one for each scenario), impact of human water use and reservoirs on the low flow regime can be studied. Additionally, this enables a comparison between the impact of climate change and human water abstraction on the changes in the low flow regime. The impact (in percent) of human influence on the low flow regime is calculated by:

$$dVTMhuman_t = \frac{HumanVTM_t - PrisVTM_t}{PrisVTM_t} \times 100 \tag{10.8}$$

where $dVTMhuman_t$ is the change in the low flow regime, $PrisVTM_t$ and $HumanVTM_t$ are the transient variable thresholds for the pristine and human scenario, respectively. Thereafter, the VTM_t of the pristine scenario was used to calculate the drought characteristics, for both the pristine and human scenario. By selecting the pristine VTM_t the relative impact of human influences could be calculated and compared to the impact of climate change. The increase in the ensuing deficit volumes calculated compared to the pristine condition is thus an indication of the anthropogenic intensification of hydrological drought. The relative impact (in percent) of human water abstraction and reservoirs on the deficit volume is given by:

$$dDef_{human} = \frac{HumanDef - PrisDef}{PrisDef} \times 100 \tag{10.9}$$

where $dDef_{human}$ is the relative impact of humans on the drought deficit volume, $HumanDef$ and $PrisDef$ are the drought deficit volumes under the human and pristine scenario, respectively.

The combined impact of both climate change, and human water use and reservoirs has been studied, by comparing the control period for the pristine scenario with the future period of the human scenario. The relative total impact (in percent) on the deficit volume is given by:

$$dDef_{combi} = \frac{HumanDef_{future} - PrisDef_{ctrl}}{PrisDef_{ctrl}} \times 100 \tag{10.10}$$

where $dDef_{combi}$ is the relative combined impact of climate change, and human water use and reservoirs on the drought deficit volume, $PrisDef_{ctrl}$ is the deficit volume for the control period under pristine conditions and $HumanDef_{future}$ is the drought deficit volume for the future period under the human scenario.

The differences between the scenarios were studied for major river basins of the world, where drought events are known to be influenced by human water abstraction and reservoirs regulations (Wada et al., 2013). This would give insight in the hydrological processes and the impact of humans on a river basins scale. Drought characteristics were calculated for the last 30 years of the 21^{st} century. Thereafter, the results are presented on a global scale to assess the regions in which humans have a larger impact than climate on future hydrological drought.

10.3 Results

10.3.1 Climate impact on a global scale

On a global scale the impact of climate change on the low flow regime ($dVTMclim_t$, Equation 10.6) has been evaluated and compared for the control and the future period (Figure 10.2). It is shown that climate change has a negative impact on the low flow regime (decrease of 10% or more) in South-America, Australia, Southern-Africa, Southeast Asia and the Mediterranean. Positive impacts on the low flow regime are found in Northwest Africa and large parts of Northern Europe, Russia and Canada. Differences between RCPs are small, whereas a slightly larger impact is found for the higher CO2 emission scenarios (e.g., RCP6.0 and 8.5).

The impact of climate change on the drought deficit volumes ($dDef_{clim}$, Equation 10.7) is projected to be severe in large parts of the world (Figure 10.3). This is especially true for regions in Northern Africa, Eastern part of the United States and Southern Europe. In these regions drought deficit will likely increase by more than 100%, and for some regions it will increase even up to over 200%. A slightly negative impact (about 10%) exists on the $dVTMclim_t$ for regions in Southeast Asia and South-America, however, this does not result in a negative impact on the $dDef_{clim}$. The agreement amongst different RCP scenarios is strong and only small uncertainty remains in the projections for North-America and Europe.

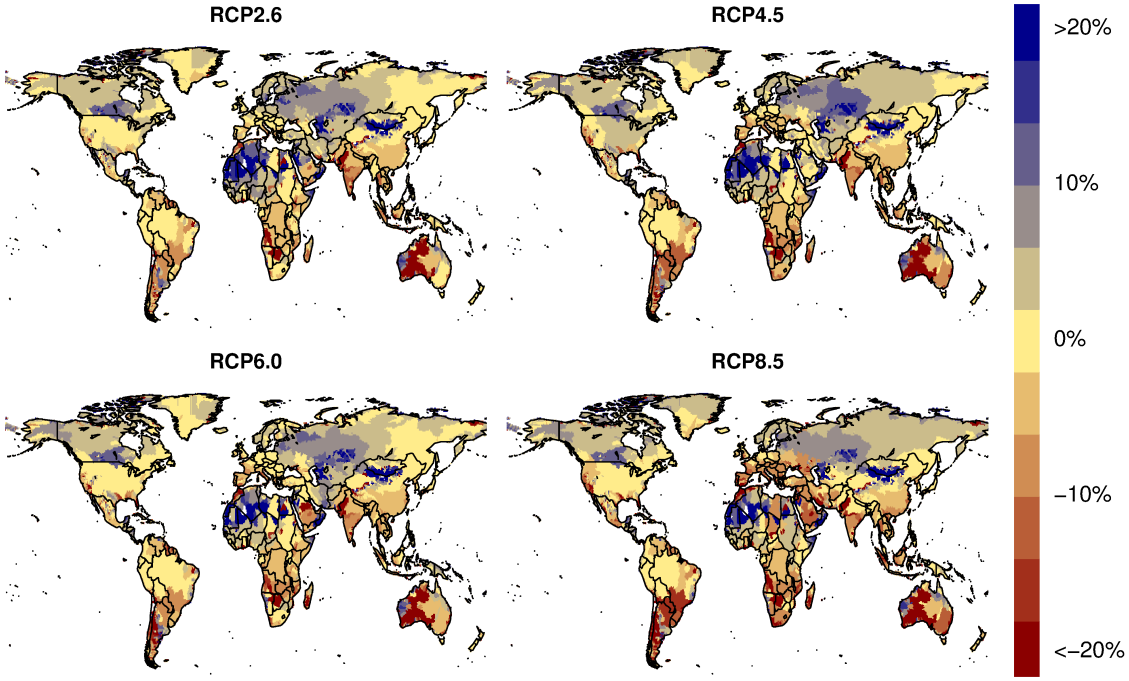

Figure 10.2 Climate impact on drought threshold (Q_{90}, $dVTM_t$) compared between the periods 1971-2000 and 2070-2099. Impact is calculated as a percentage where positive percentages indicate an increase in the Q_{90} and negative percentages indicate a decrease in the Q_{90} as a result of climate change. Each plot gives the ensemble mean impact derived from 5 GCMs for different RCPs.

It is concluded that the impact of climate change on hydrological drought characteristics is large and associated uncertainties amongst RCPs are low. Although some regions show a negative impact in the low flow regime, this does not necessarily result in increased drought deficit volumes. Overall, drought conditions in most of the world are projected to be negatively impacted by climatic changes.

10.3.2 Impact of human water use on a global scale

On a global scale the thresholds for the pristine scenario and the human scenario ($dVTMhuman_t$, Equation 10.8) have been compared (Figure 10.4). As expected the $dVTMhuman_t$ decreased in Asia and the Mediterranean, where the impact of human water use exceeds the compensating effect brought by reservoir operations. The water abstraction in these regions results in a negative impact on the low flow regime, where low flows reduce as a result of the water abstraction. For central Europe and the United States the reservoir regulation measures compensate the negative impact caused by water abstraction and overall human influences have a positive impact on the low flows. Similar to the climate change impacts, differences between different

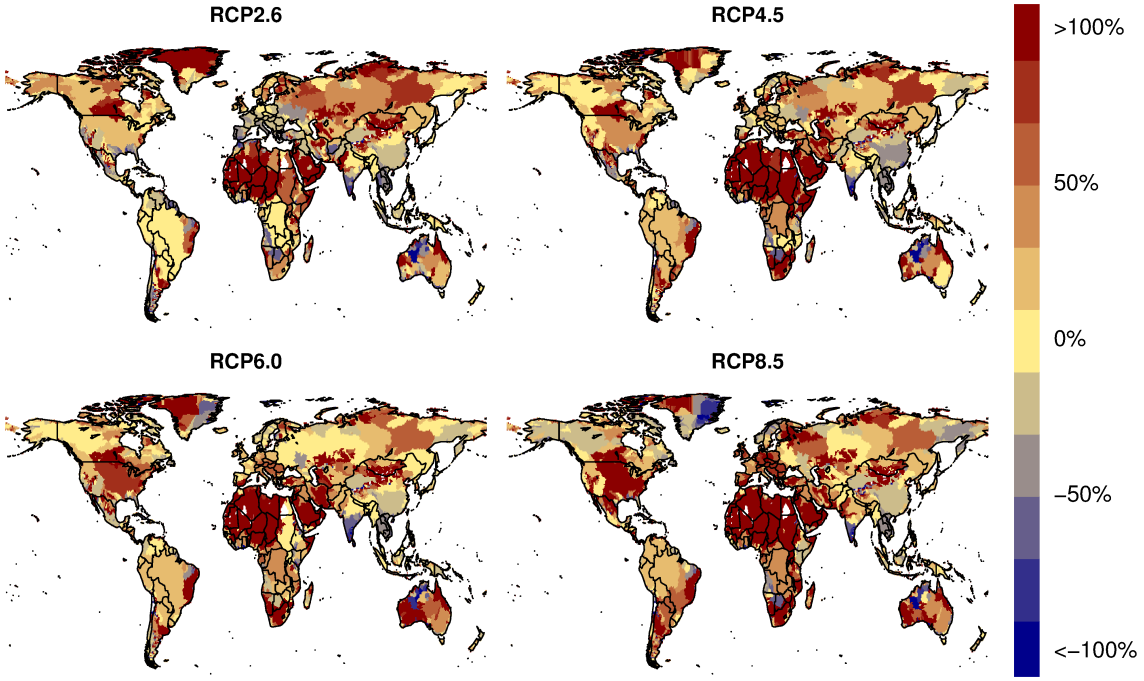

Figure 10.3 Climate impact on drought deficit volume ($dDef$), compared between the periods 1971-2000 and 2070-2099. Each plot gives the annual average impact derived from 5 GCMs for different RCP scenarios. Impact is calculated as a percentage, where positive percentages indicate a decrease in the drought deficit volume and negative percentages indicate an increase in the drought deficit volume as a result of climate change.

RCP scenarios are small, with only slightly higher $dVTMhuman_t$ values for RCP2.6. This is likely caused by the relatively small impact of the climate on $dVTMhuman_t$ compared to that of human water abstraction. For RCP8.5 the impact of climate change is projected to be more severe compared to the human contribution to the overall changes in the low flow regime.

The impact of humans on the drought deficit volumes ($dDef_{human}$, Equation 10.9) is more pronounced than the impact on the $dVTMhuman_t$ (Figure 10.5), which is mainly caused by the reduced water availability as a result of water use. In some regions abstractions and water regulation measures account for almost 200% of the net increase in deficit volume for the 21^{st} century. A negative $dDef_{human}$ is found where water regulating measures reduce drought deficits as a direct result of water retention over the year. This effect is found in large parts of Europe, where a large number of reservoirs exist. Additionally, regions in Southern Africa and South America show an impact of the reservoirs operations on the drought deficit volumes. Differences between RCPs are minor, indicating that the contribution of humans to the changes in drought deficit is proportional to the changes in the climate. From this analysis it was derived that the mechanisms between drought, and human water use and

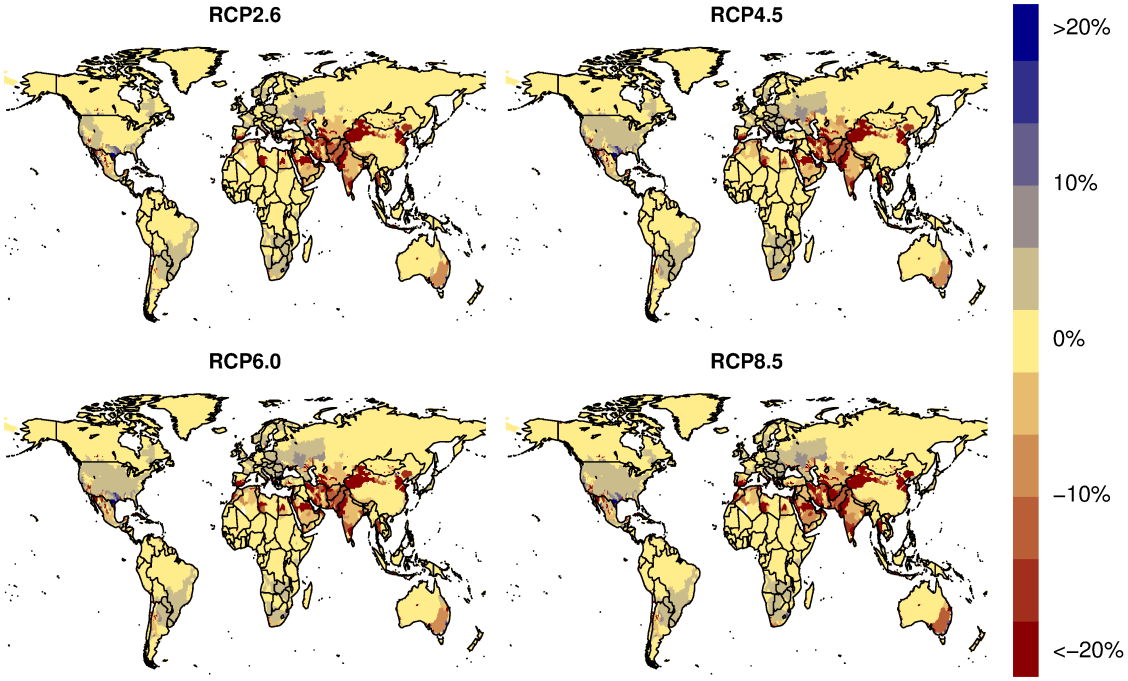

Figure 10.4 Impact of reservoirs and human water use on drought threshold (Q_{90}) compared to the pristine conditions ($dVTMhuman_t$), for the period 2070-2099. Impact is calculated as a percentage where positive percentages indicate an increase in the Q_{90} and negative percentages indicate a decrease in the Q_{90} as a result of human water use and reservoirs. Each plot gives the ensemble mean impact derived from 5 GCMs for different RCPs.

reservoir regulation measures are nontrivial. The combined effect of human water use and river regulations could result in both a positive or negative impact on the low flow regime.

10.3.3 Combined impact on a global scale

The impact of climate change, and human water use and reservoirs has been studied for the changes in deficit volumes ($dDef_{combi}$, Equation 10.10). To this end, the pristine scenario under the control period was compared to the human scenario under the future period (i.e., the end of this century, Figure 10.6). It is clear that the combined impact results in severely increased drought deficit volumes, up to 200% from the control period. Regions include Southeast Asia and the Mediterranean, which are not projected to be impacted by climate change (Figure 10.3), but which will likely be heavily impacted by the additional driving force of the human water use. The severity of the $dDef_{combi}$ increase is less severe for regions in Russia, Europe and North-America. Allthough different RCP scenarios agree upon to a large extent,

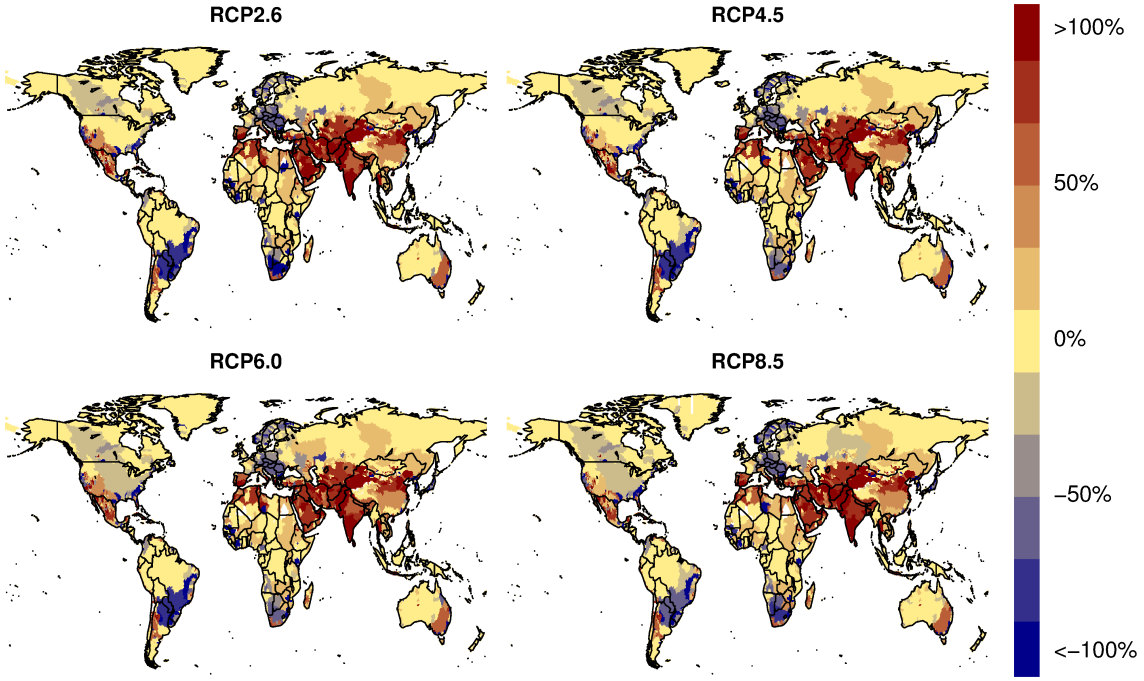

Figure 10.5 Impact of reservoirs and human water use on drought deficit volume compared to the pristine conditions ($dDef_{human}$), for the period 2070-2099. Each plot gives the annual average impact derived from 5 GCMs for different RCP scenarios. Impact is calculated as a percentage, where positive percentages indicate a decrease in the drought deficit volume and negative percentages indicate an increase in the drought deficit volume as a result of human water use and reservoirs.

for Europe the directionality of the changes is expected to be dependent on the RCP. It is concluded that the combined impact overall results in increased drought deficit volumes and hence increases drought vulnerability, especially for Southeast Asia, Middle East and North-Africa.

10.3.4 Impact of climate and human water use - seasonal

The impacts of climate change, reservoirs and human water use on the drought deficit have been studied for each season separately. To assess the impact of climate change the control and future period under the pristine scenario were compared (Figure 10.7), while for the impact of human water use and reservoirs the human and pristine scenario have been compared for the period 2070-2099 (Figure 10.8). For these analyses, the simulations for all RCPs were averaged, because it was shown by our previous analyses (see Figure 10.2, 10.3, 10.4 and 10.5) that the differences between RCPs are minor.

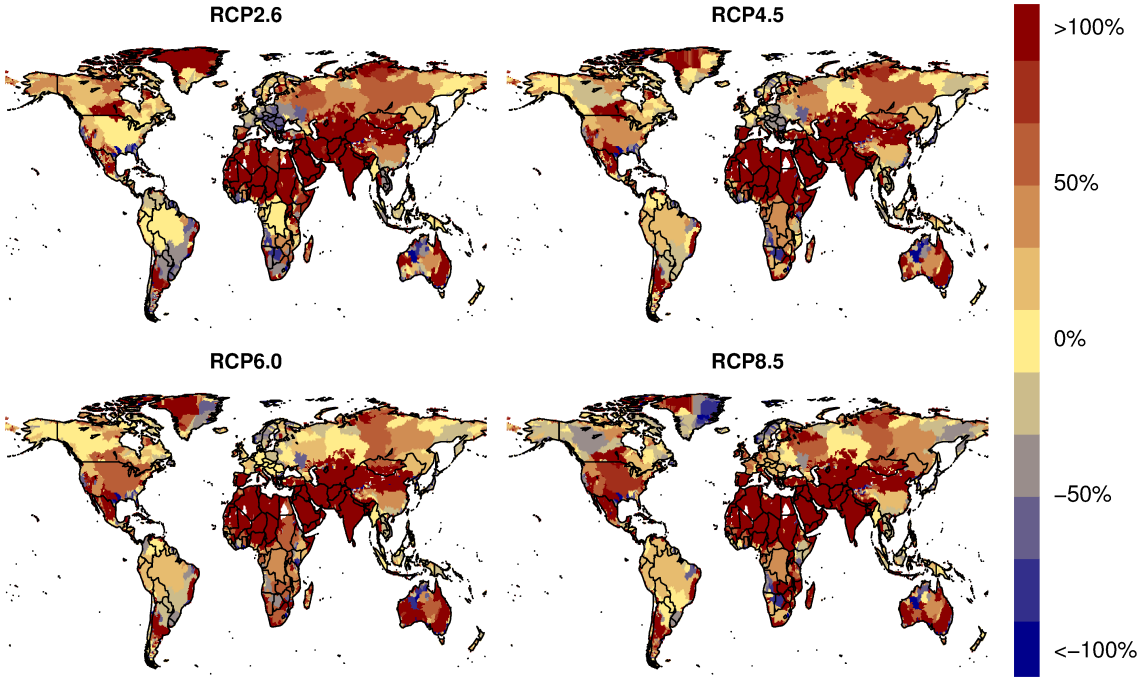

Figure 10.6 Impact of climate change, human water use and reservoirs on drought deficit volume ($dDef_{combi}$), comparison between the periods 1971-2000 (pristine scenario) and 2070-2099 (water use scenario). Each plot gives the annual average impact derived from 5 GCMs for different RCP scenarios. Impact is calculated as a percentage, where positive percentages indicate a decrease in the drought deficit volume and negative percentages indicate an increase in the drought deficit volume as a result of climate change, human water use and reservoirs.

The impact of climate change is visible throughout the world (Figure 10.7), where the largest impacts are again found in Northern Africa, the Eastern part of the United States and Southern Europe. Seasonality in the projected changes is mainly found in Europe and North-America, where the biggest negative impact is found in winter (December - January - February). In the other seasons the impact of climate change is projected to be less or even positive on the observed drought deficit volumes. A non-seasonal or constant water use impact is found for Northern-Africa (negative) and Southeast Asia (positive).

Clear patterns are also visible for the impact of human water use and reservoirs, for example in Asia and the Mediterranean, again showing a positive $dDef_{human}$. The magnitude of the $dDef_{human}$ varies over the year, with a peak in the respective dry season for each region. For the United States, spring droughts are projected to be more severe as a result of water retention of the snow melt peak in reservoirs. This does not, however, decrease the drought deficit volumes in summer and autumn, when more water is available than under pristine conditions. In Europe, reservoirs result

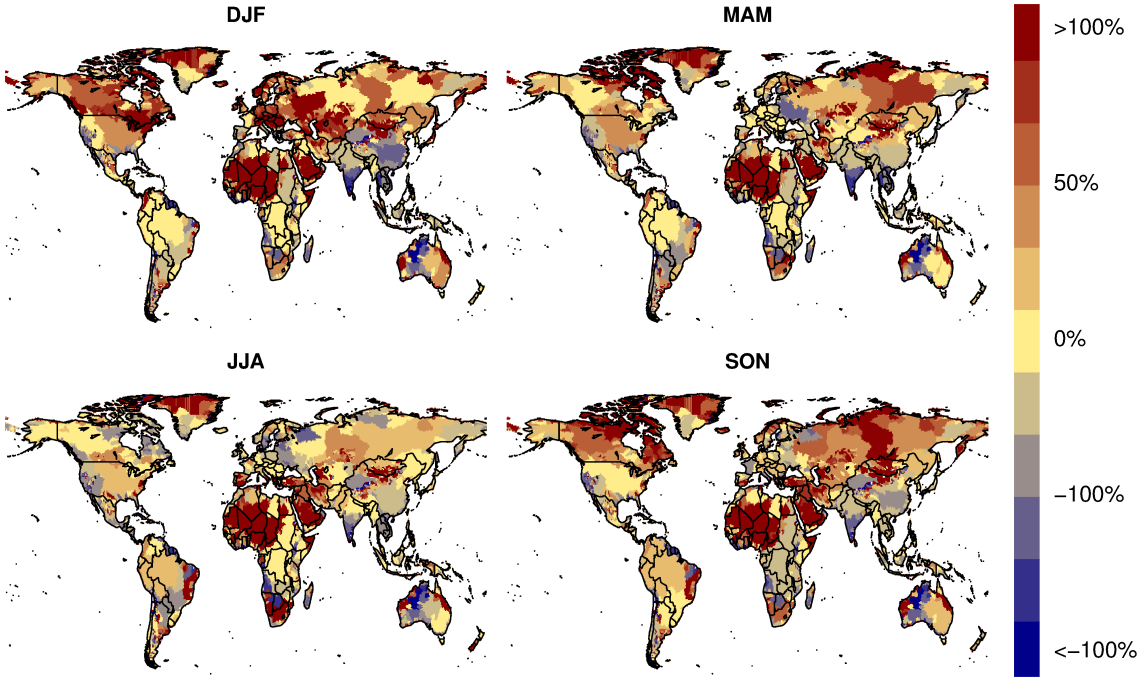

Figure 10.7 Impact of climate change on drought deficit volume ($dDef$) comparison between the periods 1971-2000 and 2070-2099. Each plot gives the seasonal average derived from 5 GCMs and 4 RCPs. Impact is calculated as a percentage, where positive percentages indicate a decrease in the drought deficit volume and negative percentages indicate an increase in the drought deficit volume as a result of climate change.

in a longer retention of water throughout the year, leading to less seasonal discharge and hence lower deficit volumes.

10.3.5 River discharge simulation and impact of human water use per basin

For selected river basins (e.g. Mississippi and Indus) the discharges of the pristine and human scenarios have been compared, to study the impact of reservoirs and human water use on the discharge regime (Figures 10.9 and 10.10). As expected, annual discharge decreased as a result of increased evapotranspiration due to irrigation water use. However, the addition of reservoirs to the river network has a dampening impact on the annual cycle in the discharge regime. Although annual average discharge generally decreased as a result of increased evapotranspiration from the water surface of the reservoirs and irrigation, the decrease is not equally distributed throughout the year. In general, peak flows are reduced as a result of the buffering capacity of the reservoirs and low flow levels are increased even though the water abstraction results in overall lower water availability. The dampening effect for some rivers is projected to result in a decreased drought severity in the low flow season due to increased water

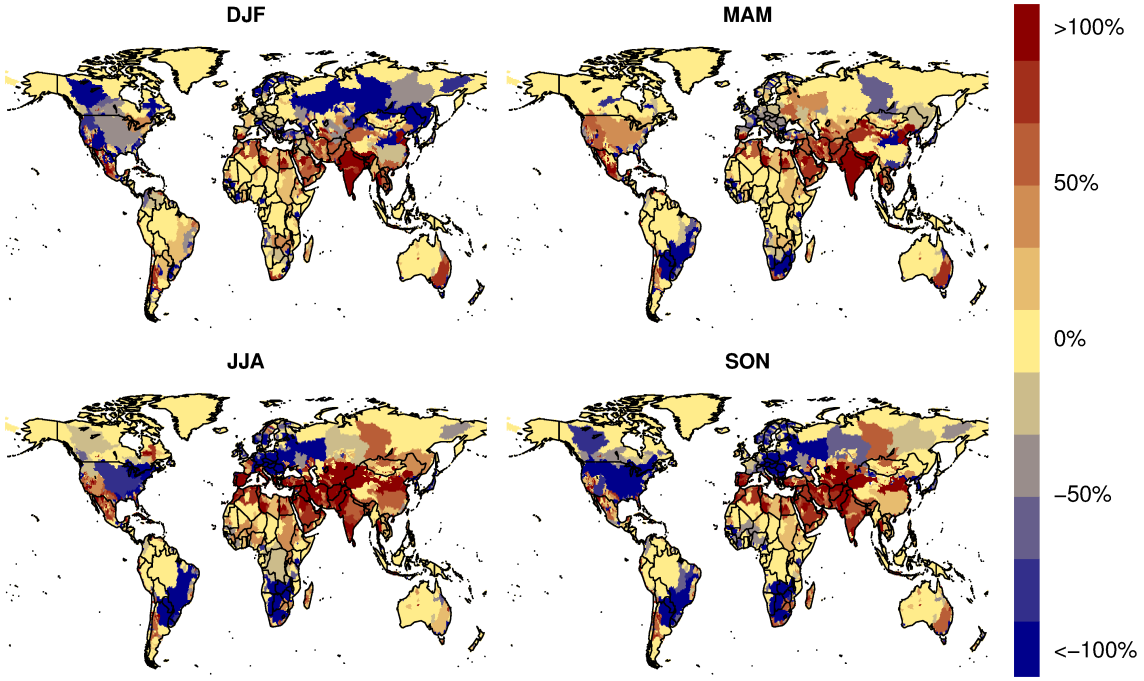

Figure 10.8 Impact of reservoirs and human water use on drought deficit volume compared to the pristine conditions ($dDef_{human}$) per season, for the period 2070-2099. Each plot gives the seasonal average derived from 5 GCMs and 4 RCPs. Impact is calculated as a percentage, where positive percentages indicate a decrease in the drought deficit volume and negative percentages indicate an increase in the drought deficit volume as a result of human water use and reservoirs.

availability. This effect is obvious in some, mostly strongly regulated, river basins in the world where human water abstraction does not exceed the compensating effect (i.e., buffering capacity) of the reservoirs on the low flows. These river basins are mainly situated in Europe and North America (e.g. Mississippi, Figure 10.9). The dampening effect is mainly important in the low flow season when discharge rates are low and droughts tend to have the largest impact on the natural ecosystem and society.

Other major river basins suffer from large abstractions of water for irrigation, resulting in an overall decreased water availability throughout the year. For these basins, the reservoir regulating measures are not enough to compensate the abstraction, and thus the low flow regime changes to even drier conditions. This effect is especially strong for some major river basins in the Middle East and Asia (e.g. Indus, Figure 10.10). In these regions, human water abstractions are large and have a strong negative impact on the drought severity and vulnerability. The projected impacts vary slightly for different RCPs, however, the trend directionalities are similar. For the Mississippi (Figure 10.9) the largest impact of different RCPs is projected, which results in the

shift in the high flow season towards earlier peak flows for the RCPs with a higher temperate rise (RCP6.0 and 8.5), leading to increased and earlier snowmelt. This also impacts the timing and level of the low flow regime. For the Indus (Figure 10.10) the water availability is projected to increase from RCP2.6 to RCP8.5. However, the water abstraction is also projected to increase towards RCP8.5, leading to a significant reduction of the low flow level.

The changes in the streamflow climatology show a decrease in total water availability for the selection of the major river basins (Figure 10.11). On average the streamflow climatology will likely be smoothed throughout the year due to reservoir regulation. The combined impact of this reduced water availability and regulation measures does not always result in a reduction of the threshold as is shown in Figure 10.12. The threshold under human influence is not always lower than the pristine threshold (e.g. Mississippi, Colorado, Volga) and the regulation measures counteract the reduced water availability.

Drought characteristics have been calculated to analyse the impact of reservoirs and human water use on the severity and frequency of drought events (Tables 10.3 and 10.4) for selected river basins. In the current situation (1971-2000) the drought frequency, severity and intensity are increased due to human influences for almost all rivers. The human impact is very large in regions known to be affected by severe water abstractions such as Asia and North America. For example, the Huang He and Colorado are severely impacted and drought characteristics are intensified by five to tenfold compared to the natural conditions. In general, drought events tend to be more severe and frequent for the selected river basins. When the VTM_t is applied to the future period, drought characteristics in the pristine simulation do not significantly change. However, since the VTM_t is adapted to the climatology, the actual low flow level might still reduce significantly, as shown in Figure 10.12. The human influence on drought shows that the drought intensity increases for all rivers, with the exception of the Mississippi and Danube. In these rivers, the reservoirs result in more regulated discharge leading to longer, but less severe drought events. The increase in deficit volume impacts the severity of the drought events and likely increases the vulnerability of our society and nature. The relative increase in drought deficits is largest for the Indus and Huang He, while for the Mississippi the impacts are minor as a result of strong river regulation measures. It should be noted that for many river basins in the world no impact was found since human water use is negligible and reservoir regulations are minimal or reservoirs are absent. In general, human water use increases drought duration and severity, however, this effect can be (partly) compensated by reservoir regulations that retain the water for prolonged periods.

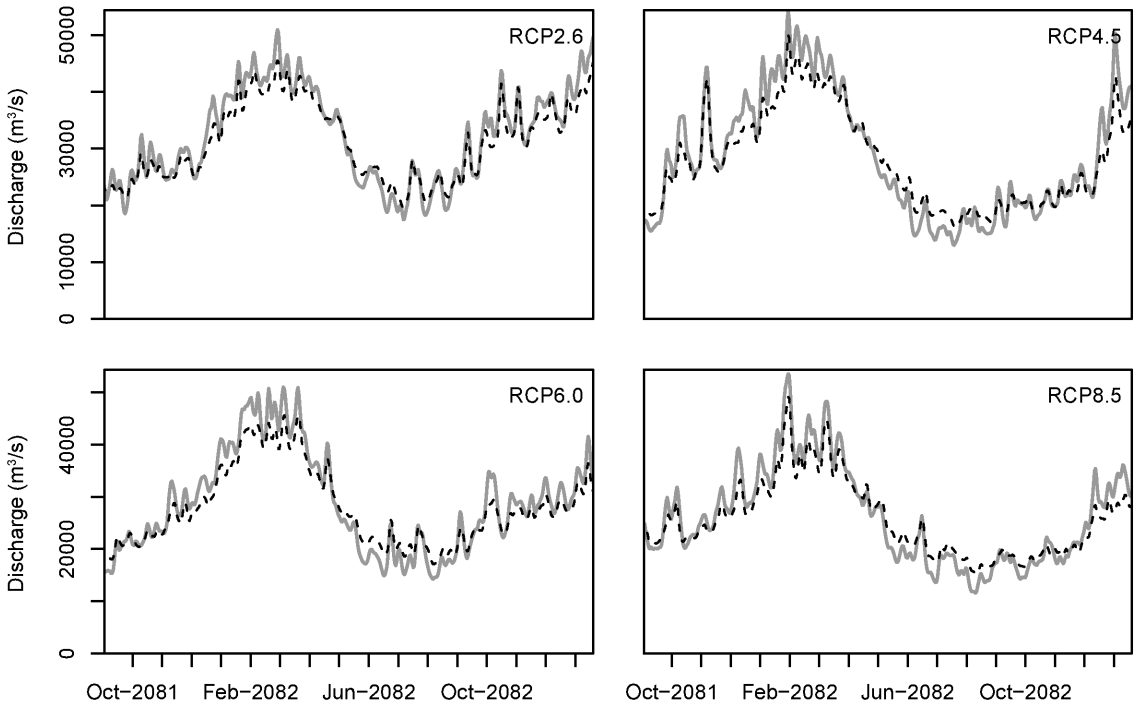

Figure 10.9 Average discharge over 5 GCMs per RCP for the Mississippi river. Solid line indicates the natural scenario without human water abstractions and reservoirs, and the dashed line gives the river discharge under human influences.

10.4 Discussion and Conclusions

In this study the impact of climate change, and human water use and reservoirs on projected hydrological drought characteristics for the 21^{st} century has been studied. Obtained future simulation results were compared to the control period or the pristine scenario (climate change only) and the relative contribution of humans was compared to the impact of climate change. The impact of climate change on the low flow regime and hydrological drought characteristics is projected to be severe. Large regions are expected to suffer from a negative impact of climate change on drought deficit volumes. Additionally, it was found that the impact of water use and reservoirs on hydrological drought characteristics is non-trivial and can vary depending on the local climate and available water resources.

The approach used here is limited by the analysis of only one GHM, where it would be more comprehensive to use an ensemble of GHMs (e.g. Prudhomme et al., 2014; Van Huijgevoort et al., 2014). However, due to the fact that many GHMs do not incorporate the human water abstraction or reservoir regulations, this type of analysis

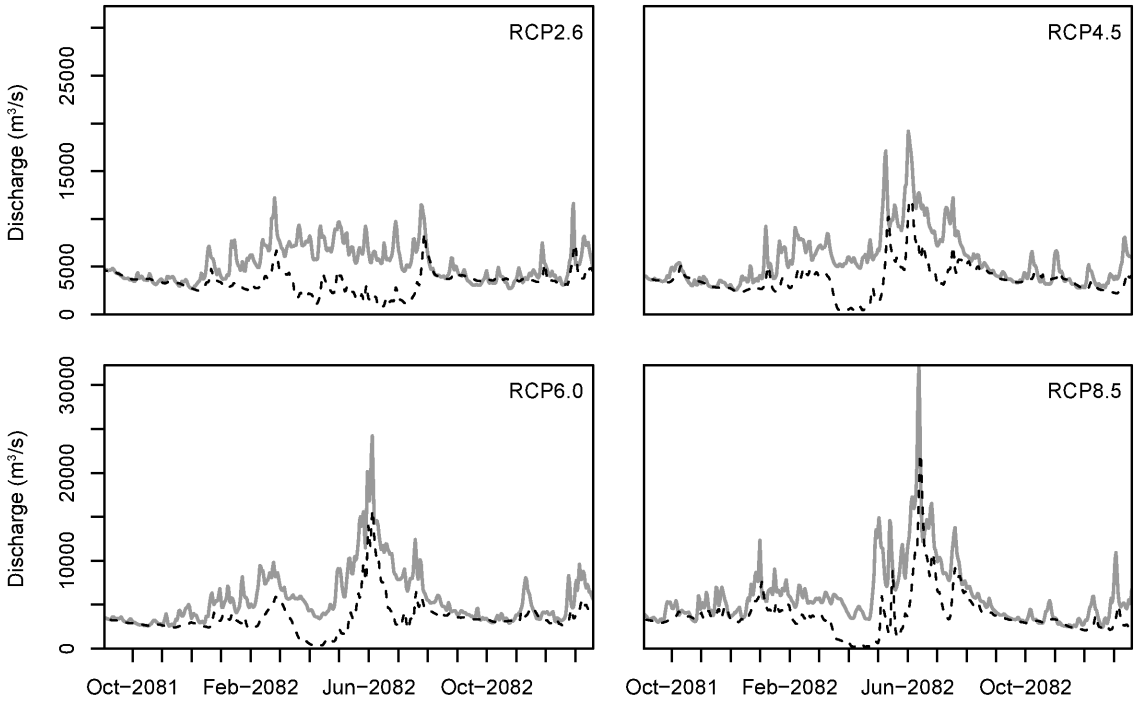

Figure 10.10 Average discharge over 5 GCMs per RCP for the Indus river. Solid line indicates the natural scenario without human water abstractions and reservoirs, and the dashed line gives the river discharge under human influences.

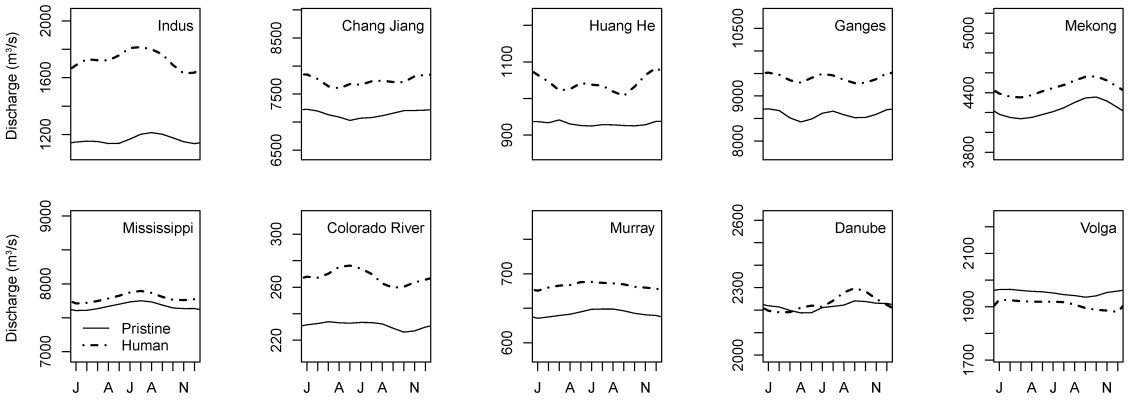

Figure 10.11 Average discharge climatology derived from 5 GCMs and 4 RCPs for 10 selected river basins, for the period 2070-2099. The pristine scenario (solid line) and scenario with human influences (dashed line) are given.

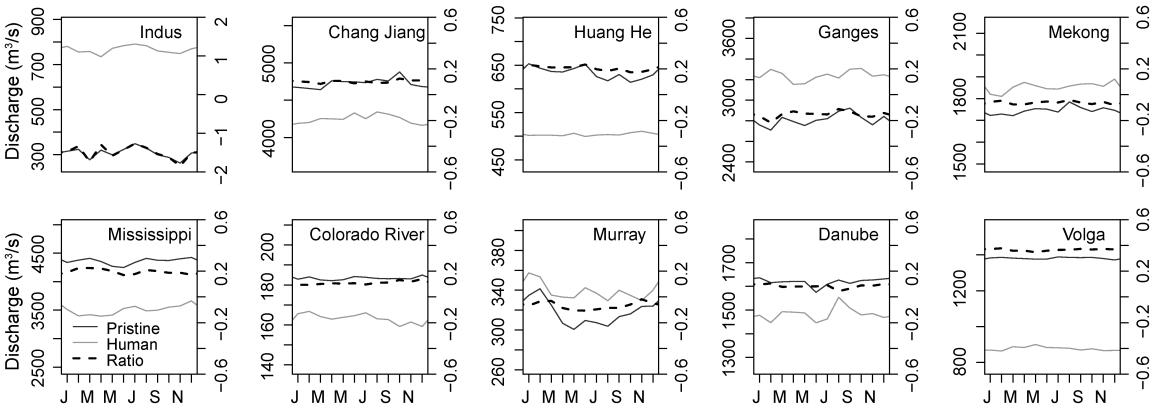

Figure 10.12 Average low flow regime (i.e. thresholds) derived from 5 GCMs and 4 RCPs for 10 selected river basins, for the period 2070-2099. Solid lines indicate the pristine (black) and water demand (grey) scenarios, dashed line gives the ratio between the two discharge climatologies. In other words, the dashed lines show the change in the low flow regime as a result of reservoirs and human water abstractions, where a positive ratio indicates increased mean annual discharge.

Table 10.3 Impact of reservoirs and human water abstractions on drought characteristics compared to the pristine conditions, for the period 1971-2000 and selected rivers. Average drought duration, deficit volume per drought event and the total drought intensity are given. The drought characteristics are obtained with the pristine threshold (derived from the period 1971-2000). The characteristics are averaged over all RCPs and GCMs.

	Pristine			Human		
	Average event		Drought	Average event		Drought
River name	Duration (d)	Deficit (m^3s^{-1})	Intensity $(m^3s^{-1}d^{-1})$	Duration (d)	Deficit (m^3s^{-1})	Intensity $(m^3s^{-1}d^{-1})$
Indus	6.68	3642	545	32.59	67098	2059
Yangtze	5.68	9324	1640	10.36	32223	3110
Huang He	3.42	449	131	32.26	43753	1356
Ganges	4.57	5973	1306	10.92	22438	2054
Mekong	12.96	9344	721	21.72	21504	990
Mississippi	12.71	36501	2873	16.47	43569	2645
Colorado	5.26	494	94	26.83	5452	203
Murray-Darling	29.69	11934	402	37.81	17409	460
Danube	8.48	7581	893	13.88	10549	760
Volga	11.67	7179	615	25.66	46129	1797

Table 10.4 Impact of reservoirs and human water abstractions on drought characteristics compared to the pristine conditions, for the period 2070-2099 and selected rivers. Average drought duration, deficit volume per drought event and the total drought intensity are given. The drought characteristics are obtained with the transient pristine threshold (derived from the period 30-year moving window). The characteristics are averaged over all RCPs and GCMs.

	Pristine			Human		
	Average event		Drought	Average event		Drought
River name	Duration (d)	Deficit (m^3s^{-1})	Intensity ($m^3s^{-1}d^{-1}$)	Duration (d)	Deficit (m^3s^{-1})	Intensity ($m^3s^{-1}d^{-1}$)
Indus	7.75	4866	628	33.65	70173	2085
Yangtze	6.58	11481	1744	10.51	33011	3142
Huang He	4.27	535	125	28.84	37828	1312
Ganges	4.07	4507	1107	13.00	24083	1852
Mekong	15.60	11601	743	27.50	31481	1145
Mississippi	15.68	50522	3221	17.91	50342	2810
Colorado	6.21	691	111	25.56	4855	190
Murray-Darling	38.15	17076	448	52.50	27947	532
Danube	9.31	9324	1002	15.44	13033	844
Volga	11.43	9083	794	24.62	36724	1492

is difficult. Nevertheless, a multi GHM analysis would increase our understanding of uncertainties in future projections of the impact of humans on hydrological drought.

A limitation of the present study is that the abstraction of water is related to the current extent of agricultural irrigation for each region. Expected expansion of irrigated areas is projected to further increase irrigation water demand in some regions (e.g., Africa, South America). Additionally, population growth will result in increased demand for drinking water and industrial activities (Wada et al., 2013), leading to a higher water demand. Especially in areas like Africa, the population is projected to increase substantially. The changes in land use could also significantly alter the propagation of drought and hydrological drought characteristics (Van Lanen et al., 2013). The projected changes in population and land use were currently not included, due to data availability and uncertainty, but could be important when higher accuracy is warranted for future projections. Future hydrological drought characteristics may be altered for regions like Africa, where changes are expected, in both water demand and land use.

Since the relative contribution of human influence on hydrological drought for the 21^{st} century has not been studied globally to our knowledge, it is difficult to compare the obtained results with existing studies. However, areas with a high human impact

as identified in this study have been identified by previous studies (e.g. Wada et al., 2014). One of the main conclusions from this study is that the increased drought vulnerability as a direct result of human water abstraction can be compensated by river regulating measures by reservoirs. Reservoirs retain the water for longer times compared to pristine conditions and thus lead to a smoothed hydrograph, with lower peak flows and higher low flows. This will also directly impact the severity of droughts in the human-controlled systems, where the low flows are partly compensated by extra water availability due to retention in the reservoirs. This phenomenon is mainly found in the United States and Europe, where the number of reservoirs is large.

Furthermore, it is found that human influence can account for almost 100% of the changes in future hydrological drought in areas such as Asia, Middle East and the Mediterranean. These areas are heavily impacted by water abstraction and reservoirs are not enough to compensate for these severe water abstractions. In these regions low flows are expected to be even lower in the future and drought deficit volumes will likely increase significantly. The differences among the RCPs in the obtained results are minor, indicating that the impact of human influence is proportional to the magnitude of the climate change.

Finally, the seasonal changes in drought characteristics were studied by looking at the projected drought events for the period 2070-2099 and the relative contribution of climate change and humans to these events. Climate change is projected to result in increased deficit volumes in large parts of the world, however, seasonal effects play an important role. The impact of summer drought in the Northern Hemisphere is expected to be lower or sometimes result in decreased drought deficit volumes. It is shown that reservoirs increase the drought deficit volumes in the wet season, when the water availability is high, and reduces the deficit volume in the dry season. In the dry season the retained water in the reservoirs is slowly released, positively impacting deficit volumes compared to the pristine scenario. In large parts of Asia, the Middle East and the Mediterranean a high impact of human water abstraction on future drought deficits is found. The impact varies throughout the year and shows a high correlation with the temporal pattern in human water demand. In the crop growing season, water abstractions are projected to be more severe, leading to more severe drought events, while the impact is expected to be reduced in the wet season, due to large water availability and lower human water demands.

It is concluded that the human impact on projected hydrological drought is severe, which has been neglected in most projections for future hydrological drought. Better scenarios of future human water demand could lead to a more skilful projection for the 21^{st} century, however, they are not available yet due to the lack of comprehensive future socio-economic and land use projections that are consistent with one another. Human water use and reservoirs have nowadays substantial impacts on global hydrology and water resources, and should therefore be included in global hydrological models that are used for projections of the future hydrological droughts. This will

significantly improve our understanding of future hydrology and the changes in hydrological drought characteristics.

Acknowledgments

This work has been supported by the framework of ISI-MIP funded by the German Federal Ministry of Education and Research (BMBF) (Project funding reference number: 01LS1201A).

11 Synthesis

Hydrological extremes have an important impact on society. Accurate simulations and early-warning systems for these extremes could significantly reduce damage and the number of fatalities. Hydrological simulations are hampered by uncertainty in various components (e.g. input data, model parameterization). Uncertainty can be found at all timescales, ranging from historic simulations or reanalysis to forecast and projections of future hydrology. Observations could be used to constrain model results thereby reducing the uncertainty. An additional problem for modelling hydrological extremes is the vagueness that comes with the definition of either flood or drought events and how we describe and define extremes.

The main objective of this thesis is: *To reduce uncertainty in simulations, reanalysis, monitoring, forecasting and projections of hydrological extremes for large river basins.* The impact of satellite observations in hydrological model simulations, the human impact on hydrological drought and the vagueness in drought terminology have been dealt with in this thesis and the main findings will be discussed below.

11.1 Impact of ground-based and satellite observations on uncertainty in hydrological model simulations

Satellite observations are frequently used in hydrological analysis and modelling. Examples include, precipitation (Kummerow et al., 2001; Huffman et al., 2010), snow cover (Immerzeel et al., 2009), land surface temperature (Holmes et al., 2009), evaporation (Miralles et al., 2011). A disadvantage of these observations is that they require some form of ground-truth and validation. Recently more research has been focussed on the estimation of soil moisture from space and the applicability of these observations. The launch of the Soil Moisture Ocean Salinaty mission (SMOS, Kerr et al., 2012) and the planned launch of Soil Moisture Active Passive mission beginning 2015 (SMAP, Entekhabi et al., 2010) generated extra attention for this important hydrologic variable. A large number of studies evaluated the performance of SMOS and compared it to Advanced Microwave Scanning Radiometer for the Earth Observing System (AMSR-E, Njoku et al., 2003; Owe et al., 2008), Advanced Scatterometer (ASCAT, Naeimi et al., 2009) or land surface models.

In chapter 2 a detailed evaluation was performed of the accuracy of satellite remote sensing products from SMOS, AMSR-E and ASCAT over Spain. Satellite soil moisture observations were compared to high resolution probabilistic modelling of the unsatured zone and the full error structure of the satellite observations was obtained. Additionally, the satellite retrieval uncertainty was compared to factors such as veg-

etation density, terrain topography and distance to the sea. This detailed evaluation of the error structure provided valuable information for applications that use these surface soil moisture retrievals as observations. It was shown that retrieval errors are largely related to land surface properties and sea salinity in the scene. As a result of that, the errors have a strong spatially correlated error structure. This information on the retrieval error has major implications for the use of these data in hydrological modelling, for example in studies that assume no cross-covariance, like triple collocation or in some data assimilation applications. The information on the cross-covariance in the satellite retrieval error was also used in the following chapters.

In chapter 3 the detailed information on the soil moisture uncertainty together with satellite land surface temperature estimates were used to reduce retrieval uncertainty in a satellite derived real-time precipitation product over the United States. With a particle filter based approach, uncertainty in precipitation retrievals was reduced. A synthetic experiment showed that the potential for improved rainfall estimates was high using both surface soil moisture and land surface temperature retrievals. However, the potential of observed satellite soil moisture retrievals proved to be limited. This was caused by the noise between sequential soil moisture retrievals, which could not always be related to precipitation events. This retrieval noise significantly limits the application of these data for improving the retrieval accuracy of satellite precipitation. On the other hand, satellite retrievals of land surface temperature showed very promising results and the accuracy of satellite precipitation was improved significantly. The results from this study show that it is possible to reduce uncertainty in satellite precipitation. Satellite precipitation is used in many meteorological, agricultural and hydrological applications (especially over data-sparse regions) and the results from this study will improve the accuracy of these applications.

In chapter 4 uncertainty in precipitation estimates and model parameterization was reduced by assimilation of discharge observations. This type of ground-based observation contains valuable information on the integrated state of the catchment and hence could lead to improved estimates of states and parameters. A global hydrological model was used to simulate global discharge and the parameterization and precipitation estimates were corrected with an Ensemble Kalman Filter approach. It was shown that global precipitation estimates need to be reduced to match the observed discharge, model parameters could be estimated successfully with high accuracy and uncertainty in model simulated discharge was reduced. This new simulation provides the first multi-ensemble and water balance preserving terrestrial hydrological reanalysis product and shows that by including observations, simulation of the global hydrological cycle can be significantly improved.

In chapter 5 an Ensemble Kalman Filter approach was successfully applied to estimate model parameters with ground-based discharge and remotely sensed soil moisture observations in the Upper-Danube catchment. Using an identical approach to chapter 4, the uncertainty in hydrological model parameterization was reduced significantly. Apart from discharge, satellite soil moisture observations were used to

increase information on important hydrological processes (e.g. overland flow). Moreover, the information on the spatial error structure of the satellite retrievals from chapter 2 was used to improve the performance of the Ensemble Kalman Filter. The added satellite soil moisture observations were found to reduce uncertainty in the parameterization of the land-surface processes. The reduced uncertainty in parameterization leads to an improved simulation of the discharge and soil moisture in the upper parts of the catchment. In these regions surface runoff generated in the model by saturation excess of the soil moisture is important. It was shown that the combined assimilation of ground-based and satellite observations increases the potential for model calibration to reduce uncertainty in model parameterization and will allow for calibration in regions where ground-based observations are not available.

In chapter 6 the improved calibration for the Upper-Danube (chapter 5) was used in a hindcasting experiment in the European Flood Awareness System (EFAS). In this experiment, observations of discharge at various locations in the catchment and satellite soil moisture were assimilated into a forecasting system and the forecasting performance was evaluated against a scenario without assimilation. It was shown that the addition of satellite soil moisture contributes to an improved forecasting skill of EFAS, especially for shorter lead times (up to 4 days). Additionally, the bias in the forecast was reduced by the assimilation of satellite soil moisture. However, assimilation of additional discharge observations has a bigger impact on the reduction of the uncertainty for longer lead times. This study showed the potential of satellite soil moisture to improve operational flood forecasting in large river basins and has implications for the forecast quality at short lead times.

The combination of detailed evaluation of the satellite soil moisture retrieval errors, calibration of a hydrological model with these observations and application to an operational flood forecasting system, clearly shows the potential and limitations of remotely sensed data. It was also shown that extra ground-based or remote sensing observations could be used to reduce uncertainty in ground-based or satellite precipitation observations, with the help of a Bayesian framework. This work focussed on the implications for large river basins and provided one of the first examples where real satellite data are used to improve hydrological simulations at these scales. The potential positive impact of satellite soil moisture could be even higher in smaller catchments, since fast runoff processes (often related to soil moisture conditions) play a more important role at that scale. However, satellite soil moisture observations are hampered by a low spatial resolution, which impacts their potential for small scale application. The potential to reduce uncertainty in large-scale hydrological simulations by assimilation of satellite observations is present and could improve accuracy of not only hydrological, but also meteorological and agricultural applications at large scales.

11.2 Vagueness in drought terminology

In chapter 7 a comparison between 12 frequently used drought indicators was made on a global scale. These drought indicators were used for drought monitoring related to different parts of the hydrological cycle (meteorological, soil moisture, hydrological drought). It was found that the correlation between drought indicators is low, even when they are designed to monitor the same drought type. The highest correlation is found amongst indicators that are designed to monitor hydrological droughts, while the interchangeability of meteorological drought indicators is very low. Additionally, it was shown that it is important to select a drought indicator based on the drought type under study (e.g. precipitation, soil moisture or hydrological drought). The correlation between indicator time series is low and the results will change significantly when the incorrect indicator is used to study, for example, a soil moisture drought. From these results it is clear that scientists and policy makers should not have the desire to use a single indicator to monitor drought and drought indicators should be chosen based on the drought type of interest.

In chapter 8 a global hydrological model was used to simulate the changes in hydrological drought for the 21^{st} century. From chapter 8 it was found that a fixed threshold to determine drought events does not acknowledge the definition of drought and provides limited information on the changes that occur. Therefore, a transient threshold was developed that uses the climatology of the previous year to study hydrological drought. Results show that the transient approach allows for better understanding of changes in future hydrological drought, where people and nature will adjust to changes in the hydrological regime. Furthermore, it was found that the uncertainty that is derived from the GCM forcing and the climate change scenarios is limited compared to changes in hydrological drought. It is clear that the transient approach should be the new standard for drought analysis in the 21^{st} century, since a conventional fixed threshold does not provide enough information on the impact of climate change. Moreover, the results obtained with fixed threshold often only show increases in drought severity, while in reality society and nature will adjust to new conditions over a period of 30 years.

Reducing the vagueness in drought terminology should be a topic to be dealt with before policy makers are provided with information. Currently, no clear guidelines exist to provide policy makers with the information they need in order to implement adaptation strategies. Moreover, the output from decision support systems should be customized to the local stakeholders or the policy makers that use the system. We should be aware that drought is a complex hydrological extreme, which cannot be characterized by a single indicator or threshold. Also, it should be realized that both society and nature will adjust to climate change. For instance, if water availability increases, people will grow different (more productive) crops, which will increase their drought vulnerability and vice versa. These positive feedbacks between nature and society require dynamic approaches to the concept of drought and calls for further

research. The adaptation of society and nature to changing hydroclimatic conditions should be included in current and future drought simulations to reduce the vagueness in drought terminology.

11.3 Uncertainty associated with the human and climate impact on projections of hydrological drought

In chapter 9 a synthetic hydrological model was used to study the impact of climate change on hydrological drought. It was shown that the impact of a changing climate on hydrological drought is significant. General Circulation Models (GCMs) show a high skill to reproduce hydrological drought, but lack skill in the polar regions where snow accumulation takes place in most times of the year. The agreement amongst GCMs is high and they all show that hydrological drought severity will strongly increase in warm to temperate regions. In the cold regions a shift is projected to occur to less frequent winter drought and an increase in summer drought severity.

In chapter 10 the relative impact of human water demand on hydrological drought for the 21^{st} century was studied. The impact of human water use is more important for some regions than the impact of climate change. Human water abstraction has a strong negative impact on the drought severity, while river regulating measures show a reduction of drought severity for the 21^{st} century. This is the first projection of the impact of human water use on future hydrological drought for an ensemble of GCMs and climate change scenarios. From these results it can be concluded that it is highly important to include the human influence on hydrological drought for projections of the future hydrological regime.

The approach presented in this thesis allows to separate the impact of climate change and human water use on future hydrological drought, and shows that these projections still require considerable improvements. Currently, including human influence on the future hydrological regime is not standard practice, while the impact of humans is considerable. Furthermore, it is shown that the potential impact of climate change in the snow-dominated and polar regions is currently underexposed. The emphasis of most research is placed on the potential changes in desert areas, where the impact on drought events is small. Moreover, the results show that a regime shift occurs in the cold climates which will have a major impact on hydrological management and hydrological extremes in these regions.

11.4 Future perspectives

The aim of this thesis was to quantify and reduce uncertainty and vagueness in simulations of hydrological extremes in large river basins. Bayesian frameworks were used

to combine observational and model data to reduce uncertainty in simulations, reanalysis, forecasts and projections of hydrological extremes. The vagueness in drought terminology was reduced or at least assessed by revisiting the drought definitions and by using dynamic drought definitions and a global evaluation of drought terminology. The findings in this thesis have some major implications for the quality of simulations of hydrological extremes. With the methods, concepts and frameworks that have been developed here, improvements can be made to existing decision support systems and could bring advances to other related fields (e.g meteorological and agricultural modelling). This section is dedicated to the further perspectives and applicability of the methods, concepts and frameworks developed in this thesis.

11.4.1 Satellite observations for hydrological modelling

Satellite observations have proven to be a valuable source of information to reduce uncertainty in hydrological simulations. Although satellite observations are sometimes hampered by high observation uncertainty, correct and accurate characterization of the error structure improves their usability. The major advantage of space-born observations is that they provide a global estimates of land-surface variables with a high temporal resolution. I believe that the results from this thesis show that the combination of data assimilation, satellite data and model simulation could bring major advances in the field of flood forecasting and hydrological modelling in general.

Although data assimilation techniques are standard practice in meteorological simulations and weather predictions, they are underutilized in hydrological simulations (Liu et al., 2012). Particularly, in flood forecasting data-assimilation can be used to improve estimates of current hydrological conditions and thereby reduce forecasting uncertainty. Additionally, data assimilation proved to be a valuable tool to improve hydrological simulations and improve simulations of historic hydrologic events, given that observations are available (Van Dijk et al., 2014). All types of observational data (e.g. satellite, ground-based or historic records) could be simultaneously used in a data assimilation approach, where the optimal state is found based on the ratio between uncertainty in observations and model simulations. This thus greatly increases the amount of suitable observations, especially in data-sparse regions where satellite observations provide estimates of important land surface fluxes and storage. The impact is expected to be most prominent in large scale river basins, because the spatial resolution of most Earth observing satellite sensors is coarse and matched the spatial scale often used for large scale river basin modelling.

Although the theoretical basis to use satellite data in hydrological simulations is present, researchers are often hampered by a lack of knowledge on the implementation of satellite data in hydrological modelling. In this thesis it was shown that satellite observations could be used to reduce the uncertainty in precipitation estimates, hydrological simulations and flood forecasts. Satellite observations show high

potential, and it is my believe that they are currently underutilized in hydrological applications. Possible reasons for the underutilization of remote sensing data are: difficult data formats, large data volumes, relatively new products, sub-optimal access to the satellite data or observations that require expert knowledge to interpret. In the remote sensing community efforts are made to improve usability of remote sensing data, which also creates opportunities for the hydrological community to use satellite observations of important land surface fluxes and storages. The combination of satellite observations and model simulations integrated with data assimilation approaches was proven to reduce uncertainty in hydrological simulations in this thesis and hence improves our understanding of the terrestrial water cycle. A disadvantage of some data assimilation approaches (e.g. Ensemble Kalman Filter) is that they require an ensemble of hydrological model simulations to be used. This in turn increases calculation time and certainly the computational demand. However, with the current advances in the field of computational hydrology and supercomputing facilities, this should be of no concern. In this study multiple realizations of a large scale hydrological model have been used in an ensemble simulation, showing that with the current resources this is feasible. Hydrologists should be more focussed on the accuracy of their simulations, than on potential increase in computational demands. Moreover, the use of an ensemble simulation will improve insight in the diversity amongst models and model parameterizations and the resulting uncertainty in the hydrological simulations.

11.4.2 Projection of future hydrological drought

This thesis showed that the impact of climate change on future hydrological drought is highly dependent on the local climatology and the impact of human influence. Although most drought studies focus on changes in regions where a semi-arid climate is present, the impact of the changes is limited for these climates. More severe changes can be expected in the snow-dominated regions, where the timing of the snowmelt plays an important role in the water availability throughout the year. Here, shifts in the timing of the snowmelt peak will occur, which in turn will likely impact summer water availability for crops and drinking water. With higher temperatures the evaporation will increase and since most of the water is not available in the catchment (since it has melted) more severe water deficits will occur. This will in turn increase summer drought vulnerability in the cold regions, where water availability was no problem before climate change. This calls for more research on the feedback processes between climate change and water availability throughout the year. These processes will play an important role with respect to the energy and agricultural sector and could potentially be harmful to the local economy in these cold regions.

The impact of humans on hydrological drought has been largely neglected in projections and simulations of hydrological drought (Wada et al., 2013). The main reason for this shortcoming in hydrological simulations is that most models designed to sim-

ulate large-scale hydrological processes, do not incorporate human influence on the hydrological cycle. In this thesis it was shown that for some regions this impact cannot be neglected and our perspective on future hydrological drought will change if we include human interactions in hydrological models. Humans are not only important for large-scale hydrology, but also in the smaller catchments. In many small catchments the surface runoff in urban areas has a distinct impact on the observed hydrograph and should be incorporated in the hydrological models. At larger scales, water abstraction and consumption will decrease water availability and hence lead to dry conditions. Although it is difficult to obtain abstraction data, these processes should be included as realistically as possible to have a more realistic portrayal of hydrology in our models.

11.4.3 Drought definitions

This study showed that there are multiple ways to identify drought events and that the impact of climate changes on drought identification is significant. It was concluded that the definition of drought should use a transient approach (especially with respect to climate change) and should be adjusted to the drought type of interest. For example, when the impact of drought on irrigation demand is studied, there is no need to know the anomalies in reservoir storage. Therefore, it is advised to provide policy makers with a selection of drought indicators that could be adjusted to the impacted part of the hydrological cycle of interest (e.g. precipitation, soil moisture, discharge). Drought monitoring systems or drought projections should therefore provide policymakers and stakeholders with the information based on their interest. It is also important that for cold regions, where snow accumulation is relevant, snow processes are incorporated in the drought definition. Most drought indicators that are currently used do not respect processes related to snow accumulation or increased water availability due to snow melt.

When projections for the 21^{st} century are provided, drought definitions should be adjusted to the changes in climate and the changing impact of humans on natural water availability. A non-transient approach would not do justice to the ever changing climatology. Since extremes are defined as exception with respect to the climatology (last 30 years) the common understanding of a hydrological extreme will change over time. Additionally, more information should be provided on the uncertainty in the hydrological simulations and projections. This would advance the field of drought monitoring and forecasting with more custom-made simulations that provide useful information for stakeholders and include information on simulation uncertainty. This uncertainty information will also provide knowledge on the skill of the projections and the probability that an area is really affected by a change in local climatology.

11.4.4 Uncertainty in simulations of hydrological extremes for large river basins

This thesis showed that it is possible to reduce the uncertainty in the simulations of hydrological extremes with existing data, models and frameworks. The ultimate goal is to combine all possible sources of information/observations into a data-assimilation framework that will improve the simulations and forecasting of hydrological extremes in large river basins. This improved framework will utilize the information coming from multiple sources and will be a major advance in the quality of decision support system in data-sparse regions. These often vulnerable regions will benefit from the improved preparedness, resulting in a lower number of fatalities and reduced economic damage caused by hydrological extremes. The developments of the last decade in the field of large-scale hydrology will help to put this new framework in place and provide a solid scientific basis for the research. Therefore, I believe that the field of hydrology can make advances in this new era in which more data and more computer power can be combined with our increased understanding of hydrological processes in large river basins.

Appendix A Time series of satellite and modelled soil moisture

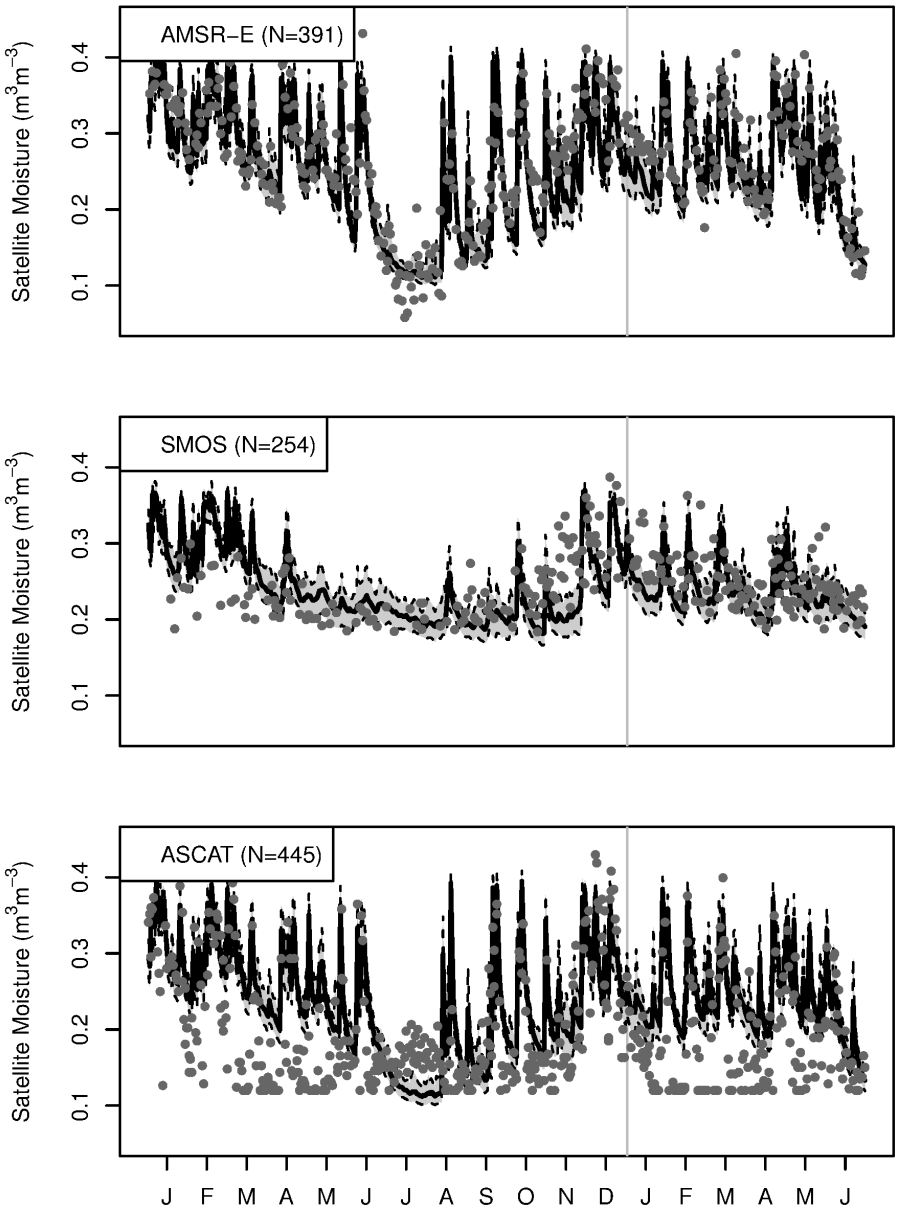

Figure A.1 Three example time series for AMSR-E, SMOS and ASCAT compared with the satellite support averaged SWAP soil moisture (black line), including 95% confidence interval (grey), N is the number of satellite soil moisture retrievals for one location in South Spain (36.8° N, 2.4° W).

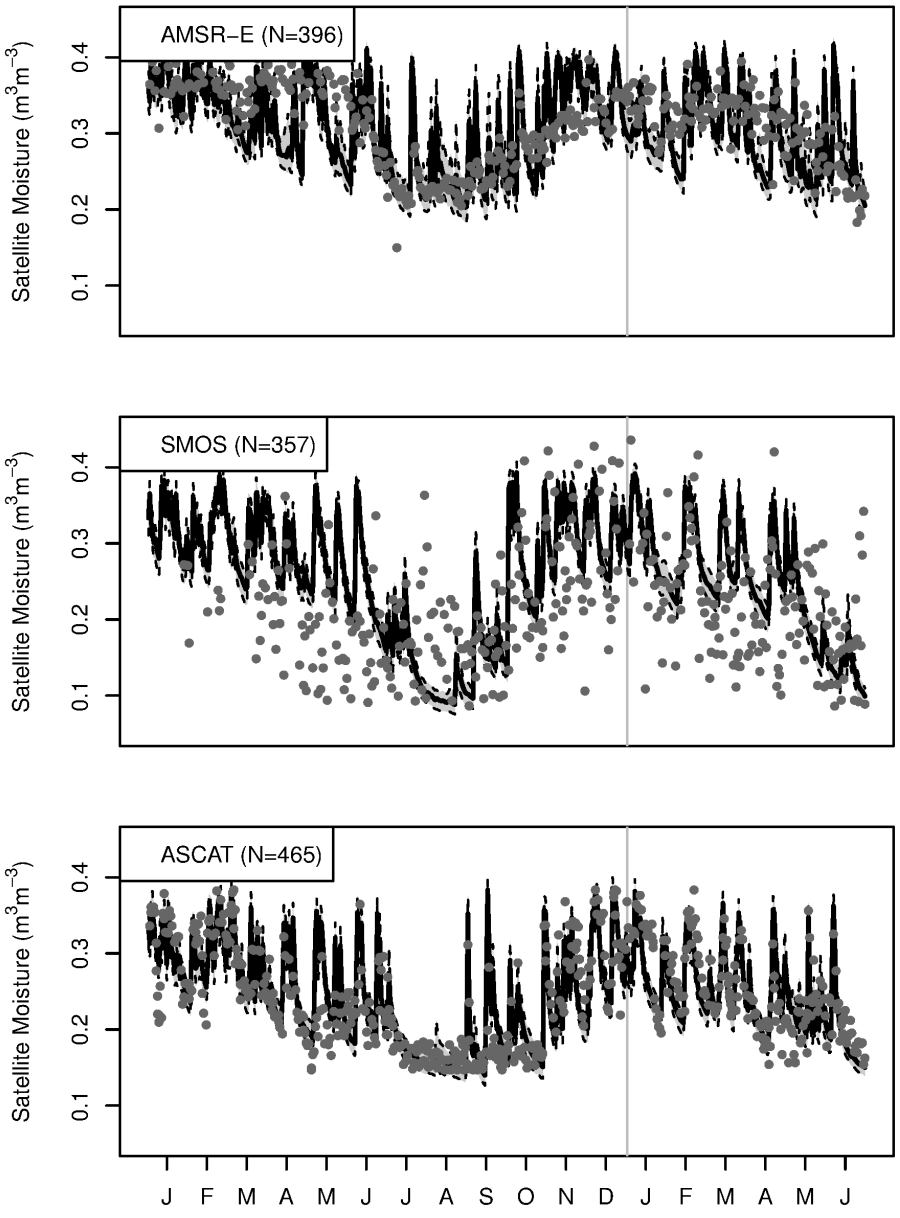

Figure A.2 Three example time series for AMSR-E, SMOS and ASCAT compared with the satellite support averaged SWAP soil moisture (black line), including 95% confidence interval (grey), N is the number of satellite soil moisture retrievals for one location in Northeast Spain (42.8° N, 1.6° W).

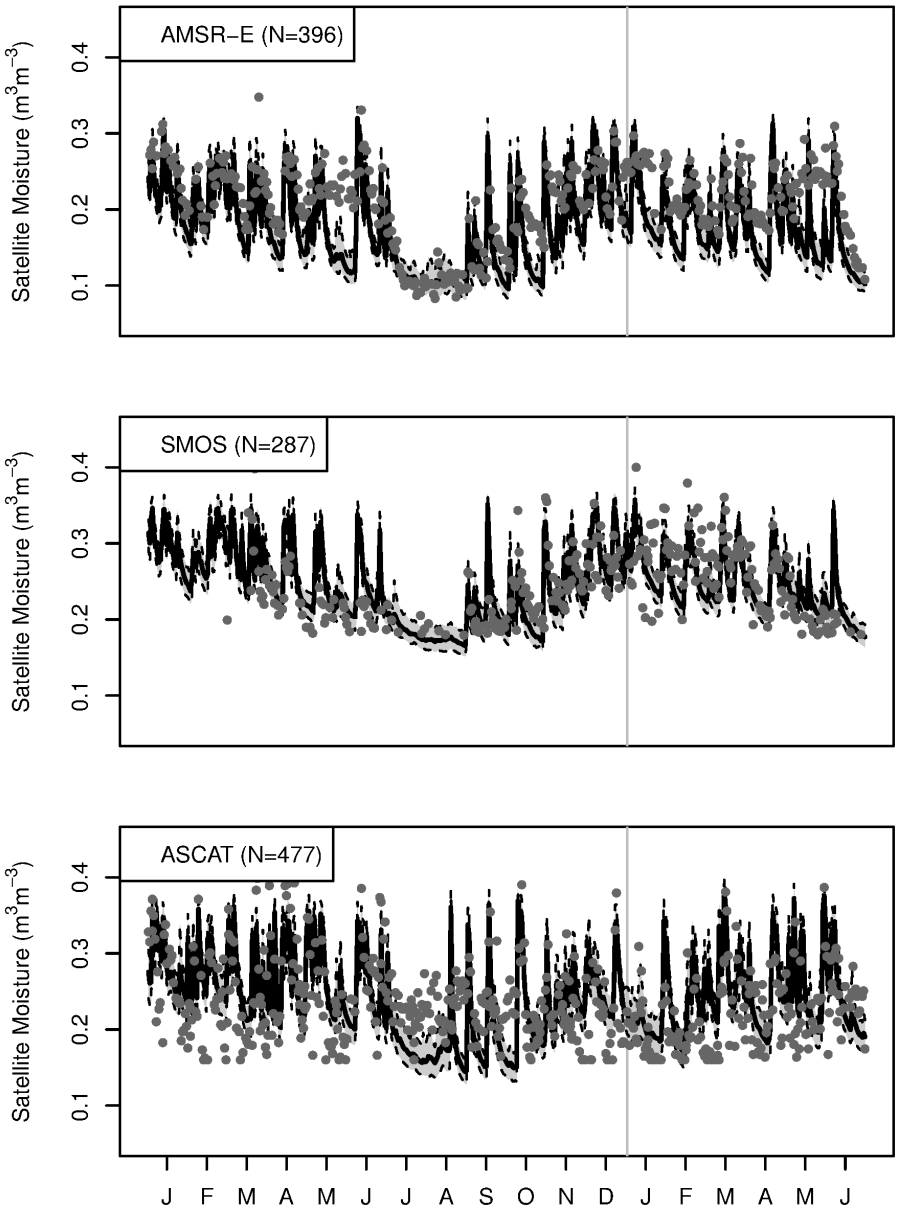

Figure A.3 Three example time series for AMSR-E, SMOS and ASCAT compared with the satellite support averaged SWAP soil moisture (black line), including 95% confidence interval (grey), N is the number of satellite soil moisture retrievals for one location in central Spain (41.7° N, 4.8° W).

References

Adam, J. C. and D. P. Lettenmaier (2003), Adjustment of global gridded precipitation for systematic bias. Journal of Geophysical Research: Atmospheres 108, 4257.

Agboma, C., S. Yirdaw and K. Snelgrove (2009), Intercomparison of the total storage deficit index (TSDI) over two Canadian prairie catchments. Journal of Hydrology 374, 351 – 359.

Albergel, C., P. d. Rosnay, C. Gruhier, J. Muñoz Sabater, S. Hasenauer, L. Isaksen, Y. Kerr and W. Wagner (2012), Evaluation of remotely sensed and modelled soil moisture products using global ground-based in situ observations. Remote Sensing of Environment 118, 215 – 226.

Alderlieste, M. A. A., H. A. J. Van Lanen and N. Wanders (2014), Future low flows and hydrological drought: how certain are these for Europe. In: T. Daniell, H. Van Lanen, S. Demuth, G. Laaha, E. Servat, G. Mahe, J.-F. Boyer, J.-E. Paturel, A. Dezetter and D. Ruelland, eds., Hydrology in a Changing World: Environmental and Human Dimensions, no. 363 in IAHS Publications, 60–65.

Alfieri, L., P. Burek, E. Dutra, B. Krzeminski, D. Muraro, J. Thielen and F. Pappenberger (2013), GloFAS-global ensemble streamflow forecasting and flood early warning. Hydrology and Earth System Sciences 17, 1161–1175.

Allen, R., L. Pereira, D. Raes and M. Smith (2006), FAO Irrigation and Drainage Paper No. 56 - Crop Evapotranspiration. Food and Agriculture Organization.

Alley, W. (1984), The Palmer Drought Severity Index: limitations and assumptions. Journal of Climate and Applied Meteorology 23, 1100 – 1109.

Andreadis, K. M., E. A. Clark, A. W. Wood, A. F. Hamlet and D. P. Lettenmaier (2005), Twentieth-century drought in the conterminous united states. Journal of Hydrometeorology 6, 985–1001.

Andreu, J., J. Ferrer-Polo, M. Pérez and A. Solera (2009), Decision support system for drought planning and management in the jucar river basin, Spain. In: 18 th World IMACS/MODSIM Congress, Cairns, Australia.

Anterrieu, E. (2011), On the detection and quantification of RFI in L1a signals provided by SMOS. IEEE Transactions on Geoscience and Remote Sensing 49, 3986 –3992.

Aon Benfield (2013), Impact forecasting - June 2013. Global Catastrophe Recap report.

Aon Benfield (2014), Annual global climate and catastrophe report impact forecasting - 2013. Global Catastrophe Recap report.

Arguez, A. and R. S. Vose (2010), The definition of the standard WMO climate normal: The key to deriving alternative climate normals. Bulletin of the American Meteorological Society 92, 699–704.

Arnell, N. W. (2003), Effects of IPCC SRES emissions scenarios on river runoff: a global perspective. Hydrology and Earth System Sciences 7, 619–641.

Arulampalam, M., S. Maskell, N. Gordon and T. Clapp (2002), A tutorial on particle filters for online nonlinear/non-gaussian bayesian tracking. Signal Processing, IEEE Transactions on 50, 174–188.

Aubert, D., C. Loumagne and L. Oudin (2003), Sequential assimilation of soil moisture and streamflow data in a conceptual rainfallrunoff model. Journal of Hydrology 280, 145 – 161.

Baroni, G., A. Facchi, C. Gandolfi, B. Ortuani, D. Horeschi and J. C. van Dam (2010), Uncertainty in the determination of soil hydraulic parameters and its influence on the performance of two hydrological models of different complexity. Hydrology and Earth System Sciences 14, 251–270.

Bartalis, Z., R. Kidd and K. Scipal (2006a), Development and implementation of a discrete global grid system for soil moisture retrieval using the MetOp ASCAT scatterometer. In: 1st EPS/MetOp RAO Workshop, Frascati, Italy: ESA SP-618. 15-17 May 2006.

Bartalis, Z., K. Scipal and W. Wagner (2006b), Azimuthal anisotropy of scatterometer measurements over land. IEEE Geoscience and Remote Sensing Society 44, 2083–2092.

Bartholmes, J. C., J. Thielen, M. H. Ramos and S. Gentilini (2009), The European Flood Alert System EFAS–part 2: Statistical skill assessment of probabilistic and deterministic operational forecasts. Hydrology and Earth System Sciences 13, 141–153.

Bates, B., Z. Kundzewicz, S. Wu. and J. Palutikof (2008), Climate Change and Water. Technical Paper of the Intergovernmental Panel on Climate Change, Intergovernmental Panel on Climate Change, Geneva.

Bergström, S. (1995), The HBV model, in Computer Models of Watershed Hydrology. Highlands Ranch, Colorado, U.S.A.: Water Resour. Publ.

Beven, K. (2006), A manifesto for the equifinality thesis. Journal of Hydrology 320, 18 – 36.

Beven, K. and A. Binley (1992), The future of distributed models: Model calibration and uncertainty prediction. Hydrological Processes 6, 279–298.

Beven, K. and P. Young (2013), A guide to good practice in modeling semantics for authors and referees. Water Resources Research 49, 5092–5098.

Bierkens, M. F. P., P. A. Finke and P. De Willigen, eds. (2000), Upscaling and Downscaling Methods for Environmental Research, vol. 88 of *Developments in Plant and Soil Sciences*. Kluwer academic publishers.

Bisselink, B., E. van Meijgaard, A. J. Dolman and R. A. M. De Jeu (2011), Initializing a regional climate model with satellite-derived soil moisture. Journal of Geophysical Research-Space Physics 116, D02121.

Black, T. A., W. R. Gardner and G. W. Thurtell (1969), The prediction of evaporation, drainage, and soil water storage for a bare soil. Soil Science Society of America Proceedings 33, 655–660.

Blamey, R. C. and C. J. C. Reason (2012), The role of mesoscale convective complexes in southern Africa summer rainfall. J. Climate 26, 1654–1668.

Bloomfield, J. P. and B. P. Marchant (2013), Analysis of groundwater drought building on the standardised precipitation index approach. Hydrology and Earth System Sciences 17, 4769–4787.

Bolten, J., W. Crow, X. Zhan, T. Jackson and C. Reynolds (2010), Evaluating the utility of remotely sensed soil moisture retrievals for operational agricultural drought monitoring. Selected Topics in Applied Earth Observations and Remote Sensing, IEEE Journal of 3, 57–66.

Bourzac, K. (2013), Water: The flow of technology. Nature 501, S4–S6.

Brier, G. (1950), Verification of forecasts expressed in terms of probability. Monthly Weather Review 78, 1–3.

Brocca, L., F. Melone, T. Moramarco, W. Wagner, V. Naeimi, Z. Bartalis and S. Hasenauer (2010), Improving runoff prediction through the assimilation of the ascat soil moisture product. Hydrology and Earth System Sciences 14, 1881–1893.

Brocca, L., S. Hasenauer, T. Lacava, F. Melone, T. Moramarco, W. Wagner, W. A. Dorigo, P. Matgen, J. Martínez-Fernández, P. Llorens, J. Latron, C. Martin and M. Bittelli (2011), Soil moisture estimation through ASCAT and AMSR-E sensors: An intercomparison and validation study across Europe. Remote Sensing of Environment 115, 3390–3408.

Brocca, L., T. Moramarco, F. Melone, W. Wagner, S. Hasenauer and S. Hahn (2012), Assimilation of surface- and root-zone ASCAT soil moisture products into rainfall runoff modeling. IEEE Transactions on Geoscience and Remote Sensing 50, 2542–2555.

Brocca, L., T. Moramarco, F. Melone and W. Wagner (2013), A new method for rainfall estimation through soil moisture observations. Geophysical Research Letters 40, 853–858.

Brocca, L., L. Ciabatta, C. Massari, T. Moramarco, S. Hahn, S. Hasenauer, R. Kidd, W. Dorigo, W. Wagner and V. Levizzani (2014), Soil as a natural rain gauge: Estimating global rainfall from satellite soil moisture data. Journal of Geophysical Research: Atmospheres 119, 5128–5141.

Burgers, G., P. Van Leeuwen and G. Evensen (1998), Analysis scheme in the Ensemble Kalman Filter. Monthly Weather Review 126, 1719–1724.

Burke, E. J., S. J. Brown and N. Christidis (2006), Modeling the recent evolution of global drought and projections for the twenty-first century with the Hadley centre climate model. Journal of Hydrometeorology 7, 1113–1125.

Byun, H. and D. Wilhite (1999), Objective quantification of drought severity and duration. Bulletin of the American Meteorological Society 12, 2747 – 2756.

Camporese, M., C. Paniconi, M. Putti and P. Salandin (2009), Ensemble Kalman filter data assimilation for a process-based catchment scale model of surface and subsurface flow. Water Resources Research 45, W10421.

Chen, F., W. T. Crow, P. J. Starks and D. N. Moriasi (2011), Improving hydrologic predictions of a catchment model via assimilation of surface soil moisture. Advances in Water Resources 34, 526 – 536.

Clark, M. P., D. E. Rupp, R. A. Woods, X. Zheng, R. P. Ibbitt, A. G. Slater, J. Schmidt and M. J. Uddstrom (2008), Hydrological data assimilation with the Ensemble Kalman Filter: Use of streamflow observations to update states in a distributed hydrological model. Advances in Water Resources 31, 1309 – 1324.

Clyde, G. (1931), Snow melting characteristics. Utah Agricultural Experiment Station bulletin 231, 1–23.

Collins, E. H. (1934), Relationship of degree-days above freezing to runoff. Transactions of the American Geophysical Union, Reports and Papers, Hydrology 15, 624–629.

Corzo Perez, G. A., M. H. J. van Huijgevoort, F. Voss and H. A. J. van Lanen (2011a), On the spatio-temporal analysis of hydrological droughts from global hydrological models. Hydrology and Earth System Sciences 15, 2963–2978.

Corzo Perez, G. A., H. A. J. Van Lanen, N. Bertrand, C. Chen, D. Clark, S. Folwell, S. N. Gosling, N. Hanasaki, J. Heinke and F. Voss (2011b), Drought at the global scale in the 21st Century. Tech. Rep. 43, EU WATCH (Water and global Change) project.

Cressie, N. A. C. (1993), Statistics for spatial data. Wiley series in Probability and mathematical statistics.

Crow, W. T. and J. D. Bolten (2007), Estimating precipitation errors using spaceborne surface soil moisture retrievals. Geophysical Research Letters 34, L08403.

Crow, W. T. and D. Ryu (2009), A new data assimilation approach for improving runoff prediction using remotely-sensed soil moisture retrievals. Hydrology and Earth System Sciences 13, 1–16.

Crow, W. T. and X. Zhan (2007), Continental-scale evaluation of remotely sensed soil moisture products. IEEE Geoscience and Remote Sensing Letters 4, 451–455.

Crow, W. T., G. J. Huffman, R. Bindlish and T. J. Jackson (2009), Improving satellite-based rainfall accumulation estimates using spaceborne surface soil moisture retrievals. Journal of Hydrometeorology 10, 199–212.

Crow, W. T., D. G. Miralles and M. H. Cosh (2010), A quasi-global evaluation system for satellite-based surface soil moisture retrievals. IEEE Transactions on Geoscience and Remote Sensing 48, 2516–2527.

Crow, W. T., M. J. van den Berg, G. J. Huffman and T. Pellarin (2011), Correcting rainfall using satellite-based surface soil moisture retrievals: The Soil Moisture Analysis Rainfall Tool (SMART). Water Resources Research 47, W08521.

Crow, W. T., A. A. Berg, M. H. Cosh, A. Loew, B. P. Mohanty, R. Panciera, P. de Rosnay, D. Ryu and J. P. Walker (2012), Upscaling sparse ground-based soil moisture observations for the validation of coarse-resolution satellite soil moisture products. Reviews of Geophysics 50, RG2002.

Dai, A. (2011), Drought under global warming: a review. Wiley Interdisciplinary Reviews: Climate Change 2, 45–65.

Dai, A. (2013), Increasing drought under global warming in observations and models. Nature Climate Change 3, 52–58.

Dai, A. and K. E. Trenberth (2002), Estimates of freshwater discharge from continents: Latitudinal and seasonal variations. Journal of Hydrometeorology 3, 660–687.

Dai, A., K. Trenberth and T. Qian (2004), A global dataset of palmer drought severity index for 1870 - 2002: Relationship with soil moisture and effects of surface warming. Journal of Hydrometeorology 5, 1117 – 1130.

Dall'Amico, J., F. Schlenz, A. Loew and W. Mauser (2012), First results of SMOS soil moisture validation in the Upper Danube catchment. IEEE Transactions on Geoscience and Remote Sensing 50, 1507–1516.

Davie, T. (2008), Fundamentals of Hydrology. Routledge fundamentals of physical geography series, Routledge.

De Graaf, I. E. M., L. P. H. Van Beek, Y. Wada and M. F. P. Bierkens (2014), Dynamic attribution of global water demand to surface water and groundwater resources: Effects of abstractions and return flows on river discharges. Advances in Water Resources 64, 21 – 33.

De Jeu, R. A. M. and M. Owe (2003), Further validation of a new methodology for surface moisture and vegetation optical depth retrieval. International Journal of Remote Sensing 24, 4559–4578.

De Jeu, R. A. M., W. Wagner, T. R. H. Holmes, A. J. Dolman, N. C. Van de Giesen and J. Friesen (2008), Global soil moisture patterns observed by space borne microwave radiometers and scatterometers. Surveys in Geophysics 28, 399–420.

De Lannoy, G. J. M., P. R. Houser, V. R. N. Pauwels and N. E. C. Verhoest (2006), Assessment of model uncertainty for soil moisture through ensemble verification. Journal of Geophysical Research-Space Physics 111, D10101.

De Roo, A., C. Wesseling and W. Van Deursen (2000), Physically-based river basin modelling within a GIS: The LISFLOOD model. Hydrological Processes 14, 1981–1992.

De Rosnay, P., M. Drusch, D. Vasiljevic, G. Balsamo, C. Albergel and L. Isaksen (2013), A simplified extended kalman filter for the global operational soil moisture analysis at ECMWF. Quarterly Journal of the Royal Meteorological Society 139, 1199–1213.

Dee, D. P., S. M. Uppala, A. J. Simmons, P. Berrisford, P. Poli, S. Kobayashi, U. Andrae, M. A. Balmaseda, G. Balsamo, P. Bauer, P. Bechtold, A. C. M. Beljaars, L. van de Berg, J. Bidlot, N. Bormann, C. Delsol, R. Dragani, M. Fuentes, A. J. Geer, L. Haimberger, S. B. Healy, H. Hersbach, E. V. Hólm, L. Isaksen, P. Kållberg, M. Köhler, M. Matricardi, A. P. McNally, B. M. Monge-Sanz, J.-J. Morcrette, B.-K. Park, C. Peubey, P. de Rosnay, C. Tavolato, J.-N. Thépaut and F. Vitart (2011), The ERA-Interim reanalysis: configuration and performance of the data assimilation system. Quarterly Journal of the Royal Meteorological Society 137, 553–597.

Dharssi, I., K. J. Bovis, B. Macpherson and C. P. Jones (2011), Operational assimilation of ASCAT surface soil wetness at the met office. Hydrology and Earth System Sciences 15, 2729–2746.

Di Baldassarre, G. and A. Montanari (2009), Uncertainty in river discharge observations: a quantitative analysis. Hydrology and Earth System Sciences 13, 913–921.

Dirmeyer, P. A., A. J. Dolman and N. Sato (1999), The pilot phase of the Global Soil Wetness Project. Bulletin of the American Meteorological Society 80, 851–878.

Döll, P., F. Kaspar and B. Lehner (2003), A global hydrological model for deriving water availability indicators: model tuning and validation. Journal of Hydrology 270, 105 – 134.

Dorigo, W. A., K. Scipal, R. M. Parinussa, Y. Y. Liu, W. Wagner, R. A. M. de Jeu and V. Naeimi (2010), Error characterisation of global active and passive microwave soil moisture datasets. Hydrology and Earth System Sciences 14, 2605–2616.

Dorigo, W. A., W. Wagner, R. Hohensinn, S. Hahn, C. Paulik, A. Xaver, A. Gruber, M. Drusch, S. Mecklenburg, P. van Oevelen, A. Robock and T. J. Jackson (2011), The international soil moisture network: a data hosting facility for global in situ soil moisture measurements. Hydrology and Earth System Sciences 15, 1675–1698.

Doucet, A., S. Godsill and C. Andrieu (2000), On sequential Monte Carlo sampling methods for Bayesian filtering. Statistics and Computing 10, 197–208.

Dracup, J., K. Lee and E. Paulson Jr (1980), On the definition of droughts. Water Resources Research 16, 297 – 302.

Draper, C., J. P. Walker, P. Steinle, R. A. M. De Jeu and T. R. H. Holmes (2009), An evaluation of AMSR-E derived soil moisture over australia. Remote Sensing of Environment 113, 703–710.

Draper, C., J.-F. Mahfouf, J.-C. Calvet, E. Martin and W. Wagner (2011), Assimilation of ASCAT near-surface soil moisture into the sim hydrological model over france. Hydrology and Earth System Sciences 15, 3829–3841.

Draper, C. S., R. H. Reichle, G. J. M. De Lannoy and Q. Liu (2012), Assimilation of passive and active microwave soil moisture retrievals. Geophysical Research Letters 39, L04401.

Drusch, M. (2007), Initializing numerical weather prediction models with satellite-derived surface soil moisture: Data assimilation experiments with ECMWF's integrated forecast system and the TMI soil moisture data set. Journal of Geophysical Research-Space Physics 112, D03102.

Drusch, M., E. F. Wood and T. J. Jackson (2001), Vegetative and atmospheric corrections for the soil moisture retrieval from passive microwave remote sensing data: Results from the southern great plains hydrology experiment 1997. Journal of Hydrometeorology 2, 181–192.

Drusch, M., E. F. Wood, H. Gao and A. Thiele (2004), Soil moisture retrieval during the Southern Great Plains Hydrology Experiment 1999: A comparison between experimental remote sensing data and operational products. Water Resources Research 40, W02504.

EEA (2010), Mapping the impact of natural hazards and technological accidents in Europe. An overview of the last decade. Tech. Rep. 13/2010, EEA, Copenhagen.

Engman, E. T. and N. Chauhan (1995), Status of microwave soil moisture measurements with remote sensing. Remote Sensing of Environment 51, 189 – 198.

Entekhabi, D., E. Njoku, P. O'Neill, K. Kellogg, W. Crow, W. Edelstein, J. Entin, S. Goodman, T. Jackson, J. Johnson, J. Kimball, J. Piepmeier, R. Koster, N. Martin, K. McDonald, M. Moghaddam, S. Moran, R. Reichle, J. Shi, M. Spencer, S. Thurman, L. Tsang and J. Van Zyl (2010), The Soil Moisture Active Passive (SMAP) mission. Proceedings of the IEEE 98, 704 –716.

European Union (2007a), Addressing the challenge of water scarcity and droughts in the European Union. Communication from the Commission to the European Parliament and the Council, European Commission, DG Environment, Brussels.

European Union (2007b), Directive 2007/60/EC of the European Parlement and of the Council - on the assessment and management of flood risks.

European Union (2009), Adapting to climate change: Towards a European framework for action. White Paper.

Evensen, G. (1994), Sequential data assimilation with a nonlinear quasi-geostrophic model using Monte Carlo methods to forecast error statistics. Journal of Geophysical Research: Oceans 99, 10143–10162.

Evensen, G. (2003), The Ensemble Kalman Filter: theoretical formulation and practical implementation. Ocean Dynamics 53, 343–367.

Evensen, G. (2009), The Ensemble Kalman Filter for combined state and parameter estimation. IEEE Transactions on Control Systems and Technology 29, 83 –104.

Feddes, R. A., P. Kabat, P. J. T. Van Bakel, J. J. B. Bronswijk and J. Halbertsma (1988), Modelling soil water dynamics in the unsaturated zone state of the art. Journal of Hydrology 100, 69 – 111.

Fekete, B. M., C. J. Vrsmarty, J. O. Roads and C. J. Willmott (2004), Uncertainties in precipitation and their impacts on runoff estimates. Journal of Climate 17, 294–304.

Feyen, L. and R. Dankers (2009), Impact of global warming on streamflow drought in Europe. Journal of Geophysical Research-Space Physics 114, D17116.

Fichefet, T. and M. A. M. Maqueda (1997), Sensitivity of a global sea ice model to the treatment of ice thermodynamics and dynamics. Journal of Geophysical Research-Space Physics 102, 12609–12646.

Fiedler, K. and P. Döll (2007), Global modelling of continental water storage changes sensitivity to different climate data sets. Adv. Geosci. 11, 63–68.

Finke, P. A., J. H. M. Wösten and M. J. W. Jansen (1996), Effects of uncertainty in major input variables on simulated functional soil behaviour. Hydrological Processes 10, 661–669.

Fischlin, A., G. Midgley, J. Price, R. Leemans, B. Gopal, C. Turley, M. Rounsevell, O. Dube, J. Tarazona and A. Velichko (2007), Climate Change 2007: Impacts, Adaptation and Vulnerability. Contribution of Working Group II to the Fourth Assessment Report of the Intergovernmental Panel on Climate Change, chap. Ecosystems, their properties, goods, and services. Cambridge: Cambridge University Press, 211–272.

Fleig, A., L. Tallaksen, H. Hisdal and S. Demuth (2006), A global evaluation of streamflow drought characteristics. Hydrology and Earth System Sciences 10, 535 – 552.

Forzieri, G., L. Feyen, R. Rojas, M. Flörke, F. Wimmer and A. Bianchi (2014), Ensemble projections of future streamflow droughts in europe. Hydrology and Earth System Sciences 18, 85–108.

Gao, H., E. F. Wood, M. Drusch, W. Crow and T. J. Jackson (2004), Using a microwave emission model to estimate soil moisture from ESTAR observations during SGP99. Journal of Hydrometeorology 5, 49–63.

Gebremichael, M. and F. Hossain (2010), Satellite rainfall applications for surface hydrology. Springer.

Geiger, R. (1954). In: Landolt-Börnstein Zahlenwerte und Funktionen aus Physik, Chemie, Astronomie, Geophysik un Technik, vol. 3 of *alte Serie*, chap. Klassifikation der Klimate nach W. Köppen, Springer, Berlin, 603 – 607.

Geiger, R. (1961), Überarbeitete Neuausgabe von Geiger, R.: Köppen-Geiger / Klima der Erde. Wandkarte 1:16 Mill. Klett-Perthes, Gotha.

Gleick, P. H. (2000), A look at twenty-first century water resources development. Water International 25, 127–138.

Gleick, P. H. (2010), Roadmap for sustainable water resources in southwestern North America. Proceedings of the National Academy of Sciences 107, 21300–21305.

Goosse, H. and T. Fichefet (1999), Importance of ice-ocean interactions for the global ocean circulation: A model study. Journal of Geophysical Research-Space Physics 104, 23337–23355.

Groisman, P. Y. and D. R. Legates (1994), The accuracy of United States precipitation data. Bulletin of the American Meteorological Society 75, 215–227.

Groisman, P. Y., V. V. Koknaeva, T. A. Belokrylova and T. R. Karl (1991), Overcoming biases of precipitation measurement: A history of the USSR experience. Bulletin of the American Meteorological Society 72, 1725–1733.

Gudmundsson, L., L. M. Tallaksen, K. Stahl, D. B. Clark, E. Dumont, S. Hagemann, N. Bertrand, D. Gerten, J. Heinke, N. Hanasaki, F. Voss and S. Koirala (2012), Comparing large-scale hydrological model simulations to observed runoff percentiles in europe. Journal of Hydrometeorology 13, 604–620.

Haddeland, I., D. B. Clark, W. Franssen, F. Ludwig, F. Vo, N. W. Arnell, N. Bertrand, M. Best, S. Folwell, D. Gerten, S. Gomes, S. N. Gosling, S. Hagemann, N. Hanasaki, R. Harding, J. Heinke, P. Kabat, S. Koirala, T. Oki, J. Polcher, T. Stacke, P. Viterbo, G. P. Weedon and P. Yeh (2011), Multimodel estimate of the global terrestrial water balance: Setup and first results. Journal of Hydrometeorology 12, 869–884.

Haerter, J. O., S. Hagemann, C. Moseley and C. Piani (2011), Climate model bias correction and the role of timescales. Hydrology and Earth System Sciences 15, 1065–1079.

Hagemann, S. and L. D. Gates (2003), Improving a sub-grid runoff parameterization scheme for climate models by the use of high resolution data derived from satellite observations. Climate Dynamics 21, 349–359.

Hagemann, S., C. Chen, J. O. Haerter, J. Heinke, D. Gerten and C. Piani (2011), Impact of a statistical bias correction on the projected hydrological changes obtained from three GCMs and two hydrology models. Journal of Hydrometeorology 12, 556–578.

Hamon, W. R. (1963), Computation of direct runoff amounts from storm rainfall. IAHS Publucation 63, 52–62.

Hannah, D. M., S. Demuth, H. A. J. van Lanen, U. Looser, C. Prudhomme, G. Rees, K. Stahl and L. M. Tallaksen (2011), Large-scale river flow archives: importance, current status and future needs. Hydrological Processes 25, 1191–1200.

Harding, R., M. Best, E. Blyth, S. Hagemann, P. Kabat, L. M. Tallaksen, T. Warnaars, D. Wiberg, G. P. Weedon, H. v. Lanen, F. Ludwig and I. Haddeland (2011), WATCH: Current knowledge of the terrestrial global water cycle. Journal of Hydrometeorology 12, 1149–1156.

Harris, I., P. Jones, T. Osborn and D. Lister (2014), Updated high-resolution grids of monthly climatic observations - the CRU TS3.10 Dataset. International Journal of Climatology 34, 623–642.

Harter, T. and J. Hopmans (2004), Unsaturated-Zone Modeling: Progress, Challenges, and Applications, chap. Role of vadose-zone flow processes in regional-scale hydrology: review, opportunities and challenges. Wageningen University, Wageningen, The Netherlands, 179–208.

Hempel, S., K. Frieler, L. Warszawski, J. Schewe and F. Piontek (2013), A trend-preserving bias correction - the ISI-MIP approach. Earth System Dynamics 4, 219–236.

Henderson-Sellers, A. (1996), Soil moisture: A critical focus for global change studies. Global and Planetary Change 13, 3–9.

Hendricks Franssen, H. J., H. P. Kaiser, U. Kuhlmann, G. Bauser, F. Stauffer, R. Müller and W. Kinzelbach (2011), Operational real-time modeling with Ensemble Kalman Filter of variably saturated subsurface flow including stream-aquifer interaction and parameter updating. Water Resources Research 47, W02532.

Hengl, T. and N. Toomanian (2006), Maps are not what they seem: representing uncertainty in soil property maps. In: M. Caetano and M. Painho, eds., 7th International Symposium on Spatial Accuracy Assessment in Natural Resources and Environmental Sciences.

Hersbach, H. (2000), Decomposition of the continuous ranked probability score for ensemble prediction systems. Weather and Forecasting 15, 559–570.

Hijmans, R. J., S. E. Cameron, J. L. Parra, P. G. Jones and A. Jarvis (2005), Very high resolution interpolated climate surfaces for global land areas. International Journal of Climatology 25, 1965–1978.

Hirabayashi, Y., S. Kanae, S. Emori, T. Oki and M. Kimoto (2008), Global projections of changing risks of floods and droughts in a changing climate. Hydrological Sciences Journal 53, 754–772.

Hirabayashi, Y., R. Mahendran, S. Koirala, L. Konoshima, D. Yamazaki, S. Watanabe, H. Kim and S. Kanae (2013), Global flood risk under climate change. Nature Climate Change 3, 816–821.

Hisdal, H., L. Tallaksen, E. Peters, K. Stahl and M. Zaidman (2001), Drought event definition, Technical Report No. 6. Tech. Rep., Final report to the Europian Union - ARIDE project.

Hisdal, H., L. M. Tallaksen, B. Clausen, E. Peters and A. Gustard (2004), Hydrological drought characteristics. In: L. M. Tallaksen and H. A. J. Van Lanen, eds., Hydrological Drought: Processes and estimation methods for streamflow and groundwater, no. 48 in Development in Water Science, Elsevier, 139 – 198.

Holmes, T. R. H., R. A. M. De Jeu, M. Owe and A. J. Dolman (2009), Land surface temperature from Ka band (37 GHz) passive microwave observations. Journal of Geophysical Research: Atmospheres 114, D04113.

Hong, Y., R. F. Adler, F. Hossain, S. Curtis and G. J. Huffman (2007), A first approach to global runoff simulation using satellite rainfall estimation. Water Resources Research 43, W08502.

Hossain, F. and G. J. Huffman (2008), Investigating error metrics for satellite rainfall data at hydrologically relevant scales. Journal of Hydrometeorology 9, 563–575.

Hourdin, F., I. Musat, S. Bony, P. Braconnot, F. Codron, J.-L. Dufresne, L. Fairhead, M.-A. Filiberti, P. Friedlingstein, J.-Y. Grandpeix, G. Krinner, P. LeVan, Z.-X. Li and F. Lott (2006), The LMDZ4 general circulation model: climate performance and sensitivity to parametrized physics with emphasis on tropical convection. Climate Dynamics 27, 787–813.

Howitt, R., J. Medelln-Azuara, D. MacEwan, J. Lund and D. Sumner (2014), Economic analysis of the 2014 drought for california agriculture. Report of UC Davis, Center for Watershed Sciences.

Huffman, G., R. Adler, D. Bolvin and E. Nelkin (2010), The TRMM Multi-satellite Precipitation Analysis (TMPA), chap. Chapter 1 in Satellite Rainfall Applications for Surface Hydrology. Springer, 3–22.

Huffman, G. J., D. T. Bolvin, E. J. Nelkin, D. B. Wolff, R. F. Adler, G. Gu, Y. Hong, K. P. Bowman and E. F. Stocker (2007), The TRMM Multisatellite Precipitation Analysis (TMPA): Quasi-global, multiyear, combined-sensor precipitation estimates at fine scales. Journal of Hydrometeorology 8, 38–55.

Immerzeel, W., P. Droogers, S. de Jong and M. Bierkens (2009), Large-scale monitoring of snow cover and runoff simulation in Himalayan river basins using remote sensing. Remote Sensing of Environment 113, 40–49.

Joyce, R., J. Janowiak and G. Huffman (2001), Latitudinally and seasonally dependent zenith-angle corrections for geostationary satellite IR brightness temperatures. Journal of Applied Meteorology and Climatology 40, 689–703.

Joyce, R. J., J. E. Janowiak, P. A. Arkin and P. Xie (2004), CMORPH: A method that produces global precipitation estimates from passive microwave and infrared data at high spatial and temporal resolution. Journal of Hydrometeorology 5, 487–503.

Jungclaus, J. H., N. Keenlyside, M. Botzet, H. Haak, J.-J. Luo, M. Latif, J. Marotzke, U. Mikolajewicz and E. Roeckner (2006), Ocean circulation and tropical variability in the coupled model ECHAM5/MPI-OM. Journal of Climate 19, 3952–3972.

Karssenberg, D., O. Schmitz, P. Salamon, K. de Jong and M. F. P. Bierkens (2010), A software framework for construction of process-based stochastic spatio-temporal models and data assimilation. Environmental Modelling & Software 25, 489 – 502.

Kavetski, D. and F. Fenicia (2011), Elements of a flexible approach for conceptual hydrological modeling: 2. application and experimental insights. Water Resources Research 47, W11511.

Kerr, Y., P. Waldteufel, J.-P. Wigneron, J. Martinuzzi, J. Font and M. Berger (2001), Soil moisture retrieval from space: the Soil Moisture and Ocean Salinity (SMOS) mission. IEEE Transactions on Geoscience and Remote Sensing 39, 1729 –1735.

Kerr, Y., P. Waldteufel, J. Wigneron, S. Delwart, F. Cabot, J. Boutin, M. Escorihuela, J. Font, N. Reul, C. Gruhier, S. Juglea, M. Drinkwater, A. Hahne, M. Martín-Neira and S. Mecklenburg (2010), The SMOS mission: New tool for monitoring key elements of the global water cycle. Proceedings of the IEEE 98, 666 –687.

Kerr, Y., P. Waldteufel, P. Richaume, J.-P. Wigneron, P. Ferrazzoli, A. Mahmoodi, A. Al Bitar, F. Cabot, C. Gruhier, S. Juglea, D. Leroux, A. Mialon and S. Delwart (2012), The SMOS soil moisture retrieval algorithm. SMOS special issue of IEEE TGRS 50, 1384 – 1403.

Keyantash, J. and J. Dracup (2002), The quantification of drought: An evaluation of drought indices. Bulletin of the American Meteorological Society 83, 1167 – 1180.

Kim, D., H. Byun and K. Choi (2009), Evaluation, modification and application of the effective drought index to 200-year drought climatology of Seoul, Korea. Journal of Hydrology 378, 1 – 12.

Kinter, J. L. and J. Shukla (1990), The global hydrologic and energy cycles: Suggestions for studies in the pre-Global Energy and Water Cycle Experiment (GEWEX) period. Bulletin of the American Meteorological Society 71, 181–189.

Komma, J., G. Blöschl and C. Reszler (2008), Soil moisture updating by Ensemble Kalman Filtering in real-time flood forecasting. Journal of Hydrology 357, 228 – 242.

Köppen, W. (1900), Versuch einer klassifikation der klimate, vorzugsweise nach ihren beziehungen zur pflanzenwelt. Geografische Zeitschrift 6, 593 – 611, 657 – 679.

Kraijenhof van de Leur, D. (1962), Some effects of the unsaturated zone on nonsteady free-surface groundwater flow as studied in a sealed granular model. Journal of Geophysical Research-Space Physics 67, 4347–4362.

Kroes, J. G., J. C. van Dam, P. Groenendijk, R. F. A. Hendriks and C. M. J. Jacobs (2008), SWAP version 3.2 - Theory description and user manual. Alterra, Wageningen.

Kummerow, C., W. S. Olson and L. Giglio (1996), A simplified scheme for obtaining precipitation and vertical hydrometeor profiles from passive microwave sensors. Geoscience and Remote Sensing, IEEE Transactions on 34, 1213–1232.

Kummerow, C., Y. Hong, W. S. Olson, S. Yang, R. F. Adler, J. McCollum, R. Ferraro, G. Petty, D.-B. Shin and T. T. Wilheit (2001), The evolution of the Goddard Profiling algorithm (GPROF) for rainfall estimation from passive microwave sensors. Journal of Applied Meteorology 40, 1801–1820.

Kundzewicz, Z. W. and Z. Kaczmarek (2000), Coping with hydrological extremes. Water International 25, 66–75.

Laio, F. and S. Tamea (2007), Verification tools for probabilistic forecasts of continuous hydrological variables. Hydrology and Earth System Sciences 11, 1267–1277.

Laurent, H., N. D'Amato and T. Lebel (1998), How important is the contribution of the mesoscale convective complexes to the sahelian rainfall? Physics and Chemistry of the Earth 23, 629 – 633.

Le Dimet, F.-X. and O. Talagrand (1986), Variational algorithms for analysis and assimilation of meteorological observations: theoretical aspects. Tellus Series A-dynamic Meteorology and Oceanography 38A, 97–110.

Lee, H., D.-J. Seo and V. Koren (2011), Assimilation of streamflow and in situ soil moisture data into operational distributed hydrologic models: Effects of uncertainties in the data and initial model soil moisture states. Advances in Water Resources 34, 1597–1615.

Lee, H., D.-J. Seo, Y. Liu, V. Koren, P. McKee and R. Corby (2012), Variational assimilation of streamflow into operational distributed hydrologic models: effect of spatiotemporal adjustment scale. Hydrology and Earth System Sciences 16, 2233–2251.

Lehner, B., P. Döll, J. Alcamo, T. Henrichs and F. Kaspar (2006), Estimating the impact of global change on flood and drought risks in Europe: A continental, integrated analysis. Climatic Change 75, 273–299.

Lehner, B., C. R. Liermann, C. Revenga, C. Vörösmarty, B. Fekete, P. Crouzet, P. Döll, M. Endejan, K. Frenken, J. Magome, C. Nilsson, J. C. Robertson, R. Rödel, N. Sindorf and D. Wisser (2011), High-resolution mapping of the world's reservoirs and dams for sustainable river-flow management. Frontiers in Ecology and the Environment 9, 494–502.

Liang, X., D. P. Lettenmaier, E. F. Wood and S. J. Burges (1994), A simple hydrologically based model of land surface water and energy fluxes for general circulation models. Journal of Geophysical Research: Atmospheres 99, 14415–14428.

Liang, X., E. F. Wood and D. P. Lettenmaier (1996), Surface soil moisture parameterization of the VIC-2L model: Evaluation and modification. Global and Planetary Change 13, 195 – 206. Soil Moisture Simulation.

Liu, Q., R. H. Reichle, R. Bindlish, M. H. Cosh, W. T. Crow, R. A. M. De Jeu, G. J. M. De Lannoy, G. J. Huffman and T. J. Jackson (2011a), The contributions of precipitation and soil moisture observations to the skill of soil moisture estimates in a land data assimilation system. Journal of Hydrometeorology 12, 750–765.

Liu, Y. and H. V. Gupta (2007), Uncertainty in hydrologic modeling: Toward an integrated data assimilation framework. Water Resources Research 43, W07401.

Liu, Y., A. H. Weerts, M. Clark, H.-J. Hendricks Franssen, S. Kumar, H. Moradkhani, D.-J. Seo, D. Schwanenberg, P. Smith, A. I. J. M. van Dijk, N. van Velzen, M. He, H. Lee, S. J. Noh, O. Rakovec and P. Restrepo (2012), Advancing data assimilation in operational hydrologic forecasting: progresses, challenges, and emerging opportunities. Hydrology and Earth System Sciences 16, 3863–3887.

Liu, Y. Y., R. M. Parinussa, W. A. Dorigo, R. A. M. De Jeu, W. Wagner, A. I. J. M. Van Dijk, M. F. McCabe and J. P. Evans (2011b), Developing an improved soil moisture dataset by blending passive and active microwave satellite-based retrievals. Hydrology and Earth System Sciences 15, 425–436.

Loew, A., T. R. H. Holmes and R. A. M. De Jeu (2009), The European heat wave 2003: Early indicators from multisensoral microwave remote sensing? Journal of Geophysical Research-Space Physics 114, D05103.

Lorenz, C. and H. Kunstmann (2012), The hydrological cycle in three state-of-the-art reanalyses: Intercomparison and performance analysis. Journal of Hydrometeorology 13, 1397–1420.

Lü, H., Z. Yu, Y. Zhu, S. Drake, Z. Hao and E. A. Sudicky (2011), Dual state-parameter estimation of root zone soil moisture by optimal parameter estimation and extended kalman filter data assimilation. Advances in Water Resources 34, 395 – 406.

Madec, G., P. Delecluse, M. Imbard and L. C. (1998), OPA version 8.1 Ocean General Circulation Model reference manual. University Paris VI, Paris, notes du pole de model. 11 edn.

Marsh, T. and S. Parry (2012), An overview of the 2010-12 drought and its dramatic termination. Report NERC/Centre for Ecology & Hydrology, Wallingford, UK.

Martínez-Fernández, J. and A. Ceballos (2003), Temporal stability of soil moisture in a large-field experiment in Spain. Soil Science Society of America Journal 67, 1647–1656.

Matgen, P., F. Fenicia, S. Heitz, D. Plaza, R. de Keyser, V. R. Pauwels, W. Wagner and H. Savenije (2012), Can ASCAT-derived soil wetness indices reduce predictive uncertainty in well-gauged areas? A comparison with in situ observed soil moisture in an assimilation application. Advances in Water Resources 44, 49 – 65.

McCollum, J. R. and W. F. Krajewski (1998), Investigations of error sources of the global precipitation climatology project emission algorithm. Journal of Geophysical Research: Atmospheres 103, 28711–28719.

McKee, T., N. Doesken and J. Kleist (1993), The relationship of drought frequency and duration to time scales. In: Eighth Conference on Applied Climatology, 17-22 January, Anaheim, California.

McMahon, T. A., M. C. Peel, L. Lowe, R. Srikanthan and T. R. McVicar (2013), Estimating actual, potential, reference crop and pan evaporation using standard meteorological data: a pragmatic synthesis. Hydrology and Earth System Sciences 17, 1331–1363.

McMillan, H. K., E. O. Hreinsson, M. P. Clark, S. K. Singh, C. Zammit and M. J. Uddstrom (2013), Operational hydrological data assimilation with the recursive Ensemble Kalman filter. Hydrology and Earth System Sciences 17, 21–38.

Meesters, A. G. C. A., D. J. R.A.M. and M. Owe (2005), Analytical derivation of the vegetation optical depth from the microwave polarization difference index. IEEE Geoscience and Remote Sensing Letters 2, 121–123.

Mendicino, G., A. Senatore and P. Versace (2008), A groundwater resource index for drought monitoring and forecasting in a mediterranean climate. Journal of Hydrology 357, 282 – 302.

Mendoza, P. A., J. McPhee and X. Vargas (2012), Uncertainty in flood forecasting: A distributed modeling approach in a sparse data catchment. Water Resources Research 48, W09532.

Merz, B. and E. Plate (1997), An analysis of the effects of spatial variability of soil and soil moisture on runoff. Water Resources Research 33, 2909–2922.

Meyer, P. D., M. L. Rockhold and G. W. Gee (1997), Uncertainty Analyses of Infiltration and Subsurface Flow and Transport for SDMP Sites. Tech. Rep. NUREG/CR-6565 PNNL-11705, U.S. Nuclear Regulatory Commission Office of Nuclear Regulatory Research, Washington.

Milly, P. C. D., K. A. Dunne and A. V. Vecchia (2005), Global pattern of trends in streamflow and water availability in a changing climate. Nature 438, 347–350.

Miralles, D. G., W. T. Crow and M. H. Cosh (2010), Estimating spatial sampling errors in coarse-scale soil moisture estimates derived from point-scale observations. Journal of Hydrometeorology 11, 1423–1429.

Miralles, D. G., T. R. H. Holmes, R. A. M. De Jeu, J. H. Gash, A. G. C. A. Meesters and A. J. Dolman (2011), Global land-surface evaporation estimated from satellite-based observations. Hydrology and Earth System Sciences 15, 453–469.

Mishra, A. K. and V. P. Singh (2010), A review of drought concepts. Journal of Hydrology 391, 202 – 216.

Mitchell, T. and P. Jones (2005), An improved method of constructing a database of monthly climate observations and associated high-resolution grids. International Journal of Climatology 25, 693 – 712.

Montzka, C., H. Moradkhani, L. Weihermüller, H.-J. H. Franssen, M. Canty and H. Vereecken (2011), Hydraulic parameter estimation by remotely-sensed top soil moisture observations with the particle filter. Journal of Hydrology 399, 410 – 421.

Moradkhani, H., S. Sorooshian, H. V. Gupta and P. R. Houser (2005), Dual state-parameter estimation of hydrological models using Ensemble Kalman Filter. Advances in Water Resources 28, 135 – 147.

Myneni, R., Y. Knyazikhin, J. Glassy, P. Votava and N. Shabanov (2003), User's Guide FPAR, LAI (ESDT: MOD15A2) 8-day Composite NASA MODIS Land Algorithm. NASA - Terra MODIS Land Team.

Naeimi, V., K. Scipal, Z. Bartalis, S. Hasenauer and W. Wagner (2009), An improved soil moisture retrieval algorithm for ERS and METOP scatterometer observations. IEEE Transactions on Geoscience and Remote Sensing 47, 1999–2013.

Nakićenović, N. and R. Swart (2000), Special Report on Emissions Scenarios: A special report of Working Group III of the Intergovernmental Panel on Climate Change. Cambridge University Press.

Naresh Kumar, M., C. Murthy, M. Sesha Sai and P. Roy (2009), On the use of Standardized Precipitation Index (SPI) for drought intensity assessment. Meteorological Applications 16, 381 – 389.

Nash, J. and J. Sutcliffe (1970), River flow forecasting through conceptual models part I: A discussion of principles. Journal of Hydrology 10, 282 – 290.

National Oceanic and Atmospheric Administration (2012). Www.ncdc.noaa.gov/sotc/drought/2012, viewed on 14-11-2014.

Nester, T., J. Komma, A. Viglione and G. Blöschl (2012), Flood forecast errors and ensemble spread - a case study. Water Resources Research 48, W10502.

Njoku, E., T. J. Jackson, V. Lakshmi, T. Chan and S. Nghiem (2003), Soil moisture retrieval from AMSR-E. IEEE Transactions on Geoscience and Remote Sensing 41, 215 – 229.

Njoku, E. G. and J. A. Kong (1977), Theory for passive microwave remote sensing of near-surface soil moisture. Journal of Geophysical Research-Space Physics 82, 3108–3118.

Njoku, E. G. and L. Li (1999), Retrieval of land surface parameters using passive microwave measurements at 6-18 GHz. IEEE Transactions on Geoscience and Remote Sensing 37, 79 –93.

Ntegeka, V., P. Salamon, G. Gomes, H. Sint, V. Lorini, J. Thielen and H. Zambrano (2013), EFAS-Meteo: A European daily high-resolution gridded meteorological data set for 1990 2011. Tech. Rep., Publications Office of the European Union, Luxembourg.

Oki, T. and S. Kanae (2006), Global hydrological cycles and world water resources. Science 313, 1068–1072.

Oki, T., Y. Agata, S. Kanae, T. Saruhashi, D. Yang and K. Musiake (2001), Global assessment of current water resources using total runoff integrating pathways. Hydrological Sciences 46, 983–995.

Olson, W. S., C. D. Kummerow, Y. Hong and W.-K. Tao (1999), Atmospheric latent heating distributions in the tropics derived from satellite passive microwave radiometer measurements. Journal of Applied Meteorology and Climatology 38, 633–664.

Orlowsky, B. and S. I. Seneviratne (2013), Elusive drought: uncertainty in observed trends and short- and long-term CMIP5 projections. Hydrology and Earth System Sciences 17, 1765–1781.

Owe, M., R. A. M. De Jeu and T. R. H. Holmes (2008), Multisensor historical climatology of satellite-derived global land surface moisture. Journal of Geophysical Research-Space Physics 113, F01002.

Palmer, W. (1965), Meteorological drought. U.S. Weather Bureau Research Paper No. 45, 58 pp.

Pan, M., H. Li and E. Wood (2010), Assessing the skill of satellite-based precipitation estimates in hydrologic applications. Water Resources Research 46, W09535.

Pan, M., A. K. Sahoo, T. J. Troy, R. K. Vinukollu, J. Sheffield and E. F. Wood (2011), Multisource estimation of long-term terrestrial water budget for major global river basins. J. Climate 25, 3191–3206.

Pan, M., A. K. Sahoo and E. F. Wood (2014), Improving soil moisture retrievals from a physically-based radiative transfer model. Remote Sensing of Environment 140, 130 – 140.

Parinussa, R. M., A. G. C. A. Meesters, Y. Y. Liu, W. A. Dorigo, W. Wagner and R. A. M. de Jeu (2011), Error estimates for near-real-time satellite soil moisture as derived from the land parameter retrieval model. IEEE Geoscience and Remote Sensing Letters 8, 779 –783.

Parrens, M., E. Zakharova, S. Lafont, J. C. Calvet, Y. Kerr, W. Wagner and J. P. Wigneron (2012), Comparing soil moisture retrievals from SMOS and ASCAT over France. Hydrology and Earth System Sciences 16, 423–440.

Parry, S., C. Prudhomme, J. Hannaford and B. Lloyd-Hughes (2010), Examining the spatio-temporal evolution and characteristics of large-scale European droughts. In: C. Kirby, ed., Role of Hydrology in Managing Consequences of a Changing Global Environment. Proceedings of the BHS Third International Symposium, British Hydrological Society, 135–142.

Pauwels, V. R., R. Hoeben, N. E. Verhoest and F. P. D. Troch (2001), The importance of the spatial patterns of remotely sensed soil moisture in the improvement of discharge predictions for small-scale basins through data assimilation. Journal of Hydrology 251, 88 – 102.

Pauwels, V. R. N. and G. J. M. De Lannoy (2009), Ensemble-based assimilation of discharge into rainfall-runoff models: A comparison of approaches to mapping observational information to state space. Water Resources Research 45, W08428.

Pederson, N., A. R. Bell, T. A. Knight, C. Leland, N. Malcomb, K. J. Anchukaitis, K. Tackett, J. Scheff, A. Brice, B. Catron, W. Blozan and J. Riddle (2012), A long-term perspective on a modern drought in the American Southeast. Environmental Research Letters 7, 014034.

Pellarin, T., A. Ali, F. Chopin, I. Jobard and J.-C. Bergs (2008), Using spaceborne surface soil moisture to constrain satellite precipitation estimates over West Africa. Geophysical Research Letters 35, L02813.

Pellarin, T., S. Louvet, C. Gruhier, G. Quantin and C. Legout (2013), A simple and effective method for correcting soil moisture and precipitation estimates using AMSR-E measurements. Remote Sensing of Environment 136, 28 – 36.

Penna, D., H. J. Tromp-van Meerveld, A. Gobbi, M. Borga and G. Dalla Fontana (2011), The influence of soil moisture on threshold runoff generation processes in an alpine headwater catchment. Hydrology and Earth System Sciences 15, 689–702.

Peters, E., P. J. J. F. Torfs, H. A. J. van Lanen and G. Bier (2003), Propagation of drought through groundwater - a new approach using linear reservoir theory. Hydrological Processes 17, 3023 – 3040.

Peters, E., G. Bier, H. A. J. van Lanen and P. J. J. F. Torfs (2006), Propagation and spatial distribution of drought in a groundwater catchment. Journal of Hydrology 321, 257 – 275.

Piani, C., J. Haerter and E. Coppola (2010a), Statistical bias correction for daily precipitation in regional climate models over europe. theoretical and Applied Climatology 99, 187–192.

Piani, C., G. Weedon, M. Best, S. Gomes, P. Viterbo, S. Hagemann and J. Haerter (2010b), Statistical bias correction of global simulated daily precipitation and temperature for the application of hydrological models. Journal of Hydrology 395, 199 – 215.

Portmann, F., S. Siebert and P. Döll (2010), Mirca2000 - global monthly irrigated and rainfed crop areas around the year 2000: A new high-resolution data set for agricultural and hydrological modeling. Global Biogeochemical Cycles 24, GB1011.

Prudhomme, C., S. Parry, J. Hannaford, D. B. Clark, S. Hagemann and F. Voss (2011), How well do large-scale models reproduce regional hydrological extremes in europe? Journal of Hydrometeorology 12, 1181–1204.

Prudhomme, C., I. Giuntoli, E. L. Robinson, D. B. Clark, N. W. Arnell, R. Dankers, B. M. Fekete, W. Franssen, D. Gerten, S. N. Gosling, S. Hagemann, D. M. Hannah, H. Kim, Y. Masaki, Y. Satoh, T. Stacke, Y. Wada and D. Wisser (2014), Hydrological droughts in the 21^{st} century, hotspots and uncertainties from a global multimodel ensemble experiment. Proceedings of the National Academy of Sciences 111, 3262 3267.

Rakovec, O., A. H. Weerts, P. Hazenberg, P. J. J. F. Torfs and R. Uijlenhoet (2012), State updating of a distributed hydrological model with Ensemble Kalman Filtering: effects of updating frequency and observation network density on forecast accuracy. Hydrology and Earth System Sciences 16, 3435–3449.

Redmond, K. (2000), Monitoring drought using the Standardized Precipitation Index. In: D. Wilhite, ed., Drought: A global assessment (vol. 1), Routledge, 145 – 158.

Reichle, R. H. (2008), Data assimilation methods in the earth sciences. Advances in Water Resources 31, 1411 – 1418. Hydrologic Remote Sensing.

Reichle, R. H. and R. D. Koster (2004), Bias reduction in short records of satellite soil moisture. Geophysical Research Letters 31, L19501.

Reichle, R. H., D. B. McLaughlin and D. Entekhabi (2002), Hydrologic data assimilation with the Ensemble Kalman Filter. Monthly Weather Review 130, 103–114.

Richards, L. (1931), Capillary conduction of liquids through porous mediums. Zoom Lenses Iii 1, 318.

Ritzema, H. (1994), Subsurface flow to drains. In: H. Ritzema, ed., Drainage Principles and Applications, International Institute for Land Reclamation and Improvement, second edn., 263 – 303.

Rodell, M., H. K. Beaudoing, T. S. L'Ecuyer, W. S. Olson, J. S. Famiglietti, P. R. Houser, B. M. G. Adler, R., C. A. Clayson, D. Chambers, E. J. Clark, E. Fetzer, X. Gao, G. Gu, G. J. Hilburn, K. Huffman, D. P. Lettenmaier, F. R. Liu, W. T. Robertson, C. A. Schlosser, J. Sheffield and E. F. Wood (2014), The observed state of the water cycle in the early 21^{st} century. Journal of Climate under review.

Roeckner, E., G. Bäuml, L. Bonaventura, R. Brokopf, M. Esch, M. Giorgetta, S. Hagemann, I. Kirchner, L. Kornblueh, E. Manzini, A. Rhodin, U. Schlese, U. Schulzweida and A. Tompkins (2003), The atmospheric general circulation model ECHAM5 Part I. Tech. Rep. 349, Max-Planck-Institut für Meteorologie.

Romm, J. (2011), Desertification: The next dust bowl. Nature 478, 450–451.

Royer, J.-F., D. Cariolle, F. Chauvin, M. Dqu, H. Douville, R.-M. Hu, S. Planton, A. Rascol, J.-L. Ricard, D. S. Y. Melia, F. Sevault, P. Simon, S. Somot, S. Tyteca, L. Terray and S. Valcke (2002), Simulation des changements climatiques au cours du XXIe siècle incluant l'ozone stratosphérique. Comptes Rendus Geoscience 334, 147 – 154.

Rüdiger, C., J. C. Calvet, C. Gruhier, T. R. H. Holmes, R. A. M. De Jeu and W. Wagner (2009), An intercomparison of ERS-Scat and AMSR-E soil moisture observations with model simulations over France. Journal of Hydrometeorology 10, 431–447.

Salas-Mélia, D. (2002), A global coupled sea ice-ocean model. Ocean Modelling 4, 137 – 172.

Sánchez, N., J. Martínez-Fernández, A. Calera, E. Torres and C. Pérez-Gutiérrez (2010), Combining remote sensing and in situ soil moisture data for the application and validation of a distributed water balance model (HIDROMORE). Agricultural Water Management 98, 69–78.

Santanello, J., C. D. Peters-Lidard, M. E. Garcia, D. M. Mocko, M. A. Tischler, M. S. Moran and D. Thoma (2007), Using remotely-sensed estimates of soil moisture to infer soil texture and hydraulic properties across a semi-arid watershed. Remote Sensing of Environment 110, 79 – 97.

Sapiano, M. R. P. and P. A. Arkin (2009), An intercomparison and validation of high-resolution satellite precipitation estimates with 3-hourly gauge data. Journal of Hydrometeorology 10, 149–166.

Schneider, U., T. Fuchs, A. Meyer-Christoffer and B. Rudolf (2008), Global precipitation analysis products of the GPCC. Global Precipitation Climatology Centre (GPCC). Retrieved from gpcc.dwd.de on 15-02-2012.

Schuurmans, J. M., M. F. P. Bierkens, E. J. Pebesma and R. Uijlenhoet (2007), Automatic prediction of high-resolution daily rainfall fields for multiple extents: The potential of operational radar. Journal of Hydrometeorology 8, 1204–1224.

Scipal, K., M. Drusch and W. Wagner (2008), Assimilation of a ERS scatterometer derived soil moisture index in the ECMWF numerical weather prediction system. Advances in Water Resources 31, 1101 – 1112.

Seager, R. (2007), The turn of the century North American drought: Global context, dynamics, and past analogs. Journal of Climate 20, 5527–5552.

Seibert, J. (2002), HBV light version 2 Users Manual. Stockholm University, Department of Physical Geography and Quaternary Geology.

Seneviratne, S. I., N. Nicholls, D. Easterling, C. M. Goodess, S. Kanae, J. Kossin, Y. Luo, J. Marengo, K. McInnes, M. Rahimi, M. Reichstein, A. Sorteberg, C. Vera and X. Zhang (2012), Changes in climate extremes and their impacts on the natural physical environment, chap. A Special Report of Working Groups I and II of the Intergovernmental Panel on Climate Change (IPCC). Cambridge, UK, and New York, NY, USA: Cambridge University Press, 109–230.

Sepulcre-Canto, G., S. Horion, A. Singleton, H. Carrao and J. Vogt (2012), Development of a combined drought indicator to detect agricultural drought in europe. Natural Hazards and Earth System Science 12, 3519–3531.

Sheffield, J. and E. Wood (2008), Projected changes in drought occurrence under future global warming from multi-model, multi-scenario, IPCC AR4 simulations. Climate Dynamics 31, 79–105.

Sheffield, J. and E. F. Wood (2011), Drought: Past Problems and Future Scenarios. Earthscan, London.

Sheffield, J. and F. Wood (2007), Characteristics of global and regional drought, 1950 - 2000: Analysis of soil moisture data from off-line simulation of the terrestrial hydrologic cycle. Journal of Geophysical Research-Space Physics 112, D17115.

Sheffield, J., K. Andreadis, E. Wood and D. Lettenmaier (2009), Global and continental drought in the second half of the twentieth century: Severity-area-duration analysis and temperol variability of large-scale events. Journal of Climate 22, 1962 – 1981.

Sheffield, J., E. F. Wood and M. L. Roderick (2012), Little change in global drought over the past 60 years. Nature 491, 435–438.

Sheffield, J., E. F. Wood, N. Chaney, K. Guan, S. Sadri, X. Yuan, L. Olang, A. Amani, A. Ali, S. Demuth and L. Ogallo (2014), A drought monitoring and forecasting system for sub-Sahara African water resources and food security. Bulletin of the American Meteorological Society 95, 861–882.

Shepard, D. (1968), A two-dimensional interpolation function for irregularly-spaced data. In: Proceedings of the 1968 23rd ACM National Conference, ACM '68, New York, NY, USA: ACM, 517–524.

Shukla, S. and A. W. Wood (2008), Use of a standardized runoff index for characterizing hydrologic drought. Geophysical Research Letters 35, L02405.

Sida, L., B. Gray and E. Asmare (2012), Real-time evaluation of the humanitarian response to the Horn of African drought crises. Tech. Rep., Inter-Agency Standing Committee.

Siebert, S., P. Döll, S. Feick, J. Hoogeveen and K. Frenken (2007), Global map of irrigation areas version 4.0.1. Map.

Singh, R., J. G. Kroes, J. C. van Dam and R. A. Feddes (2006), Distributed ecohydrological modelling to evaluate the performance of irrigation system in sirsa district, India: I. current water management and its productivity. Journal of Hydrology 329, 692–713.

Smakhtin, V. (2001), Low flow hydrology: a review. Journal of Hydrology 240, 147 – 186.

Smakhtin, V. and D. Hughes (2007), Automated estimation and analyses of meteorological drought characteristics from monthly rainfall data. Environmental Modelling & Software 22, 880 – 890.

Solomon, S., D. Qin, M. Manning, Z. Chen, M. Marquis, K. Averyt, M. Tignor and H. Miller (2007), Contribution of Working Group I to the Fourth Assessment Report of the Intergovernmental Panel on Climate Change, 2007. Tech. Rep., IPCC, Cambridge, United Kingdom and New York, NY, USA.

Sperna Weiland, F. C., L. P. H. van Beek, J. C. J. Kwadijk and M. F. P. Bierkens (2010), The ability of a GCM-forced hydrological model to reproduce global discharge variability. Hydrology and Earth System Sciences 14, 1595–1621.

Stahl, K., L. M. Tallaksen, L. Gudmundsson and J. H. Christensen (2011), Streamflow data from small basins: A challenging test to high-resolution regional climate modeling. Journal of Hydrometeorology 12, 900–912.

Stahl, K., L. M. Tallaksen, J. Hannaford and H. A. J. van Lanen (2012), Filling the white space on maps of European runoff trends: estimates from a multi-model ensemble. Hydrology and Earth System Sciences 16, 2035–2047.

Staudinger, M., K. Stahl and J. Seibert (2014), A drought index accounting for snow. Water Resources Research 50, 78617872.

Su, F., Y. Hong and D. P. Lettenmaier (2008), Evaluation of TRMM Multisatellite Precipitation Analysis (TMPA) and its utility in hydrologic prediction in the La Plata Basin. Journal of Hydrometeorology 9, 622–640.

Sutanudjaja, E. H., L. P. H. van Beek, S. M. de Jong, F. C. van Geer and M. F. P. Bierkens (2011), Large-scale groundwater modeling using global datasets: a test case for the Rhine-Meuse basin. Hydrology and Earth System Sciences 15, 2913–2935.

Sutanudjaja, E. H., S. M. De Jong, F. C. Van Geer and M. F. P. Bierkens (2013), Using ERS spaceborne microwave soil moisture observations to predict groundwater head in space and time. Remote Sensing of Environment 138, 172–188.

Sutanudjaja, E. H., L. P. H. van Beek, S. M. de Jong, F. C. van Geer and M. F. P. Bierkens (2014), Calibrating a large-extent high-resolution coupled groundwater-land surface model using soil moisture and discharge data. Water Resources Research 50, 687705.

Tallaksen, L. M. and H. A. J. Van Lanen (2004), Hydrological Drought: Processes and estimation methods for streamflow and groundwater. No. 48 in Development in water science, Elsevier.

Tallaksen, L. M., H. Madsen and B. Clausen (1997), On the definition and modelling of streamflow drought duration and deficit volume. Hydrological Sciences 42, 15 – 33.

Tallaksen, L. M., H. Hisdal and H. A. J. Van Lanen (2009), Space-time modelling of catchment scale drought characteristics. Journal of Hydrology 375, 363 – 372.

Thielen, J., J. Bartholmes, M. Ramos and A. de Roo (2009), The European Flood Alert System Part 1: Concept and development. Hydrology and Earth System Sciences 13, 125–140.

Tijdeman, E., A. F. Van Loon, N. Wanders and H. A. J. Van Lanen (2012), The effect of climate on droughts and their propagation in different parts of the hydrological cycle. Tech. Rep. 2, EU-Drought-R-SPI.

Tong, J.-X., B. Hu and J.-Z. g. Yang (2012), Using an Ensemble Kalman Filter method to calibrate parameters and update soluble chemical transfer from soil to surface runoff. Transport in Porous Media 91, 133–152.

Trenberth, K. E., G. W. Branstator and P. A. Arkin (1988), Origins of the 1988 North American drought. Science 242, 1640–1645.

Trenberth, K. E., L. Smith, T. Qian, A. Dai and J. Fasullo (2007), Estimates of the global water budget and its annual cycle using observational and model data. Journal of Hydrometeorology 8, 758–769.

Trenberth, K. E., J. T. Fasullo and J. Mackaro (2011), Atmospheric moisture transports from ocean to land and global energy flows in reanalyses. J. Climate 24, 4907–4924.

Trenberth, K. E., A. Dai, G. van der Schrier, P. D. Jones, J. Barichivich, K. R. Briffa and J. Sheffield (2014), Global warming and changes in drought. Nature Climate Change 4, 17–22.

Troch, P. A., F. Vandersteene, Z. Su, R. Hoeben and M. Wuethrich (1996), Estimating microwave observation depth in bare soil through multi-frequency scatterometry. In: Proceedings of the First EMSL User Workshop, SAI, JRC, Ispra, Italy.

Tustison, B., D. Harris and E. Foufoula-Georgiou (2001), Scale issues in verification of precipitation forecasts. Journal of Geophysical Research: Atmospheres 106, 11775–11784.

United Nations (2011), Humanitarian Requirements for the Horn of Africa Drought 2011. Tech. Rep., Office for the Coordination of Humanitarian Affairs (OCHA), New York and Geneva.

Uppala, S. M., P. W. Kallberg, A. J. Simmons, U. Andrae, V. D. C. Bechtold, M. Fiorino, J. K. Gibson, J. Haseler, A. Hernandez, G. A. Kelly, X. Li, K. Onogi, S. Saarinen, N. Sokka, R. P. Allan, E. Andersson, K. Arpe, M. A. Balmaseda, A. C. M. Beljaars, L. V. D. Berg, J. Bidlot, N. Bormann, S. Caires, F. Chevallier, A. Dethof, M. Dragosavac, M. Fisher, M. Fuentes, S. Hagemann, E. Hólm, B. J. Hoskins, L. Isaksen, P. A. E. M. Janssen, R. Jenne, A. P. McNally, J. F. Mahfouf, J. J. Morcrette, N. A. Rayner, R. W. Saunders, P. Simon, A. Sterl, K. E. Trenberth, A. Untch, D. Vasiljevic, P. Viterbo and J. Woollen (2005), The ERA-40 re-analysis. Quarterly Journal of the Royal Meteorological Society 131, 2961–3012.

Van Beek, L. P. H. (2008), Forcing PCR-GLOBWB with CRU data. Tech. Rep., Department of Physical Geography, Utrecht University, Utrecht, The Netherlands. URL `http://vanbeek.geo.uu.nl/suppinfo/vanbeek2008.pdf`.

Van Beek, L. P. H., Y. Wada and M. F. P. Bierkens (2011), Global monthly water stress: I. Water balance and water availability. Water Resources Research 47, W07517.

Van Dam, J. C. (2000), Field scale water flow and solute transport. SWAP model concepts, parameter estimation and case studies. Ph.D. thesis, Wageningen University.

Van Der Knijff, J. M., J. Younis and A. P. J. De Roo (2010), LISFLOOD: a GIS based distributed model for river basin scale water balance and flood simulation. International Journal of Geographical Information Science 24, 189–212.

Van Dijk, A. I. J. M., L. J. Renzullo, Y. Wada and P. Tregoning (2014), A global water cycle reanalysis (2003-2012) merging satellite gravimetry and altimetry observations with a hydrological multi-model ensemble. Hydrology and Earth System Sciences 18, 2955–2973.

Van Genuchten, M. T. (1980), A closed-form equation for predicting the hydraulic conductivity of unsaturated soils. Soil Science Society of America Journal 44, 892–898.

Van Huijgevoort, M. H. J., P. Hazenberg, H. A. J. Van Lanen and R. Uijlenhoet (2012), A generic method for hydrological drought identification across different climate regions. Hydrology and Earth System Sciences 16, 2437–2451.

Van Huijgevoort, M. H. J., P. Hazenberg, H. A. J. van Lanen, A. J. Teuling, D. B. Clark, S. Folwell, S. N. Gosling, N. Hanasaki, J. Heinke, S. Koirala, T. Stacke, F. Voss, J. Sheffield and R. Uijlenhoet (2013), Global multimodel analysis of drought in runoff for the second half of the twentieth century. Journal of Hydrometeorology 14, 1535–1552.

Van Huijgevoort, M. H. J., H. A. J. Van Lanen, A. J. Teuling and R. Uijlenhoet (2014), Identification of changes in hydrological drought characteristics from a multi-GCM driven ensemble constrained by observed discharge. Journal of Hydrology 512, 421434.

Van Lanen, H. A. J., F. M., E. Kupczyk, A. Kasprzyk and W. Pokojski (2004), Flow generating processes. In: L. M. Tallaksen and H. A. J. van Lanen, eds., Hydrological Drought: Processes and estimation methods for streamflow and groundwater, no. 48 in Development in Water Science, Elsevier, 53 – 98.

Van Lanen, H. A. J., N. Wanders, L. M. Tallaksen and A. F. Van Loon (2013), Hydrological drought across the world: impact of climate and physical catchment structure. Hydrology and Earth System Sciences 17, 1715–1732.

Van Leeuwen, P. J. (2009), Particle filtering in geophysical systems. Monthly Weather Review 137, 4089–4114.

Van Liedekerke, M., A. Jones and P. Panagos (2006), 1km Raster version of the European Soil Database (v. 2.0). Tech. Rep. EUR 19945 EN, European Soil Bureau Network & European Commission.

Van Loon, A. F. and H. A. J. Van Lanen (2012), A process-based typology of hydrological drought. Hydrology and Earth System Sciences 16, 1915–1946.

Van Loon, A. F., M. H. J. Van Huijgevoort and H. A. J. Van Lanen (2012), Evaluation of drought propagation in an ensemble mean of large-scale hydrological models. Hydrology and Earth System Sciences 16, 4057–4078.

Van Loon, A. F., E. Tijdeman, N. Wanders, H. A. J. Van Lanen, A. J. Teuling and R. Uijlenhoet (2014), How climate seasonality modifies drought duration and deficit. Journal of Geophysical Research: Atmospheres 119, 46404656.

Van Vliet, M. T. H., J. R. Yearsley, F. Ludwig, S. Vogele, D. P. Lettenmaier and P. Kabat (2012), Vulnerability of US and European electricity supply to climate change. Nature Climate Change 2, 676–681.

Van Vuuren, P., J. Edmonds, M. Kainuma, K. Riahi, A. Thomson, K. Hibbard, G. Hurtt, T. Kram, V. Krey, J.-F. Lamarque, T. Masui, M. Meinshausen, N. Nakicenovic, S. Smith and S. Rose (2011), The representative concentration pathways: an overview. Climatic Change 109, 5–31.

Verdin, K. L. and S. K. Greenlee (1996), Development of continental scale digital elevation models and extraction of hydrographic features. In: Paper presented at 3rd International Conference/Workshop on Integrating GIS and Environmental Modeling, Santa Barbara, California, United States: National Center for Geographic Information and Analysis.

Vidal, J.-P., E. Martin, N. Kitova, J. Najac and J.-M. Soubeyroux (2012), Evolution of spatio-temporal drought characteristics: validation, projections and effect of adaptation scenarios. Hydrology and Earth System Sciences 16, 2935–2955.

Villarini, G. and W. F. Krajewski (2007), Evaluation of the research version TMPA three-hourly $0.25° \times 0.25°$ rainfall estimates over Oklahoma. Geophysical Research Letters 34, L05402.

Vincente-Serrano, S., J. Gonzalez-Hidalgo, M. Luis and J. Raventos (2004), Drought pattern in the mediterranean area: the valencia region (eastern Spain). Climate Research 26, 5 – 15.

Von Hoyningen-Hüne, J. (1983), Die interception des niederschlags in landwirtschaftlichen pflanzenbeständen. Schriftenreihe DVWK 57, 17898.

Vörösmarty, C. J., B. M. Fekete, M. Meybeck and R. B. Lammers (2000a), A simulated topological network representing the global system of rivers at 30-minute spatial resolution (STN-30). Global Biogeochemical Cycles 14, 599–621.

Vörösmarty, C. J., P. Green, J. Salisbury and R. B. Lammers (2000b), Global water resources: Vulnerability from climate change and population growth. Science 289, 284–288.

Vrugt, J., H. Gupta, B. Nuallin and W. Bouten (2006), Real-time data assimilation for operational ensemble streamflow forecasting. Journal of Hydrometeorology 7, 548–565.

Vrugt, J. A., C. J. F. ter Braak, M. P. Clark, J. M. Hyman and B. A. Robinson (2008), Treatment of input uncertainty in hydrologic modeling: Doing hydrology backward with Markov chain Monte Carlo simulation. Water Resources Research 44, W00B09.

Wada, Y., L. P. H. van Beek, C. M. van Kempen, J. W. T. M. Reckman, S. Vasak and M. F. P. Bierkens (2010), Global depletion of groundwater resources. Geophysical Research Letters 37, L20402.

Wada, Y., L. P. H. van Beek and M. F. P. Bierkens (2011a), Modelling global water stress of the recent past: on the relative importance of trends in water demand and climate variability. Hydrology and Earth System Sciences 15, 3785–3808.

Wada, Y., L. P. H. van Beek, D. Viviroli, H. H. Drr, R. Weingartner and M. F. P. Bierkens (2011b), Global monthly water stress: 2. water demand and severity of water stress. Water Resources Research 47, W07518.

Wada, Y., L. P. H. van Beek and M. F. P. Bierkens (2012), Nonsustainable groundwater sustaining irrigation: A global assessment. Water Resources Research 48, W00L06.

Wada, Y., L. P. H. van Beek, N. Wanders and M. F. P. Bierkens (2013), Human water consumption intensifies hydrological drought worldwide. Environmental Research Letters 8, 034036.

Wada, Y., D. Wisser and M. F. P. Bierkens (2014), Global modeling of withdrawal, allocation and consumptive use of surface water and groundwater resources. Earth System Dynamics 5, 15–40.

Wagner, W., G. Lemoine and H. Rott (1999), A method for estimating soil moisture from ERS scatterometer and soil data. Remote Sensing of Environment 70, 191 – 207.

Wagner, W., G. Blöschl, P. Pampaloni, J. C. Calvet, B. Bizzarri, J. P. Wigneron and Y. Kerr (2007), Operational readiness of microwave remote sensing of soil moisture for hydrologic applications. Nordic Hydrology 30, 1 – 20.

Walker, J. P. and P. R. Houser (2004), Requirements of a global near-surface soil moisture satellite mission: accuracy, repeat time, and spatial resolution. Advances in Water Resources 27, 785 – 801.

Wan, Z. (2008), New refinements and validation of the MODIS land-surface temperature/emissivity products. Remote Sensing of Environment 112, 59 – 74.

Wand, M. P. and M. C. Jones (1995), Kernel Smoothing. Chapman and Hall, London.

Wanders, N., H. A. J. Van Lanen and A. F. Van Loon (2010), Indicators for drought characterization on a global scale. Tech. Rep. 24, EU-WATCH.

Warszawski, L., K. Frieler, V. Huber, F. Piontek, O. Serdeczny and J. Schewe (2014), The inter-sectoral impact model intercomparison project (ISIMIP): Project framework. Proceedings of the National Academy of Sciences 111, 3228 3232.

Weedon, G., S. Gomes, P. Viterbo, H. Österle, J. Adam, N. Bellouin, O. Boucher and M. Best (2010), The WATCH Forcing Data 1958-2001: A Meteorological forcing dataset for land surface- and hydrological models. Tech. Rep. 22, EU WATCH (Water and global Change) project.

Weedon, G. P., S. Gomes, P. Viterbo, W. J. Shuttleworth, E. Blyth, H. sterle, J. C. Adam, N. Bellouin, O. Boucher and M. Best (2011), Creation of the WATCH forcing data and its use to assess global and regional reference crop evaporation over land during the twentieth century. Journal of Hydrometeorology 12, 823–848.

Weerts, A. H. and G. Y. H. El Serafy (2006), Particle filtering and Ensemble Kalman Filtering for state updating with hydrological conceptual rainfall-runoff models. Water Resources Research 42, W09403.

Wells, N., S. Goddard and M. Hayes (2004), A self-calibrating palmer drought severity index. Journal of Climate 17, 2335 – 2351.

Wesseling, C. G., D.-J. Karssenberg, P. A. Burrough and W. P. A. Van Deursen (1996), Integrating dynamic environmental models in GIS: The development of a dynamic modelling language. Transactions in GIS 1, 40–48.

Western, A. W., R. B. Grayson and G. Blöschl (2002), Scaling of soil moisture: a hydrologic perspective. Annual Review of Earth and Planetary Sciences 30, 149–180.

Wigneron, J. P., A. Chanzy, J. C. Calvet and N. Bruguier (1995), A simple algorithm to retrieve soil moisture and vegetation biomass using passive microwave measurements over crop fields. Remote Sensing of Environment 51, 331 – 341.

Wilhite, D. (2000), Drought: A global assessment. Routledge.

Wilhite, D., M. Svoboda and M. Hayes (2005), Monitoring drought in the United States: status and trends. In: K. Boken, A. Cracknell and R. Heathcote, eds., Monitoring and Predicting Agricultural Drought: A Global Study, Oxford University Press, 121 – 131.

Wilhite, D. A. and M. H. Glantz (1985), Understanding: the drought phenomenon: The role of definitions. Water International 10, 111–120.

Wilson, D., H. Hisdal and D. Lawrence (2010), Has streamflow changed in the Nordic countries? recent trends and comparisons to hydrological projections. Journal of Hydrology 394, 334 – 346.

Wong, W. K., S. Beldring, T. Engen-Skaugen, I. Haddeland and H. Hisdal (2011), Climate change effects on spatiotemporal patterns of hydroclimatological summer droughts in norway. Journal of Hydrometeorology 12, 1205–1220.

Wood, A. W. and D. P. Lettenmaier (2008), An ensemble approach for attribution of hydrologic prediction uncertainty. Geophysical Research Letters 35, L14401.

Wood, E. F., J. K. Roundy, T. J. Troy, L. P. H. van Beek, M. F. P. Bierkens, E. Blyth, A. de Roo, P. Döll, M. Ek, J. Famiglietti, D. Gochis, N. van de Giesen, P. Houser, P. R. Jaffé, S. Kollet, B. Lehner, D. P. Lettenmaier, C. Peters-Lidard, M. Sivapalan, J. Sheffield, A. Wade and P. Whitehead (2011), Hyperresolution global land surface modeling: Meeting a grand challenge for monitoring earth's terrestrial water. Water Resources Research 47, W05301.

World Meteorological Organization (2007), The role of climatological normals in a changing climate. WCDMP-No. 61, WMO-TD/No. 1377.

World Meteorological Organization (2009), Experts agree on a universal drought index to cope with climate risks. Press release No. 872.

Wu, H., M. Svoboda, M. Hayes, D. Wilhite and W. Fujiang (2006), Approproate application of the standardized precipitation index in arid locations and dry seasons. International Journal of Climatology 27, 65 – 79.

Wu, H., R. F. Adler, Y. Hong, Y. Tian and F. Policelli (2012), Evaluation of global flood detection using satellite-based rainfall and a hydrologic model. Journal of Hydrometeorology 13, 1268–1284.

Xia, Y., K. Mitchell, M. Ek, B. Cosgrove, J. Sheffield, L. Luo, C. Alonge, H. Wei, J. Meng, B. Livneh, Q. Duan and D. Lohmann (2012), Continental-scale water and energy flux analysis and validation for North American Land Data Assimilation System project phase 2 (NLDAS-2): 2. Validation of model-simulated streamflow. Journal of Geophysical Research: Atmospheres 117, D03110.

Yang, W., B. Tan, D. Huang, M. Rautiainen, N. Shabanov, Y. Wang, J. Privette, K. Huemmrich, R. Fensholt, I. Sandholt, M. Weiss, D. Ahl, S. Gower, R. Nemani, Y. Knyazikhin and R. Myneni (2006), MODIS leaf area index products: from validation to algorithm improvement. IEEE Transactions on Geoscience and Remote Sensing 44, 1885 –1898.

Yevjevich, V. (1967), An objective approach to definition and investigation of continental hydrological droughts. Hydrology papers 23, Colorado state university, Fort Collins, USA.

Yirdaw, S., K. Snelgrove and C. Agboma (2008), Grace satellite observations of terrestrial moisture changes for drought characterization in the Canadian prairie. Journal of Hydrology 356, 84 – 92.

Summary

Hydrological extremes regularly occur in all regions of the world and as such have large impacts on society. Floods and drought are the most severe hydrological extremes, in terms of their societal impact and potential economic damage. These events are amongst the most costly natural disasters, due to their often large spatial extent and high societal impact. The high numbers of economical and human losses indicate the importance of accurate monitoring, forecasting and projection of high impact hydrological driven natural disasters. This is even more urgent for regions where resilience to natural disasters is low and where these events can have a multi-year impact on the economy of the region. Hydrological extremes are often monitored and modelled with computer models that aim at accurately representing the current and future hydrological conditions. Reducing uncertainty in hydrological simulations of hydrological extremes is of major importance to reduce socio-economic impacts of these extremes. Bayesian data assimilation methods provide a framework to reduce uncertainty in large scale hydrological models by combining model simulations and observations. Additionally, the impact of different definitions for hydrological extremes has not been properly studied yet. It is important to agree upon a common terminology, which can be used for analyses of hydrological extremes. Therefore, the main objective of this thesis is: *To reduce uncertainty in simulations, reanalysis, monitoring, forecasting and projections of hydrological extremes for large river basins.*

The first part of this thesis focusses on the uncertainty in hydrological simulation and short-term flood forecasting. I try to reduce the uncertainty in, (i) precipitation, (ii) historic hydrological simulations and state estimates and (iii) short term flood forecasting.
First, I focus on the uncertainty in precipitation. I used ground-based and satellite observations to reduce the uncertainty in precipitation forcing fields. Precipitation is an important hydro-meteorological variable, and is a primary driver in hydrological modelling. Improved estimates of precipitation fields lead to better simulations of soil moisture (SM) which in turn are expected to greatly increase the accuracy of flood and drought predictions. In large parts of the world, real-time ground-based observations of precipitation are sparse and satellite derived precipitation products are the only information source. Satellite derived SM and land surface temperature (LST) were used to reduce uncertainties in satellite precipitation over the continental United States. Assimilation of both satellite-based SM and LST observations reduced the false detection of precipitation and the uncertainty in the retrieved rainfall volumes. However, with SM assimilation a larger number of observed rainfall events were not detected, while LST assimilation did not have this problem. This work showed the potential of satellite based SM and LST estimates for reducing the uncertainties in satellite based precipitation estimates over sparsely gauged areas and thereby the

potential to improve hydrological modelling in these areas.
To reduce the uncertainty in historic global hydrological model simulations, observations and model simulations are combined to produce a multi-decadal "terrestrial hydrological reanalysis" dataset with retrospective and updated hydrological states and fluxes that are constrained with available in-situ river discharge measurements. With an Ensemble Kalman Filter I calibrate the model parameters of the global hydrological model PCR-GLOBWB and precipitation pre-factors to correct forcing precipitation fields based on 1495 time series of discharge observations from the Global Runoff Data Center. Results show that the model parameters can be calibrated successfully. Corrections to the rainfall fields are considerable, and topography has the largest impact on the precipitation corrections. The final outcome is the first ensemble hydrological reanalysis product that is consistent with discharge observations, has a closed water balance and provides estimates on the uncertainty in all fluxes and storage components of the terrestrial water cycle.
The final objective of this part was to reduce the uncertainty in short term flood forcasting. As it is impossible to collect ground-observations at the global scale, remotely sensed satellite observations could provide a valuable source of observations for many components of the hydrological cycle. However, it is important to properly validate the observations and obtain an accurate estimate of the uncertainty in the satellite retrievals. The validation of remotely sensed SM products is generally hampered by the difference in spatial support of in-situ observations and satellite footprints. Unsaturated zone modelling may serve as a valuable validation tool because it could bridge the gap between different spatial supports. A time series analysis was performed to compare surface SM from the SWAP unsaturated zone model to surface SM retrievals from three different microwave sensors, including AMSR-E, SMOS and ASCAT. Results suggest that temporal dynamics compared to SWAP are captured by satellite derived SM products, however, not all with similar quality. Additionally, it was found that satellite uncertainty is spatially correlated and distinct spatial patterns are found.
Thereafter, a dual state and parameter Ensemble Kalman Filter was used to calibrate the hydrological model LISFLOOD for the Upper Danube. Calibration is done with discharge and remotely sensed SM data. Calibration with discharge data improves the estimation of parameters linked to groundwater and routing processes. Calibration with only remotely sensed SM results in an accurate identification of parameters related to land surface processes. It was shown that remotely sensed SM holds potential for calibration of hydrological models, leading to a better simulation of SM content throughout the catchment and a better simulation of discharge in upstream areas.
In addition, the calibration results were used to study the added value of assimilated remotely sensed SM and discharge for the European Flood Awareness System (EFAS) and its potential to improve the prediction of the timing and height of the flood peak and low flows. The results show that the accuracy of flood forecasts is increased when more discharge observations are assimilated. The additional inclusion of satellite data results in a further increase of the performance: forecasts of base flows are

better and the uncertainty in the overall discharge is reduced. The assimilation of SM data reduces the timing errors in the flood predictions, especially for shorter lead times and imminent floods can be forecasted with more skill. This is the first work that shows the potential of remotely sensed SM observations to improve near-real time flood forecasting in large catchments.

In the second part of the thesis I focus on the vagueness in drought terminology by studying the definitions that are used to identify and quantify drought. I present an intercomparison between frequently used drought indicators to study their differences and provide a solution to define drought under a changing climate.
A selection of frequently used indicators for different drought types was used to investigate their potential to monitor drought on a global scale. Correlation between indicators was calculated for the major climates and for the whole globe to quantify the unique information content of each indicator and their intersubstitutability. Indicators used for precipitation drought show low correlations although most of them are calculated in a similar way. Indicators for soil moisture drought show even lower similarity, while indicators for streamflow drought show the highest correlation. Additionally, meteorological drought indicators are not capable to correctly describe either SM drought or streamflow drought. These findings have implications for drought monitoring systems: (i) for each drought type, which is associated with one or more impacted sectors, a different indicator should carefully be identified; (ii) drought indicators that are designed to monitor the same drought type should also be carefully identified, because they show large discrepancies in their anomalies and hence drought detection.
Under a changing climate our perception of drought might change as well. This work quantifies the impact of climate change on future low flows and associated hydrological drought characteristics (drought in groundwater and streamflow) on a global scale using an alternative drought identification approach that considers adaptation to future changes in hydrological regime. The transient variable threshold is a non-stationary approach that adjusts to gradual changes in the hydrological regime as response to climate change. In 27% of the world both the drought duration and the deficit volume are expected to increase when applying the transient threshold. However, this area will significantly increase to 62% when a non-transient threshold is applied. This work illustrates that an alternative drought identification that considers adaptation to an altered hydrological regime, has a substantial influence on future hydrological drought characteristics.

In the final part of the thesis, the hydrological drought projections are studied in more detail. Magnitude and directionality of changes in hydrological drought characteristics are largely unknown. I evaluated the impact of the climatology and catchment characteristics as well as the impact of human water use on future hydrological drought. First the impact of climatology and catchment characteristics is studied by using a conceptual hydrological model that was forced by downscaled and bias-corrected outcome from three General Circulation Models (GCM) for the SRES A2 emission

scenario (GCM forced models), and the WATCH forcing re-analysis dataset (reference model). The threshold level method was applied to investigate drought occurrence, duration and deficit volume. Results for the control period (1971-2000) show that the drought characteristics of each GCM forced model reasonably agree with the reference model for most of the climate types, suggesting that the climate models after post-processing produce realistic outcome for global drought analyses. For the near future (2021-2050) and far future (2071-2100), the GCM forced models show a decrease in drought occurrence for all major climates around the world and an increase of both average drought duration and deficit volume of the remaining drought events. On a global scale the increase in hydrological drought duration and severity in multiple regions will lead to a higher impact of drought events, which urges water resources managers to timely anticipate on the increased risk of more severe drought in groundwater and streamflow, and to design proactive measures.
Secondly the PCR-GLOBWB model was forced with the latest CMIP5 climate projections taken from five GCMs and four Representative Concentration Pathways (RCPs) to study the impact of human water use on future hydrological drought. A natural or pristine scenario has been used to calculate the impact of the changing climate on hydrological drought and has been compared to a scenario with human influences. Results show a significant impact of climate change and human water use in large parts of Asia, Middle East and the Mediterranean. The differences between RCPs are small, indicating that human water use is proportional to the changes in the climate. Reservoirs tend to reduce the impact of drought by water retention in the wet season, which in turn will lead to increased water availability in the dry season, especially for large regions in Europe and North America. This work illustrates that the impact of human water use and reservoirs is nontrivial and can vary substantially per region and per season.

The results from this thesis show that the inclusion of data assimilation, satellite data and model simulation is beneficial in the field of flood forecasting and hydrological modelling in general. This is shown by the results obtained in the first part of this thesis, where I successfully integrated different sources of observations to reduce uncertainty in hydrological model simulations. It was also proven in the second part of this work that there are multiple ways to identify drought events and that the impact of climate change on drought identification is significant. This impact of a changing climate contributes to the current vagueness in drought terminology and should be taken into account when studying the phenomena drought. Finally, I showed that the impact of climate change on future hydrological drought is highly dependent on the local climatology and the impact of human influence. This thesis showed that it is possible to reduce the uncertainty in the simulations of hydrological extremes by combining existing data, models and frameworks. These findings can bring major advances in the field of hydrological modelling to support monitoring and forecasting of hydrological extremes in large river basins.

Nederlandse samenvatting

In grote delen van de wereld zijn hydrologische extremen een regelmatig terugkerend verschijnsel met grote maatschappelijke gevolgen. Wat betreft economische schade en verlies aan mensenlevens zijn overstromingen en droogte de belangrijkste hydrologische extremen. Het is daarom van groot belang om deze hydrologisch gedreven natuurrampen goed te kunnen monitoren en voorspellen, zowel op de korte als lange termijn. Dit is nog belangrijker voor gebieden waar de weerbaarheid tegen natuurrampen laag is en waar de economische gevolgen meerdere jaren merkbaar kunnen zijn.

Hydrologische extremen worden vaak gemonitord en gesimuleerd met computermodellen die proberen de huidige en toekomstige hydrologische situatie zo nauwkeurig mogelijk na te bootsen. Hoewel hydrologische modellen steeds beter worden, gaan de modelsimulaties gepaard met aanzienlijke onzekerheid. Het is van groot belang om deze onzekerheid te reduceren, opdat het voorkomen van droogtes en overstromingen en mogelijke gevolgen daarvan beter voorspeld kunnen worden. Data-assimilatiemethodes bieden de mogelijkheid om de onzekerheid te reduceren door modelsimulaties te combineren met observaties. Daarbij is het van groot belang dat er in de wetenschappelijke wereld overeenstemming is over wanneer een hydrologisch extreme gebeurtenis een overstroming of droogte genoemd wordt. Het hanteren van een gezamenlijke terminologie maakt extreme gebeurtenissen op verschillende locaties en tijdstippen beter vergelijkbaar en leidt uiteindelijk tot betere analyses van de frequentie en grootte van hydrologische extremen. Tezamen leidt dit tot het hoofddoel van deze thesis: het reduceren van de onzekerheid in hydrologische simulaties en het met eenduidige terminologie analyseren, monitoren en voorspellen van hydrologische extremen in grote rivieren.

Het eerste deel van deze thesis richt zich op de onzekerheid in de hydrologische simulaties en korte-termijn voorspellingen. Ik probeer de onzekerheid te verminderen in (i) neerslag gegevens, (ii) schattingen van verschillende hydrologische componenten in historische hydrologische simulaties en (iii) korte-termijn overstromingsvoorspellingen.

Allereerst heb ik me gericht op de onzekerheid in de neerslag. Ik heb gebruik gemaakt van grondobservaties en neerslagschattingen van satellieten om de onzekerheid in neerslagvelden te reduceren. Neerslag is een belangrijke hydro-meteorologische variabele en van groot belang in hydrologische modellering. Verbeterde schattingen van de neerslaghoeveelheid zullen leiden tot een betere simulatie van het bodemvocht, wat op zijn beurt weer een positieve invloed heeft op de nauwkeurigheid van overstromings- en droogtevoorspellingen. In grote delen van de wereld zijn geen tot weinig actuele grondobservaties van neerslag beschikbaar. In die gebieden bieden neerslagobservaties

van satellieten een uitkomst. Satellietobservaties van bodemvocht en de oppervlaktetemperatuur zijn gebruikt om de onzekerheid in satellietneerslag te reduceren op het vaste land van de Verenigde Staten. Assimilatie van zowel bodemvocht als de temperatuur van het aardoppervlak reduceerde het aantal incorrect gemeten regenbuien en het geschatte totale regenvolume. De assimilatie van bodemvocht zorgde er echter ook voor dat een groot aantal regenbuien helemaal niet werd gedetecteerd, terwijl dit geen probleem was bij de assimilatie van de temperatuur van het aardoppervlak. Deze studie demonstreerde de mogelijkheden om met satellietobservaties van bodemvocht en temperatuur van het aardoppervlak de onzekerheden in satelliet-gebaseerde neerslagschattingen te reduceren voor gebieden met weinig grondobservaties. Dit kan de nauwkeurigheid van hydrologische modelsimulaties in slecht bemeten gebieden vergroten.

Om de onzekerheid in historische hydrologische simulaties te verkleinen, heb ik modelsimulaties gecombineerd met afvoermetingen om een hydrologische heranalyse dataset te creëren. De dataset bevat gecorrigeerde hydrologische toestandsvariabelen en fluxen over meerdere decennia. Met een ensemble Kalman filter heb ik de modelparameters en pre-factoren voor neerslagcorrecties gekalibreerd voor het mondiale hydrologische model PCR-GLOBWB. Deze analyse is gebaseerd op 1495 tijdseries van rivierafvoeren, verkregen van het Global Runoff Data Center. De resultaten laten zien dat het mogelijk is om de modelparameters te kalibreren. De correcties in de neerslagvelden zijn aanzienlijk, waarbij de lokale topografie de grootste invloed heeft op de uitgevoerde correcties. Deze studie heeft geleid tot de eerste mondiale ensemble[1] hydrologische heranalyse dataset die consistent is met gemeten rivierafvoeren, een sluitende waterbalans heeft en een schatting geeft van de onzekerheden in de fluxen en bergingen in de verschillende componenten van de terrestrische waterkringloop.

Tot slot heb ik in het eerste deel van de thesis onderzocht of het mogelijk is om de onzekerheid in korte-termijn overstromingsvoorspellingen te reduceren. Omdat het onmogelijk is om grondobservaties te verzamelen op mondiale schaal, zouden satellietobservaties een belangrijke extra bron van informatie kunnen zijn om componenten van de hydrologische kringloop beter te monitoren. Het blijft echter belangrijk om de satellietobservaties te valideren en zo een goede schatting te krijgen van de nauwkeurigheid van deze observaties. De validatie van bijvoorbeeld bodemvocht gemeten met een satelliet is over het algemeen beperkt door de verschillen in de ruimtelijke schaal van de grond-, en satellietobservaties. Het modelleren van de onverzadigde zone, en vooral het bodemvocht, kan dienen als een validatiemiddel om de schaalverschillen tussen grond- en satellietobservaties te overbruggen. Een tijdreeksanalyse is uitgevoerd om de verschillen in gemodelleerd bodemvocht uit het model SWAP te vergelijken met bodemvochtobservaties van drie verschillende satellietsensoren die meten in het microgolf-domein (AMSR-E, SMOS en ASCAT). De resultaten

[1]Met het woord “ensemble” bedoel ik dat er meerdere datasets zijn gecreëerd die even zo waarschijnlijke representaties van de werkelijkheid zijn. Hieruit kunnen we ook onzekerheden van de verschillende waterbalanstermen schatten.

laten zien dat de temporele variatie van SWAP-bodemvocht overeenkomt met de satellietobservaties, waarbij niet iedere sensor een gelijke kwaliteit levert. Verder toonde deze studie aan dat de onzekerheid in satellietobservaties in de ruimte is gecorreleerd en dat er duidelijke ruimtelijke patronen in de fout van de observaties zichtbaar zijn.

Vervolgens heb ik geëvalueerd hoe deze satellietobservaties van bodemvocht kunnen worden gebruikt bij de korte-termijn voorspelling van overstromingen. Hierbij heb ik eerst parameters gekalibreerd met behulp van satellietgegevens, en deze vervolgens gebruikt in een voorspelling van overstromingen. Bij de kalibratie maak ik gebruik van een Ensemble Kalman Filter om zowel de toestandsvariabelen als de parameters van het hydrologisch model LISFLOOD te schatten voor de bovenloop van de Donau. De kalibratie is uitgevoerd met zowel afvoermetingen als bodemvocht geschat met behulp van satellietobservaties. De kalibratie met afvoerdata zorgde voornamelijk voor een verbetering van de parameters gerelateerd aan grondwater- en afvoerprocessen. Kalibratie met alleen satellietobservaties leidde tot een nauwkeurigere identificatie van de parameters gerelateerd aan oppervlakteprocessen. Hierdoor werd het duidelijk dat satellietobservaties de potentie hebben om te helpen bij de kalibratie van hydrologische modellen. Dit zal uiteindelijk leiden tot een betere simulatie van het bodemvocht in het stroomgebied en een betere simulatie van bovenstroomse afvoeren. Vervolgens zijn de kalibratieresultaten gebruikt om de toegevoegde waarde van geassimileerd satellietbodemvocht en afvoeren te onderzoeken in het European Flood Awareness System (EFAS). Daarbij heb ik gekeken naar het effect van de assimilatie op de voorspellingen van het optreden en de hoogte van overstromingen en lage afvoeren. De resultaten laten zien dat de nauwkeurigheid van de overstromingsvoorspellingen verbetert wanneer meer afvoermetingen worden gebruikt. Wanneer tevens satellietgegevens worden gebruikt zien we een verdere verhoging van de nauwkeurigheid; de basisafvoer wordt beter geschat en de fout in de totale afvoer wordt lager. De assimilatie van bodemvocht vermindert tevens de onzekerheid in de voorspelling van het moment waarop de overstroming zal plaatsvinden, met name wanneer voorspellingen worden gedaan voor de komende paar dagen, dat wil zeggen op relatief korte termijn. Geconcludeerd kan worden dat het gebruik van satellietgegevens de onzekerheid in de voorspelling van overstromingen verlaagd. Dit is de eerste keer dat de toegevoegde waarde van satellietbodemvochtobservaties voor korte-termijn overstromingsvoorspellingen in grote riviersystemen is aangetoond.

In het tweede deel van deze thesis heb ik mij gericht op de onduidelijkheid die er bestaat over de definitie van droogte en de manier waarop droogte-indicatoren gebruikt worden om droogte te kwantificeren en te identificeren. Ik presenteer een onderlinge vergelijking van meerdere, vaak gebruikte, droogtedefinities en een droogtedefinitie die geldig blijft in een veranderend klimaat.

Een selectie van veelgebruikte droogte-indicatoren is getest op de potentie om droogte te monitoren op mondiale schaal. De correlatie tussen de verschillende indicatoren is berekend voor de belangrijkste klimaattypen en voor de wereld in zijn geheel, om de unieke waarde van elke indicator te bepalen en om te bepalen in hoeverre ze onder-

ling uitwisselbaar zijn. Indicatoren die gebruikt worden om meteorologische droogte te bepalen laten een lage uitwisselbaarheid zien, ondanks de bijna identieke manier waarop ze worden berekend. Droogte-indicatoren voor bodemvochtdroogte laten zelfs nog minder gelijkenissen zien, terwijl de indicatoren voor hydrologische droogte juist de meeste gelijkenissen vertonen. Meteorologische droogte-indicatoren blijken niet in staat te zijn om bodemvochtdroogte noch hydrologische droogte te detecteren. Deze bevindingen hebben belangrijke consequenties voor systemen die droogtecondities monitoren: (i) Voor elk droogtetype zou een aparte indicator gebruikt moeten worden die gekozen wordt op basis van het type droogte dat men wil bestuderen; (ii) droogte-indicatoren die zijn ontwikkeld om hetzelfde droogtetype te bestuderen zouden beter bestudeerd moeten worden, omdat blijkt dat er grote verschillen bestaan in de droogtedetectie van deze indicatoren.

Onder invloed van klimaatverandering verandert ook onze perceptie van droogte. Ik heb gekeken naar de invloed van klimaatverandering op lage afvoeren en hydrologische droogtekarakteristieken (droogte in grondwater en afvoer) op wereldschaal, waarbij gebruik gemaakt wordt van een definitie van droogte die rekening houdt met veranderingen in het hydrologische klimaat. De niet-stationaire variabele-drempelwaardemethode is een methode die zich aanpast aan veranderingen in het hydrologische regime als gevolg van klimaatverandering en de bijbehorende veranderingen in waterbeschikbaarheid. In 27% van de wereld nemen zowel de droogteduur als het totale watertekort toe wanneer deze niet-stationaire methode wordt gebruikt. Dit gebied zal significant toenemen tot 62% bij het gebruik van een stationaire conventionele methode. Hiermee wordt aangetoond dat de alternatieve niet-stationaire droogte identificatie, die rekening houdt met adaptatie aan een veranderd hydrologisch regime, een aanzienlijke invloed heeft op de toekomstige hydrologische droogtekarakteristieken.

In het laatste deel van deze thesis worden hydrologische droogteprojecties beter bestudeerd. De omvang en richting van de veranderingen in hydrologische droogtekarakteristieken zijn grotendeels onbekend. Ik evalueer de invloed van klimatologie en stroomgebiedskenmerken alsmede de invloed van menselijk watergebruik op toekomstige hydrologische droogte.

Als eerste is de invloed van klimatologie en stroomgebiedskenmerken bestudeerd door gebruik te maken van een conceptueel hydrologisch model, dat is gedraaid met herschaalde en voor onzuiverheid gecorrigeerde resultaten van drie General Circulation Models (GCM) voor het SRES A2 emissie scenario (GCM-modelsimulaties), en een heranalyse dataset (referentiemodel). De stationaire variabele-drempelwaardemethode is gebruikt om droogtefrequentie, -duur en -tekort te bepalen. Resultaten voor de controle periode (1971-2000) laten zien dat de droogtekarakteristieken voor de GCM-modelsimulaties redelijk overeenkomen met resultaten van het referentiemodel voor de meeste klimaattypes, wat suggereert dat de klimaatmodellen realistische uitkomsten produceren voor droogte-analyse. Voor de nabije (2021-2050) en de verre (2071-2100) toekomst laten de GCM-modelsimulaties een neerwaartse trend zien in de droogte-

frequentie voor alle klimaattypes en een toename van droogteduur en -tekort. Op wereldschaal zal de toename in droogteduur en hevigheid of tekort leiden tot een groter negatief effect van droogte in bepaalde gebieden. Daarom zullen waterbeheerders moeten nadenken over maatregelen, die de gevolgen van toenemende droogte in grondwater en afvoeren kunnen verminderen.

Om de invloed van menselijk watergebruik op hydrologische droogte te onderzoeken, heb ik vervolgens het mondiale hydrologische model PCR-GLOBWB gedraaid met gegevens van de meest recente CMIP5 klimaatvoorspellingen, afgeleid van vijf GCMs en vier Representative Concentration Pathways (RCPs). Een natuurlijk scenario is gebruikt om de invloed van klimaatverandering op hydrologische droogte te vergelijken met een scenario waarbij waterverbruik wél werd meegenomen in de simulatie. De resultaten laten zien dat naast klimaatverandering het menselijk watergebruik een belangrijke invloed heeft op droogtevoorspellingen in grote delen van Azië, het Midden-Oosten en de Mediterrane gebieden. De verschillen tussen de twee scenario's zijn groot, wat aangeeft dat de menselijke invloed op de droogtekarakteristieken vergelijkbaar is met de invloed van klimaatverandering op de droogtekarakteristieken. Reservoirs hebben de neiging om de negatieve gevolgen van droogte te verminderen door in het natte seizoen water te bergen, wat vervolgens in het droge seizoen zorgt voor een verhoogde waterbeschikbaarheid, vooral voor gebieden in Europa en Noord-Amerika. Dit werk laat zien dat de invloed van menselijk watergebruik en reservoirs op droogte niet triviaal is en sterk kan variëren per regio en seizoen.

De resultaten van deze thesis laten zien dat het gebruik van data-assimilatie om satellietobservaties en modelsimulaties te combineren kan leiden tot betere voorspellingen van overstromingen. Dit wordt vooral duidelijk in het eerste deel van de thesis, waarin ik met succes verschillende bronnen van observaties combineer en zodoende de onzekerheid in hydrologische simulaties verminder. Het tweede deel van dit werk laat zien dat er meerdere manieren zijn om droogte te identificeren en dat de gebruikte methodes een significante invloed hebben op droogtedetectie. Dit draagt bij aan vermindering van de huidige onduidelijkheid in droogteterminologie. Wetenschappers zouden in de toekomst meer aandacht moeten besteden aan een juist gebruik van droogte-indicatoren en terminologie wanneer men het fenomeen droogte bestudeert. Tot slot heb ik laten zien dat de invloed van klimaatverandering op droogte sterk afhangt van het lokale klimaat en de menselijke invloeden in het stroomgebied. Deze thesis laat zien dat het mogelijk is om de onzekerheid in simulaties van hydrologische extremen te reduceren door bestaande data, modellen en raamwerken op een slimme manier te combineren. Deze resultaten kunnen helpen bij het verbeteren van de huidige modellering en monitoring van hydrologische extremen in grote stroomgebieden.

Dankwoord

Toen was het eindelijk over met de pret, na 4 jaar PhD-onderzoek is het boekje afgerond. Uiteraard is dat niet iets wat ik zonder hulp had kunnen bereiken, en dit is het moment dat ik enkele mensen persoonlijk zou willen bedanken voor hun bijdragen en hulp. Sommige bijdragen waren intellectueel van aard, terwijl andere bijdragen vooral op het sociale vlak en alles behalve intellectueel waren; toch zijn ze allemaal even belangrijk. Alvorens ik begin en per ongeluk iemand zou vergeten, wil ik alvast iedereen bedanken die de moeite heeft genomen om het dankwoord te lezen.

Allereerst mijn begeleiders, Steven, Derek, Marc, en Ad. Jullie besloten mij aan te nemen in Utrecht bij Fysische Geografie. Nieuwe universiteit, onbekende gezichten, maar al snel was ik helemaal op mijn plek, mede dankzij jullie uitstekende begeleiding. Ik wil jullie graag bedanken voor het vertrouwen dat jullie in mij hebben gehad en de vrijheid die ik heb gekregen om mijn eigen weg te gaan tijdens het onderzoek. Het voelde als vier jaar vakantie met af en toe een deadline.
Steven de Jong, jouw persoonlijke benadering en aanstekelijke enthousiasme kan ik heel erg waarderen. Ik kon mijn eigen beslissingen maken en ik heb nooit het gevoel gehad dat jij officieel gezien mijn baas bent. Ik wil je nog het meeste bedanken voor het volledige vertrouwen en de ruimte die ik kreeg om mijn eigen plan te trekken.
Derek Karssenberg, het is fijn dat je me soms hebt afgeremd. Niet alles hoeft snel, soms kun je gewoon rustig aan doen en komt het toch goed. Soms vervloekte ik alle correcties, maar ze maakten het schrijfwerk beter. Ik heb veel geleerd op dit gebied van jou, en dat is te merken aan het dalende aantal correcties in het latere schrijfwerk.
Denktank Marc Bierkens, ik kom graag bij jou langs voor brainstormsessies gevuld met creatief en snel denken. Als ik alles zou uitvoeren wat jij hebt bedacht in deze vier jaar zou ik nog wel een tijdje in Utrecht zitten. De beste ideeën eruit filteren en gebruiken was het devies. Bedankt voor alle ideeën, suggesties, tips en trucs.
Als laatste Ad de Roo, de data stonden altijd klaar en je zorgde er altijd voor dat niks mij kon vertragen. Je had vertrouwen in mijn resultaten en mijn manier van aanpak, en het was erg fijn dat ik via jou een idee had waarvoor mijn resultaten gebruikt konden worden. Daarnaast waren de tripjes naar Italië ook zeker niet verkeerd.

Nu een onofficieel lid van het begeleidingsteam, Henny van Lanen. Ik durf met zekerheid te zeggen dat zonder jou ik niet zou zijn waar ik nu ben. Dit geldt niet alleen voor de periode tijdens mijn PhD, maar ook daarvoor al. De kansen die je mij hebt gegeven tijdens Xerochore en zeker ook daarna, hebben ervoor gezorgd dat ik mezelf heb kunnen ontwikkelen als zelfstandige wetenschapper en mens. Je was nooit te beroerd mijn werk te laten zien aan anderen, een goed woordje voor me te doen, of mij te betrekken bij jouw projecten en problemen.

Dan zijn er nog een hele hoop mensen die mij niet begeleid hebben, maar zeker wel op andere manier geholpen hebben, waarvoor ik ze graag wil bedanken. Te

beginnen met mijn paranimfen Mark en Tjalling. Jongens, bedankt dat jullie mij willen bijstaan tijdens de laatste publieke uurtjes van mijn PhD. Alle collega's bij Fysische Geografie hebben ervoor gezorgd dat ik het altijd erg gezellig vond op het werk en sommige collega's in het bijzonder. Mr Wada, I want to thank you for our nice Wanders and Wada collaborations and of course our friendship and fun along the way. Edwin, I want to thank you for being my office mate for the last three years. You never got upset with all the noise I make by talking, singing or just being there, truly remarkable. Immerzeel en Lutz voor een zeer memorabele trip naar Langtang. De mensen waarmee ik nauw samenwerkte: Emily, Geert, Inge, Judith, Liesbeth, Menno, Oliver, Patricia, Rens, Rianne, Top. De gezelligheid tijdens het schaatsen, veldwerk in Frankrijk, sushi eten of bij mijn vaste hangplek, de koffieautomaat: Anouk, Aris, Elisabeth, Harm-Jan, Jantien, Jasper, Joost, Joyce, Juul, Kay, Koko, Kor, Marjan, Martin, Nynke, Philip, Renske, Stefanie, Timothy, Wietse, Willem, Winnie, Wouter, Yvonne. De mensen die mogelijk maakten dat ik een werkende fiets had: Marcel, Chris, Henk. Daarbuiten ook mijn externe collega's, te beginnen met Lieke Melsen, die al mijn werk heeft doorgespit op fouten en voor de sessies klagen over het leven als PhD. Anne van Loon voor de begeleiding tijdens mijn MSc thesis en de samenwerkingen tijdens de PhD. Richard en Robert voor het wegwijs maken in de wondere wereld van de Microwave remote sensing.

I would like to thank the people at Princeton University who made me feel welcome during my stay: Eric, Justin, Ming, Colby, Nate, Amanda, Yoshua, Julio, Yonghun.

Natuurlijk zijn er ook altijd de mensen die niks met je onderzoek te maken willen hebben, maar er wel voor zorgen dat je een normaal sociaal leven leidt. Als eerste Dijet, Ief en Lange, thanks voor nu al 10 jaar afleiding op de vrijdagavond. De jaarclub, Casper, Erik, Matthijs, Tim, Tjalle, voor afleiding op met name dinsdagavond, JC-vakanties en vele gedeelde speciaalbiertjes. Mensen die ervoor zorgden dat ik vele gezellige kilometers heb mogen maken op de fiets, Tjalling en Nauta. Als laatste Arjan en Lieke voor afleiding in de vorm van samen eten, feestjes of bar hangen.

Pap en mam, jullie hebben me altijd gestimuleerd om naar buiten te gaan en me te verbazen over de dingen in de natuur. Onderzoek is iets wat ik al jong van jullie heb meegekregen op de Vinkenbaan, en die combinatie van onderzoek en buiten zijn heb ik gevonden in de hydrologie. Ik hou nog ontzettend van buiten zijn en het onderzoek is iets wat me nog dagelijks enthousiast maakt. Fijn dit jullie dat allemaal voor mij mogelijk hebben gemaakt! Luuk, dank je dat jij met mij vele uren buiten hebt doorgebracht, op of rond het water en op de fiets.

Dan als laatste Marjolein. Zonder jou hadden mijn begeleiders een veel zwaardere tijd gehad met het lezen van mijn thesis, en sorry dat ik soms te veel over werk praat. Veel belangrijker dan werk is dat zonder jou deze vier jaar een stuk minder leuk zouden zijn geweest. Samen op vakantie, naar buiten, kamperen, wandelen, klimmen, fietsen, of fotograferen is het beste tijdverdrijf dat er is. Bedankt voor alle mooie momenten samen!

About the author

Niko Wanders was born on 29 November 1986 in Leiden, The Netherlands. In 2005 he started with his Bachelor of Science (BSc) in Soil Water Atmosphere at Wageningen University. He continued his studies in Wageningen with a Master of Science (MSc) in Hydrology and Water Quality, with a specialization in Hydrology and Quantitative Water Management. For his internship he worked at Deltares, Utrecht in The Netherlands where he focussed on model calibration and the development of a lowland catchment model. He completed his study in 2011 with the thesis "Indicators for drought characterization on a global scale. During his MSc education he worked on three European Commission projects related to drought: EC-WATCH, EC-XEROCHORE and Drought-R&SPI. During EC-WATCHhe worked on drought analysis on a global scale, and contributed to the work package Hydrological Extremes. During EC-XEROCHORE he worked together with international experts to discuss the state of the art of drought research and to identify future research gaps. In Drought-R&SPI he worked on drought propagation through the hydrological cycle and the impact on drought characteristics.

In 2011 Niko started as a PhD researcher at the Department of Physical Geography, Faculty of Geosciences at Utrecht University. He worked on improving near real-time flood forecasting with satellite soil moisture observations using Bayesian data assimilation techniques. During his PhD he collaborated with TU Wien, ESA-ESTEC, VU Amsterdam and EC-Joint Research Centre in Ispra. Results of his PhD study are implemented in the European Flood Awareness System of the EC-Joint Research Centre and contribute to improved flood forecasting.

Niko spent two months at the Terrestrial Hydrology Research Group, Department of Civil and Environmental Engineering of Princeton University, United States, working on improving satellite precipitation estimates. Together with the Hydrology and Quantitative Water Management Group in Wageningen University he worked on research related to (hydrological) drought. At Utrecht University he contributed to MSc courses in remote sensing, natural hazards and spatial statistics during his PhD study. Thereafter, Niko was employed as a postdoc at the department of Physical Geography at Utrecht University, working on research related to flood plain simulations in a global hydrological model. Niko, will start working as a postdoc at the Terrestrial Hydrology Research Group, Department of Civil and Environmental Engineering of Princeton University, United States, on topics related to data assimilation, remote sensing, drought and global hydrological modelling.

List of publications

Accepted peer-reviewed publications

Wanders, N., Lanen, H. A. J. van. (2015), Future hydrological drought across climate regions modelled with a synthetic hydrological model forced by three General Circulation Models, Natural Hazards and Earth System Science, in press.

Wanders, N., Pan, M., Wood, E. F. (2015), Correction of real-time satellite precipitation with multi-sensor satellite observations of land surface variables, Remote Sensing of Environment, 160, 206-221, doi:10.1016/j.rse.2015.01.016.

Wanders, N., Wada, Y., Lanen, H. A. J. van. (2015), Global hydrological droughts in the 21st century under a changing hydrological regime, Earth System Dynamics, 6, 1-15, doi:10.5194/esd-6-1-2015.

Wanders, N., Wada, Y. (2014), Human and climate impacts on the 21^{st} century hydrological drought, Journal of Hydrology, in press, doi:10.1016/j.jhydrol.2014.10.047.

Parinussa, R. M., Holmes, T. R. A, Wanders, N., Dorigo, W. A., Jeu, R. A. M. de. (2014), A Preliminary Study Towards Consistent Soil Moisture from AMSR2, Journal of Hydrometeorology, in press, doi:10.1175/JHM-D-13-0200.1.

Wanders, N., Jong, S. M. de, Roo, A. de, Bierkens, M. F. P, Karssenberg, D. (2014), The benefits of using remotely sensed soil moisture in parameter identification of large-scale hydrological models, Water Resources Research, 50, 68746891, doi:10.1002/2013WR0146397.

Wanders, N., Karssenberg, D., Roo, A. de, Jong, S. M. de, Bierkens, M. F. P. (2014), The suitability of remotely sensed soil moisture for improving operational flood forecasting, Hydrology and Earth System Sciences, 18, page 2343-2357, doi:10.5194/hess-18-2343-2014.

Alderlieste, M. A. A., Lanen, H. A. J. van, Wanders, N.. (2014), Future low flows and hydrological drought: how certain are these for Europe? In: Daniell, T. M., Van Lanen, H. A. J., Demuth, S., Laaha, G., Servat, E., Mahe, G., Boyer, J-F, Paturel, J-E, Dezetter, A., Ruelland, D., Hydrology in a Changing World: Environmental and Human Dimensions, IAHS Publ. No. 363, 60-65.

Loon, A. F. van, Tijdeman, E., Wanders, N., Lanen, H. A. J. van, Teuling, A. J., Uijlenhoet, R. (2014), How climate seasonality modifies drought duration and deficit, Journal of Geophysical Research: Atmospheres, 119 (8), 4640-4656, doi:10.1002/2013JD020383.

Wada, Y., Beek, L. P. H. van, Wanders, N., Bierkens, M. F. P. (2013), Human water consumption intensifies hydrological drought worldwide, Environmental Research Letters 8, 034036, doi:10.1088/1748-9326/8/3/034036.

Lanen, H. A. J. van, Wanders, N., Tallaksen, L. M., Loon, A. F. van. (2013), Hydrological drought across the world: impact of climate and physical catchment structure, Hydrology and Earth System Sciences, 17, 1715-1732, doi:10.5194/hess-17-1715-2013.

Wanders, N., Karssenberg, D., Bierkens, M. F. P, Parinussa, R. M., Jeu, R. A. M. de, Dam, J. C. van, Jong, S. M. de. (2012), Observation uncertainty of satellite soil moisture products determined with physically-based modeling, Remote Sensing of Environment, 127, 341-35, doi:10.1016/j.rse.2012.09.004.

Peer-reviewed publications under review

Immerzeel, W. W, Wanders, N., Lutz, A. F., Shea, J. M., Bierkens, M. F. P. (2015), Reconciling Indus high altitude precipitation with glacier mass balances and runoff, Hydrology and Earth System Sciences, submitted.

Wanders, N., Sutanudjaja, E. H, Beek, L. P. H. van, Bierkens, M. F. P. (2014), The PCR-GLOBWB global hydrological reanalysis product, Journal of Advances in Modeling Earth System, under review.

Wanders, N., Loon, A.F. van, and Lanen, H. A. J. van. (2014), Uncover the real drought, Geophysical Research Letters, under review.

Other publications

Jong, S. M. de, Sutanudjaja, E. H., Wanders, N., Addink, E. A. (2013), Annual Report Remote Sensing Activities Utrecht University. EARSeL News Letter, 94, 29-32.

Tijdeman, E., Loon, A. F. van, Wanders, N., Lanen, H. A. J. van. (2013), The effect of climate on droughts and their propagation in different parts of the hydrological cycle, Tech. Rept. no. 2, EU Drought R&SPI project.

Jong, S. M. de, Wanders, N., Roo, A. de. (2012), Satellieten helpen overstromingen te voorspellen, Geografie Jaargang 21, Nummer 9.

Lanen H. A. J van, Wanders, N. (2011), High flow in the 21^{st} Century: analysis with a simple conceptual hydrological model using the input of 3 GCMs (A2 scenario). Tech. rept. no. 41, EU WATCH (Water and global Change) project.

Melsen L. A., Lanen H. A. J van, Wanders, N., Huijgevoort, M. H. J van, Weedon, G. P. (2011), Reference evapotranspiration with radiation-based and temperature-based method impact on hydrological drought using WATCH Forcing Data. Tech. rept. no. 39, EU WATCH (Water and global Change) project.

Wanders, N., Hendriks, D. M. D., Velde, Y. van der. (2011), Combined groundwater surface water modeling with a lumped hydrological model. Tech. rept. No. 1203833-000-BGS-0001, Deltares, Utrecht, The Netherlands.

Wanders, N., Lanen, H.A.J. van, Loon, A.F. van. (2010), Indicators for drought characterization on a global scale. Tech. rept. no. 24, EU WATCH (Water and global Change) project.

Lanen, H. A. J. van, Tallaksen, L. M., Morawietz, M., Wanders, N. (2010), Drought Network integrated in the European Drought Centre. Tech. rept. EU-FP7 XEROCHORE project.

Selected conference presentations as presenting author

Wanders, N., Pan, M., Wood, E. F. (2014), Correction of real-time satellite precipitation with multi-sensor satellite observations of land surface variables, Oral presentation at American Geographical Union Fall meeting, San Francisco, USA, 15-19 December.

Lanen, H. A. J. van, Wanders, N., Loon, A. F. van. (2014), Uncover the real drought, Oral presentation at American Geographical Union Fall meeting, San Francisco, USA, 15-19 December.

Wanders, N., Sutanudjaja, E. H, Beek, L. P. H. van, Bierkens, M. F. P. (2014), The PCR-GLOBWB global hydrological reanalysis product, Poster presentation at GEWEX 7th International Scientific Conference on the Global Water and Energy Cycle, The Hague, The Netherlands, 14-17 July.

Wanders, N., Pan, M., Wood, E. F. (2014), Correction of real-time satellite precipitation with multi-sensor satellite observations of land surface variables, Oral presentation at Satellite Soil Moisture validation & application workshop, Amsterdam, The Netherlands, 10-11 July.

Wanders, N., Karssenberg, D., Roo, A. de, Jong, S. M. de, Bierkens, M. F. P. (2013), The potential of remotely sensed soil moisture for operational flood forecasting, Oral resentation at American Geographical Union Fall meeting, San Francisco, USA, 9-13 December.

Lanen, H. A. J. van, Wanders, N., Wada, Y. (2013), The potential of remotely sensed soil moisture for operational flood forecasting, Oral presentation at American Geographical Union Fall meeting, San Francisco, USA, 9-13 December.

Karssenberg, D., Wanders, N., Roo, A. de, Jong, S. M. de, Bierkens, M. F. P. (2013), The benefits of using remotely sensed soil moisture in parameter identification of large-scale hydrological models, Oral presentation at American Geographical Union Fall meeting, San Francisco, USA, 9-13 December.

Bierkens, M. F. P, Wanders, N., Sutanudjaja, E. H, Beek, L. P. H. van. (2013), The PCR-GLOBWB global hydrological reanalysis product, Poster presentation at American Geographical Union Fall meeting, San Francisco, USA, 9-13 December.

Wanders, N., Karssenberg, D., Bierkens, M. F. P, Roo, A. de, Jong, S. M. de. (2013), The benefits of using remotely sensed soil moisture for large-scale hydrological modelling, Oral presentation at Satellite Soil Moisture validation & application workshop, Frascati, Italy, 1-3 July.

Loon, A. F. van, Tijdeman, E., Wanders, N., Lanen, H. A. J. van, Teuling, A., Uijlenhoet, R. (2013), Upscaling drought information from the catchment scale to the global scale: how seasonality in climate influences drought characteristics, Oral presentation at European Geosciences Union General Assembly, Vienna, Austria, 7-12 April.

Lanen, H. A. J. van, Wanders, N. (2013), Future hydrological drought in the context of water scarcity, Oral presentation at European Geosciences Union General Assembly, Vienna, Austria, 7-12 April.

Wanders, N., Bierkens, M. F. P, Jong, S. M. de, Roo, A. de, Karssenberg, D. (2013), The benefits of using remotely sensed soil moisture in parameter identification of large-scale hydrological models, Poster presentation at European Geosciences Union General Assembly, Vienna, Austria, 7-12 April.

Wanders, N., Karssenberg, D., Bierkens, M. F. P, Parinussa, R. M, Jeu, R. A. M. de, Dam, J. C. van, Jong, S. M. de. (2012), Measuring soil moisture from space; observation quality and applications, Oral presentation at Boussinesq lecture 2012, Amsterdam, The Netherlands, 11 October.

Wanders, N., Karssenberg, D., Bierkens, M. F. P, Parinussa, R. M, Jeu, R. A. M. de, Dam, J. C. van, Jong, S. M. de. (2012), Observation uncertainty of satellite soil moisture products determined with physically-based modelling, Poster presentation at ESA summer School 2012, Frascati, Italy, 30 July - 10 August.

Wanders, N., Karssenberg, D., Bierkens, M. F. P, Parinussa, R. M, Jeu, R. A. M. de, Dam, J. C. van, Jong, S. M. de. (2012), Observation uncertainty of satellite soil moisture products determined with physically-based modelling, Poster presentation at the 5th International workshop on Catchment Hydrological Modelling and Data assimilation, Enschede, The Netherlands, 9-13 July.

Wanders, N., Karssenberg, D., Bierkens, M. F. P, Parinussa, R. M, Jeu, R. A. M. de, Dam, J. C. van, Jong, S. M. de. (2012), Observation uncertainty of satellite soil moisture products determined with physically-based modelling, Oral presentation at European Geosciences Union General Assembly, Vienna, Austria, 22-27 April.

Wanders, N., Karssenberg, D., Jong, S. M de, Bierkens, M. F. P. (2011), Evaluation of SMOS soil moisture level 2A products with modeled near-surface soil moisture over Spain, SMOS 2011 workshop, Arles, France, 26-28 September.

Wanders, N., Lanen, H. A. J. van, Loon, A. F. van. (2010), Köppen Geiger map of the world using WFD data differences with other studies. Oral presentation at WATCH International Workshop on Drought and Large-scale data, Oslo, Norway, 15-17 February.